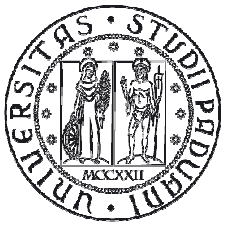

UNIVERSITÀ
DEGLI STUDI
DI PADOVA

Dipartimento di Scienze Chimiche

Sede Amministrativa: Università degli Studi di Padova

SCUOLA DI DOTTORATO DI RICERCA IN SCIENZE MOLECOLARI

INDIRIZZO SCIENZE CHIMICHE

CICLO XXIII

ELECTRONIC INTERACTIONS IN MOLECULAR DIMERS REVEALED BY LINEAR AND NON-LINEAR OPTICAL PROPERTIES

Direttore della Scuola : Ch.mo Prof. Maurizio Casarin

Coordinatore d'indirizzo: Ch.mo Prof. Maurizio Casarin

Supervisore : Prof. Camilla Ferrante

Dottorando : Eleonora Garbin

31 gennaio 2011

Contents

Abstract (English)

Aim of the research project is the investigation of the role played by molecular interactions on the linear and non-linear optical properties in dimeric structures. In particular the two-photon absorption and the excited state dynamic in different dimeric structures is studied, in order to observe to which extent dimerization affects the photophysic of the molecules.

The work is focused on three classes of molecules: i) charge transfer (CT) dimers of the radical cation of tetrathiafulvalene (TTF), ii) molecular dimers of dipolar and quadrupolar molecules, and iii) chemically linked dimers of free base- or Zn(II)-tetraphenylporphyrin (TPP).

The first system, the radical cation of TTF, in appropriate environments, can create a homo-dimer $(TTF^{\bullet+})_2$ in which a charge transfer process occurs between the two monomeric units. Principal aim of the work is the investigation of the two-photon allowed CT electronic state created from the charge transfer process in order to confirm its position and to determine its two-photon absorption (TPA) cross section, together with the non-linear refractive index for these dimers in the same spectral range. These measurements are performed using the femtosecond open- and closed-aperture Z-scan technique in the range 1300-1600 nm, in order to two-photon excite the predicted CT state between 650 nm and 800 nm. Unfortunately, contribution from linear absorption masks the signal of the TPA state.

The excited-state dynamic of both the monomer and the dimer is also investigated, finding two different time constants for both species. The decay of the dimer is globally hundred times faster than the monomer, so it can be a promising material for optical devices requiring fast response.

The second class of investigated molecules are dimers of dipolar or quadrupolar structures, synthesised in the group of Prof. A. Abbotto, University of Milano-Bicocca.

The basic units are built using the pyrrole and the pyridinium rings as donor and acceptor groups, respectively. The dimeric structures are created linking the acceptor endgroups of two dipolar or quadrupolar units through a non-conjugated saturated alkyl chain (3 or 6 carbon atoms linear alkyl chain).

All these compounds are fluorescent, so the two-photon induced fluorescence (TPIF) technique is used to measure their TPA cross section in the range 730-920 nm.

For these dimers, intermolecular interactions are too weak to produce sizeable spectroscopic effects: the one- and two-photon absorption properties of these dimers are almost the sum of those of the corresponding monomers.

In collaboration with the group of Prof. Anna Painelli from the University of Parma, a model is developed to describe the linear and non-linear optical properties of these dimers. This simple effective electronic model, that takes in account the electrostatic interactions between charges, is able to reproduce the experimental shifts of OPA and TPA spectra observed for the dimers when compared to the monomer. Although the changes upon dimerization are small, the theoretical models describe accurately the experimental data.

The third part of the work is focused on the analysis of the energy transfer processes in covalently linked homo- and hetero-dimers of porphyrins connected by a triazine moiety synthesized by the group of Tommaso Carofiglio at the University of Padova. In particular time resolved spectroscopic techniques as time resolved fluorescence measured with time correlated single photon counting (TCSPC) are used for processes in the ns regime and femtosecond transient absorption (TA) for processes in the fs and ps regime. TA experiments exciting at 400 nm and with time resolution of 80 fs are recorded in the laboratory of Prof. N.P. Ernsting at the Humboldt University in Berlin (Germany), while TCSPC measurements and TA experiments exciting at 560 nm are performed at University of Padova.

In these dimers the interactions between the units are weak, so only for the hetero-dimer it was feasible to measure a 95 ps energy transfer process, while time-resolved anisotropy measurements are needed to measure the transfer for the homo-dimers. Moreover, an unexpected dynamic is found for the second excited state decay in the dimers containing a zinc porphyrin: two decay time constants are present instead of a single one as in the monomers. The decay is faster than in the monomers and it may be related to an energy transfer directly in this S_2 state, a process that has never been clearly observed and investigated in details up to now in the literature.

Abstract (Italian)

Scopo del progetto di ricerca è lo studio del ruolo delle interazioni molecolari sulle proprietà ottiche lineari e non-lineari in strutture dimeriche. In particolare, sono stati studiati l'assorbimento a due fotoni e la dinamica degli stati eccitati in dimeri diversi, in modo da osservare in che modo la dimerizzazione influisce sulla fotofisica delle molecole.

Il lavoro si concentra su tre classi di molecole: i) il dimero a trasferimento di carica (CT) del radicale catione del tetratiafulvalene (TTF), ii) i dimeri di molecole dipolari e quadrupolari, e iii), omo e etero dimeri formati dalla porfirina libera tetrafenilporfirina (TPP) o dalla stessa porfirina metallata con Zn(II).

Il primo sistema, il radicale catione del TTF, in ambienti opportuni, forma un omo-dimero $(TTF^{\bullet+})_2$ in cui tra le due unità monomeriche avviene un processo di trasferimento di carica. Obiettivo principale del lavoro è lo studio dello stato elettronico a trasferimento di carica permesso a due fotoni creato dal processo CT, in modo da confermarne la posizione e determinarne la sua sezione d'urto di assorbimento a due fotoni (TPA). Inoltre anche l'indice di rifrazione non-lineare in questi dimeri è stato studiato nello stesso intervallo spettrale. Queste misure sono effettuate usando la tecnica *Z-scan open-* e *closed-aperture*, nell'intervallo spettrale 1300-1600 nm per poter eccitare a due fotoni lo stato CT previsto tra 650 nm e 800 nm. Purtroppo il contributo dell'assorbimento lineare maschera il segnale relativo allo stato TPA.

È stata studiata anche la dinamica degli stati eccitati sia del monomero $TTF^{\bullet+}$ che del dimero $(TTF^{\bullet+})_2$, ottenendo due diverse costanti di tempo per entrambe le specie. Il decadimento del dimero è globalmente cento volte più rapido di quello del monomero, quindi può essere considerato un materiale promettente per dispositivi ottici che richiedano un responso veloce.

La seconda classe di molecole studiate sono dimeri di molecole dipolari e quadrupolari, sintetizzate nel gruppo del Prof. A. Abbotto, Università di Milano-Bicocca. Le unità di base sono costruite usando gli anelli pirrolo e piridina come gruppi donatore e accettore, rispettivamente. Le strutture dimeriche sono create legando i gruppi terminali accettori di due

unità dipolari o quadrupolari con catene alchiliche non coniugate formate da 3 o 6 atomi di carbonio.

Tutti questi composti sono fluorescenti, quindi la tecnica di fluorescenza indotta da assorbimento a due fotoni (TPIF) è utilizzata per misurare la loro sezione d'urto TPA nell'intervallo 730-920 nm.

Per tutti questi dimeri le interazioni intermolecolari sono troppo deboli per produrre effetti spettroscopici considerevoli: le proprietà di assorbimento a uno e due fotoni di questi dimeri sono all'incirca la somma di quelle dei monomeri corrispondenti.

In collaborazione con il gruppo della Prof. Anna Painelli dell'Università di Parma, è stato sviluppato un modello per descrivere le proprietà ottiche lineari e non-lineari di questi dimeri. Questo semplice modello elettronico, che prende in considerazione le interazioni elettrostatiche tra cariche, è in grado di riprodurre gli spostamenti sperimentali degli spettri OPA e TPA osservati per i dimeri se confrontati con i monomeri. Sebbene le variazioni in seguito alla dimerizzazione siano piccole, il modello teorico descrive accuratamente i dati sperimentali.

La terza parte del lavoro è concentrata sull'analisi dei processi di trasferimento di energia in omo- e etero-dimeri di porfirine covalentemente legate da un anello triazinico, sintetizzate dal gruppo di Tommaso Carofiglio presso l'Università di Padova. In particolare, sono state usate tecniche spettroscopiche risolte nel tempo come la fluorescenza risolta nel tempo misurata con la tecnica *time correlated single photon counting* (TCSPC) per processi nel regime dei nanosecondi e l'assorbimento transiente (TA) con risoluzione dei femtosecondi per processi nei femtosecondi e nei picosecondi. Gli esperimenti di TA, eccitando a 400 nm con una risoluzione temporale di 80 fs, sono stati realizzati nei laboratori del Prof. Ernsting alla Humboldt University di Berlino (Germania). Mentre le misure TCSPC e esperimenti TA eccitando a 560 nm sono stati effettuati all'Università di Padova.

In questi dimeri le interazioni tra le unità sono deboli, quindi solo per l'etero-dimero è stato possibile misurare un processo di trasferimento di energia che avviene in 95 ps, mentre misure di anisotropia risolte nel tempo sono necessarie per misurare il trasferimento di energia negli omo-dimeri. Inoltre, è stata trovata una dinamica inaspettata per il decadimento del secondo stato eccitato nei dimeri contenenti una zinco porfirina: sono presenti due costanti di tempo di decadimento al posto di un singolo decadimento come trovato nei monomeri. Il decadimento è più veloce che nel monomero e può essere legato ad un processo di trasferimento di energia direttamente nello stato S_2, un processo che non è stato mai chiaramente osservato e studiato in dettaglio fino ad ora in letteratura.

Introduction

In supramolecular assemblies the presence of intermolecular interactions between the constituent units can modulate or even critically alter the multichromophore response if compared with the relative monomers.

The intermolecular interactions in aggregates can be of different strength, so they can lead to different modification in the optical properties. If the molecules in the array are able to interact, two limiting cases can be recognized: when the interactions are weak and it is always possible to identify which molecule is excited at a given time or when the interactions are strong and the excitation is delocalized over more than one molecule or moves rapidly from molecule to molecule. The main advantage of weak interactions in an array of molecules consist in the retention of most of the properties of the relative monomer, so it is possible to predict the properties of large assemblies before they are synthesised. However, because the interactions are weak, also the effects of these interactions can be small.

The simplest supramolecular structure that can be created is a dimer, made from only two molecules. The generation of these dimers can be a spontaneous processes or the result of the synthesis of supramolecular systems, in which the monomer are chemically bound in well defined positions. Interest in these systems arises from the possibility to use them as active material in opto-electronic devices, like optical switches, optical limiters or systems for energy storage.

In this thesis we investigate the role of molecular interactions on the linear and nonlinear optical properties of dimeric structures. Main goal is understanding in which way the intermolecular interactions act to produce and enhance the optical response with respect to the monomer units from which they arise. Furthermore also the relaxation properties of the electronic excited states are investigated, in order to observe to which extent dimerization affects the photophysic of the monomers.

In particular our research work is focused on three classes of molecules: i) CT dimer of the radical cation of tetrathiafulvalene (TTF), ii) molecular dimers of dipolar and quadrupolar

molecules and iii) chemically linked dimers of free base- or Zn(II)-tetraphenylporphyrin (TPP).

CT dimers of TTF are an example of a molecular system with strong interactions among the molecular units, which present net transfer of an electron from one unit to the other. For this dimer deep modifications of the absorption spectra have been already observed and are expected also for the non-linear optical properties. In the work done during my master thesis it was found a faster excited state dynamic for the CT dimer with respect to the monomer. Now the interest are centred onto the investigation of the presence of a two-photon allowed state created by the CT interaction between the two radical cations forming the dimer, and its influence on the magnitude of the nonlinear-optical response.

The second part of the work is focused on the understanding the role of intermolecular interactions on the TPA cross sections of dimers of dipolar and quadrupolar molecules in order to be able to design structures with enhanced TPA response. These molecules are choosen as building block because they are known to possess already strong two-photon absorption (TPA) cross-sections. In order to maintain the electronic properties of the single molecular units, the single molecules in the dimers are linked by linear alkyl chains, and therefore are characterized by weak interactions between the units.

The third system is represented by homo- and hetero-dimers of porphyrins that can be used as precursor for light-harvesting antennae complexes if an energy transfer process between the units is present. As there are only weak interactions between the porphyrin units, the Förster theory is applied to describe the transfer process. Efficiency and rate of this process will be investigated with ultrafast transient absorption measurements.

The thesis is divided in three sections and six chapters. The first section, composed from Chapter 1 and 2, includes the general theoretical background and the methods used for the investigation of the three different dimeric systems.

In Chapter 1 the theories developed to include the intermolecular interactions in the treatment of the energetic picture of an ensemble of molecules are presented, considering the two limiting cases of weakly and strongly interacting molecules. Moreover the special case in which a spin modification is included will be illustrated. In the same chapter the optical properties investigated are defined and the expected results for the different classes of molecules are stressed out. Chapter 2 concludes the introductory section of this thesis by presenting a description of the experimental techniques employed for the characterization of the linear and non-linear optical response and the excited state dynamic of the investigated systems.

The second section, devoted to molecular dimers having strong interactions, is composed only by Chapter 3, and it summarize the results obtained in the characterization of the CT-dimers of TTF.

The third section, that includes Chapters 4, 5 and 6, reports two different examples of weakly interacting dimers. In Chapter 4 the TPA characterization of dimers of dipolar and quadrupolar molecules are reported, together with an essential state model for the optical spectra of the monomer and the dimers developed in collaboration with the group of Anna Painelli (University of Parma). Chapters 5 and 6 are dedicated to the homo- and hetero-dimers of porphyrins: in chapter 5 the linear characterization is reported, while in Chapter 6 the results of the excited state dynamic measurements are reported. Part of the experimental work for these porphyrin dimers has been performed in the laboratories of Prof. Nikolaus P. Ernsting of the Humboldt Universität zu Berlin (Germany).

SECTION I

GENERAL OVERVIEW

Chapter 1

Optical properties of multichromophoric systems

1.1 Introduction

Understanding the role played by intermolecular interactions in multichromophoric systems is a necessary task for a proper design of arrays of dyes with desired properties. The presence or the absence of specific interactions can modify the properties of the arrays, therefore being able to predict these modifications can be useful to exploit them. As an example, if we focus on the optical properties, new absorption bands can be created or new process as energy transfer can be activated.

In this work different dimeric structures will be analyzed: changing the kind of molecules will lead to different type of interactions characterized by varying strength between the monomeric units.

In this chapter the description starts from the states of two non interacting molecules, and then an interaction is added to the system[1]. Two limiting cases will be considered: in the first one the interaction is weak and can be considered as a perturbation of the system, while in the second case the interaction is strong and leads to a modification of the energetic picture of the system. Moreover we will consider the cases in which a spin modification is included. In the second part of the chapter we will analyze different optical properties and how it is possible to reveal and identify molecular interactions using these properties.

1.2 Non-interacting molecules

Consider two identical molecules, in the Born-Oppenheimer approximation, for which the wavefunctions of the ground state are $\varphi_{1a}\chi_{1a}$ and $\varphi_{2a}\chi_{2a}$, where φ and χ represent electronic and nuclear wavefunctions, respectively, 1 and 2 indentify the molecules, and *a* indicates the ground state.

If the two molecules do not interact, the Hamiltonian for the dimer is just the sum of the Hamiltonians for the individual molecules:

$$\tilde{H} = \tilde{H}_1 + \tilde{H}_2 \qquad (1.1)$$

where $\tilde{H}_1$ operates only on molecule 1 and $\tilde{H}_2$ operates only on molecule 2.
The eigenfunction of the Schrödinger equation, based on Hamiltonian (1.1), for the ground state of the combined system is obtained from the product of the molecular wavefunctions:

$$\Psi_A = \varphi_{1a}\chi_{1a}\varphi_{2a}\chi_{2a} \tag{1.2}$$

If each of the individual molecules has energy E_a in the ground state, the energy of the ground state in the dimer is simply $2E_a$:

$$\begin{aligned}&\langle\varphi_{1a}\chi_{1a}\varphi_{2a}\chi_{2a}|\tilde{H}_1+\tilde{H}_2|\varphi_{1a}\chi_{1a}\varphi_{2a}\chi_{2a}\rangle = \\ &= \langle\varphi_{1a}\chi_{1a}|\tilde{H}_1|\varphi_{1a}\chi_{1a}\rangle\langle\varphi_{2a}\chi_{2a}|\varphi_{2a}\chi_{2a}\rangle + \langle\varphi_{2a}\chi_{2a}|\tilde{H}_2|\varphi_{2a}\chi_{2a}\rangle\langle\varphi_{1a}\chi_{1a}|\varphi_{1a}\chi_{1a}\rangle = \\ &= E_a + E_a = 2E_a\end{aligned} \tag{1.3}$$

If either molecule can be raised to an excited state $\varphi_b\chi_b$ with energy E_b, there are two possible excited states of the dimer, Ψ_1 in which the molecule 1 is excited and Ψ_2 where molecule 2 is excited:

$$\Psi_1 = \varphi_{1b}\chi_{1b}\varphi_{2a}\chi_{2a} \quad \text{or} \quad \Psi_2 = \varphi_{1a}\chi_{1a}\varphi_{2b}\chi_{2b} \tag{1.4}$$

As long as the two molecules do not interact, both Ψ_1 and Ψ_2 are eigenfunctions of the total Hamiltonian, and both states will have the same energy, E_a+E_b. In addition,

$$\langle\Psi_1|\tilde{H}_1+\tilde{H}_2|\Psi_2\rangle = \langle\Psi_2|\tilde{H}_1+\tilde{H}_2|\Psi_1\rangle = 0 \tag{1.5}$$

Ψ_1 and Ψ_2 are stationary states: the excitation has no tendency to hop from one molecule to the other, therefore, without interaction, no energy transfer is possible.
The wavefunction for the excited dimer could also be written as a linear combination of Ψ_1 and Ψ_2:

$$\Psi_B = C_1\Psi_1 + C_2\Psi_2 = C_1\varphi_{1b}\chi_{1b}\varphi_{2a}\chi_{2a} + C_2\varphi_{1a}\chi_{1a}\varphi_{2b}\chi_{2b} \qquad 7.6 \tag{1.6}$$

With $|C_1|^2 + |C_2|^2 = 1$. $|C_1|^2$ is the probability that molecule 1 is excited and $|C_2|^2$ the probability that the molecule 2 is excited. The coefficients can have any magnitude between -1 and +1, and they could be complex numbers. If molecule 1 is excited so that $|C_1|^2$=1, $|C_2|^2$ will remain zero indefinitely and vice versa.

If the two molecule are able to interact, an interaction term has to be included in the Hamiltonian (1.1). Two limit cases can be recognized: when the interaction is weak and it is always possible to identify which molecule is excited at a given time, or when the interaction is strong and the excitation is delocalized over more than one molecule.

1.3 Weakly interacting molecules

In the weak interaction limit, the interaction adds a new term to the Hamiltonian:

$$\tilde{H} = \tilde{H}_1 + \tilde{H}_2 + \tilde{H}' \tag{1.7}$$

Because of the perturbation represented by $\tilde{H}'$, Ψ_1 and Ψ_2 are no longer stationary states. The interaction term allows the system to change between states Ψ_1 and Ψ_2, so excitation energies can move back and forth between the two molecules. When the interaction is weak, it does not affect noticeably the energies of the stationary states and therefore a time-dependent perturbative approach that accounts only for energy transfer between excited molecules can be applied. This mechanism is called resonance energy transfer and was first described by T. Förster in 1948[2].

If the excitation is on molecule 1 at zero time, in Eq. (1.6) C_1=1 and C_2= 0. To obtain the rate of the energy transfer to molecule 2, using time dependent perturbation theory, it is possible to express the coefficient C_2 as a time dependent quantity:

$$\frac{\partial C_2}{\partial t} = -\left(\frac{i}{\hbar}\right) H_{21} \exp\left[\frac{i(E_2 - E_1)t}{\hbar}\right] \tag{1.8}$$

Where E_1 and E_2 are the energies of Ψ_1 and Ψ_2 and H_{21} is the interaction matrix element $\langle \Psi_2 | \tilde{H}' | \Psi_1 \rangle$. To find the probability that the excitation appears on molecule 2 after a time interval τ, it is necessary to obtain $C_2(\tau)$ by integrating Eq. (1.8) from t=0 to τ. If H_{21} is

independent of time and the considered intervals are short enough so that $|C_2|^2 << 1$, Eq (1.8) can be readily integrated:

$$C_2(\tau) = H_{21}(1 - \exp[i(E_2 - E_1)\tau/\hbar])/(E_2 - E_1) \tag{1.9}$$

Eq. (1.9) implies that the probability to find the excitation on molecule 2, given by the product: $C_2^*(\tau)C_2(\tau)$, can have a significant magnitude only if $|E_2 - E_1|$ is close to zero. In resonance energy transfer the energy lost by molecule 1 must match the energy gained by molecule 2 so that the energy is conserved in the overall process, and the Franck-Condon factors must be nonzero for both transitions. The rate of energy transfer for this donor-acceptor pair is given by the time derivative of the probability to find the excitation on molecule 2.

If the rate of energy transfer is measured in a population of many donor-acceptor pairs, the energy difference E_2-E_1 will vary from pair to pair because the molecules could be in many different vibrational states. In addition, the energy distribution will be broadened by relaxations of the excited states and by inhomogeneous interactions with the surroundings. For a collection of donor-acceptor pairs the measured rate will therefore depend on an integral over the distribution of energies. For each value of E_1 in a particular donor acceptor pair it is necessary to integrate over all the possible values of E_2 and viceversa. Taking into account all these possibilities the expression of the rate constant for a set of donor-acceptor is:

$$k_{rt} = \frac{2\pi}{\hbar}\int_{-\infty}^{\infty}|H_{21}|^2 \rho_{s2}(E_1)\rho_{s1}(E_1)dE_1 \tag{1.10}$$

Where $\rho_{s1}(E_1)$ and $\rho_{s2}(E_1)$ are the distributions density of the transition energies for the initial and final states on site 1 and 2, respectively, around the transition energy E_1 of the initial state. As illustrated in Figure 1.1, the transition energy must be the same for both molecules, so $E_1 = E_2$.

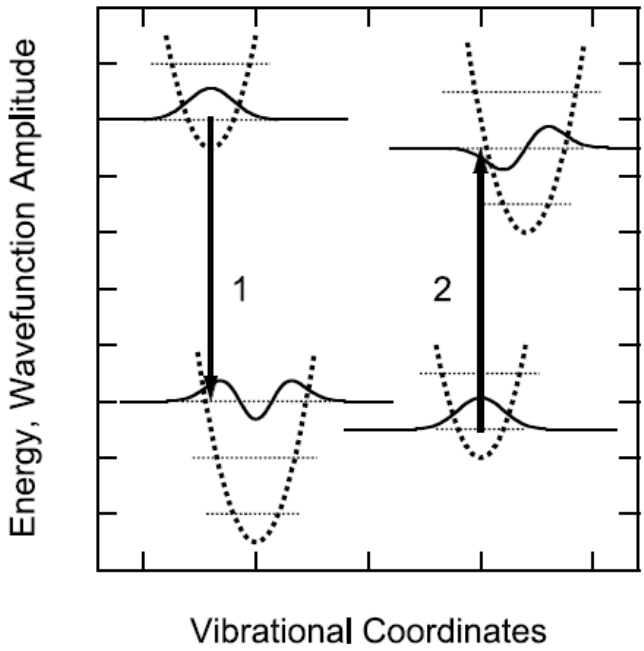

Figure 1.1: Resonance energy transfer requires coupled downward and upward vibronic transitions. The energy lost by molecule 1 must match the energy gained by molecule 2 so that the energy is conserved. The Franck-Condon factors must be nonzero for both transitions. (from Ref. 1)

The interaction matrix element H_{21} must consider the initial and final nuclear states of the energy donor and the acceptor in addition to the electronic wavefunctions, as it is schematically represented in Figure 1.1. However, if the Born-Oppenheimer approximation is valid, the nuclei will not move significantly during the energy migration, so H_{21} can be approximated as a product of a purely electronic interactions matrix element ($H_{21(el)}$) and two nuclear overlap integrals:

$$H_{21} = \langle \varphi_{1a}\varphi_{2b} | \tilde{H}' | \varphi_{1b}\varphi_{2a} \rangle \langle \chi_{1a} | \chi_{1b} \rangle \langle \chi_{2b} | \chi_{2a} \rangle = H_{21(el)} \langle \chi_{1a} | \chi_{1b} \rangle \langle \chi_{2b} | \chi_{2a} \rangle \tag{1.11}$$

The nuclear wavefunctions χ_b and χ_a are composed from many different vibrational states of the systems weighted by the appropriate Boltzmann factor:

$$k_{rt} = \frac{2\pi}{\hbar} |H_{21(el)}|^2 \left[\sum_n \sum_m \frac{\exp(-E_{n(1)}/k_B T)}{Z_1} |\langle \chi_{1m} | \chi_{1n} \rangle|^2 \times \sum_u \sum_w \frac{\exp(-E_{u(2)}/k_B T)}{Z_2} |\langle \chi_{2w} | \chi_{2u} \rangle|^2 \right] \delta(\Delta E_1 - \Delta E_2) \tag{1.12}$$

In this expression $\left|\langle \chi_{1m} | \chi_{1n} \rangle\right|^2$ is the Frank-Condon factor for vibrational levels *n* and *m* in the excited and ground states, respectively, of molecule 1; $E_{n(1)}$ is the energy of vibrational level *n* relative to the zero-point level of excited state of molecule 1, and Z_1 is the vibrational partition function for molecule 1 in the excited state. Similar consideration are valid for molecule 2.

The first two sums in Eq. (1.12) run over all vibrational states of molecule 1 and the second two sums run over all vibrational states of molecule 2. The delta function $\delta(\Delta E_1 - \Delta E_2)$ is 1 if the energy of the downward vibronic transition of molecule 1 is the same as the energy of the upward vibronic transition of molecule 2 and zero otherwise. The delta function ensures that energy is conserved in the overall process.

Considering the electronic interaction energy $H_{21(el)}$, we assume that the dominant electronic interactions are simply Coulombic:

$$H_{21(el)} = \langle \varphi_{1a}\varphi_{2b} | \tilde{H}' | \varphi_{1b}\varphi_{2a} \rangle \approx (f^2/n^2) \iint \varphi_{1a}^* \varphi_{2b}^* \frac{e^2}{r_{21}} \varphi_{1b}\varphi_{2a} dr_1 dr_2 \tag{1.13}$$

Where r_{21} is the distance between electron 1 on molecule 1 and electron 2 on molecule 2, and the integration parameters dr_1 and dr_2 are the coordinates of the two electrons. The factor (f^2/n^2) represents the local-field effect and dielectric screening in a medium with refractive index n, under suitable approximations.

If the molecules have no net charges and are sufficiently far apart relative to the molecular dimensions, the main contribution to $H_{21(el)}$ usually comes from dipole-dipole interactions (see Figure 1.2). $\tilde{H}'$ then can be replaced by the operator for the energy of interaction of electric point dipoles located at the centres of the two chromophores.

$$\tilde{V}' = (f^2/n^2)\left[(\tilde{\mu}_1 \cdot \tilde{\mu}_2)|R_{21}|^{-3} - 3(\tilde{\mu}_1 \cdot R_{21})(\tilde{\mu}_2 \cdot R_{21})|R_{21}|^{-5}\right] \tag{1.14}$$

Where $\tilde{\mu}_1$ and $\tilde{\mu}_2$ are the dipole operators for electrons on the two molecules and R_{21} is the vector from the center of molecule 1 to the center of molecule 2, as depicted in Figure 1.2.

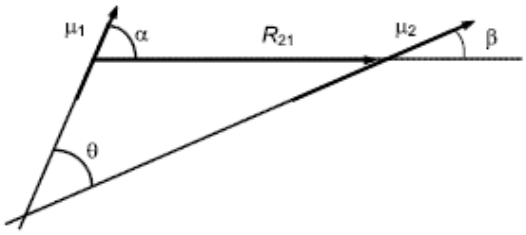

Figure 1.2: Schematic representation of the relative positions of the dipole moment of the two molecules. Definition of the distance between the two units R_{21}, and of the three angles α, β and θ. (from Ref. 1)

If we approximate $\tilde{H}'$ by $\tilde{V}'$, the electronic interaction matrix element $H_{21(el)}$ becomes:

$$H_{21(el)} = \frac{f^2}{n^2}\left(\frac{\langle\varphi_{1b}|\mu_1|\varphi_{1a}\rangle\cdot\langle\varphi_{2b}|\mu_2|\varphi_{2a}\rangle}{|R_{21}|^3} - 3\frac{\left(\langle\varphi_{1b}|\mu_1|\varphi_{1a}\rangle\cdot R_{21}\right)\left(\langle\varphi_{2b}|\mu_2|\varphi_{2a}\rangle\cdot R_{21}\right)}{|R_{21}|^5}\right)$$
$$= \left(\frac{f^2}{n^2}\right)\sqrt{D_{ba(1)}}\sqrt{D_{ba(2)}}\kappa|R_{21}|^{-3} \qquad (1.15)$$

Here $D_{ba(1)}$ and $D_{ba(2)}$ are the dipole strengths for the transitions of the two monomers; θ is the angle between the two transition dipoles; α and β are the angles that the transition dipoles make with R_{21}; and $\kappa = (\cos\theta - 3\cos\alpha\cos\beta)$. In Figure 1.2 the three angles are defined.

Because the orientation factor κ can vary from -2 to +2 depending on the angles θ, α and β, $H_{21(el)}$ can be either positive, negative or zero. Figure 1.3 illustrates the limiting cases. The sign of κ is of no consequence for the rate of energy transfer because the rate depends on $|H_{21(el)}|^2$, which is proportional to κ^2. If the molecules tumble isotropically on a time scale that is fast relative to the lifetime of the excited donor, κ^2 has an average value of 2/3.

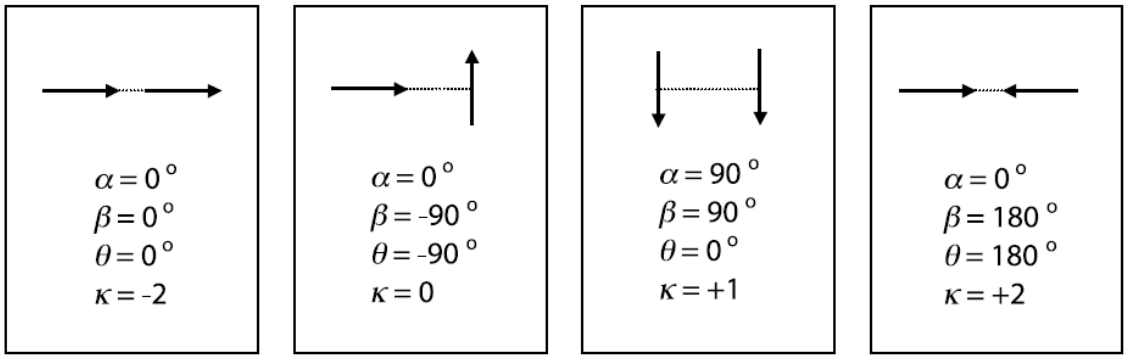

Figure 1.3: Value of κ in four different possible relative positions of the two dipole moments in the units of the dimer.

Eq. (1.12) says that the rate of transitions from state Ψ_1 to state Ψ_2 is proportional to $\left|H_{21(el)}\right|^2$, which according to Eq. (1.15) decreases with the sixth power of R_{21}. To focus on the effect of varying the intermolecular distance, it is useful to write the rate constant for resonance energy transfer (k_{rt}) in the form:

$$k_{rt} = \tau^{-1}\left(\left|R_{21}\right| / R_0\right)^{-6} \tag{1.16}$$

Where τ is the fluorescence lifetime of the energy donor in the absence of the acceptor. R_0 is the center-to-center distance at which k_{rt} is equal to the overall rate constant ($1/\tau$) for the decay of the excited state by all other mechanisms including fluorescence, so that 50% of the decay involves energy transfer. R_0 is called the Förster radius.

Eqs. (1.12) and (1.15) indicate that, for widely separated molecules with a given intermolecular distance and orientation, the rate of resonance energy transfer is proportional to the product of the dipole strengths multiplied by the thermally weighted Franck-Condon factors for the pair of downward and upward vibronic transitions that satisfy the resonance condition. Since these factors are the ones that also affect the spectral distribution of the of absorption spectrum of acceptor 2 and the emission spectrum of donor 1 (in the absence of inhomogeneous broadening), it is possible to relate the energy transfer rate constant to these experimental observables. In so doing one obtains the Forster 's expression for the rate of energy transfer:

$$k_{rt} = \left(\frac{9000\ln(10)\kappa^2 c^4 \Phi}{128\pi^5 n^4 N_A \tau}\right)\left|R_{21}\right|^{-6} J \tag{1.17}$$

Where τ and Φ are the donor's fluorescence lifetime and quantum yield in the absence of energy transfer. $|R_{21}|$ is the distance between donor and acceptor in units of centimeters. J is an overlap integral of the absorption and fluorescence spectra of the donor 1 and acceptor 2, respectively, with the contribution in each frequency interval weighted by ν^{-4}:

$$J = \frac{\int F_1(\nu)\varepsilon_2(\nu)\nu^{-4}d\nu}{\int F_1(\nu)d\nu} \tag{1.18}$$

The acceptor 's molar extinction coefficient ε_2 is in per molar per centimeter units and ν is in per second. So the overlap integral *J* has units of per molar per centimeter seconds to the forth power, and k_{rt} is in units of per second.

Although the Förster radius is evaluated from the overlap of the absorption and emission spectra of the two molecules, the resonance energy transfer mechanism does not involve emission and reabsorption of light. It occurs by a resonance between two states of the entire system.

The dependence of the rate on the sixth power of the intermolecular distance makes resonance energy transfer particularly useful for exploring the locations of binding sites for chromophores on macromolecules. By choosing appropriate donor-acceptor pairs, rates of energy transfer can be measured over distances ranging from 10 to more than 100 Å with a resolution on the order of 1 Å.

In favourable cases, the rate of energy transfer can be obtained by simply measuring the quenching of fluorescence from the donor, as we will see in 1.4.1.

The measured rates depend on the average value of κ^2, which usually is not know accurately. But a fairly limited rotational mobility of the chromophores is sufficient to make the average value of κ^2 approach 2/3, so the uncertainties in the calculated distances becomes relatively small. The motional freedom of the chromophores can be determined from measurements of fluorescence anisotropy or circular dichroism.

1.3.1 Dexter mechanism

In the energy transfer mechanism described by Förster only the spatial parts of the molecular wavefunctions is considered; the spin wavefunctions are implicitly assumed to be constant. So it can be applied only to a transition in which a molecule in an excited singlet state returns to

the singlet ground state and another molecule is elevated to an excited singlet state. It would not allow a transition in which a molecule in an excited triplet state decays to a singlet ground state, raising another molecule from a singlet to a triplet state. This last type of transfer occurs between molecules that are in close contact and it is described by a mechanism proposed by D.L. Dexter (1953)[3].

It is necessary to expand Eq. (1.13) to include spin wavefunctions. φ_{1a} and φ_{1b} are the spatial wavefunctions of molecule 1, φ_{2a} and φ_{2b} the spatial wavefunctions of molecule 2, and σ_{1a}, σ_{1b}, σ_{2a}, and σ_{2b} are the corresponding spin wavefunctions. The overall wavefunctions must be antisymmetric for an exchange of labels between any two electrons:

$$\Psi_1 = 2^{-1/2}\left[\phi_{1b}(1)\sigma_{1b}(1)\phi_{2a}(2)\sigma_{2a}(2) - \phi_{1b}(2)\sigma_{1b}(2)\phi_{2a}(1)\sigma_{2a}(1)\right] \tag{1.19a}$$

And

$$\Psi_2 = 2^{-1/2}\left[\phi_{1a}(1)\sigma_{1a}(1)\phi_{2b}(2)\sigma_{2b}(2) - \phi_{1a}(2)\sigma_{1a}(2)\phi_{2b}(1)\sigma_{2b}(1)\right] \tag{1.19b}$$

where (1) and (2) denote the coordinates of electrons 1 and 2.

With these wavefunctions, the electronic interaction matrix element becomes:

$$H_{21(el)} = H_{21}^{Coulomb} + H_{21}^{exchange} \tag{1.20}$$

Where

$$\begin{aligned} H_{21}^{Coulomb} &= \langle\phi_{1a}(1)\phi_{2b}(2)|\tilde{H}_{21}|\phi_{1b}(1)\phi_{2a}(2)\rangle\langle\sigma_{1a}(1)|\sigma_{1b}(1)\rangle\langle\sigma_{2b}(2)|\sigma_{2a}(2)\rangle \\ &= \langle\phi_{1a}(1)\phi_{2b}(2)|\frac{e^2}{r_{21}}|\phi_{1b}(1)\phi_{2a}(2)\rangle\langle\sigma_{1a}(1)|\sigma_{1b}(1)\rangle\langle\sigma_{2b}(2)|\sigma_{2a}(2)\rangle \end{aligned} \tag{1.21}$$

and

$$\begin{aligned} H_{21}^{exchange} &= -\langle\phi_{1a}(2)\phi_{2b}(1)|\tilde{H}_{21}|\phi_{1b}(1)\phi_{2a}(2)\rangle\langle\sigma_{2b}(1)|\sigma_{1b}(1)\rangle\langle\sigma_{1a}(2)|\sigma_{2a}(2)\rangle \\ &= -\langle\phi_{1a}(2)\phi_{2b}(1)|\frac{e^2}{r_{21}}|\phi_{1b}(1)\phi_{2a}(2)\rangle\langle\sigma_{2b}(1)|\sigma_{1b}(1)\rangle\langle\sigma_{1a}(2)|\sigma_{2a}(2)\rangle \end{aligned} \tag{1.22}$$

The term $H_{21}^{Coulomb}$, which is the one that the Förster theory considers, is called the *Coulomb* interaction. It pertains to a process where each electron remains on its original molecule (Figure 1.4a) and there must be no change of spin on either molecule.

The term $H_{21}^{exchange}$ is called the *exchange* interaction. Here the electrons move between the two molecules and their electron spins are interchanged, as shown in Figure 1.4b. This condition is consistent with either singlet or triplet energy transfer.

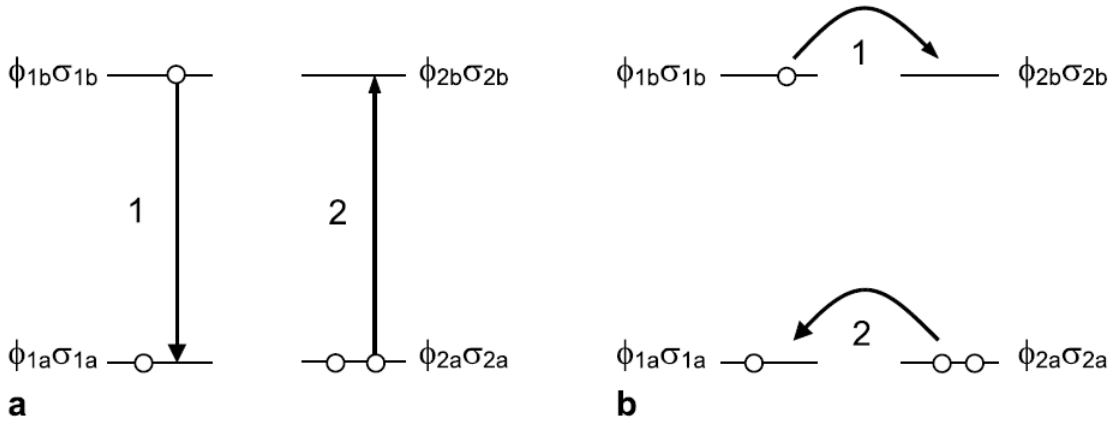

Figure 1.4: a) The Coulomb interaction describe a transition in which each electron remains on its original molecule. b)The exchange interaction represents a transition in which electrons are interchanged between the molecules. (From Ref 1)

$H_{21}^{exchange}$ in Eq. (1.22) can be appreciable only if there is significant overlap of the two molecular orbitals. The magnitude of $H_{21}^{exchange}$ generally is taken to fall off approximately as $\exp(-R_{21}/L)$, where R_{21} is the intermolecular distance between the two molecules and *L* is on the order of 1Å. $H_{21}^{Coulomb}$ therefore usually dominates over $H_{21}^{exchange}$ as long as the intermolecular distance is more than 4 or 5Å.

1.4 Strongly interacting molecules

The second limiting case is when the molecules are so close together that the time required for energy to hop from one molecule to the other becomes shorter than the time that is necessary to detect which molecule is excited at a given time.

The term exciton means an excitation that is delocalized over more than one molecule. Exciton interactions, the intermolecular interactions that cause the excitation to spread over several molecules, are physically the same as the weak interactions in resonance energy transfer. They are just stronger because the molecules are closer or have larger transition dipoles. The absorption and the fluorescence of systems with excitonic interactions can be significantly different from those of the individual molecules. However the molecules are not so close that the overlap of the molecular orbitals allows new bond to form.

Two different kind of excitons can be defined: Frenkel excitons, where an electron that has been excited to a normally empty molecular orbital remains associated with a vacancy or "hole" in a normally filled orbital as they migrate form one molecule to another; and Wannier excitons, where the electron and hole can be on separate molecules, as in the case of semiconductor materials.

The ground state and excited state wavefunctions of the dimer are described as combinations of the individual molecular wavefunctions:

$$\Psi_A = \varphi_{1a}\chi_{1a}\varphi_{2a}\chi_{2a} \tag{1.23}$$

And

$$\Psi_B = C_1\Psi_1 + C_2\Psi_2 = C_1\varphi_{1b}\chi_{1b}\varphi_{2a}\chi_{2a} + C_2\varphi_{1a}\chi_{1a}\varphi_{2b}\chi_{2b} \tag{1.24}$$

The basis states Ψ_1 and Ψ_2 for Ψ_B represent states in which the excitation is localized on molecule 1 or 2, respectively. These are not stationary states because excitations hop back and forth between the two molecules.

Let us consider how the energies of the ground and excited states described by Eq. (1.23) and (1.24) depend on the interaction term in the Hamiltonian $\tilde{H}'$, as defined in Eq. 1.7. The electronic energy of the ground state is :

$$E_A = \langle \varphi_{1a}\varphi_{2a} | \tilde{H}_1 + \tilde{H}_2 + \tilde{H}' | \varphi_{1a}\varphi_{2a} \rangle = E_{1a} + E_{2a} + \langle \varphi_{1a}\varphi_{2a} | \tilde{H}' | \varphi_{1a}\varphi_{2a} \rangle \tag{1.25}$$

Where E_{1a} and E_{2a} are the energies of the individual molecules in their ground states. Similarly the electronic energy of the excited state is:

$$\begin{aligned} E_B &= \langle C_1\Psi_1 + C_2\Psi_2 | \tilde{H}_1 + \tilde{H}_2 + \tilde{H}' | C_1\Psi_1 + C_2\Psi_2 \rangle \\ &= |C_1|^2 E_1 + |C_2|^2 E_2 + \langle C_1\Psi_1 + C_2\Psi_2 | \tilde{H}' | C_1\Psi_1 + C_2\Psi_2 \rangle \end{aligned} \tag{1.26}$$

Where $E_1 = E_{1b} + E_{2a}$ and $E_2 = E_{1a} + E_{2b}$.

The energies of both the ground and excited states thus differs from the corresponding energies of a systems in which the molecules do not interact.

If molecules 1 and 2 are uncharged and have only small permanent dipole moments, the third term in Eq. (1.25) will be relatively small and the energy of the ground state will be approximately $E_{1a} + E_{2a}$, so nearly the same as in non-interacting molecules.

To evaluate the energy of the excited state E_B and to see how it is related to the coefficients C_1 and C_2 it is necessary to write the time-independent Schrödinger equation for the excited dimer:

$$\left(\tilde{H}_1 + \tilde{H}_2 + \tilde{H}'\right)\left(C_1\Psi_1 + C_2\Psi_2\right) = E_B\left(C_1\Psi_1 + C_2\Psi_2\right) \tag{1.27}$$

From this expression is possible to obtain two equations relating E_B to C_1 and C_2:

$$C_1\left(H_{11} - E_B\right) + C_2 H_{12} = 0 \tag{1.28a}$$

and

$$C_1 H_{21} + C_2\left(H_{22} - E_B\right) = 0 \tag{1.28b}$$

Where

$$H_{11} \equiv \left\langle \Psi_1 \middle| \tilde{H}_1 + \tilde{H}' \middle| \Psi_1 \right\rangle = E_1 + \left\langle \Psi_1 \middle| \tilde{H}' \middle| \Psi_1 \right\rangle \tag{1.29a}$$

$$H_{22} \equiv \left\langle \Psi_2 \middle| \tilde{H}_2 + \tilde{H}' \middle| \Psi_2 \right\rangle = E_2 + \left\langle \Psi_2 \middle| \tilde{H}' \middle| \Psi_2 \right\rangle \tag{1.29b}$$

And

$$H_{21} \equiv \left\langle \Psi_2 \middle| \tilde{H}' \middle| \Psi_1 \right\rangle, \quad H_{12} \equiv \left\langle \Psi_1 \middle| \tilde{H}' \middle| \Psi_2 \right\rangle \tag{1.29c}$$

Because the Hamiltonian operator is Hermitian, $H_{12} = H_{21}^*$.

A trivial solution to Eq (1.28) is $C_1 = C_2 = 0$.

Another non zero solution can be obtained only if the secular determinant is zero:

$$\begin{vmatrix} \left(H_{11} - E_B\right) & H_{21} \\ H_{21} & \left(H_{22} - E_B\right) \end{vmatrix} = 0 \qquad (8.9) \tag{1.30}$$

Solving Eq. (1.30), two solutions can be obtained for E_B, called respectively E_{B+} and E_{B-} Putting these solution in Eqs. (1.29a) and (1.29b) it is possible to find the corresponding values of C_1 and C_2 and the corresponding eigenfunctions Ψ_{B+} and Ψ_{B-}.

The general solution are written as:

$$\Psi_{B+} = \sqrt{\frac{(1+s)}{2}}\Psi_1 + \sqrt{\frac{(1-s)}{2}}\Psi_2 \qquad E_{B+} = E_0 + \frac{1}{2}\sqrt{\delta^2 + 4H_{12}^2} \tag{1.31a}$$

$$\Psi_{B-} = \sqrt{\frac{(1-s)}{2}}\Psi_1 - \sqrt{\frac{(1+s)}{2}}\Psi_2 \qquad E_{B-} = E_0 - \frac{1}{2}\sqrt{\delta^2 + 4H_{12}^2} \tag{1.31b}$$

Where

$$s = \delta / \sqrt{\delta^2 + 4H_{12}^2} \tag{1.31c}$$

E_0 is the average of the energies of the two basis states $E_0 = (H_{11} + H_{22})/2$ and δ is the difference between these energies $\delta = (H_{11} - H_{22})$.

If the two basis states are widely separated in energy ($|\delta| >> |H_{21}|$) so $s \approx 1$ we obtain that

$$\Psi_{B+} \to \Psi_1 \qquad E_{B+} \to H_{11} \tag{1.32}$$
$$\Psi_{B-} \to \Psi_2 \qquad E_{B-} \to H_{22}$$

If the basis states are located close together ($|\delta| << |H_{21}|$) so $s \approx 0$ then the solutions become:

$$\Psi_{B+} = 2^{-1/2}(\Psi_1 + \Psi_2) \qquad E_{B+} = E_0 + H_{21} \tag{1.33}$$
$$\Psi_{B-} = 2^{-1/2}(\Psi_1 - \Psi_2) \qquad E_{B-} = E_0 - H_{21}$$

In this case, the two excited states are symmetric and antisymmetric combinations of Ψ_1 and Ψ_2, with an energy difference equal to $2H_{21}$. The energies of the two states splits apart to lie above and below E_0 by $\pm H_{21}$. this resonance splitting of the energies is a purely quantum mechanical effect that result from mixing of the two basis states and distribution of the excitation over the two molecules.

So for each absorption band of the individual molecules, the dimer has two absorption bands representing the transitions $\Psi_A \to \Psi_{B+}$ and $\Psi_A \to \Psi_{B-}$. The former transition has an energy of $(H_{11} + H_{22})/2 + H_{21}$, while the latter has an energy of $(H_{11} + H_{22})/2 - H_{21}$, so which energy is higher depends on the sign of H_{21}.

Once the coefficients C_1 and C_2 for the excited state are known, the transition dipoles $\vec{\mu}_{BA\pm}$ and dipole strengths $D_{BA\pm}$ of the two exciton band scan be related to the spectroscopic properties of the monomers:

$$\vec{\mu}_{BA\pm} = \langle \Psi_{B\pm} | \vec{\mu}_1 + \vec{\mu}_2 | \Psi_A \rangle = C_{1(B\pm)}\vec{\mu}_1 + C_2(B\pm)\vec{\mu}_2 \tag{1.34}$$

And

$$D_{BA\pm} = C^2_{1(B\pm)}D_{ba(1)} + C^2_{2(B\pm)}D_{ba(2)} + 2C_{1(B\pm)}C_{2(B\pm)}\vec{\mu}_{ba(1)} \cdot \mu_{ba(2)} \tag{1.35}$$

Where $\vec{\mu}_{ba(1)}$ and $\vec{\mu}_{ba(2)}$ are the transition dipole vectors of the two individual molecules, $D_{ba(1)}$ and $D_{ba(2)}$ are the monomer's dipole strengths.

For a dimer of two identical molecules ($\delta = 0$ and $D_{ba(1)} = D_{ba(2)} = D_{ba}$), Eqs (1.34) and (1.35) become:

$$\vec{\mu}_{BA+} = 2^{-1/2}\left(\vec{\mu}_{ba(1)} + \vec{\mu}_{ba(2)}\right) \tag{1.36a}$$

$$\vec{\mu}_{BA-} = 2^{-1/2}\left(\vec{\mu}_{ba(1)} - \vec{\mu}_{ba(2)}\right) \tag{1.36b}$$

$$D_{BA+} = D_{ba}\left(1 + \cos\theta\right) \tag{1.36c}$$

$$D_{BA-} = D_{ba}\left(1 - \cos\theta\right) \tag{1.36d}$$

The transition dipoles of the dimer's two bands are proportional to the vector sum and difference of the transition dipoles of the monomers, as shown in Eqs. (1.36a) and (1.36b) respectively. D_{BA+} and D_{BA-} can range from 0 to $2D_{ba}$ depending on the angle θ between the transition dipoles of the monomers.

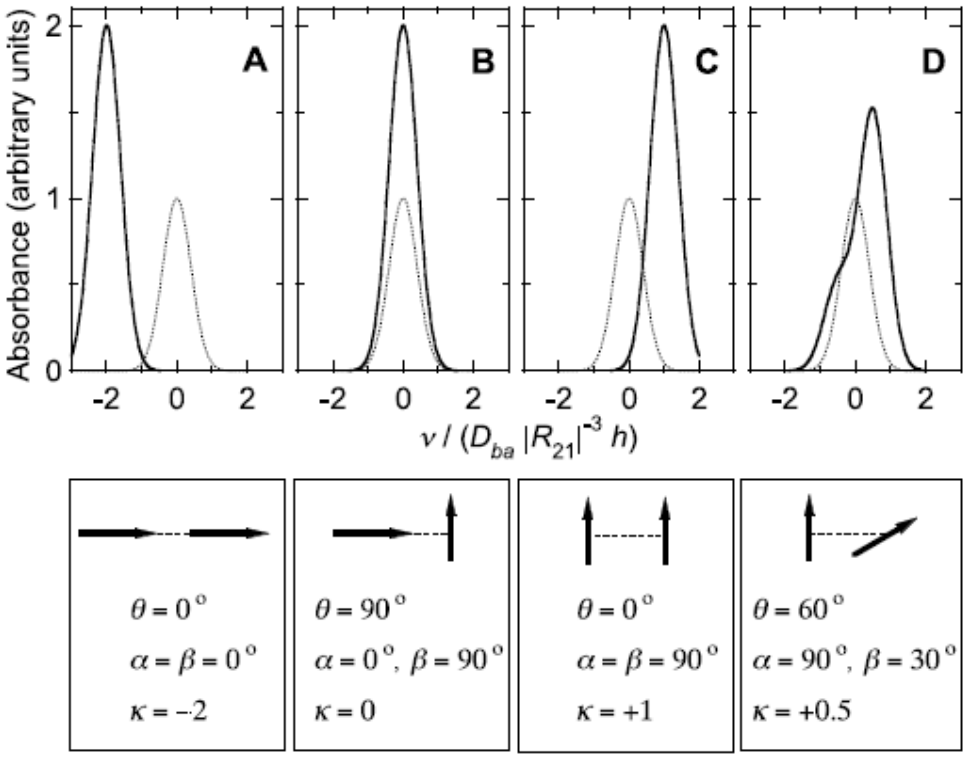

Figure 1.5: Calculated absorption spectra of homodimers with four different geometries. The absorption spectrum of the monomer is shown in a dotted line and the spectrum of the dimer with a solid line. The angles α, β and θ and the parameter κ are defined in Section 1. 2. (from Ref. 1)

Figure 1.5 illustrates the expected absorption spectra for dimers of identical molecules in different arrangements. If the transition dipoles of the monomers are parallel and are aligned along the intermolecular axis (Panel A) H_{21} is negative. Ψ_{B+} then lies lower in energy than Ψ_{B-} and all the dimer‘s dipole strength is associated with excitation to Ψ_{B+}. The higher energy excitation to Ψ_{B-} has no dipole strength because the transition dipoles of the monomers enter with opposite signs and cancel. These kind of dimers are called J aggregate.

If the two transition dipoles are perpendicular (Panel B) H_{21} is zero and the dimer's two excited states have the same energy. Transitions to both states are allowed but are indistinguishable. Instead, if the dipoles are parallel to each other but both are perpendicular to the intramolecular axis (Panel C), H_{21} is positive. In this case Ψ_{B+} is the higher energy state and all of the dimer's dipole strength goes to the higher energy excitation. This is the definition for H aggregates, Finally, in Panel D is shown an arrangement of the monomers in which both of the dimer's absorption bands have significant dipole strength. In general, $\theta < 54.7°$ for J aggregates and $\theta > 54.7°$ for H aggregate[4].

1.4.1 Charge transfer complexes

A special treatment should be applied when a charge transfer (CT) process is present, among strongly interacting molecular systems.

Such systems can be described by using the Hubbard model for strongly interacting electrons in a solid. Despite its simplicity, the Hubbard model is one of the most important model in theoretical physics and it is capable to describe different phenomena in molecular crystals formed by radical ions like: metal-to-insulator transitions, antiferromagnetism, ferrimagnetism, ferromagnetism, and superconductivity[5].

The exact treatment of electronic correlation is very complex, so in the Hubbard model the repulsion between electrons is ignored, except when electrons are in the same site.

In this model only two parameters are necessary for the characterization of the systems: the electronic correlation energy *U*, i.e. the energy necessary to arrange two electrons with paired spin in the same site, and the charge transfer integral *t*, accounting for the hopping of an electron between nearest-neighbour sites with preservation of spin orientation.

The simplest possible system is a dimer of two identical open-shell conjugated molecules interacting through their π-electron systems (symmetric dimer). Each molecule is assumed to have one electron in their frontier orbital (HOMO for the cationic molecules or LUMO for the anionic molecules).

In the case of radical cations the CT excitations correspond to:

$$\left|D^{+\bullet}D^{+\bullet}\right\rangle \xrightarrow{\hbar\omega_{CT}} \left|D^{0}D^{2+}\right\rangle \tag{1.37}$$

The CT processes in this type of open-shell molecules do not involve excitations of electrons to higher orbitals, but just all the possible distribution of the two unpaired electrons in the two frontier orbitals. The site energy difference is zero and electrons move between partially filled molecular orbitals that have the same energy

Such systems can be described by an electronic Hamiltonian:

$$H_E = -t\sum_{\sigma}\left(a_{1\sigma}^{+}a_{2\sigma} + a_{2\sigma}^{+}a_{1\sigma}\right) + U\left(n_{1\uparrow}n_{1\downarrow} + n_{2\uparrow}n_{2\downarrow}\right) \tag{1.38}$$

in which $a_{i\sigma}^{+}$ and $a_{i\sigma}$ are the creation and the annihilation operators for an electron in the i^{th} (i = 1,2) site with spin $\sigma = \uparrow, \downarrow$, while $n_{i\sigma}$ is the number operator, defined as:

$$n_{i\sigma} = a_{i\sigma}^{+}a_{i\sigma} \tag{1.39}$$

In Table 1.1 are summarized the eigenvectors and eigenvalues for the time independent Schrödinger equation for Hamiltonian (1.38) defined on a basis set of six wavefunctions [6,7].

Table 1.1: Eigenvectors and eigenvalues of the Hubbard dimer Hamiltonian

Basis set	Eigenvectors	Eigenvalues
$\left\|S^0\right\rangle = \frac{1}{\sqrt{2}}\left(a_{1\uparrow}^{+}a_{2\downarrow}^{+} + a_{2\uparrow}^{+}a_{1\downarrow}^{+}\right)\left\|0\right\rangle$	$\left\|1\right\rangle = b_1\left\|S^0\right\rangle + c_1\left\|CT_+\right\rangle = A_1^{+}\left\|0\right\rangle$	$E_1 = E_-$
$\left\|CT_+\right\rangle = \frac{1}{\sqrt{2}}\left(a_{1\uparrow}^{+}a_{1\downarrow}^{+} + a_{2\uparrow}^{+}a_{2\downarrow}^{+}\right)\left\|0\right\rangle$	$\left\|2\right\rangle = b_2\left\|S^0\right\rangle + c_2\left\|CT_+\right\rangle = A_2^{+}\left\|0\right\rangle$	$E_2 = E_+$
$\left\|CT_-\right\rangle = \frac{1}{\sqrt{2}}\left(a_{1\uparrow}^{+}a_{1\downarrow}^{+} - a_{2\uparrow}^{+}a_{2\downarrow}^{+}\right)\left\|0\right\rangle$	$\left\|3\right\rangle = \left\|CT_-\right\rangle = A_3^{+}\left\|0\right\rangle$	$E_3 = U$
$\left\|T_1\right\rangle = a_{1\uparrow}^{+}a_{2\uparrow}^{+}\left\|0\right\rangle$	$\left\|4\right\rangle = \left\|T_1\right\rangle = A_4^{+}\left\|0\right\rangle$	$E_4 = 0$
$\left\|T_0\right\rangle = \frac{1}{\sqrt{2}}\left(a_{1\downarrow}^{+}a_{2\downarrow}^{+} - a_{2\uparrow}^{+}a_{1\downarrow}^{+}\right)\left\|0\right\rangle$	$\left\|5\right\rangle = \left\|T_0\right\rangle = A_5^{+}\left\|0\right\rangle$	$E_5 = 0$
$\left\|T_{-1}\right\rangle = a_{1\downarrow}^{+}a_{2\downarrow}^{+}\left\|0\right\rangle$	$\left\|6\right\rangle = \left\|T_{-1}\right\rangle = A_6^{+}\left\|0\right\rangle$	$E_6 = 0$

The coefficients $b_{1,2}$ and $c_{1,2}$ have the following values:

$$b_{1,2} = \left[1 + \left(\frac{E_{1,2}}{2t}\right)^2\right]^{-1/2} \tag{1.40}$$

$$b_{1,2}^2 + c_{1,2}^2 = 1 \tag{1.41}$$

The energy eigenvalues E_+ and E_- are:

$$E_{\pm} = \frac{1}{2}\left(U \pm \sqrt{U^2 + 16t^2}\right) \tag{1.42}$$

The states $|1\rangle, |2\rangle$ and $|3\rangle$ are singlet states, while $|4\rangle$, $|5\rangle$ and $|6\rangle$ are triplet states. States $|1\rangle$ and $|2\rangle$ have both *gerade* symmetry; state $|3\rangle$ has *ungerade* symmetry, and it has energy U, while states $|4\rangle$, $|5\rangle$ and $|6\rangle$ are not affected by the Hubbard Hamiltonian and their energy remains zero. In this model the zero energy corresponds to the energy of two electrons on two different sites.

Defining A_n^+ and A_n as the creation and annihilation operators for the eigenstates of the Hamiltonian H_E, the latter can be rewritten as:

$$H_E = \sum_n E_n A_n^+ A_n \tag{1.43}$$

In this model, in which only one electron for site is considered, the electric dipole moment operator is expressed in the point charge approximation as:

$$\mu = -\frac{1}{2} ed\left(n_1 - n_2\right) \tag{1.44}$$

In which $n_i = n_{i\uparrow} + n_{i\downarrow}$ with $i = 1,2$, e is the electron elementary charge and d is the intermolecular distance between the two molecules in the dimer.

Eq. (1.44) can be expressed in terms of the operators A_n^+ and A_n:

$$\mu = -ed\left[c_1\left(A_1^+A_3 + A_3^+A_1\right) + c_2\left(A_2^+A_3 + A_3^+A_2\right)\right] = \tag{1.45}$$
$$= \mu_{13}\left(A_1^+A_3 + A_3^+A_1\right) + \mu_{23}\left(A_2^+A_3 + A_3^+A_2\right)$$

Using Eq. (1.45) to account for interactions with and external electromagnetic field under the dipolar approximation, it turns out that the only one-photon allowed transitions are those from the ground state $|1\rangle$ to the antisymmetric CT state $|3\rangle$ and from the latter to the symmetric CT state $|2\rangle$, as shown in Figure 1.6. Instead the transition from the ground state $|1\rangle$ to the symmetric CT state $|2\rangle$ is two photon allowed.

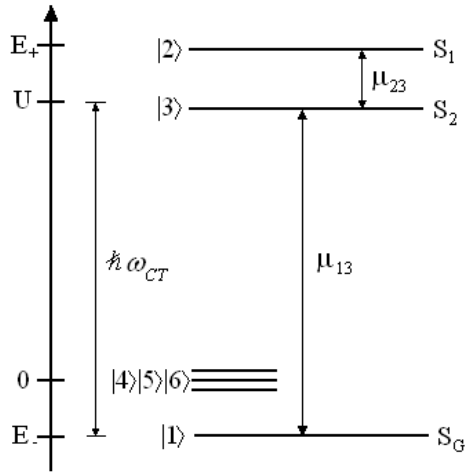

Figure 1.6: Energy levels and transition dipole moments in the Hubbard model for the symmetric dimer

The only one photon allowed transition that involves these CT states occurs at frequency:

$$\omega_{CT} = \omega_{13} = \frac{1}{2\hbar}\left[U + \left(U^2 + 16t\right)^{1/2}\right] \tag{1.46}$$

So that the position of the CT transition is directly linked to the value of correlation energy *U* and the charge transfer integral *t*.

The Hubbard Hamiltonian can be further generalized by introducing also the electron-vibration interactions (Peierls-Hubbard model)[8,9], to account for the vibronic structure of the linear and non linear absorption spectra.

1.5 Optical properties of interacting systems

In the previous paragraphs different kind of interactions between molecules are described, as well as their effect on the electronic properties of these systems. The presence and the kind of interaction occurring in selected molecular dimers can be revealed using different optical properties. In particular we have explored the linear absorption and emission properties, the two photon absorption, and the excited state dynamic.

In Chapter 2 the techniques used to measure these optical properties in different samples are presented, in the following, instead, we point out the main features that are expected for these optical properties based on the models previously described.

1.5.1 Linear absorption and fluorescence

The presence of strong or weak interactions among the electronic states of single moieties in a dimer can be readily assessed through the investigation of the linear absorption and fluorescence spectra of the monomer alone and the dimer.

In strongly interacting dimers, as shown by the model summarized in paragraph 1.3, we expect completely different linear spectra for the dimer with respect to the monomers, since the position in energy of the excited states differs noticeably for the two systems. For each absorption band of the monomer, the dimer can have up to two absorption bands separated in energy by $2H_{21}$ representing the transitions $\Psi_A \rightarrow \Psi_{B+}$ and $\Psi_A \rightarrow \Psi_{B-}$. The presence of one or two bands for the dimer is related to the symmetry properties of the dimer itself.

New transition can be added to the spectra, for example in the case of charge transfer dimers, as we have seen in 1.3.1 using the Hubbard model. An example of CT dimers will be analyzed in Chapter 3.

In weakly-interacting dimers, instead, the transition energies for linear absorption and fluorescence are retained, and the spectra of monomers and dimer show bands at the same frequency. On the other hand the fluorescence intensity can differ significantly, because it depends on the excited state dynamics, which in turn is affected by the energy transfer processes described by the Förster model. This is particularly true for heterodimers: even if the absorption spectrum is just the sum of the absorption spectra of the monomers, this is not true for the emission spectrum. If there is the presence of an energy transfer process, a reduction in the fluorescence quantum yield (FQY) of the donor is expected and at the same time an increment in the FQY of the acceptor could also appear.

We focus the attention on the reduction of the FQY of the donor, arising from excitation transfer to the acceptor, instead that dissipation by spontaneous emission. The FQY of the

isolated donor molecule can be defined as the ratio between the rate constant for radiative decay and the sum of all other rate constants accounting for all the decay processes (radiative, intersystem crossing, internal conversion) available for the emitting state[10].

$$\Phi_D = \frac{k_{rad}}{k_{rad} + k_{isc} + k_{ic}} \tag{1.47}$$

When the donor is inserted in the dimer an additional decay process is possible: energy transfer to the acceptor. The formula for the FQY is then suitably modified:

$$\Phi_{DA} = \frac{k_{rad}}{k_{rad} + k_{isc} + k_{ic} + k_{trans}} \tag{1.48}$$

If the efficiency of the energy transfer process is defined as the ratio between the rate constant due to energy transfer and the sum of all the other rate constants, it is possible to relate this efficiency to the FQY of the donor alone and in the dimer:

$$\Phi_{trans} = \frac{k_{trans}}{k_{rad} + k_{isc} + k_{ic} + k_{trans}} = 1 - \frac{\Phi_{DA}}{\Phi_D} \tag{1.49}$$

Examples of the linear optical properties of low interacting dimers will be reported in Chapter 4 and 5. In Chapter 5 the energy transfer efficiency in a heterodimer of porphyrins is calculated as presented here from the FQY of the donor alone and in the dimer.

In homo-dimers the fluorescence intensity is not affected by the energy transfer process, because the fluorescence emission of donor and acceptor are spectrally coincident, therefore, if a decrease of the dimer FQY appears, it should be promoted by new relaxation pathways made available by the dimer structure.

1.5.2 Two-photon absorption

Two-photon absorption (TPA) is a third order dissipative process characterized by the simultaneous absorption of two photons from a light source that excites a molecule from the ground state to a two-photon allowed excited state[11].

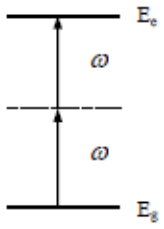

Figure 1.7: Scheme of two-photon absorption process.

If we consider a light beam with frequency ω propagating in the z direction through a system, the variation of the incident intensity with the optical path is given by:

$$\frac{dI}{dz} = -\alpha \cdot I - \beta \cdot I^2 - \gamma \cdot I^3 - \ldots \tag{1.50}$$

Where α, β, and γ are the one-, two-, and three-photon absorption coefficients, respectively. At low intensities, only the first term becomes important and the others can be neglected because their relative values are $\alpha >> \beta >> \gamma$.

These coefficients can be related with the imaginary part of the odd-order dielectric susceptibility $\chi^{(1)}$, $\chi^{(3)}$ and $\chi^{(5)}$, respectively. In particular for the TPA process it can be demonstrated that

$$\beta = \frac{2\omega}{c^2 \varepsilon_0 n^2} \cdot \left[\mathrm{Im}\, \chi^{(3)} \left(-\omega ; \omega , -\omega , \omega \right) \right] \tag{1.51}$$

Where c is the light speed, ε_0 is the vacuum permittivity and n is the refraction index of the medium at frequency ω.

In material systems with known two-photon active molecule concentration, the TPA is commonly expressed in terms of cross section per single active molecule: σ_{TPA}, expressed in Göppert-Mayer units (1GM = 10^{-50} cm^4 x s x $photons^{-1}$ x $molecule^{-1}$) and simply related to β by the relation:

$$\sigma_{TPA} = \frac{\hbar \omega}{N} \beta \tag{1.52}$$

Where N is the number density of active molecules.

Molecules with high TPA cross section can be exploited in optical limiting devices, in photodynamic therapy for the local treatment of tumours and in micro- and nano-fabrication. Exploiting the intermolecular interactions between the units in a dimer, it is possible to obtain σ_{TPA} values that are higher than two times the σ_{TPA} of the monomers. Moreover, a model for the prediction of the σ_{TPA} in dimeric structures is needed to choose the best molecules and the best linkers between the units to obtain an enhanced response. In Chapter 4, two different classes of molecules are taken into consideration: dipolar and quadrupolar chromphores, that are known to have high TPA response[12]. Different dimers are synthesized with these monomeric units and their TPA properties are investigated. A model for the prediction of the two-photon transition's position in frequency and of the σ_{TPA} is discussed in relation with the experimental results.

Moreover it is possible to detect the position of two-photon allowed states, that are not visible in the one-photon linear spectra. In Chapter 3 TPA measurements on a CT dimer are performed to confirm the position of the two-photon allowed state predicted by the Hubbard theory, as well as to asses the magnitude of the third order non-linear response of these molecular systems.

1.5.3 Excited state dynamic

Applying a short laser pulse of frequency ω corresponding to an electronic transition of a molecule, it is possible to create population in the relative excited state. After the pulse, the population in the excited state decays into other excited states of lower energy or into the ground state with characteristic time constants. To detect these decays is necessary to use pulses shorter than the lifetime of the excited states involved in the process. In Chapter 2 the pulses used to excite the molecules and the experimental procedures used to follow the decays of population from excited states are described.

When comparing the excited state dynamic of a dimer with strong interactions between the units to the dynamic of the relative monomer, a complete different picture is expected. The position in energy and the number of the excited states is different due to the excitonic interaction. Moreover, the higher number of deactivation pathways leads often to a fastest dynamic in dimers and multichromophores with respect to the monomers. An example of excited state dynamic in high interacting systems is reported in Chapter 3, where a CT dimer is examined.

When instead the interactions are weak, the position in energy of the excited states of the monomers is retained, so the same dynamic is expected. In particular for homodimers no

information about the presence of an energy transfer between the units can be gained from excited state dynamic measurements. The forward and backward rates of energy migration between the two units are equal thus the observed decay becomes invariant to the energy migration processes.

Different is the case of heterodimers, in which the energy transfer , if present, is directed from the donor to the acceptor that absorb and emit in different spectral regions. In this case a reduction of the lifetime of the donor is an index of the presence of the energy transfer. Experimentally the transient bands relative to the donor decrease in intensity, while the ones of the acceptor increase with the same time constant.

An estimate of the transfer efficiency can be obtained from the excited state lifetime of the donor alone (τ_D) and in the dimer (τ_{DA}):

$$\frac{1}{\tau_D} = k_{rad} + k_{isc} + k_{ic} \tag{1.53a}$$

$$\frac{1}{\tau_{DA}} = k_{rad} + k_{isc} + k_{ic} + k_{trans} \tag{1.53b}$$

$$\Phi_{trans} = \frac{k_{trans}}{k_{rad} + k_{isc} + k_{ic} + k_{trans}} = 1 - \frac{\tau_{DA}}{\tau_D} \tag{1.54}$$

Moreover, from these lifetimes it is also possible to obtain the rate of energy transfer, which is an important parameter to characterize the transfer process.

$$k_{trans} = \frac{1}{\tau_{DA}} - \frac{1}{\tau_D} \tag{1.55}$$

So, time resolved measurements are necessary to measure the energy transfer rates in weakly interacting heterodimers. Different techniques can be used to determine the donor lifetime: time resolved fluorescence experiments performed with time correlated single photon counting or through fluorescence up-conversion techniques or transient absorption measurements.

In Chapter 6 the excited states dynamic in different homo and hetero dimers of porphyrins is presented, in order to study the energy transfer process in these structures.

1.5.4 Time-resolved anisotropy

If a sample of randomly oriented molecules is illuminated with linearly polarized light with polarization parallel to the laboratory‘s z-axis, the light will selectively excite molecules that have their transition dipole μ_{ba} oriented parallel to this same axis. Molecules with off-axis orientations will also be excited with a probability that depends on $\cos^2\theta$, where θ is the angle from the z-axis.

The fractions of the molecules that have μ_{ba} oriented with angle θ between θ and $\theta + d\theta$, and with ϕ between ϕ and $\phi + d\phi$, where ϕ is the angle of rotation in the xy plane, is proportional to the area element $\sin\theta d\theta d\phi$ on the surface of a sphere of unit radius. The fraction of the excited molecules with this orientation, $W(\theta,\phi)d\theta d\phi$, is given by:

$$W(\theta,\phi)d\theta d\phi = \frac{\cos^2\theta \sin\theta d\theta d\phi}{\int_0^{2\pi} d\phi \int_0^{\pi} \cos^2\theta \sin\theta d\theta} \tag{1.56}$$

The integral in the denominator, which simply counts all the molecules that can be excited, evaluates to $4\pi/3$, so

$$W(\theta,\phi)d\theta d\phi = (3/4\pi)\cos^2\theta \sin\theta d\theta d\phi \tag{1.57}$$

After excitation the molecules can return to the ground state by different deactivation processes, among which there is s fluorescence. If absorption and emission involve the same electronic transition and the excited molecule does not change its orientation before it emits, the transition dipole for emission will be parallel to the transition dipole for absorption. For each molecule in the sample, the probability that the emission is polarized along the z-axis (parallel to the excitation polarization) again depends on $\cos^2\theta$. Integrating over all possible orientations of the molecule gives

$$\begin{aligned} F_{pa} &\propto \int_0^{2\pi} d\phi \int_0^{\pi} W(\theta,\phi)\cos^2\theta d\theta \\ &= (3/4\pi)\int_0^{2\pi} d\phi \int_0^{\pi} \cos^4\theta \sin\theta d\theta = (3/4\pi)(4/5\pi) = 3/5 \end{aligned} \tag{1.58}$$

Similarly, the probability that a given molecule emits with polarization along the x-axis (perpendicular to the excitation) is proportional to $\left|\mu_{ab}\cdot\hat{x}\right|^2$, which depends on $\sin^2\theta\cos^2\phi$. Integrating over all orientations again gives

$$\begin{aligned} F_{pe} &\propto \int_0^{2\pi}\cos^2\phi d\phi\int_0^{\pi}W(\theta,\phi)\sin^2\theta d\theta \\ &= (3/4\pi)\int_0^{2\pi}\cos^2\phi d\phi\int_0^{\pi}\cos^2\theta\sin^3\theta d\theta = 1/5 \end{aligned} \tag{1.59}$$

Comparing Eqs. (1.58) and (1.59), fluorescence polarized parallel to excitations is 3 times as strong as the fluorescence polarized perpendicular to the excitation. Fluorescence anisotropy (r) is a measure of this relative intensity:

$$r = \frac{\left(F_{pa} - F_{pe}\right)}{F_{pa} + 2F_{pe}} \tag{1.60}$$

If a sample contains a mixture of components with different anisotropies, the observed anisotropy is simply the sum:

$$r = \sum_i \Phi_i r_i \tag{1.61}$$

Where r_i is the anisotropy of component i and Φ_i is the fraction of the total fluorescence emitted by this component.

Inserting the values for F_{pa} and F_{pe} from Eqs. (1.58) and (1.59) gives r = 2/5 for an immobile system. This is the maximum anisotropy for a systems with a single excited state. In systems with multiple excited states, like porphyrins, the initial anisotropy could be as high as 1.0 at very early times[13,14,15]. Interactions with the surroundings usually cause the wavefunctions to get out of phase within a few picoseconds, so r decays rapidly to 0.4 or lower.

The observed anisotropy will decrease if the emission and absorption transition dipoles are not parallel or if the molecule rotates before it fluoresces.

If the transition dipole for emission makes an angle ζ with respect to the transition dipole for absorption, r for an immobile molecule becomes:

$$r' = \left(3\cos^2 \zeta - 1\right)/5 \tag{1.62}$$

These expressions come into play if the molecules relaxes to a different excited electronic state before it fluoresce.

Let allow the excited molecule to rotate randomly so that the transition dipole explores all possible orientations. If the sample is excited with a single short pulse at time t=0, the initial fluorescence anisotropy immediately after the excitation (r_0) will be 0.4 or the value given by Eq. (1.62) if internal conversion to a different electronic state occurs very rapidly. The anisotropy will decay to zero as the excited molecules rotate into new orientations. By examining the decay kinetics of the anisotropy, it is possible to learn how rapidly the molecules rotates.

Another process that cause the decrease of the anisotropy signal in time is energy transfer from one chromophore to another one with a different orientation. This is the only method to reveal energy transfer in homo-dimers. In Chapter 6 preliminary results on the anisotropy decay in homodimers of porphyrins are reported: both rotational motions and energy transfer contributes to the decay and a direct understanding of the results requires the development of appropriate models that describe the rotational motion of the moieties in the dimer as well as the energy transfer process .

References

[1] W. W. Parson, *Modern Optical Spectroscopy*, Springer-Verlag Berlin, Heidelberg, **2007**

[2] T. Förster, in *Modern quantum chemistry part III*, Academic, New York, **1965**

[3] D.L. Dexter, *J. Chem. Phys*, **1953**, 21, 836

[4] P.O.J. Scherer, in *J Aggregates*, T. Kobayashi (ed.), World Scientific, Singapore, **1996**

[5] Tasaki, H. *J. Phys. : Condens. Matter* **1998***, 10*, 4353

[6] Harris, A. B.; Lange, R. B. *Phys. Rev.* **1967***, 157*, 295.

[7] Hubbard, J. *Proc. Roy. Soc. (London) A* **1963***, 276*, 238.

[8] R. Bozio, C. Pecile, in *Spectroscopy of Advanced Materials*, R.J.H. Clark e R.E. Hester (eds.), J. Wiley&Sons, Chichester, **1990**

[9] D. Pedron, A. Speghini, V. Mulloni, R. Bozio, *J. Chem. Phys*., **1995**, *103*, 2795; V. Mulloni, D. Pedron, R. Bozio, *Chem. Phys. Lett.,* **1996**, *263*, 331

[10] J.S. Hsiao, B. P. Krueger, R. W. Wagner, T.E. Johnson, J.K. Delaney, D.C. Mauzerall, G. R. Fleming, J.S. Lindsey, D.F. Bocian, R.J. Donohoe*, J. Am. Chem. Soc*., **1996**, 118(45), 11181.

[11] Boyd, R. W. *Nonlinear optics*, Academic Press, **1992**

[12] Terenziani, F.; Katan, C.; Blanchard-Desce, M.; Badaeva, E.;Tretiak, S. *Adv. Mater.* **2008**, *20*, 4641. He, G. S.; Tan, L. S.;Zheng, Q.; Prasad, P. N. *Chem. Rev.* **2008**, *108*, 1245. Pawlicki,M.; Collins, H. A.; Denning, R. G.; Anderson, H. L. *Angew. Chem., Int.Ed.* **2009**, *48*, 3244.

[13] K. Razi, Naqvi, R.E. Dale, *Chem. Phys. Lett*., **2002**, 357, 147

[14] K.Wynne, R.M. Hochstrasser, *Chem. Phys*., **1993**, 171, 179

[15] M. Goutermann, L. Stryer, *J. Chem. Phys*. **1962**, 37 (10), 2260

Chapter 2

Characterization techniques

2.1 Introduction

In order to investigate the influence of the molecular interactions on the optical properties presented in Chapter 1, different techniques have been used for the linear and non-linear characterization of the molecules investigated.

First of all linear characterization will be presented, including also the detailed procedure for the estimate of the fluorescence quantum yield.

Then the two-photon absorption measurements are analyzed. Two different techniques have been used, depending on the properties of the molecules. If the molecules are fluorescent and the interesting transition is in the range 720-940 nm, as the dimers of dipolar and quadrupolar molecules described in Chapter 4, the two photon induced fluorescence (TPIF) technique can be used. If the molecules are not fluorescent, as the charge transfer (CT) dimer of tetrathiafulvalene in Chapter 3, the Z-scan technique must be used. Moreover the investigated transitions for CT dimers fall outside the wavelength range allowed by our TPIF setup. With the Z-scan technique it is also possible to measure the nonlinear refractive index of the investigated molecules.

At last the techniques to study the excited state dynamic are presented: in the nanosecond regime time resolved fluorescence measured with the time correlated single photon counting (TCSPC) technique has been used, while with transient absorption (TA) experiments the region from 100 fs to 1 ns was investigated. Two different setup were used, one at the University of Padova and the other at the Humboldt University of Berlin. The procedure for the multivariate analysis (MVA) of the TA data is also described.

2.2 Linear absorption

UV-visible absorption measurements are performed on a Varian Cary 5 spectrophotometer, in the range 250-2000 nm. For the measurements, quartz cuvettes with optical path of 1 cm or 1 mm are used.

The extinction coefficients are calculated using the Lambert-Beer equation. In order to have an accurate determination of the absolute value of the extinction coefficient, these measurements are performed on three different solutions prepared weighting approximately 3 mg of sample and dissolving it in 10 mL of solvent. These solution are then diluted at half the initial concentration for two times, in order to have nine final solutions of known concentration. The absorption spectra of these solution are recorded and the final extinction coefficients are obtained from the average of the nine values obtained.

2.3 Linear emission

Fluorescence spectra were recorded with a FluoMax P (Jobin–Yvon) spectrophotometer, using 1 cm quartz cuvettes. The solutions used have maximum absorbance 0.15 at the excitation wavelength as well as in the whole spectral range, to avoid reabsorption.

2.3.1 Fluorescence quantum yield (FQY) measurements

The method used to estimate the FQY of a fluorophore consists in the comparison between the emission spectra of dilute solutions of the sample and of a standard compound, used as reference material with known quantum yield.

The common formula for the determination of the FQY is[1]:

$$\Phi_s = \Phi_r \left(\frac{A_r(\lambda_r)}{A_s(\lambda_s)} \right) \left(\frac{I(\lambda_r)}{I(\lambda_s)} \right) \left(\frac{n_s^2}{n_r^2} \right) \left(\frac{D_s}{D_r} \right) \tag{2.1}$$

In these equations, $I(\lambda)$ is the relative intensity of the exciting light at wavelength λ, n is the average refractive index of the solution, D is the integrated area under the corrected emission spectrum and $A(\lambda)$ is the absorbance of the solution at the exciting wavelength λ.

Eq. (2.1) is valid if many assumptions are satisfied; for both compound the integrated luminescence intensity is assumed to be proportional to the fraction of absorbed light, all geometrical factors to be identical, the excitation beams to be monochromatic, internal reflection effects to be the same, reabsorption and reemission to be negligible and the emission to be isotropic. It is often difficult to take into account all of these effects, but it is possible to employ some cautions in order to minimize errors in the determination of FQY.

A maximum absorbance of about 0.15 is used for the solutions, in order to minimize the reabsorption and the quenching effects. Both the standard and the unknown sample solutions are prepared so to have similar absorbance at the excitation wavelength: by this way the

attenuation of the excitation source along the optical path in the cuvette is analogous in both cases and the number of the excited molecules can be considered similar.

To account for the reabsorption of the excitation beam, we consider that the number of absorbed photons is proportional to $(1\text{-}10^{-AL/2})$ instead of AL. L is the optical path of the cuvette and $L/2$ is the thickness across the excited sample.

Also the emitted photon can be reabsorbed from the solutions, and we use the Lamber-Beer law to take in account this correction. We consider that the spectrometer measures an apparent corrected emission spectrum of the sample $F_a(\bar{\nu})$ which is not the same as the molecular emission spectrum $F(\bar{\nu})$. From Beer's law $F_a(\bar{\nu})$ and $F(\bar{\nu})$ are related by:

$$F_a(\bar{\nu}) = F(\bar{\nu}) 10^{-AL/2} \tag{2.2}$$

These two factors induce a correction of about 5-10% for absorbance lower than 0.2.

In the choice of the standard compound for FQY measurements, it is also important to look for a standard whose fluorescence overlaps spectrally with the one of the unknown sample, in order to reduce the experimental errors.

The fluorescence standards used are Fluorescein in water at pH > 10, FQY = 0.93[2], Coumarin 540A in ethanol, FQY = 0.56[3], Cresyl Violet in methanol FQY = 0.66[4], Perylene in cyclohexane FQY = 0.94[5]. Usually at least two different standards are used to measure the FQY of a sample.

Another factor that can be a source of error in the FQY determination is the response of the detector at different wavelengths. It is necessary to correct the emission spectrum for the efficiency curve of the detector, that is provided by the instrument manufacturer or that can be determined using a calibrated lamp. We choose to independently perform the calibration of the detector unit and use the obtained curve for the spectra correction.

2.4 TPA measurements

As described in Chapter 1, TPA involves a transition from the ground state of a molecule to an excited state by the simultaneous absorption of two photons from the incident radiation field.

In order to measure experimentally TPA cross-sections two different techniques can be used, depending on the characteristics of the molecule under investigation. If the molecules are fluorescent (at least 1% of fluorescence quantum yield) we can use two-photon induced fluorescence (TPIF), otherwise we have to adopt Z-scan technique.

2.4.1 Z-Scan

The Z-scan technique is a method used to measure both non-linear absorption and non-linear refraction properties[6]. In this experiment we record the transmittance of a focused beam as a function of the sample position along the Z direction of propagation of the focalized beam. During the experiment the cross section area of the beam decreases, hence the irradiance (power per unit area) increases, as the sample approaches the focal plane. A scheme of the setup is reported in Figure 2.1. Away from the focus, the beam irradiance is low and non-linear phenomena do not occur; hence, the transmittance remains constant. As the sample is brought closer to the focus, non-linear processes are activated: the transmitted light changes both in intensity and in spatial distribution. When the sample goes beyond the focusing point, the irradiance decreases, non-linear absorption phenomena are negligible and the transmittance is constant and equal to the initial value. When the whole transmitted light from the sample is collected ("open-aperture" configuration), the transmittance can either decrease, in the case of multiphoton absorption, or increase, if there is saturable absorption. In the "closed-aperture" configuration we place a diaphragm with known linear transmittance between the focusing lens and the detector. This device allows us to measure the changes in the spatial intensity distribution of the light beam promoted by the non-linear refractive index in the sample.

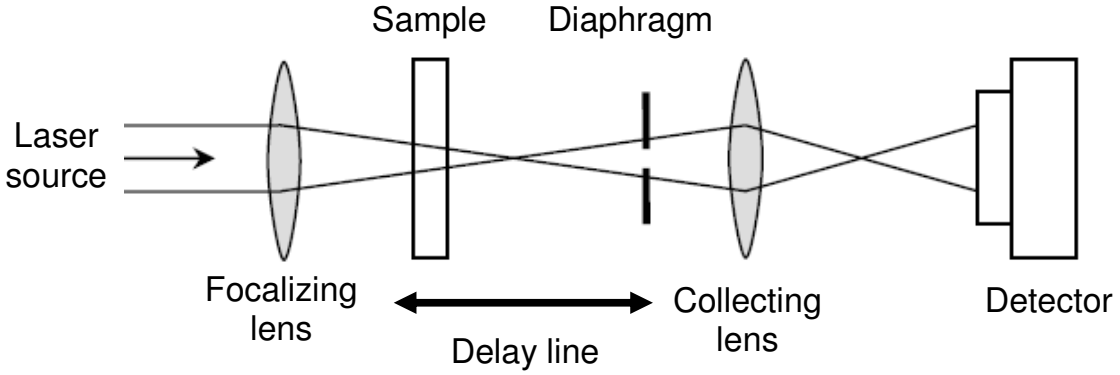

Figure 2.1: Scheme of a closed-aperture Z scan experiment. Removing the diaphragm the open-aperture Z-scan configuration is obtained.

Let's start considering the case of closed-aperture Z-scan measurements to determine the non-linear refractive index. Assume a material with a negative nonlinear refractive index. As the sample approaches the focus the beam irradiance increases and the sample itself acts as a defocusing lens. This additional lens prior to the focus will tend to collimate the beam, causing a beam narrowing at the aperture, which results in an increase in the measured transmittance. As the sample passes the focal plane to positive Z (on the side of the detector),

the same self-defocusing increases the beam divergence, leading to beam broadening at the aperture and thus a decrease in transmittance.

So, a pre-focal transmittance maximum (peak) followed by a post-focal transmittance minimum (valley) is, therefore, the Z-scan signature of a negative nonlinear refractive index. Positive nonlinear refractive index gives rise to an opposite valley-peak configuration.

This description considers that the sample nonlinearity is purely refractive, assuming that no absorptive nonlinearities (as multiphoton absorption or saturable absorption) are present. Qualitatively, multiphoton absorption suppresses the peak and enhances the valley, while saturation produces the opposite effects. The sensitivity to nonlinear refraction is entirely due to the aperture, and removal of the aperture completely eliminates the effect. However, the Z-scan is still sensitive to nonlinear absorption.

Let consider a Gaussian beam with beam waist ω_0 propagating along the Z direction of the reference system. If the sample length L is small enough that changes in the beam diameter within the sample due to diffraction or non-linear refraction are negligible, then the "thin" sample approximation can be applied. For linear diffraction this implies that $L<<Z_0$, where $Z_0=\pi\omega_0^2/\lambda$ is the diffraction length of the Gaussian beam. For the nonlinear refraction instead $L<<Z_0/\Delta\varphi_0$, where $\Delta\varphi_0$ is the maximum phase shift induced by non-linear effects. Usually, in a Z-scan experiment, the second criteria is satisfied since $\Delta\varphi_0$ is small.

Under these two approximations of Gaussian beam and thin sample, phase and amplitude of the electric field are given by:

$$\frac{d\Delta\varphi}{dz'} = k\Delta n(I) \tag{2.3}$$

$$\frac{dI}{dz'} = -\alpha(I)I \tag{2.4}$$

Where *z'* is the propagation coordinate of the beam in the sample, that has not to be confused with the position Z of the sample relative to the focus. $\Delta n(I)$ is the non-linear variation of the refractive index. The term $\alpha(I)$ takes into account the linear and non-linear absorption coefficients. In the case of a cubic nonlinearity and negligible nonlinear absorption, Eq. (2.3) and (2.4) are solved to give the phase shift at the exit surface of the sample:

$$\Delta\varphi(Z,r,t)=\frac{\Delta\varphi_0(t)}{1+Z^2/Z_0^2}e^{-2r^2/\omega^2(Z)} \tag{2.5}$$

Where the beam radius is

$$\omega^2(Z)=\omega_0^2\left(1+Z/Z_0^2\right) \tag{2.6}$$

and

$$\Delta\varphi_0(t)=k\Delta n_0(t)L_{eff} \tag{2.7}$$

In which $k=2\pi/\lambda$ is the wave vector and λ is the laser wavelength.

L_{eff} is the effective sample thickness, with L the sample length and α the linear absorption coefficient. L_{eff} coincides with L for low absorbance values.

$$L_{eff}=\frac{\left(1-e^{-\alpha L}\right)}{\alpha} \tag{2.8}$$

$\Delta n_0=n_2 I_0(t)$, where n_2 is the non-linear refractive index and $I_0(t)$ is the irradiance at the focus.

The normalized transmittance read by the detector can be written in the form:

$$T(Z,\Delta\varphi_0)=1-\frac{4\Delta\varphi_0 x}{\left(x^2+9\right)\left(x^2-1\right)} \tag{2.9}$$

Where $x=Z/Z_0$. Using Eq. (2.9) and knowing the laser wavelength λ, the sample length L, the laser irradiance $I_0(t)$, the linear absorption coefficient α, and the beam waist ω_0, it is possible to obtain the non-linear refractive index n_2.

Removing the diaphragm, Z-scan can be used to determine non-linear absorptive effects, and this new configuration for the experiment is called open-aperture Z-scan. Under the same approximation adopted for closed-aperture Z-scan, the normalized transmittance measured in open-aperture is given by:

$$T(Z)=\frac{1}{\sqrt{\pi}q_0(Z)}\int_{-\infty}^{+\infty}\ln[1+q_0(Z)\exp(-\tau^2)]d\tau \tag{2.10}$$

$$q_0(Z)=\frac{\beta I_0 L_{eff}}{1+Z^2/Z_0^2} \tag{2.11}$$

where β is the TPA coefficient and all the other parameters have been already defined in the closed-aperture description.

If $|q_0| < 1$, the logarithm function in Eq. (2.10) can be expanded in a Taylor series and the resulting formula is:

$$T(Z) = \sum_{m=0}^{\infty} \frac{[-q_0(Z)]^m}{(m+1)^{3/2}} \tag{2.12}$$

Usually, the first six terms of the summation are sufficient to have accurate results. The open-aperture Z-scan traces measured in this thesis are fitted by an expression of T cut at the sixth-term, where q_0 is the fitting parameter from which it is possible to obtain the value of β. From β we can calculate the value of the TPA cross-section per single molecule, as expressed by the relation

$$\sigma = \frac{\hbar\omega\beta}{N} \tag{2.13}$$

where N is the number density of absorbing species. It is therefore important to know the concentration of the absorbing dye for the determination of the σ.

All the Z-scan experiments are performed with a femtosecond amplified laser system by Spectra Physics, presented in Figure 2.2.

A continuous Nd:YVO_4 laser (Millennia Vs) pumps a Titanium:Sapphire laser oscillator (Tsunami) producing ultrashort pulses with a duration of 100 fs and a repetition rate of 82 MHz. The output wavelength is set at 806 nm and the energy per pulse is approximately 5 nJ. These pulses are then directed to a regenerative amplifier (Spitfire), which uses as the active medium a crystal of Ti:sapphire, and where the pulses are first temporally extended, then amplified and in the end recompressed to their initial duration. This amplifier is pumped by a Q-switched Nd:YLF laser (Merlin).

The laser pulses produced have a 150-200 fs duration, maximum energy of 800 μJ, repetition rate ranging from 1 Hz to 1 kHz and the wavelength set at 806 nm. The optical parametric amplifier (OPA800C) is used to tune the output wavelength from 480 to 2000 nm. Usually in

Z-scan experiments the repletion rates used are 200Hz or 20 Hz to avoid thermal effects in the sample.

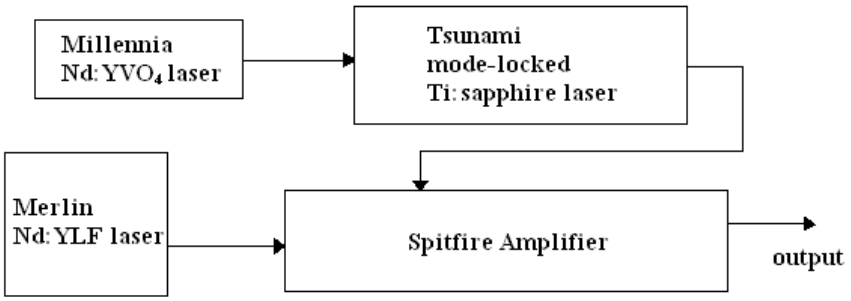

Figura 2.2: General scheme of the laser system used

For the Z-scan experiments, the linearly polarized laser beam from the laser is focused with a 200 mm focal length lens and the sample is moved across the focus by means of a computer controlled micrometric translation stage. The beam waist at the focus is typically 22 ± 5 μm. The pulse energy is suitably attenuated by means of neutral density filters. The input pulse energy in the experiments shows typical values in the range 0.1-0.5 μJ. After the sample the beam is recollected by a second lens and, after suitable attenuation, it is detected by a photodiode. The signal is averaged by an oscilloscope and then processed by a PC acquisition program.

Open- and closed-aperture Z-scan measurements are performed on CT dimer of the radical cation of TTF, reported in Chapter 3.

2.4.2 Two-photon induced fluorescence (TPIF)

TPIF is a technique that allow us to obtain the TPA cross section σ of the sample, using a reference with known TPA cross-section.

Because the TPIF is a third-order process, its intensity depends quadratically on the intensity of the incident laser light. If the linear absorption is negligible, the attenuation of the incident beam in a material due to two-photon absorption process at a given time is described by:

$$\frac{dI}{dz} = -\beta I^2 \tag{2.14}$$

where I is the intensity of the beam, z is the direction of propagation and β is the two-photon absorption coefficient.

The number of fluorescence photons collected per unit time is given by the relation:[7]

$$F(t)=1/2\phi\Phi_s N_{abs} \tag{2.15}$$

In this expression, Φ_s is the fluorescence quantum yield of the sample, N_{abs} is the number of photons absorbed per molecule and unit time and ϕ is the fluorescence collection efficiency of the measurement system. The factor 1/2 is added in order to account for the two-photon process which involves the emission of one photon after the absorption of two photons. Eq. (2.15) is valid in the assumption of no stimulated emission and self-quenching. If stimulated emission occurs, Φ_s increases and ϕ should account for the preferential direction of the stimulated emission; if the fluorescence is partially quenched the effective Φ_s is reduced. The number of absorbed photons is proportional to the two-photon absorption cross-section σ and to the square of the incident intensity. N_{abs} is also a function of the local dye concentration $C(\bar{r},t)$ and the illuminated sample volume:

$$N_{abs}(t)=\int_V \sigma C(\bar{r},t) I^2(\bar{r},t)dV \tag{2.16}$$

If saturation and photobleaching effects are not present, the concentration can be considered constant. When the time and space dependence of the intensity can be separated, Eq. (2.16) becomes:

$$N_{abs}(t)=\sigma C I_o{}^2(t)\int_V S^2(\bar{r})dV \tag{2.17}$$

$I_0(t)$ and $S(\bar{r})$ are the temporal and spatial distribution of the incident beam, respectively. Experimentally, it is possible to measure only a time-average of the photon flux expressed in (2.18):

$$\langle F(t)\rangle=1/2\,\phi\eta_S C\sigma\langle I_0^2(t)\rangle\int_V S^2(\bar{r})\,dV \tag{2.18}$$

Because most detectors measure the average of $I_0(t)$, it is possible to rewrite the expression (2.18) as:

$$\langle F(t)\rangle = 1/2\, g\, \phi \eta_S C \sigma \langle I_0(t)\rangle^2 \int_V S^2(\bar{r})\, dV \tag{2.19}$$

Where g is a measure of the second-order temporal coherence of the excitation source:

$$g = \langle I_0^2(t)\rangle \Big/ \langle I_0(t)\rangle^2 \tag{2.20}$$

Eq. (2.19) identifies the parameters necessary for the determination of the absolute value of the TPA cross-section:

- the spatial distribution of the laser beam $\int_V S^2(\bar{r})\, dV$ that depends on the shape of the beam.
- the degree of the second-order temporal coherence g, that for a mode-locked Ti:Sapphire laser with repetition rate ~ 100 MHz and pulse duration ~ 100 fs, g is 10^5 approximately.
- the fluorescence quantum yield Φ_s.
- and the fluorescence collection efficiency ϕ.

This last parameter can be expressed as:[8]

$$\phi = \phi_{dispers} \times \phi_n \tag{2.21a}$$

$$\phi_{dispers} = \left[\int f_{fluo}(\lambda) \times f_{PMT}(\lambda) \times \prod_i T_i(\lambda)\, d\lambda \right] \Big/ \int f_{fluo}(\lambda)\, d\lambda \tag{2.21b}$$

Eq. (2.21b) is the correction factor for the wavelength dispersion of the instrument response functions: $f_{fluo}(\lambda)$ is the fluorescence spectrum of the emitting dye, $f_{PMT}(\lambda)$ is the response function of the photomultiplier tube (PMT), $T_i(\lambda)$ is the transmission spectrum of the filter i, generally used in front of the PMT to block the laser light. The integrals are calculated over the wavelength range of the fluorescence spectrum. The second factor ϕ_n takes into account the solid angle under which the emitting volume of the solution is seen from the detector.

The determination of all the factors involved in the Eq. (2.19) is generally difficult, so a relative method has been proposed, that consists of using the same set-up for the measurement of the fluorescence emission for the sample and for a compound whose TPA spectrum and FQY are known in the literature.

We can write Eq. (2.19) for the sample and an analogous one for the reference. If we divide the two relations and reorganize them, we obtain:

$$\sigma^S = \sigma^R \frac{\langle F \rangle_S}{\langle F \rangle_R} \frac{C_R}{C_S} \frac{\Phi_R}{\Phi_S} \frac{\phi_R}{\phi_S} \tag{2.22}$$

In this relation, σ is the two-photon absorption cross section, $\langle F \rangle_S$ is the signal read by the detector, quadratically dependent on the excitation intensity, C is the concentration of the compound and Φ is the FQY. Finally, ϕ is the correction factor for the collection efficiency, having the same general formula reported in Eq. (2.21). The subscripts R and S refer to reference and sample, respectively.

The optical set-up is schematically represented in Fig. 2.3.

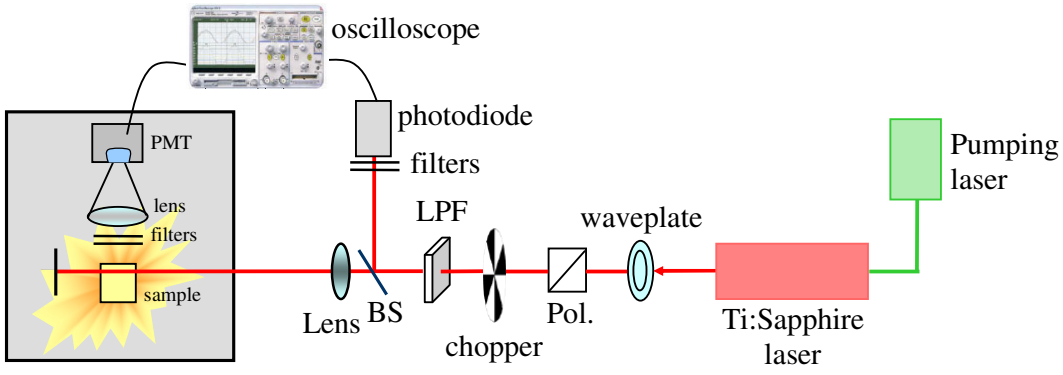

Figure 2.3: Optical set-up for Two-photon Induced Fluorescence measurements

The excitation source is an ultrafast mode-locked Ti:Sapphire laser (*Coherent*- Mira 900-F), pumped by a compact diode-pumped Nd:YVO4 laser emitting at 532 (*Coherent*-Verdi V-5). The laser pulse duration is approximately 130 fs and the repetition rate is 76 MHz. The wavelength range is tuneable between 720 and 930 nm. The output wavelength can be simply modified by changing the birefringent filter position and moving the Brewster prism compensator in the Ti-sapphire laser cavity.

The average power is 600-800 mW. For the experiment the laser intensity can be gradually varied by using the combination of a half-waveplate and a linear polarizer.

The use of a chopper, at an arbitrary frequency of 215 Hz, is necessary for the detection of the signal by a photodiode or a phototube.

The spurious laser components at low wavelength (< 550 nm) are absorbed by the long-pass filter (LPF), because these components can linearly excite the chromophore inducing interference with the two-photon excitation process. Then a beamsplitter divides the beam into two parts: approximately 10% of the overall intensity is sent to a photodiode that measures the incident energy and the remaining is used for the excitation of the sample.

The laser beam is focalized into the sample by a 40 cm focal length lens. For liquid samples a quartz cuvette with optical path of 10 mm is employed, and the fluorescence is collected by a photomultiplier tube at a 90° geometry. Because the Rayleigh range of the lens is about 10 mm, the beam can be approximately considered collimated along the entire sample cell. The beam passes near the wall of the cuvette (about 1mm) in order to reduce the reabsorption of the fluorescence signal before the detector.

Also the scattering from the solution and the cell can arrive to the detector. This component must be eliminated, especially when fluorescence is weak. Laser light scattering has a linear proportionality with the incident energy and can interfere with the square dependence of the TPIF signal. For this reason, we use a set of short pass filters before the phototube to stop the scattered laser light. After the filters the fluorescence is focused onto the active area of the photomultiplier tube (*Hamamatsu*- R636-10) by a 4 cm lens. The entire collection unit is set into a black box which guarantees the reduction of the internal reflexions of the pump beam, as well as spurious signal from diffuse light in the room.

The method chosen to collect the TPIF data is analogous to that described by Rumi et al. in Ref. [8]. At every excitation wavelength we collect the integrated intensity of the emission spectrum of the active dye as a function of the incident intensity, which is varied from 0 up to 100 MW/cm^2. In order to eliminate the residual scattering contribution, we subtract the signal measured with a cell containing the pure solvent to the fluorescence signal emitted by the dye in solution. This procedure is applied to both the sample and the standard compound.

As standards we used Fluorescein (in H_2O pH>11, FQY=0.9) and Rhodamine B (in methanol, FQY=0.7), whose TPA spectra are reported in the literature[9].

The typical concentrations are 2-5×10^{-5} M, for chromophores with high fluorescence quantum yields, but they increase up to 5×10^{-4} M if the FQY and σ_{TPA} value are low.

One of the assumptions of the TPIF theory is that the excitation process does not influence the emission properties of the fluorophore, i.e. the emitting state is the same if either one- or two-photon excitation is applied. In order to confirm this hypothesis we measure the fluorescence spectrum of the sample, using two-photon excitation in a back-scattering geometry, and compare it to the one-photon excitation spectrum.

The laser beam and the TPA induced fluorescence are focused and collected by the same microscope objective (10X, NA=0.25). The fluorescence light is separated from the exciting laser beam by a dichroic filter, which reflects the low excitation wavelengths, and then sent to a fiber coupled with a monochromator and a PMT tube. Short pass filters were used in front of the fiber to suppress the residual laser light.
In Chapter 4 the TPIF measurements on dimers of dipolar and quadrupolar molecules are reported.

2.5 Excited state dynamic

Different techniques can be used to investigate the excited state dynamic of the samples. In this work only two methods are used, time resolved fluorescence measured with time correlated single photon counting for the nanosecond regime and transient absorption for the temporal range from 100 fs to 1 ns. The main difference between these techniques depends on the time response of the detection system. For the nanosecond regime investigated by time resolved fluorescence it is possible to have detectors that reach a resolution sufficient to follow the dynamics in this timescale. Instead, no detectors are available to examine the dynamic of many processes that occur in the time scale of few pico- or femtoseconds in real time. So indirect method like transient absorption have been set up, in which the resolution does not depend from the response time of the detector.

2.5.1 Time resolve fluorescence measured by Time Correlated Single Photon Counting

Time-Correlated Single Photon Counting (TCSPC) is used to investigate the fluorescence lifetimes of the sample in the nanosecond regime.
TCSPC is based on the detection of single photons emitted by the sample as a function of the delay between the time in which the molecule is excited and the time when the photon reaches the detector and on the reconstruction of the waveform from the individual time measurements.
The method makes use of the fact that for low level, high repetition rate signals the light intensity is usually so low that the probability to detect one photon in one signal period is much less than one. Therefore, the detection of several photons simultaneously by the detector can be neglected.
When a photon is detected, the time of the corresponding detector pulse is measured. The events are collected in a memory by adding a ‘1’ in a memory location with an address proportional to the detection time. After collection of many photons, an histogram of the

number of photons against detection times builds up in the memory of the TCSPC electronics, and this histogram depicts the fluorescence decay curve.

The experimental lay-out for these fluorescence decay measurments is described in the following. The excitation beam at 400 nm, delivered by the frequency-doubled Ti:Sapphire femtosecond laser system (Coherent Mira 900-F) at 76 MHz repetition rate, is focused through a 20× Plan Apochromatic microscope objective (Olympus) into the solution. The emitted fluorescence is collected through the same objective and is spatially and spectrally filtered using a 150 μm diameter pinhole and appropriate long-pass and band-pass filters to remove out-of-focus fluorescence and the Rayleigh scattering from the sample. The emission beam is focused onto a single-photon avalanche photodiode (PDM series, MPD, Italy); each photon pulse is register by the TCSPC counting module (PicoHarp 300, PicoQuant GmbH, Germany). The instrumental response function (IRF) has a 200 ps full width at half-maximum. The fluorescence lifetime curves are analysed by the SymPhoTime software.

2.5.2 Transient absorption measurements

In transient absorption (TA) experiments two beams of different intensity are used: the less intense is called *probe,* while the other is the *pump*. These two beams travel different optical paths to cross spatially on the sample; the temporal delay of the probe with respect to the pump is then defined by the relation:

$$\Delta t = \frac{\Delta x}{c} \tag{2.23}$$

Where Δx is the difference of optical path and c is the speed of light. The signal observed in these measurements and collected by the detector is the intensity of the probe pulse as a function of the pump-probe delay. Following the probe pulse intensity against this delay time it is possible to monitor the dynamic of the processes studied.

In these experiments the time resolution of the detector is of no influence and the experimental time resolution is limited just by the duration of the pump and probe pulses. If the frequencies of the pump and the probe are the same we talk of single colour experiments, otherwise, if the frequency of the probe is different from that of the pump is a two colours experiment or transient absorption. These measurements allow us to obtain information about the relaxation dynamic of excited states and on their absorption properties.

Single color experiments give limited information and with this kind of measurements it is difficult to distinguish the electronic relaxation from the vibrational relaxation or to distinguish the individual behaviors of many absorbing species. However, single wavelength experiments can reveal significant information about the reorientational motions and the energy transfer when polarized light is used for excitation and probe.

If you want to record the dynamic free from any reorientational contribution, the probe should have a polarization of 54.7° with respect to the pump beam. The reorientational contribution can instead be studied directly by combining measurements with the probe beam polarization parallel and then perpendicular to the pump beam[10].

The simplest photophysic event is the excitation of molecules from their ground electronic state to their first electronic excited state, followed by the return of the molecules to the ground state by fluorescence and/or internal conversion. The decay process can be followed by changes in the transmission of a weak probe beam through the sample as a function of the delay time after the arrival of the strong pump pulse:

$$\Delta T(t) = \frac{I(t) - I(\infty)}{I(\infty)} \tag{2.24}$$

Consider a system at equilibrium where, in the absence of external excitations, all molecules are in the ground state g and the Lambert-Beer law is valid to describe the attenuation of a weak probe pulse with intensity I_0 incident on a sample with N molecules per unit volume and thickness L.

$$\frac{dI(z)}{dz} = -\sigma_G N I(z) \tag{2.25}$$

$$I(\infty) = I_0 \exp(-\sigma_G N L) \tag{2.26}$$

Where $I(\infty)$ is the intensity of the probe after the sample (without pump) and σ_G is the absorption cross section of the ground state.

When the pump is applied, a non zero population is generated in the excited states and the intensity of the probe will depend on how many molecules are left in the ground state and are therefore still able to absorb. The probe intensity when the pump is also applied will be greater than the intensity of the probe alone. By increasing the delay t, the number of the

molecules found in the excited states decreases, and thus also the intensity of the probe will vary. The time dependence of the probe beam intensity is described by:

$$\begin{aligned}\frac{dI(z)}{dz} &= -N_g(t)\sigma_G I(z) + \sum_i N_i(t)\left(\sigma_{em,i} - \sigma_{E,i}\right)I(z) \\ &= -\left[N - \sum_i N_i(t)\right]\sigma_G I(z) + \sum_i N_i(t)\left(\sigma_{em,i} - \sigma_{E,i}\right)I(z)\end{aligned} \tag{2.27}$$

Defining N as

$$N = N_g(t) + \sum_i N_i(t) = N_g(t) + N_e(t) \tag{2.28}$$

Where the sum is over all the populated excited states *i*, $N_i(t)$ is the population of the excited state *i* at time t, and $N_e(t)$ is the population in all the excited states at time *t*. The cross-sections for the ground state absorption, the excited state absorption and the stimulated emission are σ_G, σ_E and σ_{em}, respectively. Integration of Eq. (2.27) with respect to z gives:

$$I(t) = I_0 \exp\left\{-\sigma_G L[N - N_e(t)] + \sum_i N_i(t)\left(\sigma_{em,i} - \sigma_{E,i}\right)L\right\} \tag{2.29}$$

Putting Eqs. (2.25) and (2.29) in (2.24) the signal obtained is:

$$\Delta T(t) = \frac{I(t) - I(\infty)}{I(\infty)} = \exp\left\{L\left[\sigma_G N_e(t) + \sum_i N_i(t)\left(\sigma_{em,i} - \sigma_{E,i}\right)\right]\right\} - 1 \tag{2.30}$$

Rearranging we have:

$$1 + \Delta T(t) = \exp\left\{L\left[\sigma_G N_e(t) + \sum_i N_i(t)\left(\sigma_{em,i} - \sigma_{E,i}\right)\right]\right\} \tag{2.31}$$

$$\ln[1 + \Delta T(t)] = L\left[\sigma_G N_e(t) + \sum_i N_i(t)\left(\sigma_{em,i} - \sigma_{E,i}\right)\right] \tag{2.32}$$

If $\Delta T(t) << 1$, so if the change in transmittance of the sample after pumping is small, then it is possible to expand in series the first term in Eq. (2.32) and cut the expansion at the first order:

$$\ln(1+x) \approx x \qquad \text{con x} << 1 \tag{2.33}$$

then

$$\Delta T(t) \approx \frac{I(t) - I(\infty)}{I(\infty)} \approx L\left[\sigma_G N_e(t) + \sum_i N_i(t)\left(\sigma_{em,i} - \sigma_{E,i}\right)\right] \tag{2.34}$$

The signal obtained thus depends on the cross-section for the processes involved, from the populations of the excited state as function of the time, and the optical path travelled by the beam.

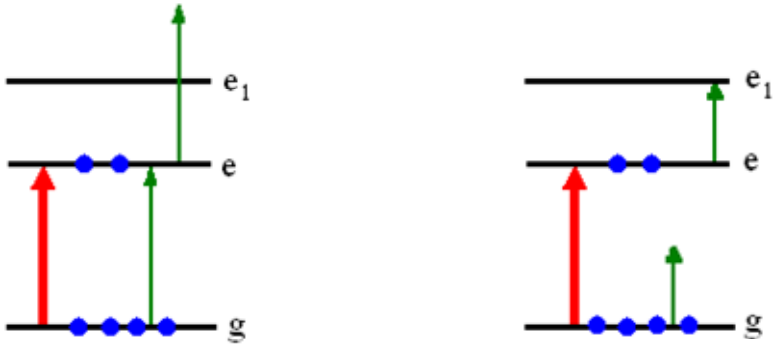

Figure 2.4: Schematic representation of the bleaching and excited state absorption processes.

In the following we neglect the process of stimulated emission. The $\Delta T(t)$ value will be positive if the wavelength of the probe is equal to that of the pump and if the cross section for the ground state absorption is greater than that for the excited state absorption. The ground state absorption will be lower (bleaching) than in the case where the pump is not present because some of the molecules can not absorb any more as they are already in the excited state. The signal will instead be negative if the energy of the probe is suitable to populate an higher excited state (Excited State Absorption ESA) and the cross section for the excited state absorption is greater than that for the ground state absorption.

In the following chapters the curves obtained in the transient absorption experiments are represented in the ordinate axis as $\Delta OD(t) = -\Delta T(t)$.

TA experiments are extremely useful to characterize the properties of relaxation dynamics, energy transfer or charge transfer of electronic excited states of complex molecular systems and they have been used to characterize these processes in homo and hetero dimers of porphyrins, reported in Chapter 6.

Two different setup have been used for the TA measurements, one in Padova and one in Berlin, that are presented in Section 2.5.2 and 2.5.3 respectively. Moreover also the data analysis is different.

2.5.3 Transient absorption setup in Padova

The laser system used for the TA measurements is the same used for Z-scan measurements, described in Chapter 2.4.1

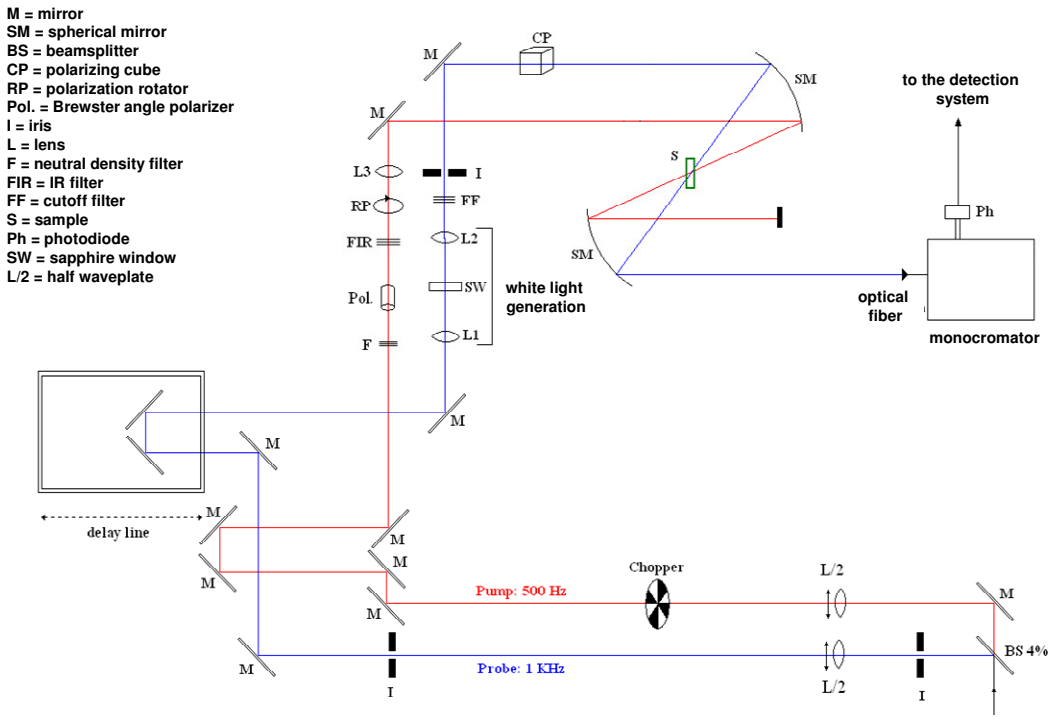

Figure 2.5: Set-up used for the TA experiments in Padova

The beam generated from the femtosecond amplified laser system is used to generate the two beams: the pump is represented in red in Figure 2.5, while the probe is in blue in Figure 2.5. Pumps at different wavelengths are used to excite different samples: the fundamental at 806 nm is used to excited $(TTF^{\bullet+})_2$, while the monomer $TTF^{\bullet+}$ is excited using a 403 nm pump, obtained from the fundamental with a BBO doubling crystal. In order to excite the porphyrins dimer in Chapter 6 in the first excited state, a 560 nm pump was obtained using the OPA system.

The pump pulse repetition rate is halved to 500 Hz by a chopper synchronized with the laser pulse train. The pump passes through a thin quartz slab at the Brewster angle acting as polarizer that select only vertical polarization; then a half waveplate is used to rotate the polarization between 0 and 90 degrees. The lens L3 widens the pump beam so that in the sample position it will have a diameter larger than the probe beam, to ensure the complete spatial overlap of the two beams.

The probe passes through a computer controlled motorized delay line: in this way it is possible to change the beam path during the measurements; after that, the beam passes two lenses (L1 and L2) and a sapphire window, for the generation of white light pulses. The sapphire window should be placed on the focus of L1 (otherwise it does not produce white light), while the position of L2 should guarantee that the light produced is collimated. White light is stable in energy when it is formed by a central white spot surrounded by a red halo, which is cut through the iris placed after the telescope.

The spectrum of white light produced has a strong component at the wavelength of the pump beam (806 nm) that can significantly interfere with the signal. To eliminate or drastically reduce this component, short pass or long pass cut off filters are used depending on the wavelengths range: below 750 nm or above 850 nm. When investigating the area between 750 and 850 nm neutral density filters are used to attenuate the beam.

The white light thus produced retains only part of the polarization, which is restored when passing through a cube polarizer (optimized for wavelengths between 700 and 900 nm). It is then directed onto the sample, placed between two spherical mirrors, where it overlaps spatially the pump beam and then sent to an optical fiber, connected to a monochromator.

The output signal from the monochromator is read by a photodiode connected to a lock-in amplifier. The photodiode used is a silicon photodiode that reads well in the visible region and in the NIR up to 1000-1100 nm. In the area of the IR (for wavelengths above 1000 nm) an InGaAs photodiode (Hamamatsu) is used.

In signal detection the lock-in amplifier is set at a reference frequency of 500 Hz, so it measures the modulation at 500 Hz of the probe intensity induced by the pump. This modulation is equal to the difference between the signal intensity of probes that passes through the sample in the presence or in absence of the pump. The lock-in amplifier also cleans the signal measured by all the "noises" characterized by a frequency different from 500 Hz. For this reason it allows recording changes in the probe transmittance signal that reach values of ~ 1 x 10^{-3}.

Single wavelength fittings are performed on the data obtained with this setup, using a sum of exponential decays. They have to be convolved with the instrumental response function (IRF). So the fitting function is:

$$f(t) = \sum_{l=1}^{n_{comp}} (\exp(-k_l t) \oplus i(t)) A_l \tag{2.35}$$

where $\oplus$ indicates convolution of the exponential decay with the IRF $i(t)$ and k_l are the decay rates. Then the final decay constants are calculated from the average of the values obtained from the fittings at different wavelengths.

2.5.4 Transient absorption setup in Berlin

Femtosecond TA spectra are measured with the pump-supercontinuum probe (PSCP) technique in the laboratory of Prof. N.P. Ernsting at Humboldt University in Berlin[11]. The basic detection scheme is shown in Figure 2.6.

A Titanium:sapphire laser system delivers 30 fs fundamental pulses with energy of 500 μJ at around 800 nm with 500 Hz repetition rate (Femtolasers sPro). Basic pulses are converted into second harmonic 400 nm, 20 μJ pulses in a β-barium borate crystal (BBO, θ = 29°, d = 0.2 mm). In order to avoid effective time broadening, the group velocity dispersion (GVD) is adjusted by a two-prism compressor. After compression, the basic beam is split into two beams with a 4:1 ratio, for optically pumping the sample and other for probing. The supercontinuum is generated by focusing the pulses onto a CaF_2 plate (1 mm) with a thin lens (f = 200 mm, fused silica). The plate remains stationary during an acquisition sequence, but it is translated in both directions orthogonal to the beam by about 100 μm whenever the delay stage moves to a new position. Rotation of the plate is avoided because of an intensity dependence on rotation angle due to nonlinear interactions[12].

The supercontinuum is filtered through a filter solution to reduce the intensity at 400 nm and passed through a pinhole of approximately 50 μm. This pinhole represents the femtosecond white-light source. The beam then is split for reference before being imaged on to the sample cell with spot size of approximately 100 μm. The sample solution typically has an absorbance of 0.7 in a flow cell with internal thickness of 0.3 mm. It is excited by 400 nm pulses of up to 3 μJ (150 μm diameter). Transmitted and reference beams are imaged on to the entrance planes of separate homemade spectrographs, where they get dispersed with a grating and finally registered by photodiode arrays with 512 pixels (S39901-512Q, Hamamatsu) covering

the spectral range 270-670 nm. Each spectrograph is equipped with a microscope which can be inserted into the beam. It allows viewing the supercontinuum, which for this purpose must be attenuated, and to center it on the input position. The latter is defined by a pinhole of 50 µm diameter which can be moved reproducibly in and out of the entrance plane. During measurement the pinholes are removed.

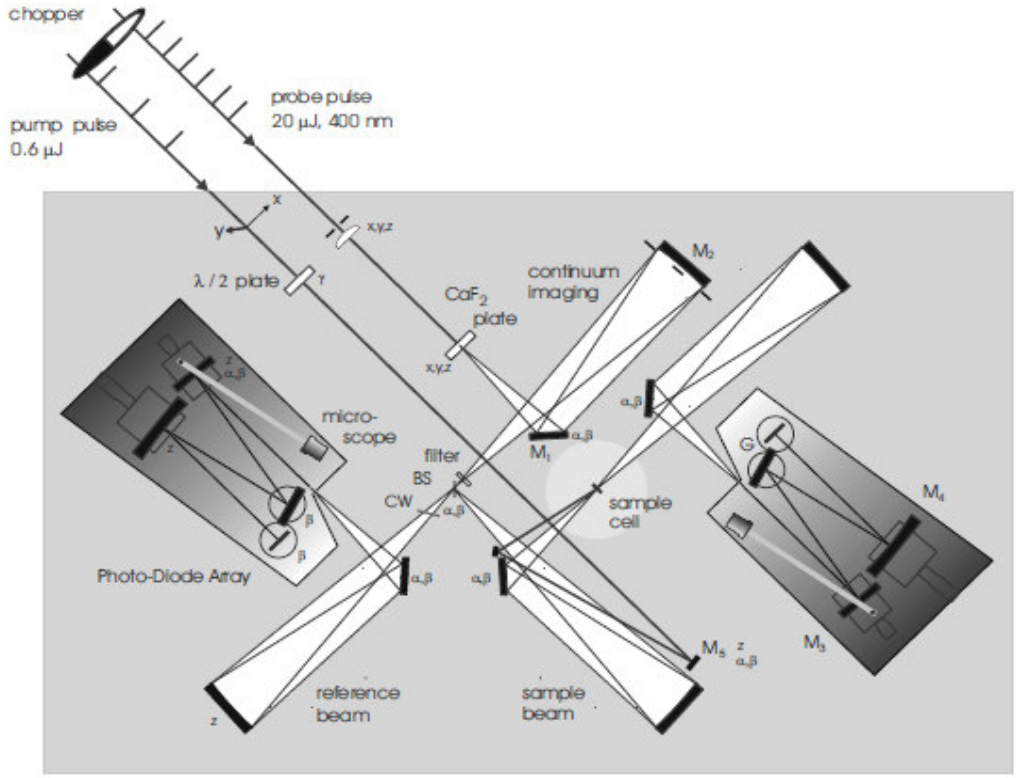

Figure 2.6: Setup for transient absorption in Berlin. (from Ref. 11)

The pump-probe cross correlation was below 100 fs over the whole spectrum.

The spectra were recorded with 6 fs and 1 ps steps, with parallel I_{pa} and perpendicular I_{pe} pump-probe polarization. To improve the signal-to-noise ratio, the data were averaged over multiple pump-probe scans (8 scans with 150 shots per temporal point).

The transient spectra were corrected for the chirp of the supercontinuum probe. Then the solvent signal is subtracted to the sample signal.

The polarization-independent dynamic of the molecules was obtained calculating the magic angle signal I_{ma} with the formula:

$$I_{ma} = \frac{I_{pa} + 2I_{pe}}{3} \tag{2.36}$$

The anisotropy spectra were obtained from:

$$r = \frac{I_{pa} - I_{pe}}{I_{pa} + 2I_{pe}} \tag{2.37}$$

2.5.4.1 Multivariate analysis

In TA experiments in which the full white light spectrum is recorded simultaneously, a series of transient spectra are obtained. They are collected in a matrix $\mathbf{M}(m \times n)$, where each column corresponds to a transient spectrum collected at one of the n different time delay and each raw represents a time decay trace at one of the m different wavelengths,. In a typical TA measurement performed with our setup $290 \le m \le 690$ nm with 0.8 nm steps and $-0.3 \le n \le 1.8$ ps with 6 fs steps or $-36 \le n \le 500$ ps with 1 ps steps.

Without a priori knowledge about a detailed kinetic model, the first step in this global analysis[13] is to fit the data with a sufficient number of exponential decays.

The experimental data **M** can be described assuming a model as[14]:

$$\mathbf{M} = \mathbf{AT} + \mathbf{E} \tag{2.38}$$

The matrix $\mathbf{T}(k \times n)$ contains the kinetic profiles of the k pure contribution in the systems at n delays and the matrix $\mathbf{A}(m \times k)$ the amplitudes of each component at m wavelength constitute the Evolution Associated Difference Spectra (EADS). The error matrix $\mathbf{E}(m \times n)$ contains the residuals. A scheme of the matricies involved in this calculation is reported in Figure 2.7. Moreover with ultrafast measurements the exponential decay has to be convolved with the instrumental response function (IRF).

The $\mathbf{T}(k \times n)$ matrix is formed by the basic time functions Gaussian G, first derivative of a Gaussian DG, second derivatives of a Gaussian DDG, convoluted step-up function CH and convoluted exponential function $CExp_m$:

$$G = \frac{1}{\sqrt{2\pi}d}\exp\left[-1/2(t/d)^2\right] \tag{2.39a}$$

$$DG = \frac{1}{\sqrt{2\pi}d^3}\exp\left[-1/2(t/d)^2\right]t \tag{2.39b}$$

$$DDG = \frac{1}{\sqrt{2\pi}d^5}\exp\left[-1/2(t/d)^2\right]\left(t^2 - d^2\right) \tag{2.39c}$$

$$CH = 1/2 erfc\left(-t/\sqrt{2d^2}\right) \tag{2.39d}$$

$$CExp_m = 1/2 \exp\left[1/2(k_m t)^2 - k_m t\right] Erfc\left[\left(d^2 k_m - t\right)/\sqrt{2d^2}\right] \tag{2.39e}$$

The pulse-width parameter d is found by fitting the pure solvent signal[15].

The global fit function becomes:

$$M(m,n) = A(m,1)G(n) + A(m,2)DG(n) + A(m,3)DDG(n) + A(m,4)CH(n) + A(m,5)CExp_1(n) + A(m,6)CExp_2(n) \tag{2.40}$$

The $A(m, j)$ are linear coefficients. Only the parameters k_1 ,k_2 in the time functions must be optimized in a gradient search. For this purpose one guesses their values and forms the matrix **T** consisting of the rows $G(n)$, $DG(n)$, $DDG(n)$, $CH(n)$, $CExp_1(n)$, $CExp_2(n)$, where k numbers the columns. The optimal coefficients which are associated with these time functions are then obtained in the **A** matrix.

The approximation to the data becomes

$$\mathbf{M}_{sim} = \mathbf{AT}. \tag{2.41}$$

The root-mean-square deviation Σ to the data is calculated from the difference $\mathbf{M}-\mathbf{M}_{sim} = \mathbf{E}$. In the search, Σ is minimized by varying the time constants in the exponential decays.

A program written in Mathematica is used to perform the fit.

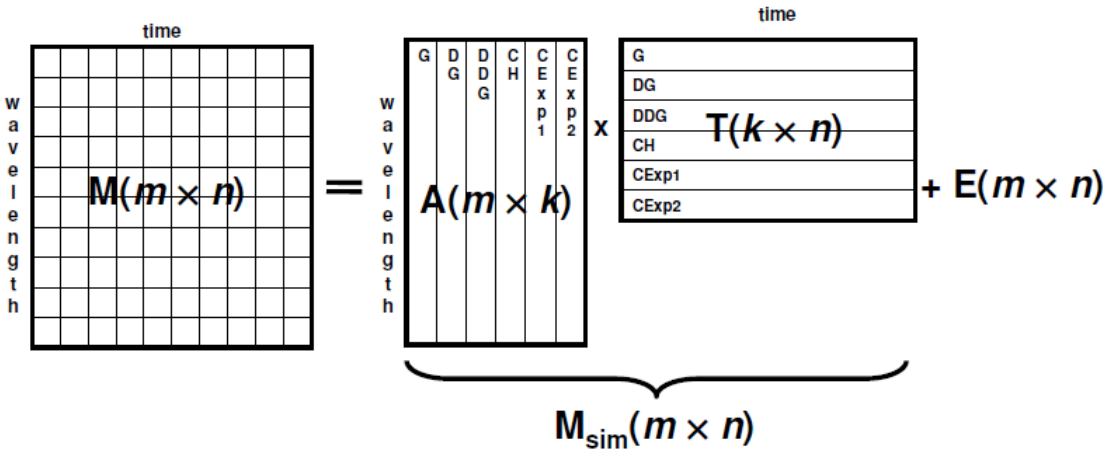

Figure 2.7: Scheme of the matrices used for the MVA of transient data.

Up to this point of the analysis, everything is independent of a kinetic model. All that is gained from this procedure are the characteristic rate constants k_i and the partition between the coherence (G, DG and DDG) and the population (CH, $CExp_1$ and $CExp_2$) in the signal.

From now on only the matrix $\mathbf{A_{cut}}(m \times k\text{-}3)$, containing the EADS relative to the populations, are considered and the three columns relative to the coherence contributions G, DG and DDG are removed.

The obtained EADS usually do not represent the real intermediate states that play a role in the decay kinetic of the system. These are the Species Associated Difference Spectra (SADS) and only for very simple systems EADS corresponds to SADS. To obtain SADS it is necessary to choose a kinetic model that describes the physical problem under investigation. Moreover, if the number of decay constant K_i in the model is higher than the number of observed decay constants k_l, some model parameters must be introduced and their values must be pre-set in order to be able to determine the entire set of molecular rate constants.

The kinetic model can be described by a square matrix $\mathbf{K}(s \times s)$ with s is the number of different species involved. Transition of population between the species are described by rate constants which constitute the off diagonal elements of the **K** matrix. The diagonal elements of **K** contain the total decay rates of each specie. For example for a sequential kinetic model $A \xrightarrow{K_1} B \xrightarrow{K_2} C$, the correspondent **K** matrix is:

$$\begin{vmatrix} -K_1 & 0 & 0 \\ K_1 & -K_2 & 0 \\ 0 & K_2 & 0 \end{vmatrix}$$

This kinetic model can be solved analytically and using the decay constants k_i found in the global fitting, the set of the molecular constants K_i can be determined. So now it is possible to obtain the model matrix $MM(s \times k\text{-}3)$that is defined as:

$$pop = MM\{1, \exp[-k_1 t], \exp[-k_2 t]\}$$

In which *pop* is the matrix that contains the populations of the s molecular species involved as function of time, and k_1 and k_2 are the rate constants found in the global fitting.

By right multiplying the matrix $\mathbf{A}_{cut}(m \times k\text{-}3)$**,** containing only the EADS of the functions relative to the populations, with the inverse of the model matrix $MM^{-1}(k\text{-}3 \times s)$, it is possible to obtain the matrix $\mathbf{S}(m \times s)$ containing the SADS for the s molecular species (Figure 2.8).

$$\mathbf{S} = \mathbf{A}_{cut}MM^{-1}$$

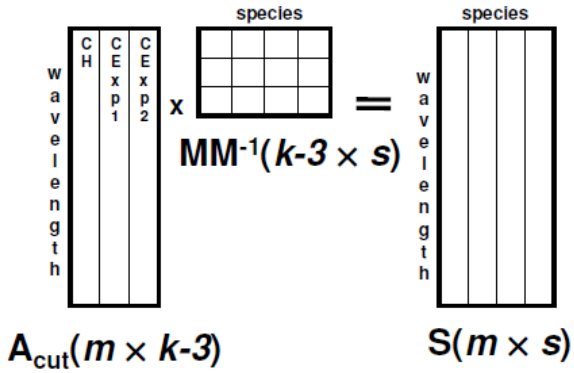

Figure 2.8: Schematic definitions of the SADS, stored in **S**, calculated from the EADS contained in matrix $\mathbf{A}_{cut}$, using the inverse of the model matrix MM obtained from a kinetic model chosen for the system under investigation.

Comparing SADS with the spectra of the species involved in the mechanism, it is possible to judge the quality of the kinetic model proposed and of the parameters chosen. If the SADS are satisfactory, the kinetic model chosen can be the right one to describe the molecular system under investigation. Otherwise a new kinetic model can be devised, the relative model matrix can be obtained and the new SADS can be evaluated.

So using global fitting combined with the development of kinetic models can give an all encompassing view inside the excited state dynamic of the analysed systems.

This method for the data analysis is applied on the TA data obtained for the homo- and hetero-dimers of porphyrins, described in Chapter 6.

References

[1] Demas, J.N. and Crosby, G.A. *J. of Phys. Chem.*, **1971**, 75, 991-1024

[2] N. Klonis, W.H. Sawyer*, J. Fluoresc*.,**1996**, 6, 147.

[3] R.F. Kubin, A.N. Fletcher, *Chem. Phys. Lett*., **1983**, 99, 49.

[4] S. J. Isak, E. M. Eyring*, J. Phys. Chem*., **1992**, 96, 1738.

[5] I. B. Berlman, *"Handbook of Fluorescence Spectra of Aromatic Molecules*", Academic Press, London, **1965**

[6] Sheik-Bahae, M. et al. *IEEE J. Quantum Electron.*, **1990**, 26, 760-769

[7] C. Xu, W.W. Webb, *J. Opt. Soc. Am. B*, **1996**, 13, 481-491

[8] M. Rumi, J.E. Ehrlich, A.A. Heikal, J. W. Perry, S. Barlow, Z. Hu, D. McCord-Maughon, T.C. Parker, H. Rockel, S. Thayumanavan, S. R. Marder, D. Beljonne, J.L. Bredas, *J. Am. Chem. Soc.* **2000**, 122, 9500-9510

[9] C. Xu, R. M. Williams, W. Zipfel, W.W. Webb, . *Bioimaging*, 1996, 4, 198-207

[10] G.R. Fleming, *Chemical Applications of Ultrafast Spectroscopy*, Oxford Press, Oxford, **1986**

[11] A.L. Dobryakov, S.A Kovalenko, A. Weigel, J.L Peres-Lustres, J. Lange, A. Muller, N.P. Ernsting, *Rev. Sci. Inst.,* **2010**, 81, 113106

[12] P.J.M Johnson, V.I. Prokshenko, R.J.D.Miller, *Opt. Express*, **2009**, 17, 21488

[13] I.H.M. van Stokkum, D.S. Larsen, R. van Grondelle, *Biochimica et Biophysica Acta*, **2004**, 1657, 82

[14] C. Ruckebush, M. Sliwa, J. Réhault, P.Naumov, J.P. Huvenne, G. Buntinx, *Anal. Chim. Acta*, **2009**, 642, 228.

[15] S.A. Kovalenko, A. L. Dobryakov, J. Ruthmann, N. Ernsting, *Phys. Rev. A*, **1999**, 59, 2369

SECTION II

STRONGLY INTERACTING DIMERS

Chapter 3

Dimer of the radical cation of tetrathiafulvalene (TTF)

3.1 Introduction

Charge-transfer (CT) complexes are an example of self-assembled structures that exhibits a deep modification of their electronic properties because of spontaneous aggregation, in comparison with the single molecule. So it is expected that linear and non-linear optical properties of these systems will be influenced by CT[1].

The electronic and vibrational properties of CT dimers, either formed by two identical molecules (homo-dimers) or by two different species (hetero-dimers) both in solutions and in molecular crystal have been thoroughly investigated. The work done was at the same time experimental (Raman, IR, UV-Vis Spectroscopy)[2,3] and oriented towards the development of theoretical models[4]. These studies demonstrated that homo-dimer or hetero-dimer formation generates additional energetic states characterised by the presence of a CT process between the two units of the dimer. These states create absorption bands in the near IR region and their position depends on the chemical and physical properties of the two molecules involved, on the distance between them and on their surrounding (solution, polymer, crystalline solid).

An example of a radical ion dimer formed by two identical monomers is taken into account in this work: if dissolved in appropriate solvents perchlorate salt of the radical cation of tetrathiafulvalene ($TTF^{\bullet+}ClO_4^-$) forms a charge transfer dimer, showing the expected CT absorption band at frequencies lower than the absorption due to excitations localized on individual molecules. (Figure 3.1)

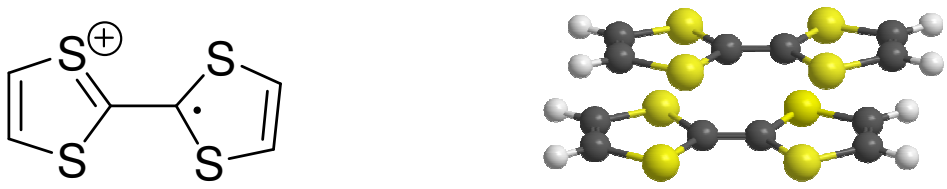

Figure 3.1: Molecular structure of the radical cation of tetrathiafulvalene and the structure of its dimer.

TTF is a non-aromatic system with 14 π electrons, in which the oxidation to radical cation and dication occurs sequentially and reversibly at relatively low potential ($E^1_{1/2} = 0.37$ V, $E^2_{1/2} = 0.67$ V in dichloromethane vs. calomelane electrode)[5]. The radical cation and the dication have planar D_{2h} symmetry, while the neutral molecule has a boat structure with C_{2v} symmetry. The radical species is stable in solution at room temperature, but it can also form dimers when present in high concentrations or at low temperature in appropriate solvents such as dimethylsulfoxide (DMSO) or ethanol.

The interest in the chemistry of the TTF[6] has grown tremendously since its synthesis in 1970[7], mainly because of its effectiveness as an electron donor to obtain metal-organic or organic superconductors[8]. The TTF is considered an important element in the construction of supramolecular structures, engineering of crystals[9] and in systems that operate as molecular machines. Important results were obtained when TTF was inserted in macromolecular structures. Oligomers, polymers[10], and dendrimers[11] containing TTF allowed the preparation of new materials that integrate the unique properties of TTF with the processability and stability that macromolecules show. The TTF molecule has also been used successfully in the construction of redox-active supramolecular systems. In addition, chemical sensors and redox ligands have been prepared using TTF, and from derivatives containing rotaxanes and catenanes[12] molecular shuttles and molecular switches have been constructed. A large synthetic effort has been devoted to the preparation of so-called organic ferromagnets[13], many of which are derived from TTF. The main objective in these systems is the introduction of ferromagnetic coupling between conduction electrons and localized electrons. Recently it was confirmed that TTF may show a nonlinear optical response (NLO) in the second and third harmonic generation[14]. This feature, combined with good thermal stability and the redox properties of TTF, provides a promising strategy for the molecular engineering of materials with modulated nonlinear optical properties. Fullerenes functionalized with TTF[15] show photophysical properties that lead to charge-separated states with long lifetimes.

In our research group the radical ion species: $TTF^{\bullet+}$ was studied in the past as a monomer or a dimer both through theoretical modelling[16] and experimentally by Raman, IR and UV-Vis[17] spectroscopy in order to determine its electronic and vibrational structure.

$TTF^{\bullet+}$ is very interesting because of its efficacy as electron donor, the high electrical conductivity of $TTF^{\bullet+}$ halogens, and the discovery of the metallic-like behaviour shown by the CT complex between the donor $TTF^{\bullet+}$ and the acceptor TCNQ (7,7,8,8 tetraciano-p-quinodimethane).

$TTF^{\bullet+}$ can create also an omo-dimer $(TTF^{\bullet+})_2$ in appropriate environment, and a charge transfer process occurs between the two monomeric units. This system is well described by the Hubbard model[18,19].

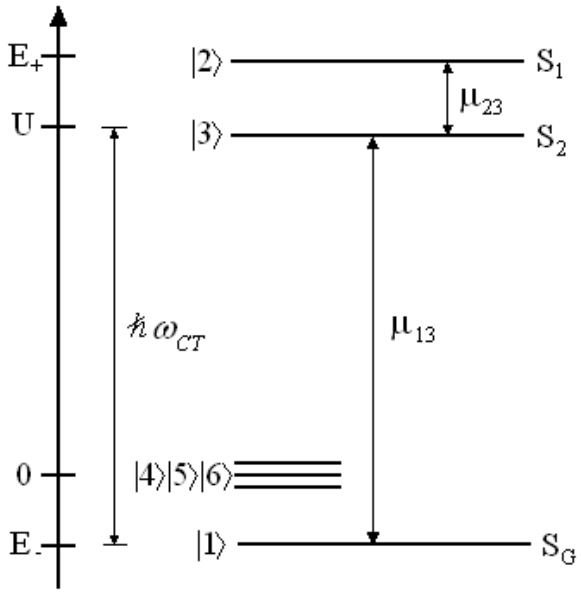

Figure 3.2: Schematic representation of energy levels in a CT dimers using Hubbard model

In this model, described in Chapter 1.4.1, each molecule is assumed to have one electron in their frontier orbital. The electronic states arising form the model are depicted in Fig. 3.2. The states $|1\rangle, |2\rangle$ and $|3\rangle$ are singlet states, while $|4\rangle$, $|5\rangle$ and $|6\rangle$ are triplet states. The only one-photon allowed transitions are those from the ground state $|1\rangle$ to the antisymmetric CT state $|3\rangle$ and from the latter to the symmetric CT state $|2\rangle$. The symmetric CT state $|2\rangle$ is two photon allowed. Using the Hubbard model it is possible to calculate the position of all the electronic states and in particular of the two-photon allowed state $|2\rangle$. The transition energy between these states depends on the crystalline form and the counter-ion of the positively charged dimer.

Pedron et al. [11] calculated for $(TTF^{\bullet+})_2(W_6O_{19})$ that U = 1.13 eV and t = 0.30 eV (see Chapter 1.4.1 for the definition of U and t), so the energy of state $|2\rangle$ is 1.65 eV, corresponding to 750 nm. We should notice that for this system, the one-photon allowed CT $|3\rangle$ state should be at 894 nm.

In the work of Torrance [17] $(TTF^{\bullet+})Cl^-$ in crystal form or in solution displays U = 1.5 eV and t = 0.275 eV, so the two-photon allowed state falls at 668 nm.

The salt under investigation in this work is $(TTF^{\bullet+})ClO_4^-$, so the parameters used in the model may be slightly different: calculating U from the position of the CT band in the absorption spectrum (U = 1.387 eV) and assuming t = 0.3 eV, the position of the two-photon allowed state should be at 679 nm.

Investigating the two-photon absorption (TPA) properties of the dimer, it would be possible to experimentally observe the existence and spectral position of this state and measure its two-photon absorption cross section. Following the predictions of the model, TPA experiments must be performed in the range 1200 - 1600 nm; this wavelength range is accessible using the OPA800C with our amplified femtosecond laser system. In addition, neither the dimer nor the monomer are fluorescent, so Z-scan technique must be used.

Moreover, since these CT dimers are expected to show different relaxation dynamic for the excited electronic states with respect to the monomer, transient absorption measurement were also performed. Results obtained from excited-state dynamic investigation, already the subject of my master thesis, will be briefly reported for completeness. The dimer is excited directly in its CT band at 806 nm, while 403 nm excitation is used for the monomer.

3.2 Sample preparation and linear characterization

The perchlorate salt of the radical cation is prepared from neutral TTF using the following procedure.

400 mg of TTF are dissolved under stirring in 16 ml of glacial acetic acid at room temperature. 0.1 ml of 35% hydrogen peroxide are added and the resulting mixture is stirred for 5 min. 0.1 ml of 70% perchloric acid are added with caution. After further 5 min agitation, the mixture is subjected to centrifugation for 5 min at 3500 rpm. The supernatant is discarded and the solid residue is suspended 3 times in 5 ml of fresh acetic acid, washed and then separated again by centrifugation. The final solid product is dried in vacuum at 40 ° C overnight. For further purification, the product can optionally be re-crystallized from 20 ml of acetonitrile, separated by filtration and dried under high vacuum.

In order to characterize the TPA of the CT dimer, it is important to have samples of known and high concentration, in which only the dimer is present. In this work many attempts have been devoted to the goal of obtaining liquid or solid samples of $TTF^{\bullet+}$ radical dimer stable and at high concentration (~ 0.1 - 0.3 M).

The first step is investigating the $TTF^{\bullet+}$ behaviour in solution. In solution the $TTF^{\bullet+}$ radical cation is not stable and dismutate to obtain the neutral molecule and the dication. Moreover

dimer formation is possible only in specific solvents, like, for example DMSO, while in acetonitrile only the monomer is present.

To identify which species are present in solution in the different environments tested, UV-Vis absorption spectra are analyzed.

The work of Torrance[20] is used as a reference. In this work the linear absorption properties of the different species involved are listed and shown in Figure 3.3: the radical cation $TTF^{\bullet+}$, its dimer $(TTF^{\bullet+})_2$ and the neutral molecule TTF^0.

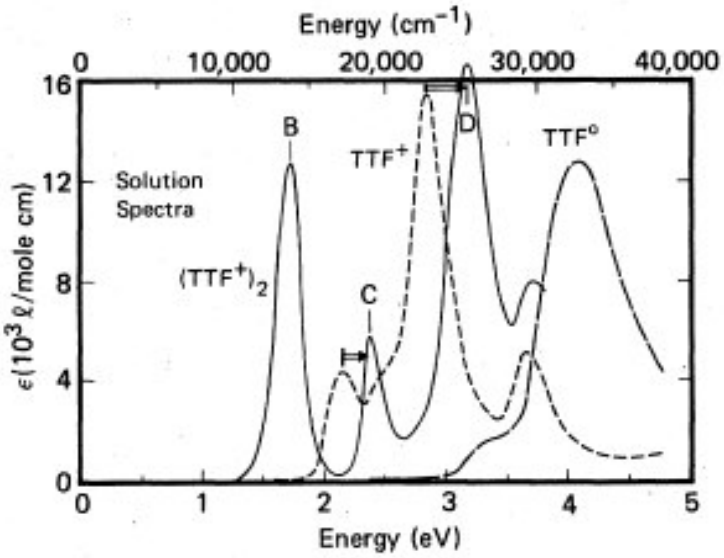

Figure 3.3: Absorption spectra of TTF^0 and $TTF^{\bullet+}$ in acetonitrile at 300 K and of the dimer $(TTF^{\bullet+})_2$ in ethanol at 225 K. The arrows represent the shift of the energies of the Davydov transitions following the dimerization. Image taken from Ref. [20].

In Figure 3.4 instead the absorption spectra of different samples prepared in our lab are reported starting from $TTF^{\bullet+}ClO_4^-$.

With the help of the literature the two bands at 2.14 eV (**A**) and 2.85 eV (**B**)[17] can be attributed to intramolecular or localized excitation of the monomer; in the dimer these two excitations are shifted to higher energy values, at 2.39 eV (**1**) and 3.18 eV (**2**) respectively. This blue shift is expected on the basis of excitonic theory which predict this kind of shift in the case of H-type dimer. So $(TTF^{\bullet+})_2$ can be considered like an H-aggregate with N=2. All these signals correspond to transitions polarized in the plane of the molecule. These intense low-energy bands are typical for the spectra of intramolecular π conjugated radicals.

In addition to these two excitations, in the dimer spectrum there is a new low-frequency absorption band at 1.60 eV (**3**), not present in the monomer spectrum. This peak corresponds to the one-photon allowed CT band predicted by the Hubbard model. In solid samples another

band can be visible in this spectral region, that accounts for the presence of H aggregates with N > 2.[21] These aggregates are never present in our samples.

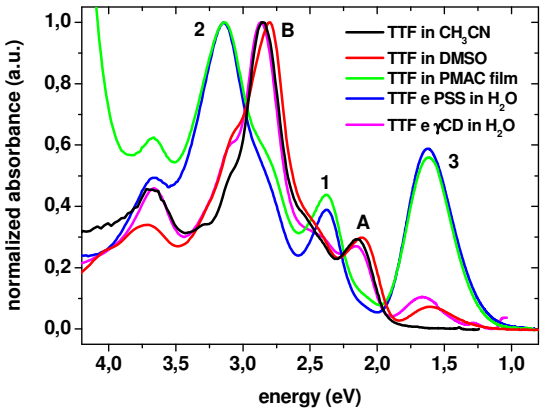

Figure 3.4: Normalized absorption spectra of $TTF^{\bullet+}$ in acetonitrile, in DMSO, in PMAC film, in water with equimolar PSS and in water with γ-CD.

As depicted in Figure 3.4 (red line), in DMSO the main component is still the monomer, but thanks to the high solubility, the dimer formation is obtained at high concentration (C ~ 0.2 M); on the other hand the dismutation is quite fast. In other solvent, like acetonitrile (black in Figure 3.4) or ethanol only the monomer is formed, and dismutation is always present. In water $TTF^{\bullet+}$ is not stable and dismutates almost instantaneously because of the insolubility of TTF^{0}. On the other hand we observed that it is possible to have the formation of $(TTF^{\bullet+})_2$ dimers (Figure 3.4, magenta line) when cyclodextrins (CD) are added to the water solution, even if the monomer is still the major component. Moreover using hydroxypropyl-γ-cyclodextrin in water the radical cation displayed a lifetime 10 times higher than in pure water and 5 times higher than in DMSO. To be able to stabilize $TTF^{\bullet+}$ in water also is a prerequisite for the preparation of solid films with the ESAM (Electrostatically Self Assembeld Multilayers) technique, as discussed in the following[22].

A strategy to stabilize the radical cation could be the preparation of solid state samples in which $TTF^{\bullet+}$ is included.

The first approach was the production of films of $TTF^{\bullet+}$ in poly-methacrylonitrile (PMAC), reported in Figure 3.5, with spin coating technique. In these films there are almost only dimers (Figure 3.4, green line), the radical cation is stable, but they have poor optical quality and obtaining high concentration in the films is difficult. The optical quality of the films was slightly improved working under N_2 atmosphere and screening different composition of the starting solution.

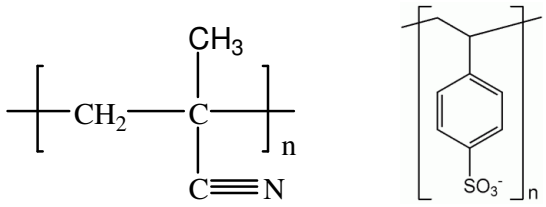

Figure 3.5: Chemical formula of PMAC (left) and PSS (right)

Another possibility explored concerned a change in the guest polymer matrix. The water soluble anionic polymer polystyrene sulphonate (PSS) (Figure 3.5) was investigated. Films preparation starts from the optimization of the solution to be used. After an initial screening of the relative concentrations of $TTF^{\bullet+}$ and PSS it was observed that equimolar solutions of PSS and $TTF^{\bullet+}ClO_4$ contain only the dimer, in addition to high solubility and high stability. With this solution, through dip-coating, multilayer films can be prepared in which only the dimer is present. In order to deposit thicker films cellulose was added to increase the solution viscosity. However, in the drying process, PSS tend to crystallize making opaque the film: these films could not be used for Z-scan and transient absorption measurements.

Another technique that could be employed to produce multilayer films is the ESAM technique[22].

This technique consist in the alternate deposition of a polication and of a polianion dipping a substrate in their aqueous solutions: it was already used in our laboratory and allowed us to obtain good optical quality films with the desiderated amount of cromophores, by changing the number of layers[23].

At the beginning our idea was to find a negatively charged polymer to build ESAM films with $TTF^{\bullet+}$ as the opposite ion-layer, so we tried to make ESAM films using DMSO solutions of PSS and $TTF^{\bullet+}ClO_4$, but DMSO is too viscous to allow homogeneous deposition and a good drying of the film. Different solvents were also tested for the two different species: distilled water for PSS and acetonitrile for $TTF^{\bullet+}ClO_4$. The deposition of a first bilayer of PSS/$TTF^{\bullet+}ClO_4$ was sucessfull, but during the following immersion in the PSS water solution, the $TTF^{\bullet+}$ previously deposited was removed from the substrate.

In conclusion the best result in the preparation of a solid sample were reached by including $TTF^{\bullet+}ClO_4$ in a PMAC matrix: the dimer is the major component and the radical cation is stable. But if high dimer concentrations are necessary, $TTF^{\bullet+}ClO_4$ solutions in DMSO are still the better solution.

3.3 Z –scan measurements

Open and closed aperture Z-scan measurements on $(TTF^{\bullet+})_2$ were performed in order to detect the presence of the two-photon allowed state predicted by the Hubbard model and to measure its TPA cross section.

All the experiments were performed with the femtosecond laser system described in Chapter 2.4.1 using the Z-scan technique as reported in Chapter 2.4.1. The output wavelength of the optical parametric amplifier was tuned in the range 1300-1600 nm, in order to two-photon excite the predicted CT state between 650 nm and 800 nm.

To investigate this large spectral range it has been chosen to perform Z-scan measurements from 1300 nm to 1600 nm every 100 nm. Because the two-photon allowed CT band should be very broad, like its one-photon analogue (half-width of about 200 nm), the chosen steps should be not too large. Since at 1400 nm there is strong absorption from water, Z-scan traces were recorded at 1300 nm, 1350 nm, 1450 nm, 1500 nm and 1600 nm.

Z-scan experiments require highly concentrated solutions, so the only solvent that affords this level of solubility for $TFF^{\bullet+}$ and enough dimer formation is DMSO. In DMSO solution a mixture of monomer, dimer and traces of TTF^0 are present, therfore it is difficult to determine precisely the amount of dimer in solution. Even in these conditions, however, it is still possible to investigate at least the spectral position of the two-photon allowed CT state of the dimer, because neither the monomer nor the neutral specie have an allowed state in this frequency range, and the presence of a maximum for the TPA coefficient β for the solution is expected if there is a TPA resonance in this frequency range. When TPA occurs, open aperture Z-scan experiments should display a dip in the normalized transmittance profile.

As shown in Figure 3.6 (left), these measurements show instead a positive peak at 1600 nm, and the same behaviour is present in all the investigated range. This feature can be attributed to saturable absorption of the one-photon allowed CT transition, displaying an extremely broad absorption band in the linear spectrum with non zero absorbance values at all the wavelengths investigated. The typical linear absorbance in this range is approximately 0.5 for our samples (optical path 1 mm, initial monomer concentration = 0.1-0.15 M).

The expected signal (a dip) for a typical TPA transition, however, is not visible in our measurements. Nevertheless we choose to fit the traces recorded at different wavelengths to follow the spectral behaviour of the β coefficient, since it is still possible that the dip is buried in the saturable absorption signal of the one-photon allowed transition, but still its contribution can be extrapolated from the spectral profile of the β coefficient. The fitting formula used for obtaining both β and n_2 in the following are reported in Chapter 2.4.1.

As can be seen in Figure 3.6 (right) the average β values obtained goes from -7×10^{-11} cm/W to -11×10^{-10} cm/W with a monotonous increase in the absolute value as the wavelength decreases, but characterized by an experimental error comparable with the observed increment. So unfortunately the intrinsic low sensibility of the Z-scan technique cannot provide clear evidence of the presence of processes due to other states, than the one-photon allowed CT state, in the wavelength range investigated.

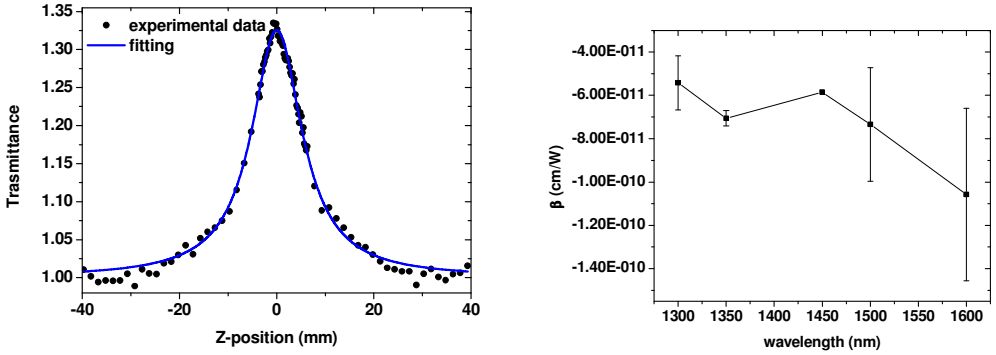

Figure 3.6: Left: Open aperture Z-scan trace of $(TTF^{+})_2$ solution in DMSO at 1600 nm. Right: Average β values in the wavelength range investigated.

Closed aperture Z-scan measurements were also performed on $(TTF^{\bullet+})_2$ solution in DMSO. These experiments allow detection of the non-linear refractive index of the material system under investigation. Also the solvent contributes with a signal that arises from its own non-linear refractive index n_2, so for each experiment both the traces for neat DMSO and $(TTF^{\bullet+})_2$ solution were collected. In Figure 3.7 (right) is reported an example of the recorded traces.

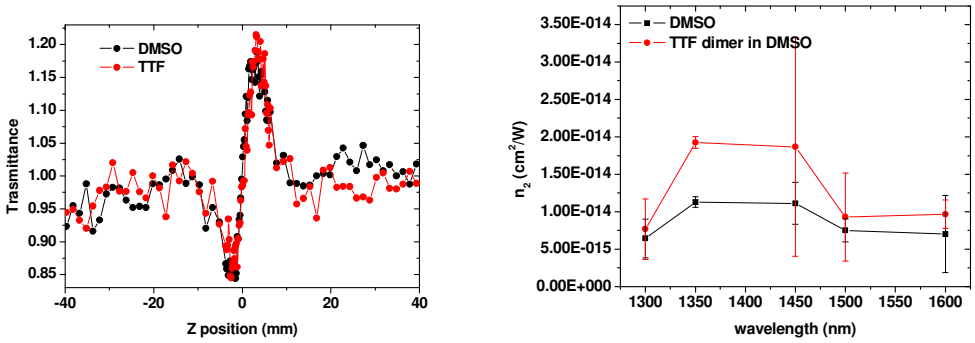

Figure 3.7: Right: Closed aperture Z-scan traces of DMSO (black) and $(TTF^{+})_2$ solution in DMSO (red) at 1600 nm. Left: n_2 values for DMSO (black) and $(TTF^{+})_2$ solution in DMSO (red) between 1300-1600 nm.

Because of the small difference between the two signals collected, we decided to fit independently the solvent signal and the solute signal and then compare the two values of the nonlinear refractive index n_2 obtained. The normal procedure instead requires that the solvent signal is subtracted from the sample signal before the fitting. In Figure 3.7 (left) the average n_2 values obtained for DMSO and $(TTF^{\bullet+})_2$ in DMSO at different wavelengths are reported. The n_2 values obtained for the $(TTF^{\bullet+})_2$ solution are always higher than for DMSO, but the error affecting these data is higher than the differences observed, making it difficult to gain meaningful information from these results.

The Z-scan experiments were performed at two different repetition rates, 200 Hz and 20 Hz, and changing the laser pulse intensity from 2×10^{-7} J to 1×10^{-6} J: no dependence from these parameters was seen in the value of β or in the nonlinear refractive index of the sample or of the solvent.

3.4 Transient absorption measurements

Transient absorption measurements were performed in DMSO solution and in PMAC film for the dimer and in acetonitrile for the monomer.

The dimer is excited at 806 nm, directly in the CT band, and probed from 675 nm to 1100 nm each 25 nm, using the laser system described in Chapter 2.4.1 and the optical setup reported in Chapter 2.5.3. After excitation, only two decay constants are present: a shorter one of 0.22 ± 0.09 ps and a longer one of 3.0 ± 1.2 ps, both in solution and in the film.

The shorter component can be attributed to the decay from the first excited state to the ground state. The longer component instead is attributed to vibrational cooling of the hot ground state, due to the interaction with the surrounding medium. This phenomena happens in few picoseconds for organic molecules at room temperature. An energy level scheme with the decay processes of the dimer is depicted in Figure 3.8.

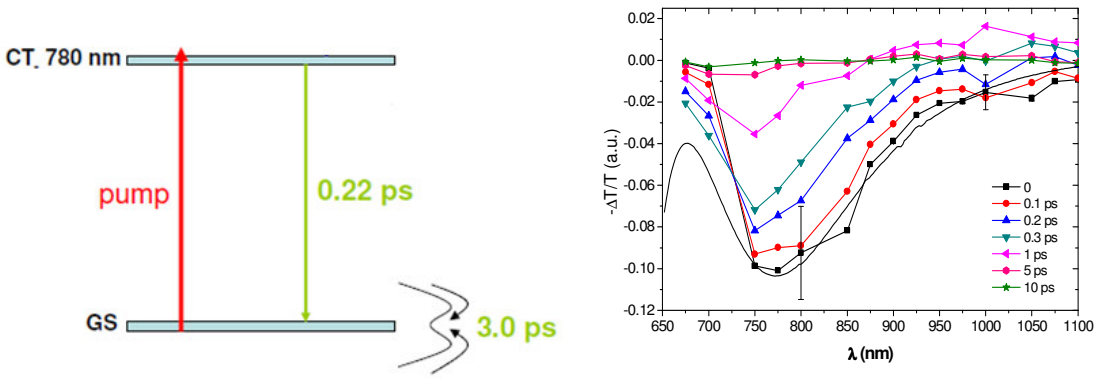

Figure 3.8: Scheme of the decay processes after excitation of the dimer (left). Transient absorption spectra at different delay times for TTF dimer in DMSO solution (right). The absorption spectrum (black line) is superimposed to TA spectra.

In the TA spectrum in Figure 3.8 a strong bleaching is present between 675 nm and 850 nm, where the CT band is absorbing. The bleaching decreases both with the decay from CT state and with vibrational cooling. In the region from 850 nm and 1000 nm an initial bleaching is observed, followed after a picosecond by excited state absorption (ESA). The bleaching follows the lifetime of the excited state, while ESA decay disappears during the time of spectral diffusion.

The monomer was excited at 403 nm, close to one of the absorption maxima of the molecule, in acetonitrile, a solvent in which only the monomer is present. The spectral range investigated goes from 425 nm to 625 nm. The transient signal is always very low, comparable with the oscillation around time zero due to the solvent and the cuvette. An example of these oscillation around time zero are reported in Figure 3.9 (left).

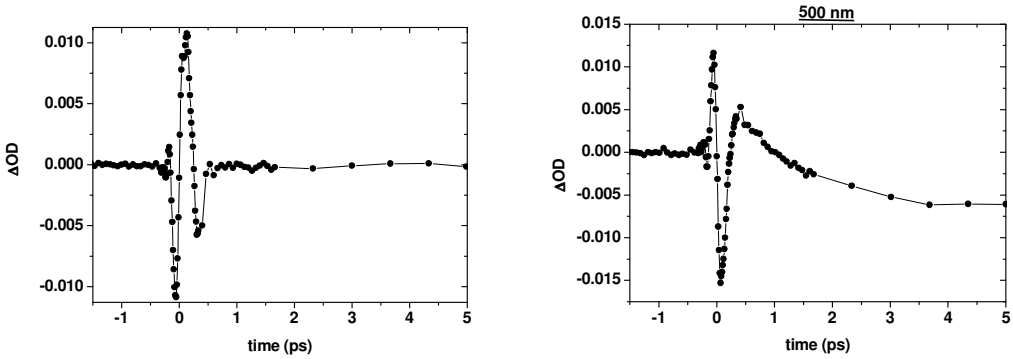

Figure 3.9: On the left transient signal relative only to the solvent and the cuvette used is reported. On the right the signal of the TTF monomer in acetonitrile probed at 500 nm is reported for comparison.

To avoid interference from these signal, the analysis of the data starts from 0.5 ps. Even in this sample, only two time constants are found.

The shorter one of 1.4 ± 0.7 ps is due to the fast decay from the initially populated state at 436 nm to the first excited state at 578 nm. The second time constant 21 ± 7 ps is related to the decay from the first excited state to the ground state.

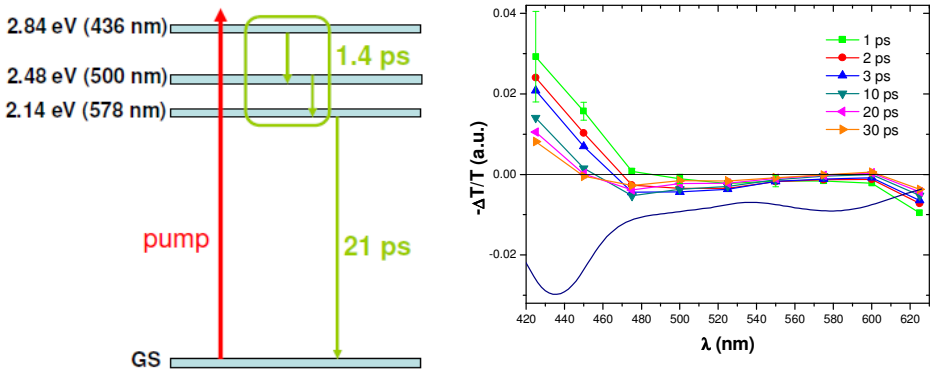

Figure 3.10: Scheme of the decay processes after excitation of the monomer (left). Transient absorption spectra at different delay times for TTF monomer in acetonitrile solution (right). The absorption spectrum (black line) is superimposed to TA spectra.

The TA spectrum shows strong ESA at 425 nm, due to transitions from the initially populated state to a two-photon allowed state above 6 eV (210 nm). From 475 nm to 625 nm a negative signal is present, due to the predominant contribution of ground state bleaching. The bleaching is less strong between 550 nm and 600 nm, where it can be balanced by the presence of a two-photon absorbing excited state. This state should be between 4.39 eV (280 nm) and 4.21 eV (295 nm), if we consider as starting point the state at 2.14 eV (578 nm) populated after 1.5 ps.

Comparing the decays of the two species studied, it is evident that the dimer is almost one hundred times faster than the monomer, probably due to the higher number of decay channels present in the dimer.

It is also important to note that the relaxation dynamic and properties of transient absorption of the dimer of $TTF^{\bullet+}$ have not changed going from solution to solid film. This behaviour makes it possible to imagine that this chromophore, incorporated in organic matrices, can be used in applications in the field of photonics, such as the construction of fast optical switches, thanks to the extremely short duration of the lifetime of the excited state.

3.5 Conclusions

In conclusion it was not feasible to detect the presence of the two-photon allowed state predicted by the Hubbard model with the Z-scan technique. Open aperture Z-scan measurements are dominated by saturable absorption of the one-photon allowed CT state that masks eventual contributions from the TPA of the second CT state. In closed aperture Z-scan experiment there is the contribution from the solvent's signal to n_2 that is of the same order of magnitude of the signal of the $(TTF^{\bullet+})_2$ in solution.

Instead, the excited- state dynamic of both the monomer and the dimer was investigated, finding two different time constants for both species. The decay of the dimer is globally one hundred times faster than the monomer, so it can be a promising material for optical devices requiring fast response.

References

[1] Mulliken, R. S.; Pearson, W. B. In *Molecular Complexes;* Wiley-Interscience: New York, 1969.

[2] Pedron, D.; Speghini, A.; Mulloni, V.; Bozio, R. *J. Chem. Phys.* **1995***, 103(8)*, 2795.

[3] Mulloni, V.; Pedron, D.; Bozio, R. *Chem. Phys. Lett.* **1996***, 263*, 331.

[4] Bozio, R.; Pecile, C. In *Charge transfer crystals and molecular conductors;* Clark, R. J. H., Hester, R. E., Eds.; Spectroscopy of Advaced Materials; J. Wiley & Sons: Chichester, 1990; Vol. 19, pp 1.

[5] C. Katan, J. Phys Chem A, 1999, 103, 1407; I. Hargittari, J. Brunvall, M. Kalanits, V. Khodorkovsky, *J. Mol. Struct*., 1994, 317, 273

[6] J. L. Segura, M. Martin, *Angew. Chem. I. E*., 2001, 40 (8), 1372

[7] F. Wudl, G.M. Smith, E. J. Hufnagel*, J. Chem. Chem Soc. Commun*., 1970, 1453

[8] M. R. Bryce, *Chem. Rev. Soc*, 1991, 20, 355

[9] G. R. Desiraju, *Crystal Engineering: The Design of Organic Solid*, Elsevier, Amsterdam, 1989

[10] S. Frenzel, S. Arndt, R. M. Gregorious, K. Mullen, *J. Mater. Chem*., 1995, 5, 1929

[11] M. R. Bryce, W. Davenport, L. M. Goldenberg, C. Wang, *Chem. Commun*., 1998, 945; M. R. Bryce, *J. Mater. Chem*., 2000, 10, 589

[12] M. B. Nielsen, C. Lomholt, J. Becher, *Chem. Rev. Soc*., 2000, 29, 153

[13] J. Roncali, *J. Mater. Chem*., 1997, 7, 2307

[14] A. I. de Lucas, N. Martin, L. Sanchez, C. Seoane, R. Andreu, J. Garin, J. Orduna, R. Alicia, B. Villacampa, *Tetrahedron*, 1998, 54, 4655; R. Andrei, A. I. De Lucas, J.Garin, N. Martin, J. Orduna, L. Sanchez, C. Seoane, *Synth. Met*., 1997, 86, 1817

[15] M. Prato, M. Maggini, C. Giacometti, G. Scorrano, G. Sandonà, G. English Oak, *Tetrahedron*, 1996, 52, 5221; N. Martin, L. Sanchez, C. Seoane, R, Andrei, J. Garin, J. Orduna, *Tetrahedron Lett.*, 1996, 37, 5979

[16] . Bozio, C. Pecile, in *Spectroscopy of Advanced Materials*, RJH Clark and R.E.Hester (eds.), J. Wiley & Sons, Chichester, 1990

[17] D. Pedron, A. Speghini, V. Mulloni, R. Bozio, J. Chem. Phys., 1995, 103, 2795; V.Mulloni, D. Pedron, R. Bozio, *Chem. Phys. Lett*, 1996, 263, 331

[18] Harris, A. B.; Lange, R. B. *Phys. Rev.* **1967***, 157*, 295.

[19] Hubbard, J. *Proc. Roy. Soc. (London) A* **1963***, 276*, 238.

[20] J. B. Torrance, B. A. Scott, B. Welber, F. B. Kaufman, P. E. Seiden, *Physical Review B*, **1979**, *19*, 730

[21] B. Scremin, Tesi di Dottorato, Università degli Studi di Padova, Padova 2000

[22] G. Decher, Nature, 1997, 77, 1232

[23] E. Garbin, Tesi di laurea, Università degli Studi di Padova, Padova 2007

SECTION III

WEAKLY INTERACTING DIMERS

Chapter 4

Dimers of dipolar and quadrupolar chromophores

4.1 Introduction

Polar and polarizable π-conjugated organic molecules have been extensively investigated in the past years for nonlinear optical (NLO) applications[1] such as electrooptic (EO) response[2] or two-photon absorption[3] (TPA). Such interest is justified by the potential use of these molecules in emerging photonic technologies, including broad-band communications and optical networking[4], holographic memories[5], two-photon laser scanning fluorescence microscopy[6], optical limiting[7], microfabrication[8], photodynamic therapy[9], and up-converted lasing[10]. By far, the most successful design strategy involved π-conjugated molecules with electron donor (D) and acceptor (A) groups.

More generally, dyes for NLO applications are highly polarizable and strongly respond to the charge distribution in the local environment[11]. Electrostatic intermolecular interactions are therefore expected to play a major role in systems like molecular crystals, films, aggregates, or multichromophoric assemblies. If properly understood, interchromophore interactions offer a powerful tool to design new materials for NLO applications.

For this reasons in our work different dimer of dipolar and quadrupolar molecules are synthesised, their linear absorption and emission properties are investigated, their TPA cross section and spectra are measured and a model that takes into account intermolecular electrostatic interactions is developed.

The systems investigated are dimers of dipolar[12,13] or quadrupolar[14,15] structures, synthesised in the group of Prof. A. Abbotto, University of Milano-Bicocca. They are chosen as model systems to understand the influence of intermolecular interactions on the TPA properties.

The basic units have a general structure D-π-A for dipolar ones, and A- π -D- π –A for quadrupolar ones, where A is an electron-withdrawing group, D is a electron-donating group and π is a conjugated chain. In particular heteroaromatic based dipolar and quadrupolar dyes have been investigated, in which the pyrrole and the pyridinium rings are used as D and A moieties, respectively.

The lowest energy absorption band of dipolar molecules is characterized by high-intensity and is related to the intramolecular charge transfer (ICT) between the D and A groups. Because of the asymmetric structure this absorption band is allowed both by one-photon absorption (OPA) and TPA. Also for quadrupolar chromphores the lowest energy OPA band is strong and related to a ICT mechanism, but, contrary to the dipolar case, the quadrupolar system has a symmetric structure and this imposes that the electronic states involved in OPA are not the same for TPA.

4.2 Dimers of dipolar chromophores

The molecular structure of the dipolar PEP + is reported in Figure 4.1. This molecule is the monomer from which the dimeric structures are created linking the two dipolar units through a non-conjugated saturated alkyl chain.

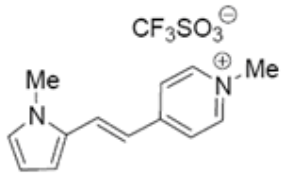

Figure 4.1: Molecular structures of PEP+.

The dye units were connected through their A endgroups (methyl-pyridinium ions), while in the past also the connection between the donors was investigated[16,17]. In this thesis work two dimers were investigated: Bis PEP+ (AA) C3 in which the linker is a linear alkyl chain with three carbon atoms, and Bis PEP+ (AA) C6 in which the carbon atoms in the chain are six. The molecular structure of the dimers is reported in Figure 4.2. The absence of π bonds in the linking chain ensures the lack of electronic conjugation between the two units, whereas the different length affords to control interchromophore distances.

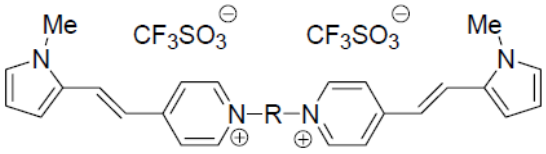

Figure 4.2: Molecular structures of Bis PEP+ (AA) C3 (if R = n-C_3H_6) and Bis PEP+ (AA) C6 (if R = n-C_6H_{12})

All molecular system, PEP+ and its dimers, are investigated in DMSO solution, and they show a strong ICT absorption band around 440 nm and high transparency in the red and NIR region (Figure 4.3). In addition, they all display very weak fluorescence emission at 530-540

nm. Table 4.1 collects the main OPA, TPA, and emission properties of dipolar monomer and dimers. Fluorescence quantum yields (FQY) are estimated against the known FQY of fluorescein in water at pH > 10 (0.1 M NaOH)[18] and of coumarin 540A in ethanol[19]. The solution used for fluorescence measurements are characterized by concentration in the range 5×10^{-6} – 5×10^{-7} M. The FQY of all these molecules is around 1%.

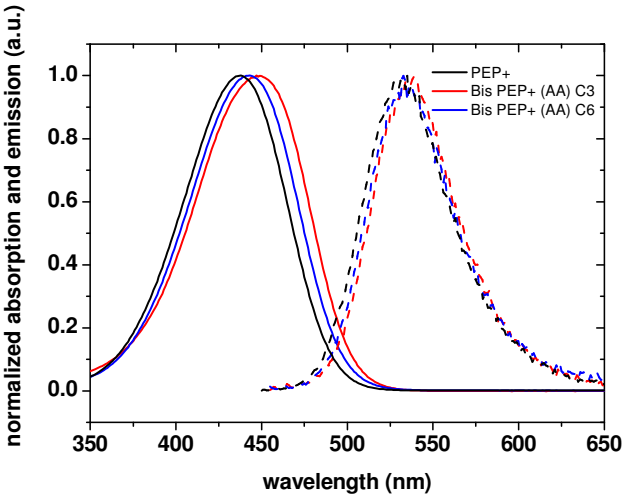

Figure 4.3: Normalized absorption and emission spectra of PEP+ and its dimers in DMSO solution.

The linear absorption maxima of both dimers are red shifted with respect to the corresponding monomer, and this shift increases as the length of alkyl chain decreases, leading to shorter intermolecular distances and hence to larger interchromophore electrostatic interactions. Instead, no significant shift is seen in emission spectra.

Nonlinear absorption spectra of all compounds are also investigated in DMSO. All these compounds are fluorescent, so the TPIF technique, described in Chapter 2.4.2, was used to measure their TPA cross section in the range 730-920 nm. For these measurements more concentrated solutions are employed, and they fall in the range 1×10^{-3} – 1×10^{-4} M. The fluorescence spectra excited by two photon absorption are also measured and compared to linear emission spectra. Figure 4.4 shows that they fall in the same spectral region and have almost identical shapes, confirming that the emitting states are the same for both processes. The shifts between the linear and two photon induced fluorescence maxima is attributed to a reabsorption effect caused by the higher concentration employed in the two photon measurements with respect to the linear one. Therefore, in the following analysis it is assumed that the fluorescence quantum yield does not change if one or two photon excitation is applied.

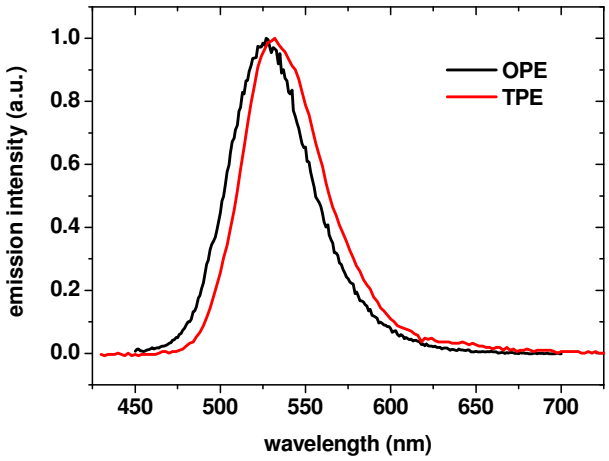

Figure 4.4: Comparison between the fluorescence spectra excited by OPA (black line) and by TPA (red line).

Figure 4.5 shows the TPA spectra (line + symbols) in DMSO of PEP+ and its dimers together with the linear absorption spectra (full lines). The wavelength scale of TPA spectra is divided by two to allow a direct comparison with OPA and the values of TPA cross-section are expressed in Göppert-Mayer units (1GM = 10^{-50} cm^4 s $photon^{-1}$ $molecules^{-1}$).

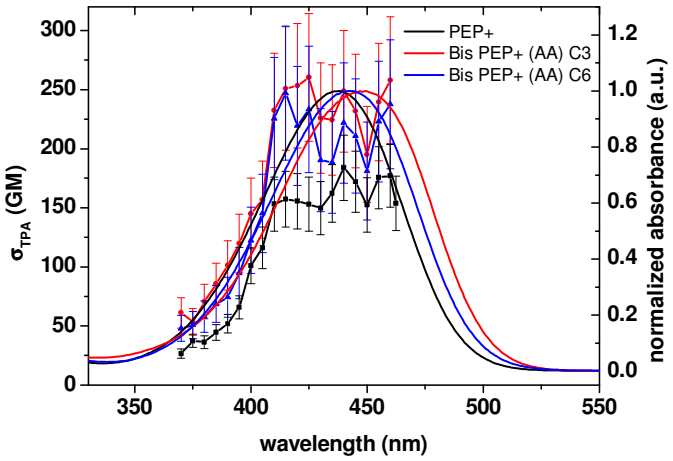

Figure 4.5: TPA (line + symbols) and OPA (full line) spectra of PEP+ and its dimers in DMSO solution.

For PEP+ and its dimers the one- and two-photon absorption maxima coincide, as expected for simple dipolar molecules. In all the experiments there is a large error bar, due mainly to

the extremely low FQY of these compounds. Nevertheless the TPIF signals show the expected quadratic behaviour with respect to the input laser intensity.

The maximum values of the TPA cross sections are summarized in Table 4.1.

Table 4.1: OPA and emission maxima (λ_{OPA} and λ_{em}), absorption cross-section (ε), fluorescence quantum yield (FQY) and TPA maxima (σ_{TPA}) for the compounds studied.

compound	**λ_{OPA} (nm)**	**λ_{em} (nm)**	**ε (cm^{-1} M^{-1})**	**FQY (%)**	**σ_{TPA} (GM)**
PEP+	438	532	37300 ± 3000	1.2 ± 0.1	160 ± 35
Bis PEP+ (AA) C3	447	537	68600 ± 2500	1.5 ± 0.3	240 ± 50
Bis PEP+ (AA) C6	443	535	65000 ± 4000	1.5 ± 0.3	210 ± 50

The TPA cross sections of PEP+ dimers are slightly less than twice the monomer cross-section. For these dimers interchromophore interactions are too weak to produce sizeable spectroscopic effects: the one- and two-photon absorption properties of Bis PEP+ (AA) C_n dimers are almost the sum of those of the corresponding monomers. In fact, PEP+ and its dimers are charge separated systems and in solution they presumably tend to keep off, in order to stabilize their charges.

In collaboration with the group of Prof. Anna Painelli from the University of Parma, a model was developed to describe the linear and non-linear optical properties of these dimers. Due to the small effect observed in the OPA and TPA properties, only an effective model was developed.

The approach used is based on the Mulliken model for charge-transfer excitations in molecular complexes. In this model the low energy states of dipolar and multipolar chromophores are dominated by charge-transfer resonances. The relevant resonance structures are then chosen as basis states in the description of the system, so that the ground and excited states are expressed as linear combination of the charge resonating states. The weight of the resonating structures in the different states is not fixed from the outset and for each molecule it readjust in response to the local environment.

Charge resonance in PEP+ can be described as the resonance between two structures: DA^+ and D^+A. PEP+ spectra are described in terms of an essential state model based on these two resonating states. The electronic two states Hamiltonian is defined by 2z, measuring the energy separation between the two basis states, DA^+ and D^+A, and by the matrix element that describes the mixing between the two states, $-\tau$. τ measures the probability of electron transfer from D to A and backward. The parameters z and τ are estimated from the OPA spectra in solvents with different dielectric constants, and are fixed to z = 1 eV and τ = 1 eV. Spectra are

calculated assigning a Lorentzian line shape to the transitions with a line-width Γ that implicitly accounts for the vibronic structures: the value of Γ is fixed from experimental data at 0.46 eV. Just these three parameters are required to reproduce the spectral position and the shape of the OPA as well as the TPA spectra for PEP+, and this model rationalize the origin and the effects of interchromophoric interactions on spectral properties.

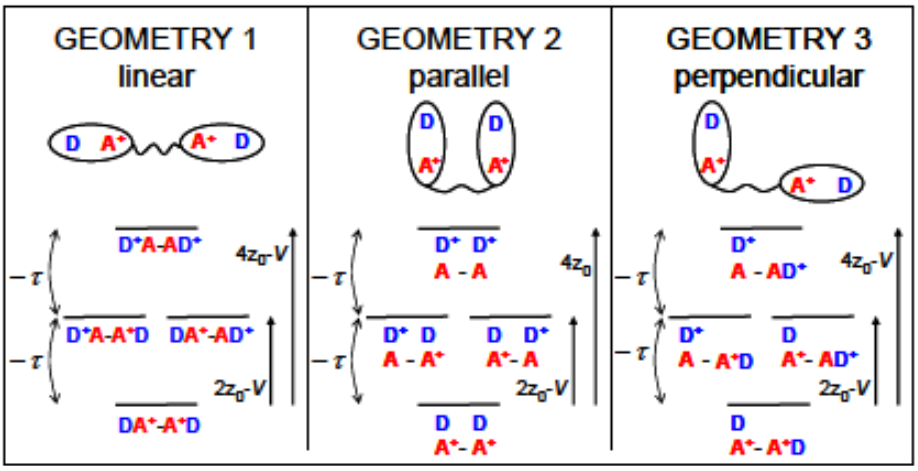

Figure 4.6: Representation for the three geometries considered for PEP+ dimers and the corresponding schemes of energy levels.

This simple model for PEP+ is easily extended to describes the two dimers: Bis PEP+ (AA) Cn. In view of the large interchromophore distances in all dimers, charge transfer between the chromophores is neglected and only electrostatic interchromophore interactions are taken in account. The parameters z, τ and Γ derived for the monomer can be directly transferred to the dimers. Only nearest neighbour electrostatic interactions between point charges, measured by the parameter V, are taken into account. The results are presented for variable V: non-interacting chromophores correspond to V=0, and V increases with decreasing distance of the two PEP+ units in the dimer. For a distance of 5 Å, V is estimated to be 0.07 eV.

In Figure 4.7 colour maps show the evolution of OPA and TPA spectra with V for three different geometries. For all three geometries the red shift observed experimentally in the OPA spectrum is reproduced. The shift of 10 nm observed for Bis PEP+ AA C3 is reproduced for V=0.1 eV, well in line with the expected value. The intensity of OPA is almost unaffected by electrostatic interactions for such small V values. A red-shift of TPA spectra is similarly expected, but hard to be confirmed in view of the large experimental errors. The results can also explain the observed small suppression of the TPA upon dimerization: in the linear and perpendicular geometries (geometries 1 and 3 in Figure 4.6) the calculated TPA is essentially

unaffected by dimerization in the relevant V range, while in the parallel geometry it sharply decreases.

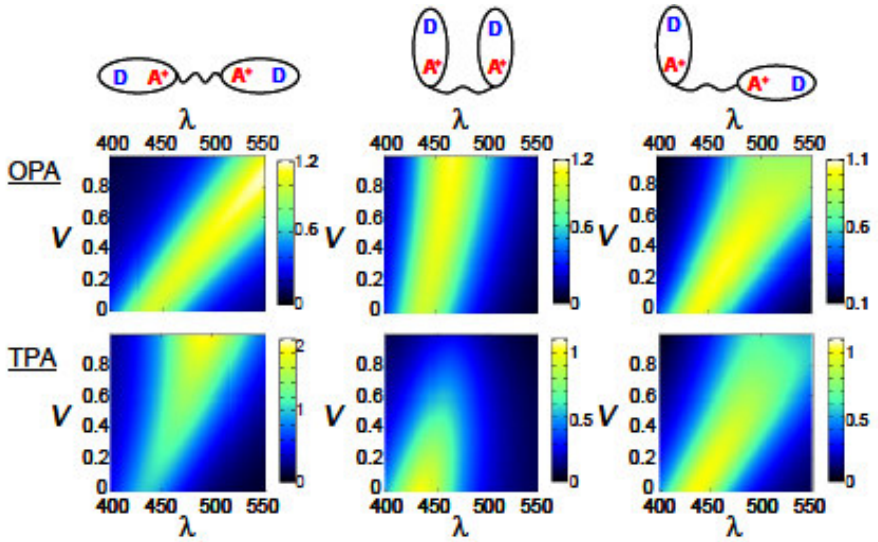

Figure 4.7: Evolution of OPA and TPA spectra (top and bottom panels, respectively) with the strength of intermolecular electrostatic interaction V calculated for three dimers of PEP+ in three different geometries. Molecular parameters for PEP+ are fixed ad z=1 eV, τ = 1 eV and Γ=0.46 eV.

Concluding, this simple effective electronic model that takes in account the electrostatic interactions between charges is able to reproduce the experimental shifts of OPA and TPA observed for the dimers of PEP+ when compared to the monomer. The effects on intensity are small, but both theoretical and experimental data are in agreement.

4.3 Dimers of quadrupolar chromophores

The second class of dimers is built using a quadrupolar chromophores PEPEP++ ((20,21 2,5-Bis[1-(4-*N*-methylpyridinium)ethen-2-yl)]-*N*-methylpyrrole ditriflate)) as monomeric unit. The chemical formula of PEPEP++ is reported in Figure 4.8. In this molecule two acceptor units (pyridinium rings) are bound to the central donor unit (methyl-pyrrole ring).

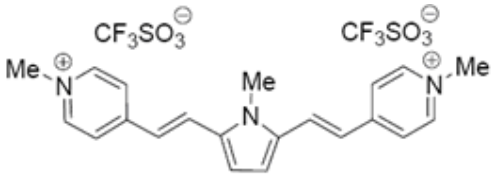

Figure 4.8: Molecular structure of PEPEP++

To obtain the dimeric structure investigated two monomers are linked from one of the periferic acceptor units using linear alkyl chains of different length: Bis PEPEP++ (AA) C3 uses a linear chain with three carbon atoms, and Bis PEPEP++ (AA) C6 have a linear chain with six carbon atoms as linker (Figure 4.9).

PEPEP++ bears two positive charges, and electrostatic interactions are expected to play a major role even in the ground state. Moreover, the two molecular arms of each PEPEP++ unit become nonequivalent in the dimer, and such symmetry lowering may induce relevant spectroscopic consequences.

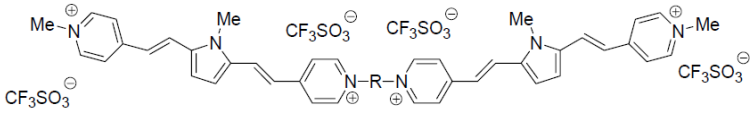

Figure 4.9: Molecular structures of Bis PEPEP++ (AA) C3 (if R = n-C_3H_6) and Bis PEPEP++ (AA) C6 (if R = n-C_6H_{12}).

Analogously to the dipolar chromophores presented before, also this group of molecules is investigated in DMSO solution. The absorption spectrum of these molecules (Figure 4.10) shows an ICT band at 515 nm. In addition, they all show fluorescence emission: PEPEP++ and the Bis PEPEP++ (AA) C6 show a sizeable fluorescence of 35%, in contrast with Bis PEPEP++ (AA) C3, where the FQY is reduced to 5%. Table 4.2 collects the main one- and two-photon absorption and emission properties of quadrupolar monomers and bichromophores.

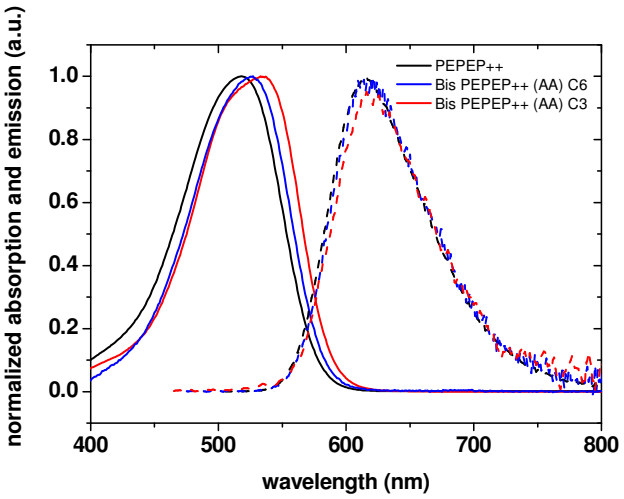

Figure 4.10: Normalized absorption and emission spectra of PEPEP++ and its dimers in DMSO solution.

A red shift in the absorption spectra of the dimers can be seen also in this class of molecules, and the shift is larger for the dimer with the shorter carbon chain in the linker. The magnitude of the shift is 10 nm, comparable with the one observed in the dipolar case. Instead, no significant shift is seen in emission spectra.

TPIF technique was used for the measurement of the TPA spectra of PEPEP++ and its dimers, with the same conditions used for the dipolar chromphores.

Figure 4.11 shows the TPA spectra (line + symbols) in DMSO of PEPEP++ and its dimers together with the linear absorption spectra (full lines). The wavelength scale of TPA spectra is divided by two to allow a direct comparison with OPA and the values of TPA cross-section are expressed in Göppert-Mayer units.

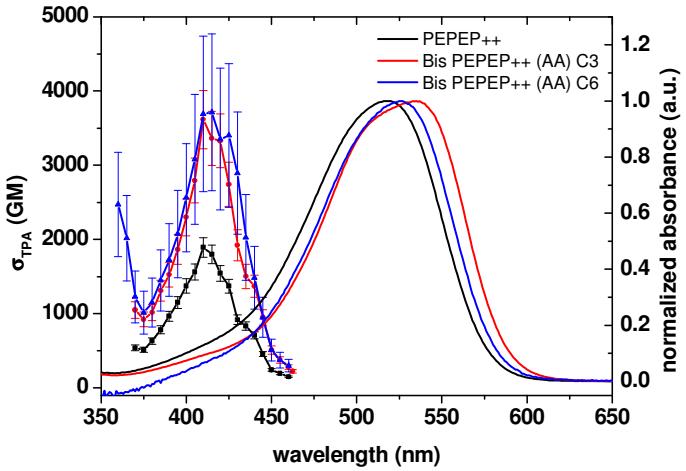

Figure 4.11: TPA (line + symbols) and OPA (full line) spectra of PEPEP++ and its dimers in DMSO solution.

The maximum values of the TPA cross sections are summarized in Table 4.2.

Table 4.2: OPA and emission maxima (λ_{OPA} and λ_{em}), absorption cross-section (ε), fluorescence quantum yield (FQY) and TPA maxima (σ_{TPA}) for the compounds studied.

compound	**λ_{OPA} (nm)**	**λ_{em} (nm)**	**ε (cm^{-1} M^{-1})**	**FQY (%)**	**σ_{TPA} (GM)**
PEPEP++	522	612	70300 ± 2500	36 ± 2	1892 ± 130
Bis PEPEP++ (AA) C3	532	615	123000 ± 4000	5.1 ± 0.8	3614 ± 373
Bis PEPEP++ (AA) C6	527	613	137000 ± 4000	35 ± 6	3714 ± 575

In PEPEP++ and in its dimers the position of the TPA maxima falls around 410 nm, in a different spectral region with respect to the OPA, as expected for quadrupolar chromophores.

The TPA state is located at higher energies than the OPA state. The TPA cross-sections for the C3 and C6 dimers are almost twice the one of the monomer, with a small drop in both dimers. Reasons for Bis PEPEP++ (AA) C3 FQY unexpected reduction will be investigated with the help of time resolved experiments to clarify the relaxation dynamic for this dimer excited states with respect to the monomer.

Also for this class of molecules, an essential state model for the optical spectra of the monomer and the dimers was developed in collaboration with the group of Anna Painelli[20].

PEPEP++ is a doubly charged quadrupolar chromophore where two acceptor groups are linked to a central donor. Its low energy physics can be understood accounting for the resonance between the three limiting structures: A^+DA^+ A^+D^+A AD^+A^+. These main resonating structures are represented in terms of three states that defines the minimal basis set to describe the electronic structure of PEPEP++. The symmetrical A^+DA^+ state φ_0 is the lowest-energy state. Two degenerate states φ_c and φ_s correspond to AD^+A^+ and A^+D^+A, respectively, and represent states where an electron is transferred from the central donor toward one of the two lateral acceptor groups. A matrix element, $-\sqrt{2}t$ mixes φ_0 with either φ_c or φ_s, to account for the finite probability of electron hopping along each molecular arm. The two degenerate states, φ_c and φ_s, are separated from φ_0 by an energy gap 2η. The electronic Hamiltonian is:

$$H_{el} = -\sqrt{2}t\left(\hat{\sigma}_c + \hat{\sigma}_s\right) + 2\eta\left(\hat{\rho}_c + \hat{\rho}_s\right) \tag{4.1}$$

Where

$$\hat{\rho}_c = \left|AD^+A^+\right\rangle\left\langle AD^+A^+\right| \tag{4.2a}$$

$$\hat{\rho}_s = \left|A^+D^+A\right\rangle\left\langle A^+D^+A\right| \tag{4.2b}$$

$$\hat{\sigma}_c = \left|A^+DA^+\right\rangle\left\langle AD^+A^+\right| + \left|AD^+A^+\right\rangle\left\langle A^+DA^+\right| \tag{4.2c}$$

$$\hat{\sigma}_s = \left|A^+DA^+\right\rangle\left\langle A^+D^+A\right| + \left|A^+D^+A\right\rangle\left\langle A^+DA^+\right| \tag{4.2d}$$

Thanks to its molecular symmetry, the charge distribution in PEPEP++ can be described in terms of a monopole and a dipole located in the molecular center. Because the monopole is invariant in all basis states it becomes irrelevant in the discussion of solvation. The dipole moment instead vanishes in the state $\varphi_{0,}$ while φ_c and φ_s have equal and opposite dipole moments of magnitude μ_0. This dipole moment refers to states where an electronic charge is

displaced along one of the molecular arms: μ_0 is therefore very large and it is possible to neglect all other matrix elements of the dipole moment operator on the chosen basis. Under this approximation the dipole moment operator is: $\hat{\mu} = \mu_0(\hat{\rho}_c - \hat{\rho}_s)$.

When an electron is transferred from the central donor toward one of the two acceptors, the relevant molecular arm relaxes: in the model this relaxation is described in terms of two effective molecular vibrations q_c and q_s with the same frequency ω_v and relaxation energy ε_v. Polar solvation enters in the model with a reaction field F_R which measures the electric field generated at the solute location by the reorientation of polar solvent molecules. The relevant relaxation energy ε_{or} increases with the solvent polarity. The electronic component of the reaction field, related to the deformation of the electronic charge distribution in solvent molecules surrounding the solute, correspond instead to a fast motion with respect to the relevant degrees of freedom of the solute. It enters the model with a renormalization of model parameters that acquire a dependence on the solvent refractive index.

The Hamiltonian describing the three electronic states coupled to the molecular coordinates and to the reaction field[21] derived in Ref. 21 was modified to introduce an additional slow degree of freedom to reproduce the large and solvent independent Stokes shift present in these molecules. The relevant mode corresponds to a molecular deformation. An effective conformational coordinate Q with frequency ω_q and relaxation energy ε_q was introduced.

The total Hamiltonian is:

$$H = H_{el} - \omega_v\sqrt{2\varepsilon_v}q_c\hat{\rho}_c - \omega_v\sqrt{2\varepsilon_v}q_s\hat{\rho}_s - \omega_Q\sqrt{2\varepsilon_Q}Q(\hat{\rho}_c + \hat{\rho}_s) - \mu_0 F_R(\hat{\rho}_c - \hat{\rho}_s) + \frac{1}{2}\left(\omega_v^2 q_c^2 + p_c^2\right)$$
$$+ \frac{1}{2}\left(\omega_v^2 q_s^2 + p_s^2\right) + \frac{1}{2}\omega_Q^2 Q^2 + \frac{\mu_0^2}{4\varepsilon_{or}}F_R^2 \qquad (4.3)$$

where H_{el} is the electronic Hamiltonian in Eq. 4.1, the second and third terms describe the linear coupling of electrons to molecular vibrations, and the fourth and fifth terms describe the coupling to the conformational coordinate and to the polar reaction field. The last four terms describe the harmonic oscillators associated with the four slow degrees of freedom in which p_c and p_s are the conjugated momenta to q_c and q_s, respectively, while the conformational coordinate Q and the solvation reaction field, F_R, are treated in the adiabatic approximation, and the relevant kinetic energy is disregarded. Moreover, linear electron-vibration coupling is taken into account, neglecting higher order, and quadratic terms.

Table 4.3: Essential state model parameters for PEPEP++

η	0.95 eV
$2^{1/2}t$	0.87 eV
ω_v	0.12 eV
ε_V	0.15 eV
ε_Q	0.25 eV
μ_0	22 D
Γ	0.1 eV
ε_{or}	0.25 eV

Table 4.3 lists the model parameters for PEPEP++, chosen to reproduce absorption, fluorescence, and TPA spectra in DMSO. Calculated TPA spectra are compared with experimental data in Figure 4.12.

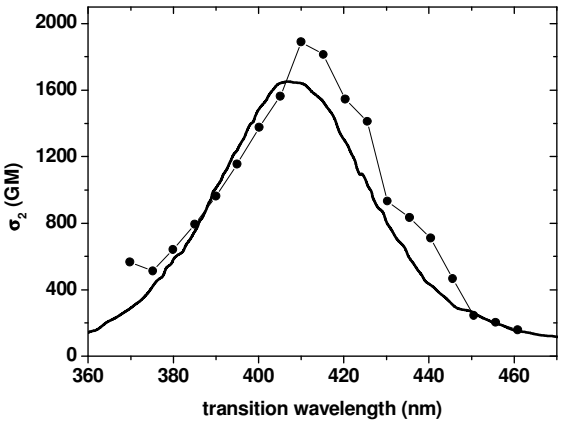

Figure 4.12: TPA spectrum of PEPEP++ in DMSO. Symbols show experimental data, the line represents the spectrum calculated using the model parameters in Table 3.

Once calculated the optical properties of the monomer, the model was applied also to the dimers. Understanding the behaviour of the PEPEP++ dimers requires a detailed modelling of electrostatic interchromophore interactions, also accounting for the screening from the surroundings solvent.

In Bis PEPEP++ (AA) C3 and Bis PEPEP++ (AA) C6, two PEPEP++ are joined by a flexible chain through one of the two terminal A sites to define an ADA-ADA dimeric unit. Accounting for three resonating structures for each chromophore, yields to nine basis states for the dimers. The two states AD^+A^+ and A^+D^+A of each one of the two chromophores,

equivalent for the isolated PEPEP++ specie, becomes non-equivalent in the dimer. For each unit in the dimer the two states AD^+A^+ and A^+D^+A are defined as φ_c or φ_s depending on the central (c) or side (s) position in each chromophore of the neutral A mojety.

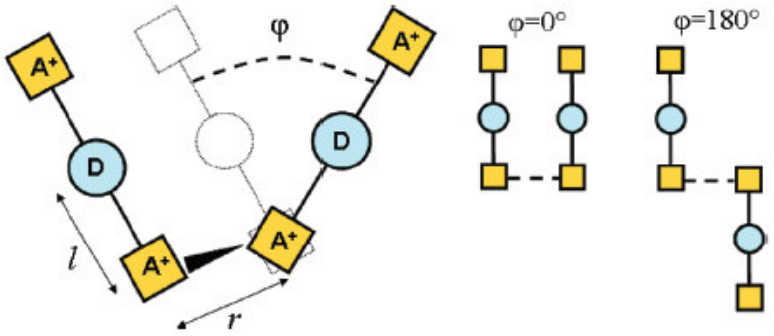

Figure 4.13: left panel: schematic view of the dimer geometry with the definition of geometrical parameters. Right panel: top view of two special cases φ = 0 and φ = 180˚.

Each chromphore is represented as a rigid rod of total length 2l (see Figure 4.13), where two positive point charges are located, depending on the state, either at the two A groups at the extreme sites of the rod and/or at the D group in the middle. The two chromophores are joined through the A sites by a linker of length r. Different geometries are defined by varying the angle φ from 0, accounting for two faced PEPEP++ units, up to 180˚, corresponding to two aligned monomer units pointing in opposite directions. In the model the two chromophores are forced to be in perpendicular planes with respect to the joining chain.

The relevant Hamiltonian is the sum of the two electronic Hamiltonian for each unit and of a term that describes electrostatic interchromophore interactions. Each chromophoric unit in the dimer is described in terms of the same model derived for the monomer.

Figure 4.14 collects information on transition energies calculated for the dimer as a function of the interchromophore distance for different angles φ. As expected, when the intermolecular distance becomes large, above 12 Å, the results for the monomer are obtained, irrespective of the mutual orientation of the chromophores. Sizeable and φ dependent excitonic effects are observed upon decreasing *r* below 10 Å.

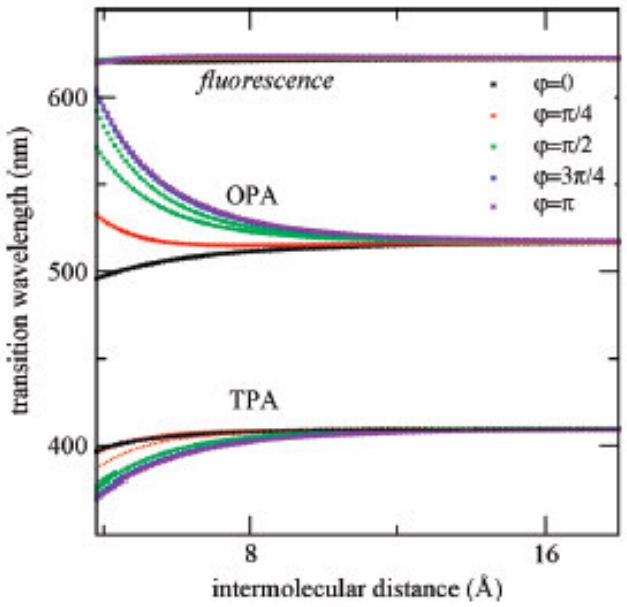

Figure 4.14: Transition (OPA, TPA and fluorescence) energies calculated in the excitonic model for PEPEP++ as a function of the intermolecular distance and for different torsion angle

With regard to OPA, the transition is red-shifted by interchromophore interactions for all angles apart from the special case of φ=0 where it is blue shifted. This special geometry is unlike to occur because of electrostatic repulsion (at least when interchromophore distances are small enough to give rise to sizable interaction). Data in Figure 4.14 nicely agree with the experimentally observed red shift of the linear absorption band upon decreasing the interchromophore distance. Results in Figure 4.14 suggest that for Bis PEPEP++ (AA) C6 with an approximate interchromophore distance of about 8 Å, OPA and TPA are marginally affected by interchromophore interactions. Instead in Bis PEPEP++ (AA) C3 $r \approx 6$ Å and a sizeable shift (≈ 10-20 nm) is predicted in OPA spectra , in good agreement with experimental data. The small red shift expected for the TPA band is hardly recognized in experimental spectra , mainly due to the intrinsic lower resolution of TPA data (spectral resolution of TPA data is dictated by the spectral width of the Gaussian shaped pulses produced by the laser).

In Figure 4.15 the evolution with interchromophoric distances of OPA and TPA spectra for a dimer with φ=135˚ is reported. These spectra are calculated assigning to each excitonic state, as obtained from the diagonalization of the excitonic model, a Gaussian line shape with FWHM of 2000 cm^{-1}.

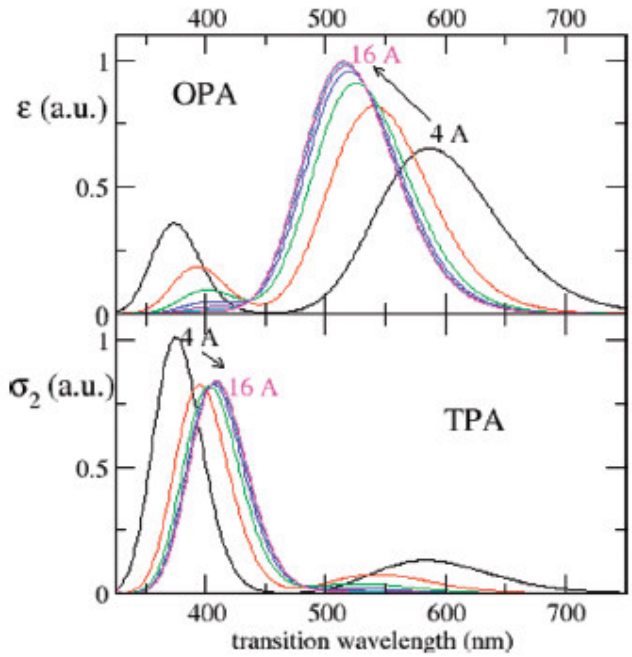

Figure 4.15: OPA and TPA spectra calculated for a dimeric unit with φ=135° and variable interchromophoric distance (from 4 to 16 Å with 2 Å steps).

The intensities of the OPA and TPA bands are only marginally affected up to the distances relevant for the species Bis PEPEP++ (AA) C3, with just a small decrease of the OPA intensity (Fig 4.15).

4.4 Conclusion

The OPA and TPA properties of different dimers of dipolar and quadrupolar charged molecules were investigated, and an essential state model was developed. The experimental results obtained for these class of molecules are well described from the model developed, both in the position and in the intensity of the different transitions.

These dimers show that simple alkyl chains are unsuitable to produce supramolecular structures with sizeable interactions between the charged dipolar chromophores forming them. An alternative way to connect the monomer units for a more efficient communication should be investigated as well as the possibility to use different non-charged dipolar or quadrupolar structures.

References

[1] D.M. Burland*, Chem. Rev.,* **1994**, 94, 1

[2] G.A. Lindsay, K.D. Singer, *Polymers for Second-Order Nonlinear Optics*, ACS Symposium Series 601, ACS, Washington, **1995**

[3] F. Terenziani, C. Katan, M. Blanchard-Desce, E. Badaeva, S. Tretiak, *Adv. Mater*., **2008**, 20, 4641

[4] H. Ma, A.K.Y. Jen, L. Dalton, *Adv. Mater***. 2002**, 14, 1339

[5] B. Kippelen, P.-A. Blanche, A. Schulzgen, C. Fuentes-Hernandez, G. Ramos-Ortiz, J.-F. Wang, N. Peyghambarian, S. R. Marder, A. Leclercq, D. Beljonne, J.-L. Bredas, *Ad*V. *Funct. Mater.* **2002**, 12, 615.

[6] W. Denk, J. H. Strickler W. W. Webb, *Science* **1990**, 248, 73

[7] R. Signorini, D. Pedron,, C. Ferrante, R. Bozio, G. Brusatin, P. Innocenzi, F. Della Negra, M. Maggini, A. Abbotto, L. Beverina, G. Pagani, *SPIE Proc*., **2003**, 4797, 1

[8] W. Zhou, S.M. Kuebler, K.L. Braun, T. Yu, J.K. Cammack, K.C. Ober, J.W. Perry, S.R. Marder, *Science*, **2002**, 296, 1106

[9] P.K. Frederiksen, M. Jorgensen, P.R. Ogilby, *J. Am. Chem. Soc.,* **2001**, 123, 1215

[10] A. Abbotto, L. Beverina, R. Bozio, S. Bradamante, C. Ferrante, G. Pagani, R. Signorini, *Adv. Mater*., 2000, 12, 1963

[11] F. Terenziani, G. D'Avino, A. Painelli, *ChemPhysChem,* **2007**, 8, 2433–2444.

[12] Barzoukas, M.; Runser, C.; Fort, A.; Blanchard-Desce, M. *Chemical Physics Letters,* **1996***, 257*, 531-537.

[13] Meyers, F.; Marder, S. R.; Pierce, B. M.; Bredas, J. L. *J. Am. Chem. Soc.* **1994***, 116*, 10703-10714

[14] Ventelon, L.; Moreaux, L.; Mertz, J.; Blanchard-Desce, M. *Synthetic Metals,* **2002***, 127*, 17-21.

[15] Hahn, S.; Kim, D.; Cho, M. *J. Phys. Chem. B* **1999***, 103*, 8221-8229.

[16] Fortunati, I.,Tesi di dottorato, Università degli Studi di Padova, Padova, **2008**.

[17] Abbotto, A.; Bellotto, L.; Bozio, R.; Ferrante, C.; Fortunati, I.; Garbin, E.; Marinzi, C.; Painelli, A.; Sissa, C.; Terenziani, F. *Proc. of SPIE,* **2008***, 6999*, 69990K-1.

[18] N. Klonis, W.H. Sawyer, J. Fluoresc. 6 (1996) 147.

[19] R.F. Kubin, A.N. Fletcher, *Chem. Phys. Lett*., **1983**, 99, 49.

[20] C. Sissa, F. Terenziani, A. Painelli, A. Abbotto, L. Bellotto, C. Marinzi, E. Garbin, C. Ferrante, R. Bozio, *J. Phys. Chem. B*, **2010**, 114, 882

[21] Terenziani, F.; Painelli, A.; Katan, C.; Charlot, M.; Blanchard-Desce, M. *J. Am. Chem. Soc.* **2006**, *128*, 15742

Chapter 5

Homo- and hetero-dimers of porphyrins: Introduction and linear characterization

5.1 Introduction

The interest towards the energy transfer processes in structure containing porphyrin moieties is due to the desire to investigate the natural photosynthetic processes through simple model systems and to emulate the high efficiency characteristic of biological light harvesting systems in order to exploit them in artificial devices[1].

Photosynthesis starts with the absorption of dilute sun light from the pigments in the antenna complexes. After excitation, energy moves between these pigments until a reaction center is reached, in which the charge separation occurs. The energy migration process is rapid and can involve hundreds of dyes[2]. Therefore the design and the characterization of synthetic analogues of antenna complexes can be used in the collection and use of solar energy. Numerous biological pigment–protein antenna complexes contain tetrapyrrolic chromophores, so, in artificial analogues, porphyrins are chosen for these structures.

The extraordinary versatility of porphyrins is an extremely valuable feature: indeed the ground state optical characteristics and excited state properties (energy, lifetime, emission yield) can be finely tuned changing the central metal or the substituents at the meso- or β-positions. The redox potential can also be varied up to 1 V using the same architectural features. In this way it is possible to modify all these properties to obtain the maximum efficiency of the molecular device under construction[3].

A number of multiporphyrins arrays have been investigated in the literature for the development of light-harvesting antennae, molecular photonic wires and optoelectronic gates. Most of the studies start from the construction of dimers and from their complete optical characterization before the development of the multichromophores. In fact the dimers are the basic constituent of all the arrays, and if the individual porphyrins are electronically weakly coupled, the key optical properties of dimers and larger arrays are the sum of those of the individual molecular components. The desired properties rationally designed into the individual chromophores or small assemblies are essentially retained when these units are

joined, thus providing a foundation for predicting and understanding the properties of increasing complexity. On the other hand, if the electronic coupling between the porphyrins were appreciable, each array would need to be considered as a super molecule rather than the sum of individual pieces.

A particular contribution in this field was given by the works of Lindsey, Holten and Bocian. One of their first studies was carried out on dimeric and trimeric porphyrin arrays where the linker is a diphenylacetylene moiety[2]. In the dimeric array with one zinc porphyrin and one free base porphyrin (Figure 5.1a) the energy transfer is highly efficient up to 95-99%. Moreover the rate constants range from 1×10^{10} s^{-1} to 4×10^{10} s^{-1}, values that are higher than those predicted by Förster mechanism, so a through bond mechanism is hypotized. Despite that, the electronic communication is weak because each porphyrin retains its intrinsic radiative and non radiative rates upon incorporation into the array. The fluorescence measurements on the trimeric linear array gives an energy transfer rate constant of 1.9×10^{10} s^{-1} in toluene at room temperature from the two zinc porphyrins to the free base one (Figure 5.1b), confirming that the inclusion of multiple isoenergetic pigments into linear or two dimensional arrays permits efficient overall energy transfer.

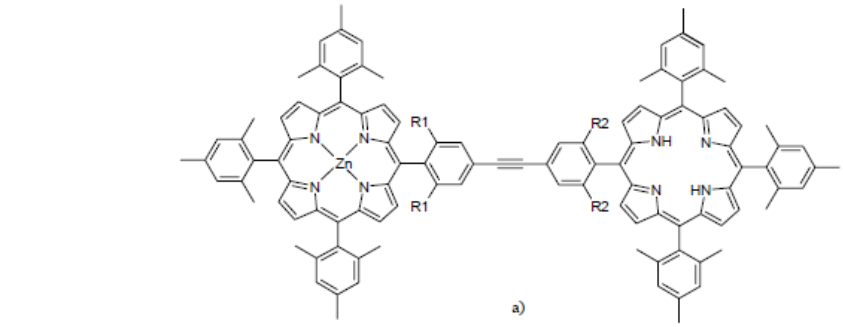

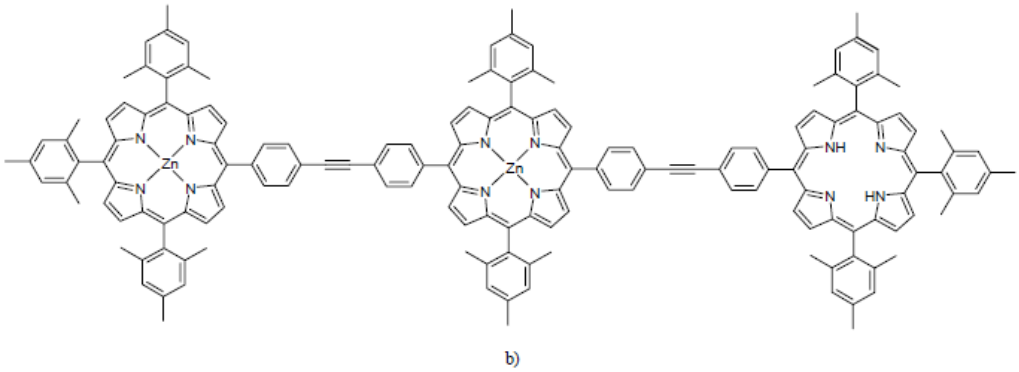

Figure 5.1: Linear dimeric and trimeric arrays with aryl-ethyne bridge investigated in Ref. 2

An important tool to modulate the energy transfer in the porphyrin array is to alter the symmetry of the H.O.M.O. varying the meso substituents: in general when the phenyl group brings electron-withdrawing substituents, such as fluorine, the H.O.M.O. of the porphyrin is the a_{1u}, which present electron density on the β-pirrole carbon atom and a node corresponding to the *meso* position of the tetrapyrrole ring. On the contrary when we have electron releasing groups like methyl group, the a_{2u} orbital becomes the H.O.M.O. of the porphyrin and this latter symmetry presents electron density on the *meso* carbon atom of the porphyrin ring. It is possible to modulate the energy transfer flow simply changing the substitution pattern at the periphery of the porphyrin as it is demonstrated in a review published by Holten, Bocian and Lindsey[3]. Since the dimer, trimer and tetramer synthesized by the authors show "through bond" energy transfer, attaching the linker to the electron-rich carbon atom means to increase the energy transfer rate, while in the opposite case the rate of the process will be slowed down.

Most of the porphyrins arrays proposed in the literature have been prepared based on linear arrangement. But for example the purple photosynthetic bacteria have two different light harvesting systems (LHCI and LHCII) with a pseudo circular arrangement of the chromophores[4]. So D. Kim and coworkers investigated the dimer, trimer and hexamer reported in Figure 5.2 by using time resolved fluorescence anisotropy[5]. Also in this case the units in the arrays are weakly coupled. The electronic interactions of the dimer and hexamer were described mainly by through space dipole-dipole interactions, although an additional interaction term arising from through bond interactions should be introduced for the trimer. This work is one of the rare case in which also the second excited state decay is investigated. The decay rates are accelerated in the order of trimer, dimer and hexamer. In the first excited state instead the energy transfer rate between the chromophores is 60 ps in the dimer and the hexamer, while is 90 ps in the trimer.

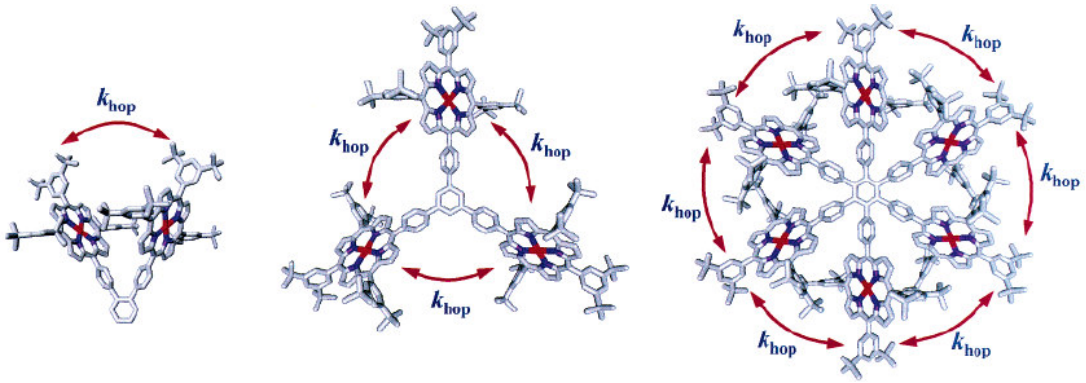

Figure 5.2: Structures of the dimer, trimer and hexamer studied in Ref 5.

Finally an example of a dendrimer is reported to show their potentiality as ordinated structures formed by a large number of pigments. Lindsey, Bocian and Holten, starting from the knowledge acquired in their previous works, present the synthesis of a dendrimeric unit made of 21 porphyrins, 20 zinc porphyrins that surround one free base porphyrin[6]. This dendrimer (Figure 5.3) shows a broadened and red shifted Soret band due to the inter porphyrin exciton coupling while the Q bands do not undergo any changes. These findings point out a relatively weak, but significant, electronic coupling between the chromophores. Fluorescence study has revealed an efficient energy transfer (92%) from the zinc porphyrins to the central free base porphyrin within 220 ps.

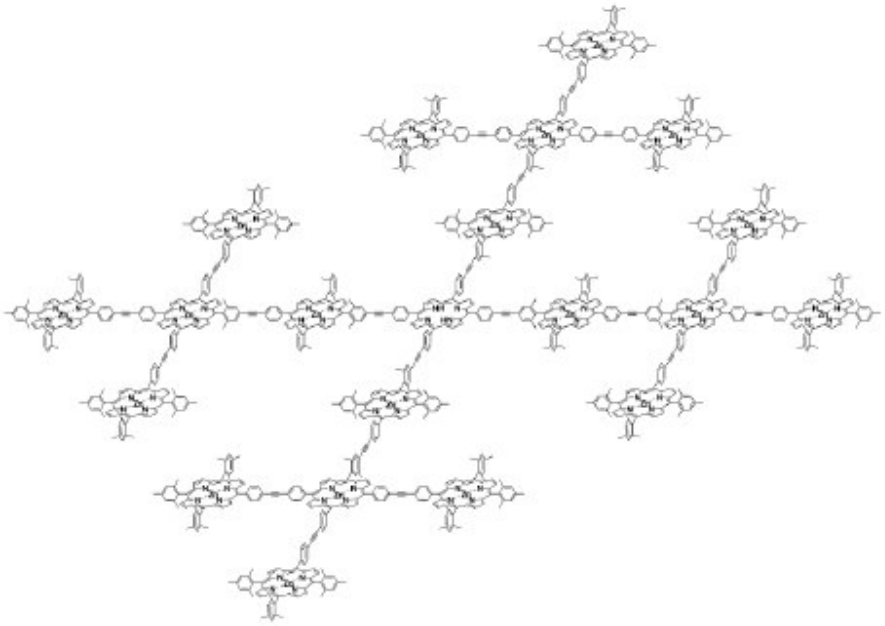

Figure 5.3: Porphyrin dendrimer developed by Lindsey, Holten and Bocian from Ref. 6

Our work was focused on the analysis of the energy transfer (ET) processes in covalently linked homo- and hetero-dimers made by the free base tetra-phenyl-porphyrin (TPP) and the Zn^{2+} tetra-phenyl-porphyrin (Zn-TPP) connected by a triazine moiety and synthesized by the group of Prof. Tommaso Carofiglio at our same Department in the University of Padova[7]. In Figure 5.4 the molecular structures of the investigated dimers are reported. In the following we will use these symbols for the different molecules: TPP and ZnTPP are the monomers, ZN and TN are the asymmetric monomers with an ammine group linked in para position to one of the phenyl groups in the monomers, ZT is the heterodimer made by a Z and T unit, ZZ and TT are the homodimers made respectively by two Z or two T units. Z and T are the monomers inside a dimer. All the measurements reported in the following are performed in THF solution.

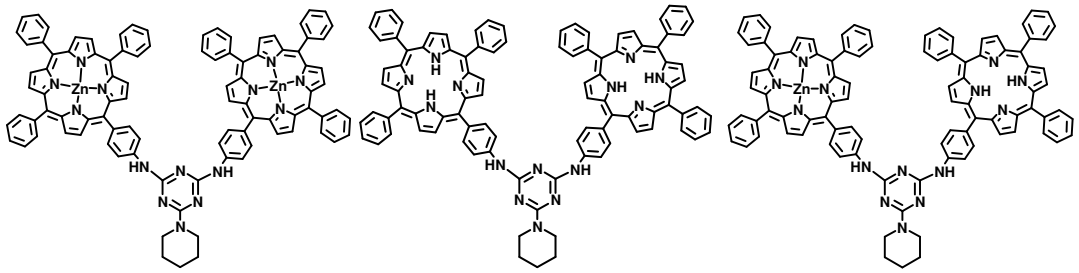

Figure 5.4: Molecular structure of ZZ dimer (left), TT dimer (center) and ZT dimer (right).

5.2 Linear characterization

The basic unit of porphyrins is the porphine, Figure 5.5. This 16-member ring with 18 π electrons is the heart responsible for the spectral features that characterize the absorption spectrum of all porphyrin derivatives. Following the Platt nomenclature, two main groups of absorption bands can be found in the porphine spectrum: B band, due to two strongly allowed electronic transitions: B_x and B_y, in the 380-430 nm region, and the Q bands, due to two quasi-allowed electronic transitions: Q_x and Q_y, in the region between 500 and 700 nm[8].

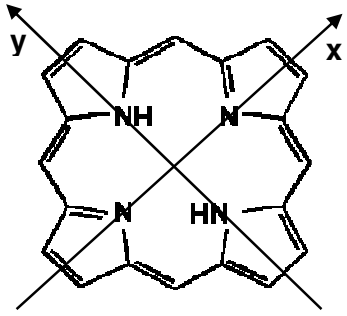

Figure 5.5: Molecular structure of porphine.

As the simplest model system for antenna structures, we started to investigate porphyrin dimers that can be the basic motif for larger dendritic structures. The two porphyrin units used to build these dimers can be used as model for the optical properties of the two main porphyrin classes: free base porphyrins and metal porphyrins.

In ZnTPP the center of the tetrapyrrolic ring is coordinated to a metal ion, in this case Zn^{2+}. In this molecule the porphine core has D_{4h} symmetry. The absorption spectrum in tetrahydrofurane (THF) is characterized by the presence of a single B band at 423 nm, that sums up two degenerate transitions: B_x and B_y , and of two Q bands, respectively the Q(0,0) at 595 nm due to the two-fold degenerate transitions Q_x and Q_y, and the Q(1,0) at 555.8 nm that includes one mode of vibrational excitation for each degenerate transition. In the emission spectrum only two bands are present: Q(0,0) at 602 nm and Q(0,1) at 656 nm, as expected from Kasha's rule, and the fluorescence quantum yield (FQY) in THF is 3.6 ± 0.9%.

TPP is an example of free base porphyrin, in which the central ring posses D_{2h} symmetry. The absorption spectrum shows a single B band at 416.2 nm (still the sum of two accidentally degenerate transitions: B_x and B_y) and four Q bands between 500 and 700 nm. Because of the two hydrogen atoms present in the central ring, the symmetry of the free base is lower than in metal porphyrins, and the Q bands degeneracy is removed. In the spectrum there are the $Q_x(0,0)$ band at 648 nm and the $Q_y(0,0)$ band at 546.8 nm, both with their corresponding $Q_x(1,0)$ and $Q_y(1,0)$ bands at 591.6 and 515.4 nm, respectively. In the emission spectrum there are two bands at 652 nm $Q_x(0,0)$ and at 718 nm $Q_x(0,1)$; the FQY in THF is 11.1 ± 3.7 %. The absorption maxima wavelengths are reported in Table 5.1, together with the FWHM of B band in wavenumbers. In Table 5.2 the wavelengths of emission maxima and FQY are summarized.

Table 5.1: Absorption properties of all the investigated compounds. In brackets the data in nm are reported

	B band absorption maximum cm^{-1} (nm)	B band FWHM cm^{-1}	Q bands absorption maxima cm^{-1} (nm)			
TPP	24027 (416.2)	690	19501 (513.2)	18281 (546.8)	16954 (591.6)	15437 (648)
TN	23912 (418.4)	1005	19395 (515.4)	18103 (552.6)	16869 (593.6)	15399 (650)
TT	23866 (419)	1011	19410 (515.4)	18149 (551.2)	16869 (593)	15413 (649.2)
ZnTPP	23641 (423)	504	-	17986 (555.8)	16812 (595)	-
ZN	23574 (424.2)	578	-	17973 (556.2)	16773 (596.4)	-
ZZ	23540 (424.8)	773	-	17960 (557.0)	16750 (597.0)	-
ZZC	23430 (426.8)	580	-	17712 (564.6)	16513 (606)	-
ZT	23540 (424.8)	913	19395 (515.4)	17992 (556.0)	16767 (596.4)	15408 (649.2)

FQY for the B band was measured using perylene in cyclohexane (FQY = 74 %[9]) as reference standard, whereas for the FQY of the Q bands Cresyl violet in methanol (FQY = 66 %[10]) was used.

Using the Strickler-Berg equation, it is possible to estimate the fluorescence lifetime (excited state lifetime) $\tau_F = \Phi \tau_R$, where Φ is the FQY and τ_R is the radiative lifetime. The latter can be calculated from linear absorption and emission data following the relation:

$$\frac{1}{\tau_R} = 2.88 * 10^{-9} n^2 \varepsilon^{\max} \left[\frac{\int F(\nu) d\nu \int \frac{\varepsilon(\nu)}{\nu} d\nu}{\int \frac{F(\nu)}{\nu^3} d\nu} \right] \tag{5.1}$$

Where $F(\nu)$ and $\varepsilon(\nu)$ are the normalized fluorescence and absorption spectral bands, $\varepsilon^{\max}$ is the extinction coefficient at the peak absorption, and *n* is the refractive index of the solvent.

Table 5.2: Emission properties of all the investigated compounds. In brackets the data in nm are reported

	B band emission maximum cm^{-1} (nm)	FQY B band %	Fluorescence lifetime (from SB)	Q bands emission maxima cm^{-1} (nm)			FQY Q bands %
TPP	-	-	-	15337 (652)	13920 (718)		11.1 ± 3.7
TN	-	-	-	15174.5 (659)	13831 (722)		10.3 ± 0.9
TT	-	-	-	15267 (655)	13870 (721)		9.6 ± 0.7
ZnTPP	23364 (427.5)	0.15 ± 0.06	1.27 ps	16584 (602)	15267 (656)		3.6 ± 0.9
ZN	23310 (429)	0.16 ± 0.06		16529 (605)	15244 (656)		3.5 ± 0.8
ZZ	23148 (433)	0.14 ± 0.07	0.987 ps	16477 (607)	15198 (658)		3.7 ± 0.3
ZZC	22936 (436)	0.115 ± 0.058	0.837 ps	16287 (617)	15015 (667)		3.3 ± 0.2
ZT	(433)	0.10 ± 0.06		16502 (607)	15267 (655)	13870 (721)	

In Figure 5.6 the absorption and emission spectra of TPP, TN and TT in THF are reported. In the B band region the TT spectrum is nearly identical to the one of TN, while TPP spectrum is peaked at lower wavelengths; the same behavior is followed also in the Q bands region and for emission spectra. Moreover also the FQY of the three compounds are nearly constant, indicating weak interactions between the two porphyrins in the ground electronic state.

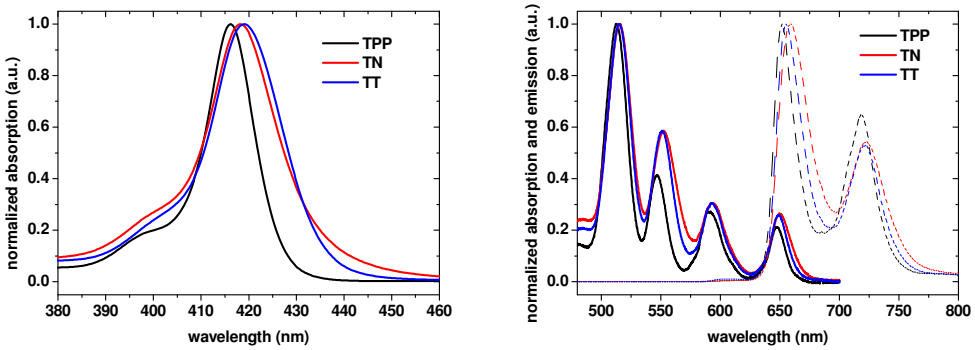

Figure 5.6: Absorption and emission spectra of TPP, TN and TT in THF.

Analogous considerations are valid for the absorption and emission spectra of ZnTPP, ZN and ZZ reported in Figure 5.7. However, it must be underlined that the B band of ZZ dimer is wider and more asymmetric with respect to the same band of both ZnTPP and ZN. This variation may suggest the presence of a non negligible although not very strong excitonic interaction between the B transitions of the two Z units in the dimer.

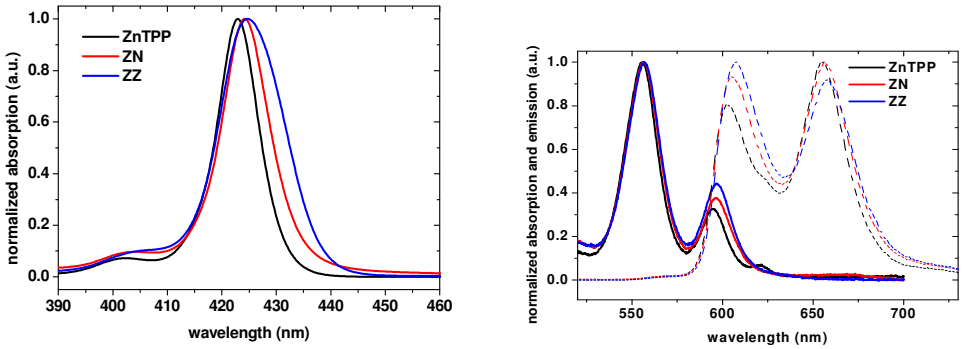

Figure 5.7: Absorption and emission spectra of ZnTPP, ZN and ZZ in THF.

The absorption spectrum of the ZT dimer shows the characteristic structure of the porphyrin spectra: B bands in the region 400-450 nm and Q bands in the region 480-680 nm.

This dimer is made from a T unit and a Z unit, but it is impossible to compare directly the absorption spectrum of the dimer and the sum of the spectra of the two monomers: TPP and ZnTPP, because all the bands of the dimer are slightly shifted towards longer wavelengths with respect to these monomers. A better result, in particular in the Q bands region, is obtained from the sum of the absorption spectra of TN and ZN, that are already red-shifted, with respect to the symmetric monomers. The red shift is likely a consequence of the electron donor substituent $-NH_2$. Since the Q bands are nearly unchanged in shape and in position, it

can be assumed that there is negligible electronic interaction between Z and T for these transitions. Comparison of the absorption spectra in the B-band region shows that ZT displays a broader band shifted towards longer wavelength with respect to the simple sum of the ZN and TN B bands. The Soret band broadening may indicate some amount of electronic communication between the B states of the two different porphyrins in the dimer.

This is the only dimer in which it is possible to have evidence of energy transfer from linear measurements. Since the energy of the first excited state of metal and free base porphyrins are 2.06 eV and 1.90 eV, respectively, energy transfer from Z unit to T unit can be revealed through fluorescence experiments.

The ZT dimer presents both S_2 and S_1 fluorescence, at 433 nm and in the 600-750 nm range, respectively. The determination of S_2 FQY and emission maximum is difficult because of its weakness and of the small Stokes shift.

Focusing the attention on the S_1 emission, the bands at 720 nm can be clearly ascribed to the $Q_x(0,1)$ transition of the T unit, while the small signal around 610 nm arises from the Q(0,0) of the Z unit. The intermediate band at 660 nm sums contribution form the Q(0,1) and the $Q_x(0,0)$ of the Z and T unit, respectively. The S_1 emission spectrum of ZT clearly shows that the fluorescence arises essentially from the T unit, irrespective from excitation of the T unit at 515 nm or the Z unit at 550 nm. These experimental findings are suggestive of energy transfer from the Z to the T unit.

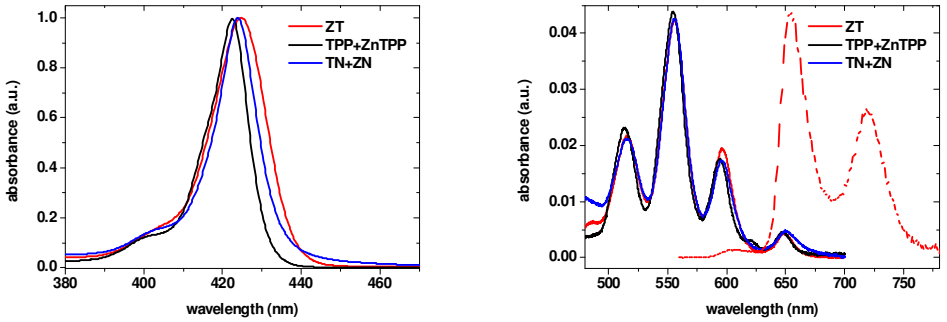

Figure 5.8: Absorption and emission spectra of ZT dimer. For comparison also the sum of the absorption spectra of the symmetric (TPP+ZnTPP) and of the asymmetric (TN+ZN) monomers are reported.

In Figure 5.9 the fluorescence spectrum of the ZT dimer is compared with the one of an equimolar mixture of the ZZ and TT dimers, both excited at 515 nm). This picture displays a marked attenuation of the fluorescence band at 610 nm, due to fluorescence of the Z unit only, from the ZT dimer to the equimolar mixture. To calculate the S_1 FQY of Z in the ZT dimer is not easy because the absorbance of Z at the excitation wavelength and the area of Z emission

are needed. But in ZT the absorption and emission spectra of T and Z are overlapped, so the absorbance is obtained reproducing the ZT absorption spectrum with ZZ and TT spectra and then reading the absorbance at the excitation wavelength in the ZZ spectrum, while the emission area is calculated reproducing the 610 nm emission band with the ZZ emission spectrum and then integrating the resulting curve. Using this method the FQY of Z in the dimer is 0.7 ± 0.2 %. In comparison with the S_1 ZnTPP monomer FQY of 3.5 ± 0.8 %, the Z unit in ZT dimer shows a 5 times lower FQY. The S_1 FQY of the T unit in the dimer is instead nearly unaltered with respect to the monomer. So, the predominant T emission even if Z is excited and the diminished FQY of Z are consistent with an energy transfer from Z to T in the S_1 state of the dimer.

Through comparison with the equimolar solution there is also the confirmation that the energy transfer happens only in moiety inside the same molecule and not between donor and acceptor on different dimers.

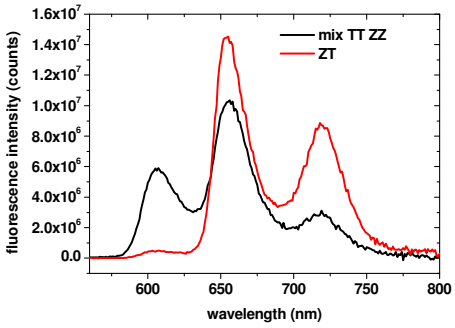

Figure 5.9: Fluorescence spectra of ZT dimer (red) and of a 50:50 mixture of ZZ and TT mixture (black) in THF solution excited at 515 nm.

The fluorescence excitation spectrum of the ZT dimer was collected in order to determine how much each cromophore contributes to the emission of the energy acceptor T in this dimer. The excitation spectrum was recorded in THF scanning the excitation from 380 to 700 nm with fixed emission at 720 nm, where only T emits. As shown in Figure 5.10, a nearly perfect coincidence at all the wavelengths in the Q bands region between the excitation and the absorption spectrum is found, sign of a high yield of energy transfer in this dimer.

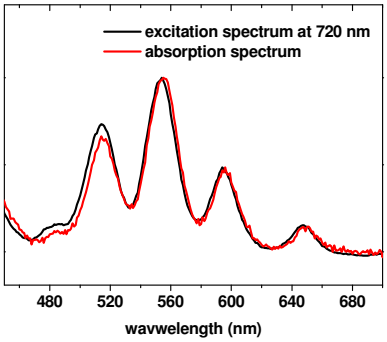

Figure 5.10: Absorption spectrum (red) and fluorescence excitation spectrum (black) collected at 720 nm of the ZT dimer in THF solution.

Using the formula obtained in Chapter 1 it is possible to obtain quantitative information on the energy transfer efficiency in this dimer, through the comparison of the FQY of the donor moiety alone Φ_D or in the dimer Φ_{DA}.

$$\Phi_{trans} = 1 - \frac{\Phi_{DA}}{\Phi_D} \tag{5.2}$$

In the ZT dimer the FQY of the donor Z is 0.7 ± 0.2 %, while in the donor alone ZnTPP is 3.5 ± 0.8%, so the energy transfer efficiency varies between 67% and 88%. The error affecting this estimate arises from the uncertainty in the evaluation of the donor fluorescence intensity in the dimer, being very low and partially superimposed to the higher acceptor fluorescence
Because of this, time resolved measurements were performed to get a more precise characterization of the efficiency and rate of the energy transfer in these dimers The results of these measurements are reported in the following Chapter.
As described in Chapter 1.3, the efficiency and the rate of energy transfer are strongly dependent not only from the electronic properties of the donor and the acceptor pair, but also from their distance in space. The linker used in these dimers is not rigid so they can have at least three limit conformations in solution, reported in Figure 5.11, and called respectively *syn-syn*, *syn-anti* and *anti-anti*. The structures reported are obtained by the group of T. Carofiglio using the CPK (Corey, Pauling and Koltun) model. The experimental data gained from experiments of optical spectroscopy do not allow determining if in solution a particular conformation dominates or if all the conformations are present.

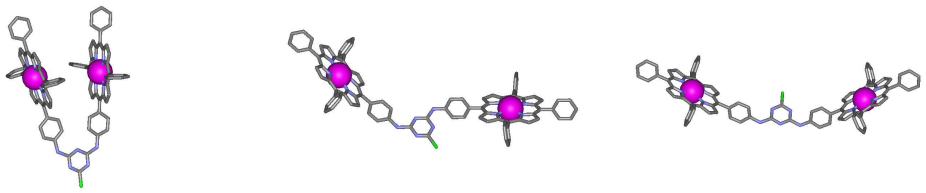

Figure 5.11: Syn-syn (left), syn-anti (center) and anti-anti (right) configuration of the ZZ dimer. These structures are obtained using CPK model.

Using the ability of the central Zn^{2+} ion in the center of the porphyrinic ring to coordinate ammine groups, the ZZ dimer has been titrated with linear diammine compounds of different length[11]. The diammine linked with the highest complexation constant is the cadaverine, a linear diammine with 5 carbon atoms, which has a global length of 7.51 Å. This length is comparable with the distance of 8.31 Å between the two zinc ions in the ZZ dimer in syn-syn configuration. This data can imply that the favorite configuration of the dimer in solution is the syn-syn, or that the conformational reorganization needs an amount of energy comparable with the ammine-metal ion interaction.

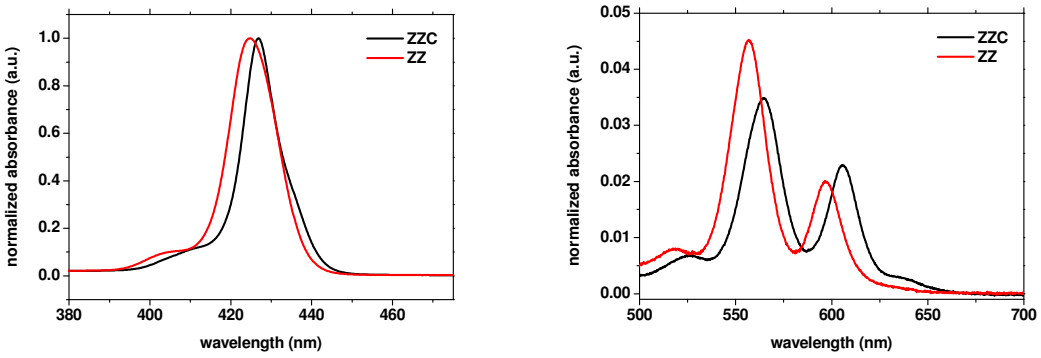

Figure 5.12: Absorption spectra of ZZC dimer. For comparison also the absorption spectra of ZZ dimer is reported

In Figure 5.12 the absorption spectrum of ZZC, the ZZ dimer complexed with cadaverine is reported. Moreover in Table 5.1 and 5.2 the absorption and emission maxima, together with the FQY of this dimer are reported.

This dimer is fixed in a position in which the two porphyrins are the nearest possible, so it is expected a higher transfer rate. Moreover the dynamic obtained will be due to a single conformation in solution and not to a mixture of different species, so it will allow a more detailed analysis of the energy transfer mechanisms in these structures.

References

[1] A. Morandeira, E. Vauthey, A. Schuwey, A. Gossauer, *J. Phys. Chem. A*, **2004**, 108 (27), 5741.

[2] J.S. Hsiao, B. P. Krueger, R. W. Wagner, T.E. Johnson, J.K. Delaney, D.C. Mauzerall, G. R. Fleming, J.S. Lindsey, D.F. Bocian, R.J. Donohoe, *J. Am. Chem. Soc*., **1996**, 118(45), 11181.

[3] D. Holten, D.F. Bocian, J.S. Lindsey, *Acc. Chem. Res*., **2002**, 35(1), 57

[4] V. Sundström; T. Pullerits; R. van Grondelle *J. Phys. Chem. B*, **1999**, *103*, 2327

[5] H. S. Cho, H. Rhee, J.K. Song, C.K. Min, M. Takase, N. Aratani, S. Cho, A. Osuka, T. Joo, D. Kim*, J. Am. Chem Soc.*, **2003**, 125, 5849

[6] J. S. Lindsey; D. Holten; D. F. Bocian; M. del Rosario Benites; T. E. Johnson; S. Weghorn; L. Yu; P. D. Rao; J. R. Diers; S. I. Yang; C. Kirmaier *J. Mater. Chem.*, **2002**, *12*, 65

[7] T. Carofiglio, A. Varotto, U. Tonellato*, J. Org. Chem*, **2004**, 69 (23), 8121

[8] M. Gouterman, in *The Porphyrins*, R. Dolphin, Academic Press, New York, **1978**

[9] I. B. Berlman, *"Handbook of Fluorescence Spectra of Aromatic Molecules*", Academic Press, London, **1965**

[10] S. J. Isak, E. M. Eyring, J. Phys. Chem., **1992**, 96, 1738

[11] A. Varotto, Tesi di laurea, Università degli studi di Padova, **2004**

Chapter 6

Homo- and hetero-dimers of porphyrins: Excited state dynamic

6.1 Introduction

In the previous Chapter, from the linear optical characterization of the hetero-dimer ZT the presence of an energy transfer process from Z to T unit in the first excited state was discovered. This process have a good efficiency, so it can be interesting in the design of an artificial antennae. From linear measurements only a rough estimation of the efficiency can be obtained, due to the very low emission of the donor in the dimer. A more precise value can be obtained from time resolved measurements; moreover from this measurements also the transfer rate can be determined, as shown in Chapter 1.5.3.

In particular time resolved spectroscopic techniques as time resolved fluorescence measured with time correlated single photon counting (TCSPC) have been used for processes in the ns regime and femtosecond transient absorption (TA) for processes in the fs and ps regime. Using these two techniques it is possible to monitor all the deactivation processes following excitation in the second excited state till all the population is back to the ground state.

The transfer time can be obtained from single wavelengths measurements of the excited stated dynamic, but a deeper view in the mechanism of this process can be obtained collecting the whole transient spectra. So TA spectra are collected with the pump-supercontinuum probe techniques, in order to follow the evolution of both the units in the dimer in the region of the B bands and of the Q bands.

All the measurements reported in this Chapter are recorded in THF solution.

6.2 Time resolved Fluorescence measured with time correlated single photon counting technique

In order to investigate the fluorescence lifetimes of the first excited state of all the compounds, the Time-Correlated Single Photon Counting (TCSPC) technique described in Chapter 2.5.1, was used, exciting in the Soret band of the porphyrins at 400 nm.

Exciting at 400 nm, the laser pulse create population in the second excited state, but due to the fast decay to the first excited state, it is possible to detect only the lifetime of S_1 state. Only processes longer than 200 ps can be followed with this technique.

Considering the symmetric monomers the lifetimes are 8.46 ns and 1.77 ns for TPP and ZnTPP respectively. The presence of the amino group in the nonsymmetric monomers TN and ZN causes a slight decrease in lifetime compared with TPP and ZnTPP, consistent with the observed slight decrease in fluorescence yield: the lifetimes measured are 7.95 ns and 1.72 ns for TN and ZN.

Fluorescence lifetime in the ZT dimer were measured using 2 different filter configuration: a 610 nm long pass filter to investigate all the Q bands fluorescence and a band pass filter in the region 580-620 nm to select only Z fluorescence and remove T fluorescence signal. When all the emission of the Q bands is collected, the decay was fitted with two time constants of 1.63 ns and 9.57 ns that are comparable with the lifetimes of the monomers. Instead, when only the Z emission is investigated, only the 1.63 ns decay is present in the measurements. No shorter components can be seen, so the transfer should be faster than the IRF of this experiment, that is 200 ps. Moreover, no quantitative data on the relative fluorescence intensity can be obtained from these measurements.

For the homodimers only a single exponential decay can be seen in the measured traces, with time constants of 7.85 ns and 1.69 ns for TT and ZZ, respectively. The measured lifetimes are in agreement with the ones obtained for the monomers, as expected for weakly interacting dimers.

All the fluorescence lifetimes measured with TCSPC are used as a long fixed decay component in the analysis of TA data, which explore the excited states dynamic up to 500 ps.

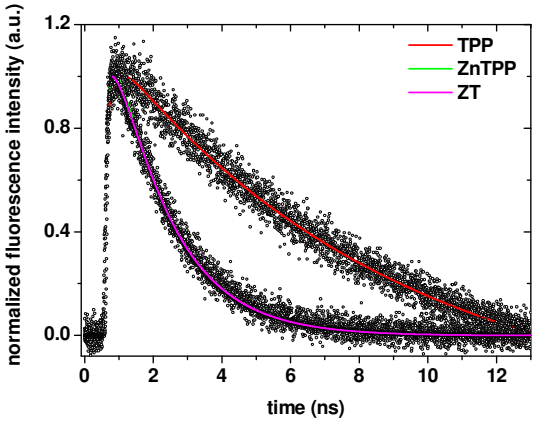

Figure 6.1: Fluorescence lifetimes of TPP, ZnTPP and ZT measured with TCSPC in THF. ZT decay is recorded only in the region of Z emission.

6.3 Transient Absorption (TA) experiments

TA experiments, exciting in the second excited state, are performed on all the compounds using 400 nm excitation with 6 fs, 200 fs and 1 ps steps, and parallel and perpendicular pump-probe polarization in the range from 290 nm to 690 nm. The measurements are performed with the experimental setup described in Chapter 2.5.4.

From these experimental traces it is possible to obtain the magic angle dynamic that it is independent from rotational motions and the anisotropy signal that reveals both the rotational dynamics and the energy transfer rates. Analysis of anisotropy is fundamental in revealing the energy transfer process in homodimers, where the donor and the acceptor molecule have equal photophysical characteristics.

The analysis of TA data is performed using a multivariate global fitting procedure to obtain the decay constants, that is described in Chapter 2.5.4.1.

First, TA measurements are performed on the monomers TPP and ZnTPP in order to confirm the literature data; then the three dimers ZT, ZZ and TT are investigated. Finally the ZZC dimer is investigated.

6.3.1 Transient absorption experiments on TPP

The TA spectrum of TPP excited at 400 nm exhibits the following characteristics. There are two broad regions of positive absorption, one at 310-380 nm and one at 430-700 nm. These region of positive absorption are overlapped by a region of negative absorption centred at 416 nm (in the Soret region, about a factor of 10 more intense) associated with ground state depletion. Features due to ground state depletion are also observed in the Q band region, at 512 nm, 548 nm, 592 nm and 652 nm. To this last feature at 652 nm also stimulated S_1 emission should contribute. As expected, the bleaching signals positions corresponds to the positions of the absorption bands in the linear spectra.

Three different decay components are required to fit the spectrum at all the wavelengths and in the full temporal regime plus a constant value related to the 8.46 ns lifetime of the lower excited state (Q-band).

In Figure 6.2 the spectra for the short time regime are reported: after the initial increase in the first 80 fs due to the convolution with the pulse, the signal slightly decreases in the B band region and increases in the Q bands region. This variation in the signal intensity is related to the first time constant that is equal to 108 fs.

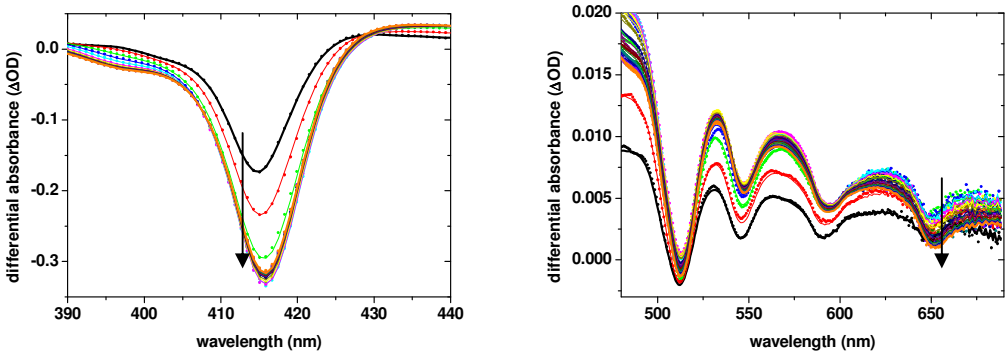

Figure 6.2: Temporal evolution of TA spectrum of TPP in THF from 0 fs (black) to 300 fs (orange) with 20 fs step. On the left in the B band region, on the right in the Q band region.

To better underline the different signs of this component, in Figure 6.3 the decay traces at some specific wavelengths are reported. At 410 nm and 420 nm the bleaching signal decreases in 108 fs and increases with the same time constant at 510 nm, 560 nm and 660 nm.

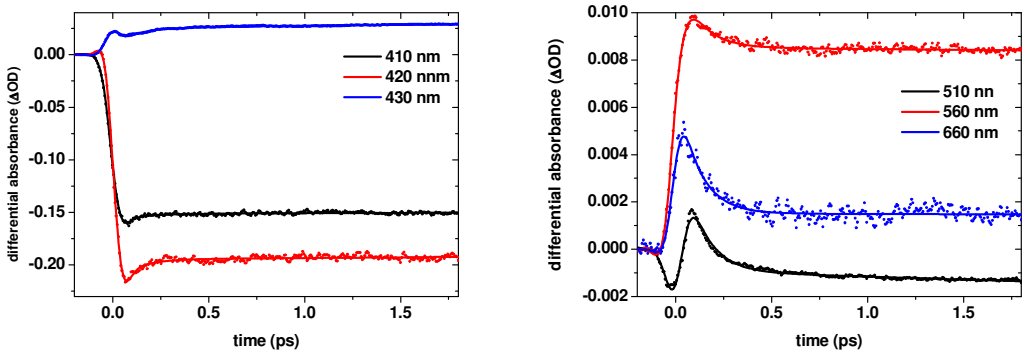

Figure 6.3: Decay traces of TA signal of TPP in the first 2 ps at 410 nm (black), 420 nm (red) and 430 nm (blue) in the left panel, at 510 nm (black), 560 nm (red) and 660 nm (blue) in the right panel.

In Figure 6.4 the evolution associated difference spectrum (EADS) for the fast component is reported: as expected it is negative in the position of the B bleaching and positive in the Q bands region. In black in Figure 6.4 is reported the EADS relative to the constant component used in the MVA (see Chapter 2.5.4.1 for details) in order to give a reference trace for the position of the B band and the Q bands in the spectrum. This consideration is valid for all the Figures that reports the EADS in this Chapter.

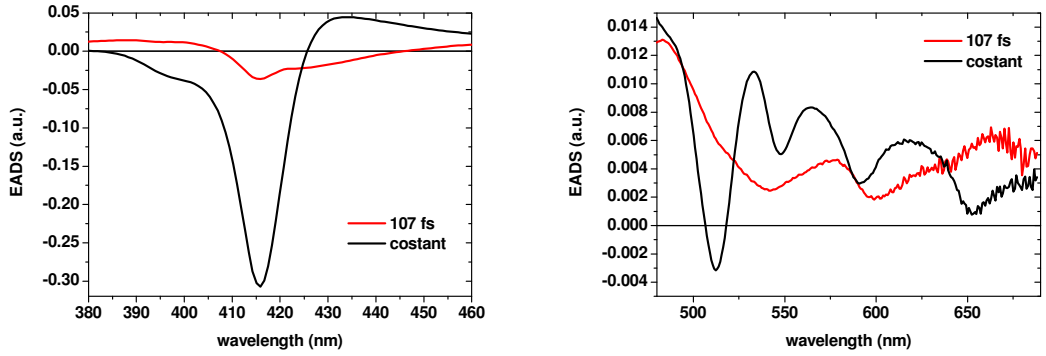

Figure 6.4: EADS relative to the 108 fs time constant in TPP decay. In black is reported the EADS relative to the infinite decay used in the fitting.

In Figure 6.5 the TA spectra from 5 ps to 40 ps each 5 ps are reported: the signal is nearly constant, only a small sharpening of the bands is present, better visible at 660 nm. This is related to the 18 ps time constant attributed to vibrational cooling. Then the signal evolves with the 8.46 ns lifetimes of this molecule, as measured by time-resolved fluorescence (TCSPC technique).

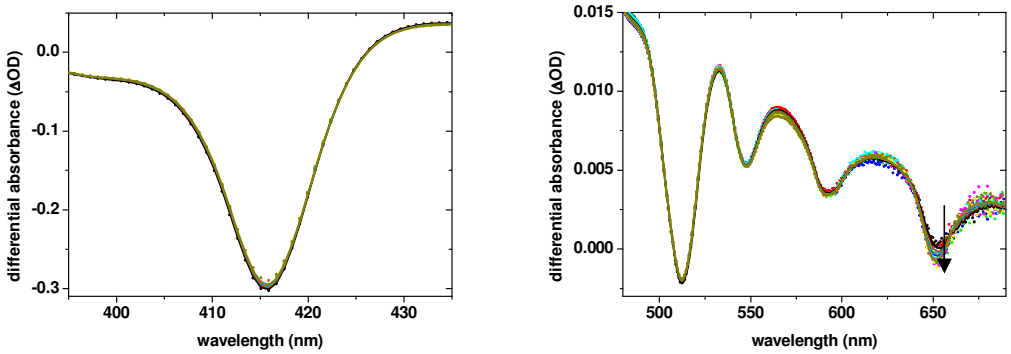

Figure 6.5: Temporal evolution of TA spectrum of TPP in THF from 5 ps (black) to 40 ps (dark green) with 5 ps step. On the left in the B band region, on the right in the Q band region.

The temporal decay of the long time measurements are reported in Figure 6.6: after the small decrease of the signal, better visible at 410 nm, 430 nm and 560 nm, the evolution is nearly constant in this time scale.

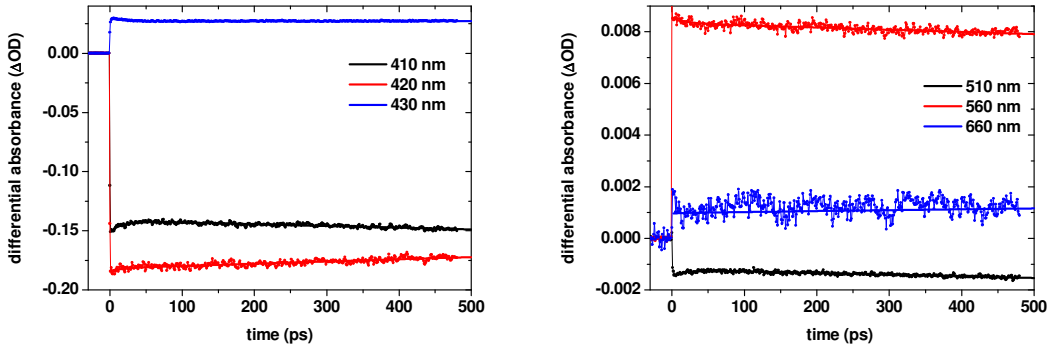

Figure 6.6. Decay traces of TA signal of TPP in THF till 500 ps at 410 nm (black), 420 nm (red) and 430 nm (blue) in the left panel, at 510 nm (black), 560 nm (red) and 660 nm (blue) in the right panel.

In Figure 6.7 the EADS relative to the 18 ps and the 8.46 ns time constants are reported: the first one in red is very small in all the spectrum, while the 8.46 ns in blue has a sigmoid shape in the B band region, is positive up to 650 nm and than becomes negative.

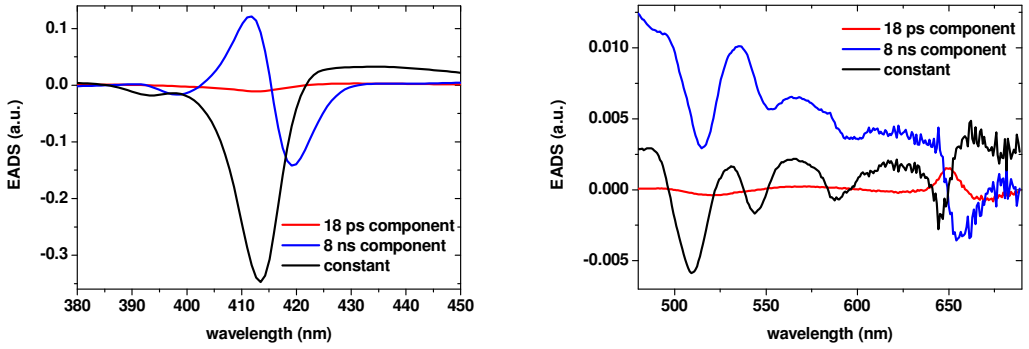

Figure 6.7: EADS relative to the 18 ps and 8.46 ns time constants in TPP decay. In black is reported the EADS relative to the infinite decay used in the fitting

6.3.2 Transient absorption experiments on ZnTPP

Transient absorption measurements are carried out on ZnTPP exciting at 400 nm in the second excited state S_2.

In the TA spectra of ZnTPP in THF there are two broad regions of positive absorption (ESA: Excited State Absorption), one at 320-390 nm and one at 440-700 nm. These region of positive absorption are overlapped by a region of negative absorption centred at 423 nm (in the Soret region, about a factor of 5 more intense) associated with ground state depletion. Features due to ground state depletion are also observed in the Q band region, at 556 nm and

599 nm. To this last feature at 599 nm should also contribute the S_1 stimulated emission (SE) that is also visible at 660 nm.

In Figure 6.8 the spectra from 10 fs to 1.8 ps are reported: the signal decreases in the B band region and in the ESA, while increases in the SE region at 660 nm. This signal evolution is related to the decay from S_2 to S_1 in 1.66 ps.

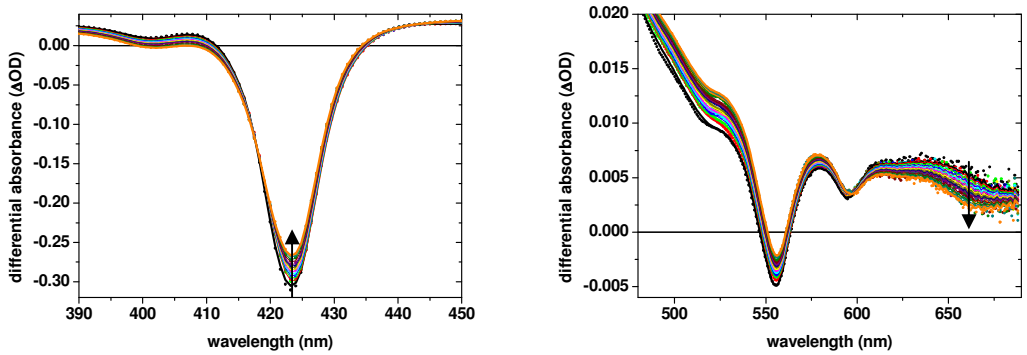

Figure 6.8: Temporal evolution of TA spectrum of ZnTPP in THF from 100 fs (black) to 1.8 ps (orange). On the left in the B band region, on the right in the Q band region.

As it is possible to see in Figure 6.9, the 1.66 ps time constant is the main component of the signal decay in this temporal window. A faster feature of less than 100 fs is visible at early times in all the curves: however with our time resolution it is difficult to define if it is a real decay time or it is part of the coherence signal of the pulse.

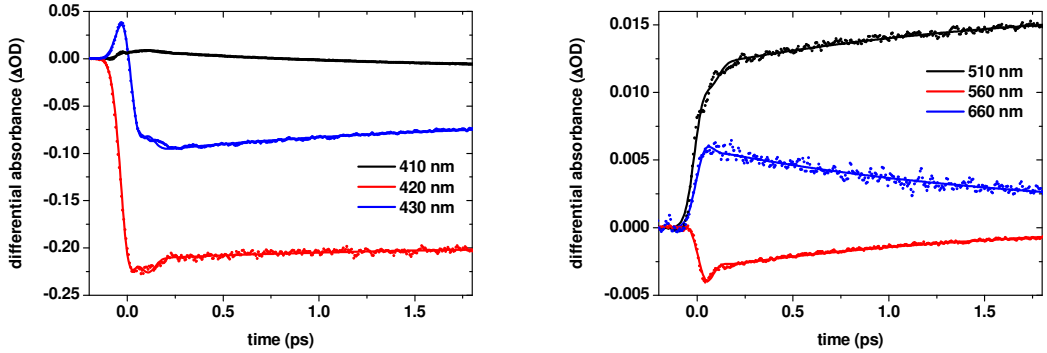

Figure 6.9: Decay traces of TA signal of ZnTPP in the first 2 ps at 410 nm (black), 420 nm (red) and 430 nm (blue) in the left panel, at 510 nm (black), 560 nm (red) and 660 nm (blue) in the right panel.

As expected the EADS relative to the 1.66 ps component is negative in the B band region, while it is positive from 600 nm to 700 nm in the Q bands region.

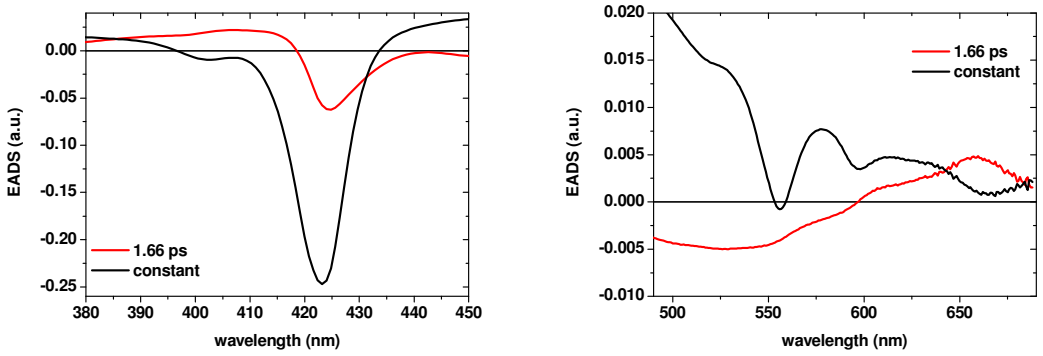

Figure 6.10: EADS relative to the 1.66 ps time constant in TPP decay. In black is reported the EADS relative to the infinite decay used in the fitting

For ZnTPP in the spectral region between 430 and 440 nm and in the short time regime it is possible to recognize the presence of oscillations with a frequency of ~ 220 cm^{-1} (Figure 6.11). No trace of oscillations can be seen in the TA decay of TPP or in other spectral regions of ZnTPP. These oscillation can be attributed to vibrational activate optical modes in this molecule.

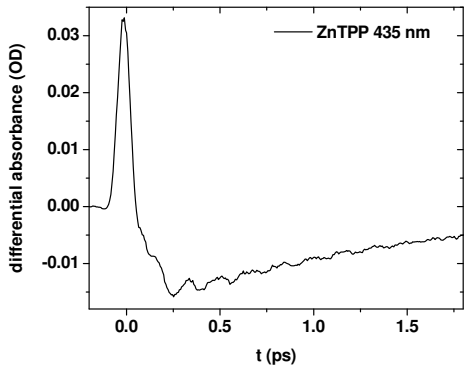

Figure 6.11: Short time measurements on ZnTPP in THF at 435 nm. In this decay trace oscillations with frequency of 220 cm^{-1} can be seen.

In Figure 6.12 TA spectra of ZnTPP in the long temporal range from 5 to 500 ps are reported: while in the B band the signal is nearly constant, in the Q band region the signal decreases.

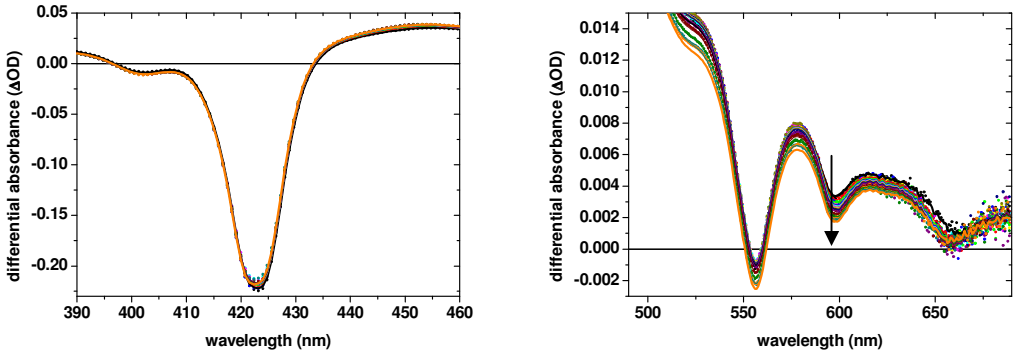

Figure 6.12: Temporal evolution of TA spectrum of ZnTPP in THF from 5 ps (black) to 500 ps (orange). On the left in the B band region, on the right in the Q band region.

Only two time constants are present in this temporal range: a smaller one of 13 ps that is attributed to vibrational cooling, while the longer one of 1.77 ns describes the recovery of the ground state from the first excited state. The 1.77 ns time constant is estimated from time-resolved fluorescence measurements, performed exciting at 400 nm,

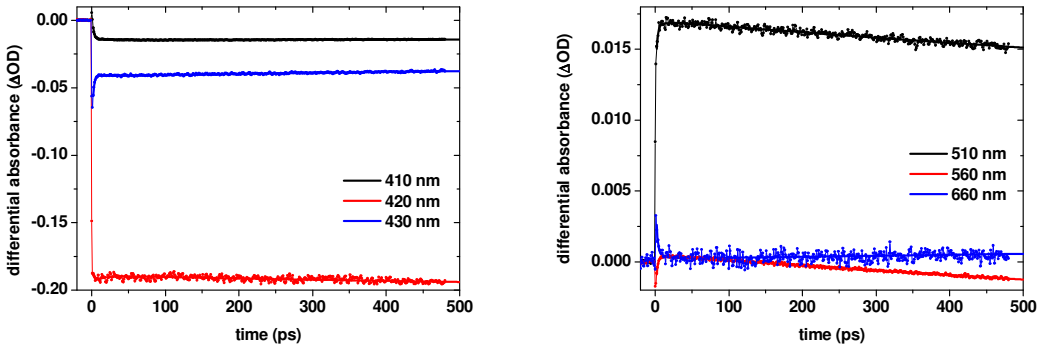

Figure 6.13: Decay traces of TA signal of ZnTPP in THF till 500 ps at 410 nm (black), 420 nm (red) and 430 nm (blue) in the left panel, at 510 nm (black), 560 nm (red) and 660 nm (blue) in the right panel.

In Figure 6.14 the EADS relative to the vibrational cooling constant reported in red is very small in all the spectra, while the EADS of the lifetime of the first exited state reported in blue has a sigmoid shape in the B band region, is positive till 640 nm and it is negative in the SE region from 640 nm to 700 nm.

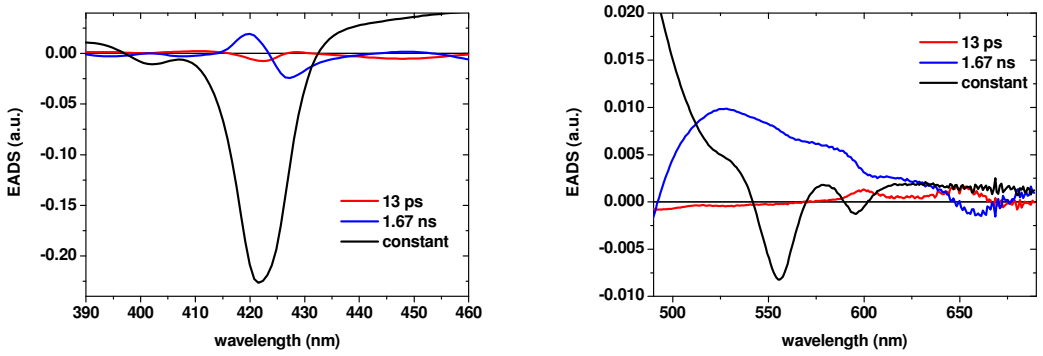

Figure 6.14: EADS relative to the 13 ps and 1.77 ns time constants in ZnTPP decay. In black is reported the EADS relative to the infinite decay used in the fitting

In Figure 6.15 is reported a scheme of the time evolution of TPP and ZnTPP when excited in the B band region: TPP displays a 108 fs time constant related to S_2-S_1 transition, then vibrational cooling in 18 ps, and decay to the ground state in 8.46 ns.

For ZnTPP the time constant describing the decay from the second excited state to the first one is approximately 1.66 ps, vibrational cooling displays a time constant of 13 ps, and the lifetime of the first excited state is kept fixed at the value obtained with TCSPC at 1.77 ns. The time constants we measured are in agreement with previous literature results[1,2] .

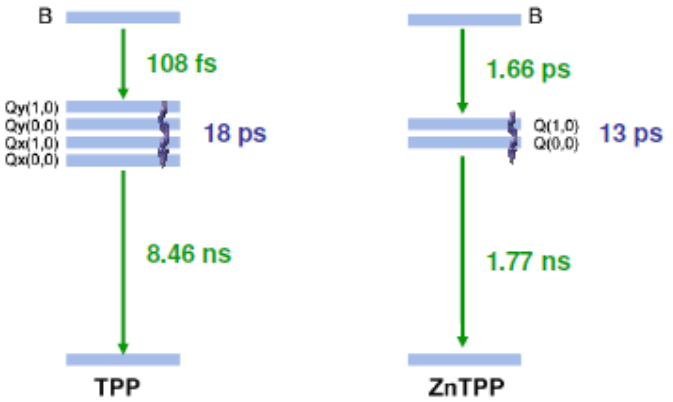

Figure 6.15: Scheme of the decay times measured in the monomers TPP and ZnTPP

6.3.3 Transient absorption experiments on ZT

Pumping ZT dimer at 400 nm both free base T and zinc moieties Z are excited, in their second excited state. The absorption cross section of TPP is almost two times the one of ZnTPP at this wavelength, so probably T is excited almost two times more than Z.

TA signal presents a deep negative peak in the region 400 - 440 nm relative to the ground state bleaching of the Soret band, a wide positive region between 320-400 and 440-690 nm due to excited state absorption (ESA), on top of which can be recognized 4 features relative to the bleaching and to the stimulated emission of the Q bands, as presented in Figure 6.16 and 6.17.

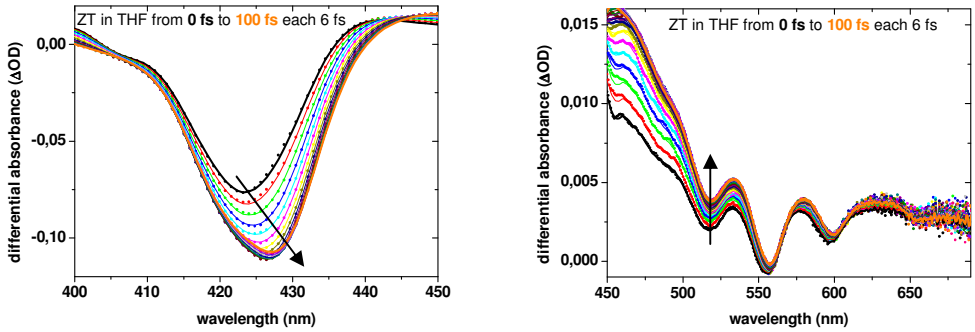

Figure 6.16: Temporal evolution of TA spectrum of the ZT dimer from 0 fs (black) to 100 fs (orange). On the left in the B band region, on the right in the Q band region.

In Figure 6.16 the experimental TA spectra (dots) and the relative fitted curves (full lines) of ZT exciting at 400 nm from 0 to 100 fs each 6 fs are reported: on the left the B band region is highlighted, on the right the Q band region. In the first 100 fs the B band bleaching increases and the position of the maximum shifts from 423.2 nm to 427.2 nm. In the Q band region the position of the peaks is constant while overall increase of the intensity of the transient spectra is mainly due to the increasing of ESA.

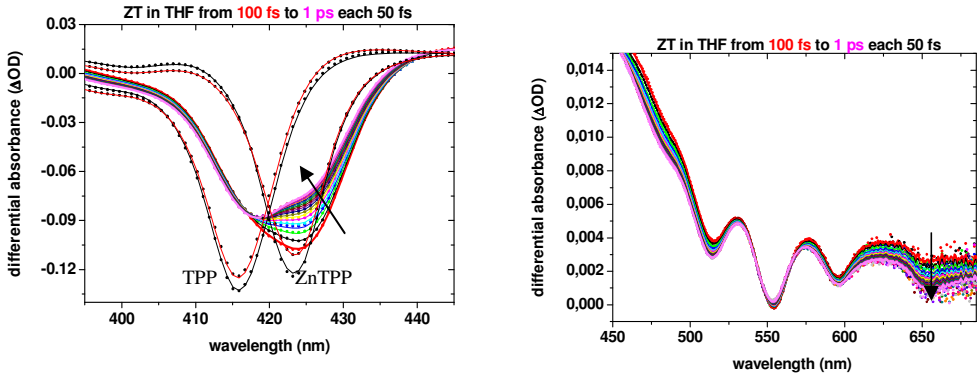

Figure 6.17: Temporal evolution of TA spectrum of the ZT dimer from 100 fs (red) to 1 ps (magenta). On the left in the B band region, on the right in the Q band region. For comparison also the B band spectra of the monomers in the same temporal interval are reported.

In Figure 6.17 the experimental TA spectra (dots) and the relative fitted curves (full lines) of ZT exciting at 400 nm from 100 fs to1 ps each 50 fs are reported: on the left the B band

region is highlighted, on the right the Q band region. In the first ps a shift towards shorter wavelengths of the B band can be recognized. The spectrum at 1 ps delay shows two different bands in the Soret signal. For comparison also TPP and ZnTPP transient spectra at 100 fs and 1 ps are reported: no shift in the peak can be seen in these two spectra.

Considering the evolution of the signal up to 2 ps, the whole transient signal at all wavelengths can be fitted with two time constants of 190 fs and 685 fs, as reported in Table 6.1.

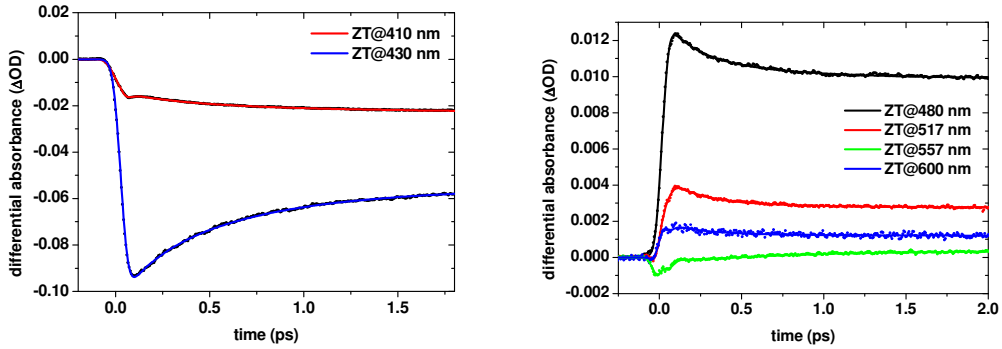

Figure 6.18: Decay traces of TA signal of ZT in the first 2 ps at 410 nm (red) and at 430 nm (blue) in the left panel, at 480 nm (black), 517 nm (red), 557 nm (green) and 6000 nm (blue) in the right panel.

In Figure 6.18 the kinetics at specific wavelengths in the B band are reported: it is clear that on a time scale of approximately 700 fs, there is an increase in the bleaching at 410 nm (red) and a decrease of the bleaching at 430 nm (blue). It is important to point out that the depopulation of the B-band of ZT occurs on a 700 fs timescale in the dimer whereas for ZnTPP and TPP on a 1.66 ps and 108 fs timescale, respectively.

Moreover in Figure 6.18 the evolution of the Q bands in the first 2 ps are reported. At 480 nm where the main component is ESA, both components of the decay are positive and describe a decrease of the transient signal. At 517 nm ESA and Q band bleaching of T are overlapped, but the behaviour is the same as that at 480 nm: both component are positive. At 557 nm instead the 190 fs component is positive, while the 685 fs component is negative: so after an initial decrease of the signal, then it increases again with 685 fs constant. At 600 nm the components are both positive again.

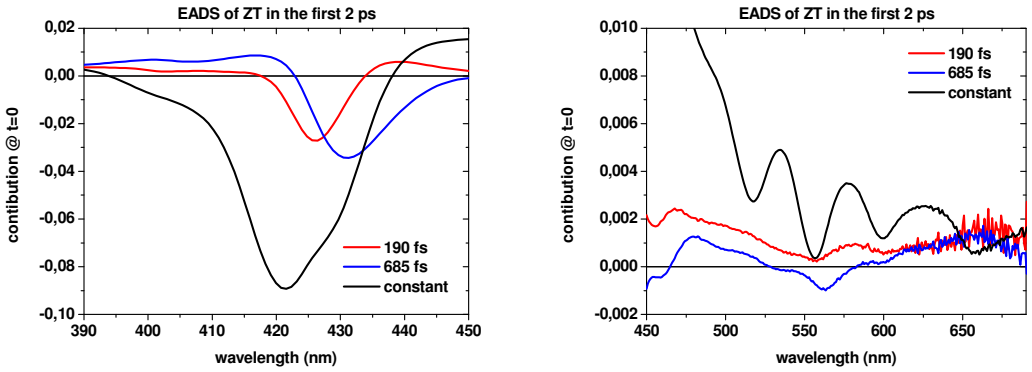

Figure 6.19: EADS relative of the first two time constants in ZT decay. In black is reported the EADS relative to the infinite decay used in the fitting.

In Figure 6.19 EADS obtained from the global fitting are reported: the two time constants have the maximum absolute value respectively at 426.4 nm and at 431.5 nm, so they are mainly centred on the Z part of B band. In the Q bands region, the 190 fs component is always positive, while the 685 fs component is negative in the range 525-575 nm and positive elsewhere.

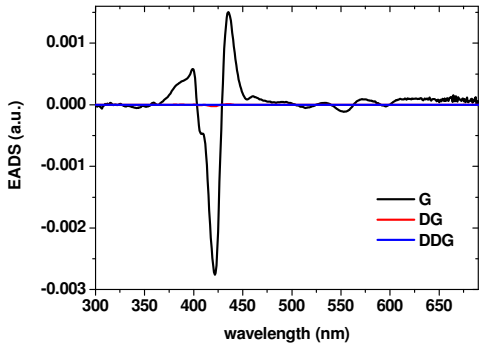

Figure 6.20: EADS associated with a Gaussian G, the first derivative of the Gaussian DG and the second derivative DDG

To better understand the detail of the fitting procedure the EADS associated to the coherence around time zero are reported in Figure 6.20: the main contribution cams from the Gaussian G while the first and the second derivatives give a nearly zero contribution. Moreover these components are much more lower than the population cotributions.

From the analysis of the decay in the first 2 ps, 2 time constants are found, but at least 4 states are involved. These time constants can be attributed to a set of molecular rate equations related to a four-state kinetic model involving the S_2 and S_1 states of Z and T. Using the

experimental constants and the model, the molecular rate constants can be found, after some initial assumptions to limit the number of independent variables.

The simplest model proposed is presented in Figure 6.21 and includes the possibility of transfer of populations between the B bands of the two units and the decay to the Q states. The two time constants that describe the decay to the Q bands are kept fixed at the value of the monomer for ZnTPP and to the minimum possible value for TPP. With this model the transfer from B_Z to B_T happens in 1.16 ps, while the back transfer from B_T to B_Z is very long, so it is nearly negligible.

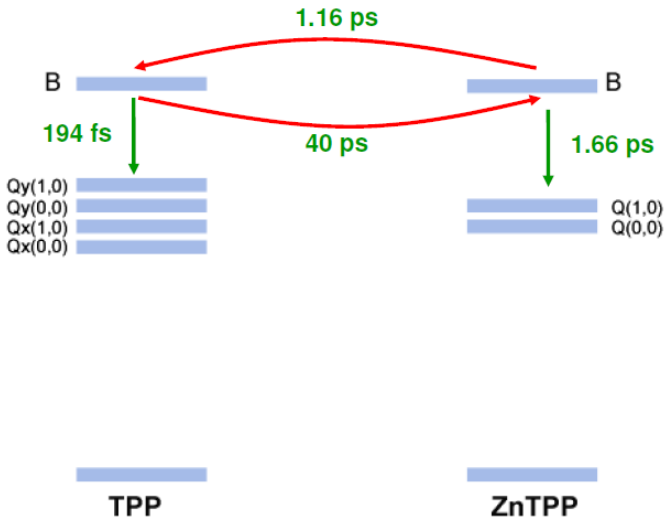

Figure 6.21: One of the tentative kinetic model used to describes the dynamic processes in the B bands of ZT dimer.

To verify the soundness of the model the SADS related to the four state involved (B_T, B_Z, Q_T, Q_Z) were calculated and are reported in Figure 6.22. In the left panel the fours SADS are reported: the black curve that describes the B band of T is centred at 424.8 nm and in the Q bands region has 4 bleaching signals but it has to be noticed that the first Q band has a lower intensity than expected. The red curve relative to B band of Z peaks at 430 nm and in the Q bands region shows a bleaching signal also around 520 nm that it is not expected for Z. The green curve represents the Q bands of T and it is centred at 421.6 nm. Also in this curve it was expected a stronger bleaching signal at 520 nm. The shape of the blue curve, that represents the Q bands of Z, is particularly strange: it has a sigmoid shape in the B band region, being negative at 420.8 nm and positives at 433.7 nm, and then it is slightly positive in all the Q bands region.

In the right panel the sum of SADS for BT and QT and for BZ and QZ are reported: the black curve relative to T has a peak at 423.2 nm, while the linear absorption maximum for the B

band of TT dimer is at 419 nm. Almost the same displacement is present in the Q bands. It has to be noticed that the first Q band at 519 nm is less intense than for a free base monomer. The red curve is instead related to Z and it has its maximum at 429.7 nm and presents a small bleaching contribution at 518.8 nm. Therefore these SADS are good but not perfect in describing the T and Z contribution, so some small modification in the model are needed.

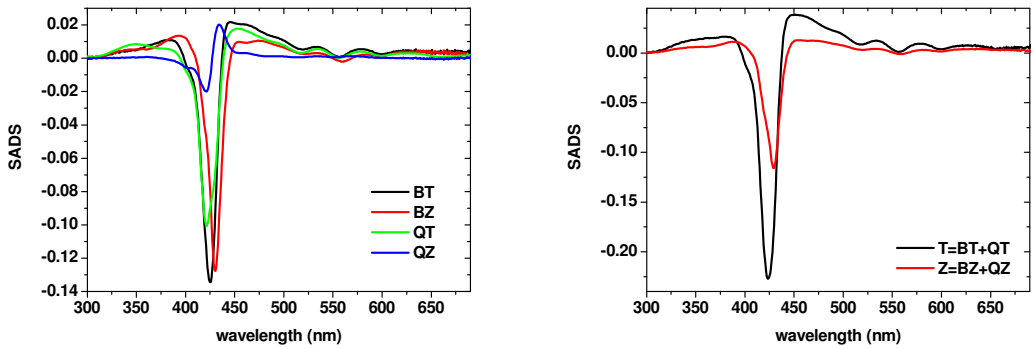

Figure 6.22: SADS relative to the 4 excited state involved in the decay from the second to the first excited state in ZT

There is another possible explanation for the presence of these two time constants. If the presence of the linker (amino group in alpha-position to the porphyrin ring) is able to remove the degeneracy between the B_x and B_y states in Z of these two states, then these states can fall at slightly different wavenumbers in the spectrum. These differences could not be distinguishable in the normal absorption spectrum, but they can be revealed through the TA spectra. The latter can discriminate between the different components in the spectrum, because of their different time evolution. In particular it can reveal the presence of energy transfer from the higher energy state to the lower one.

In order to verify if the behaviour of ZT decay in the B band region is due to the energy transfer from Z to T, or to the presence of an electron donor group linked to the porphyrin ring, 400 nm excitation TA measurements are performed also on the asymmetric monomer ZN in THF in Padova. The experimental setup used is described in Chapter 2.5.3. The signal was collected at 430 nm in the B band region: the decay constant is approximately 1.9 ps for Z, slightly smaller for ZN 1.6 ps and around 1 ps for ZZ. In all cases only a single exponential is visible at this wavelength, because of the limited time resolution of the Padova set-up. So it is not possible to exclude, at the moment, the double decay in ZN. Measurements with 400 nm excitation, the time resolution, and the full spectrum analysis as made in Berlin are needed to unravel this point.

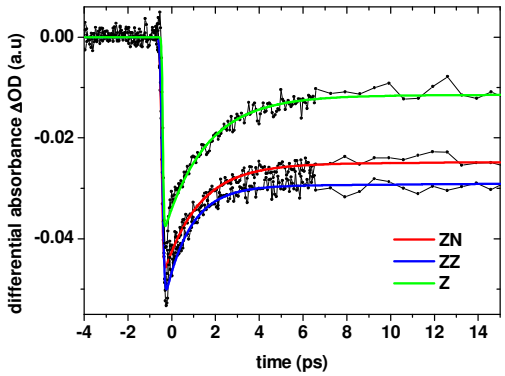

Figure 6.23: Decay traces of TA signal of Z (green), ZN (red) and ZZ (blue) in the first 15 ps at 430 nm

After the transfer of the population into the Q bands the TA signal of ZT evolves with 2 characteristic time constants, a shorter one of 25 ps and a longer one of 95 ps.

In the region 505-525 nm, where only T absorbs, both the components of 25 ps and 95 ps increase the bleaching, while in the region 550-565 nm, where both T and Z absorb, the bleaching decreases mainly with the 25 ps component. From measurements with different energy (see measurements on TT dimer), we attribute the 25 ps component to the decay of doubly excited dimers, and from the sign of this component in different spectral region we propose that the doubly excited dimer Z*T* decays to ZT* dimer. The 95 ps component can be instead attributed to the energy transfer from Z to T, because of the increase of the bleaching in the region in which only T absorbs, as reported in Figure 6.24.

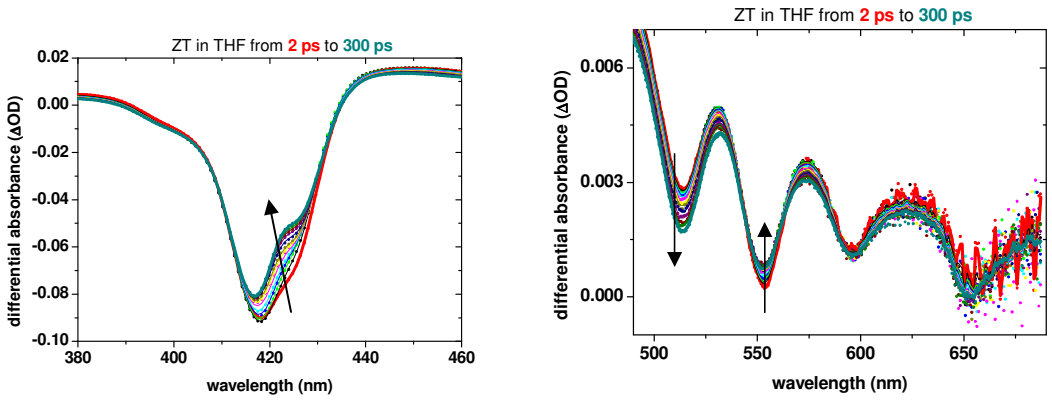

Figure 6.24: Temporal evolution of TA spectrum of ZT from 2 ps (red) to 300 ps (dark cyan). On the left in the B band region, on the right in the Q band region.

Moreover it can be noticed that in the monomers nearly no evolution is visible in the same temporal range.

In Figure 6.25 it is possible to see at 510 nm where mainly the T unit absorbs, that the relative bleaching increases, while decreases in the region of the TA spectrum in which mainly the Z unit absorbs.

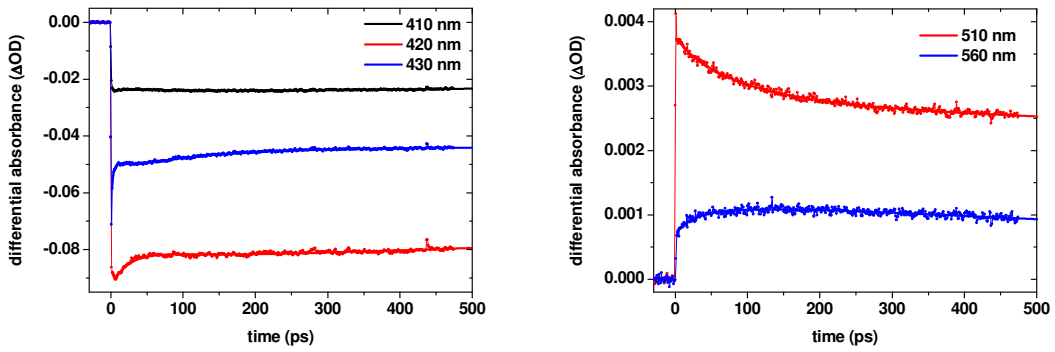

Figure 6.25: Decay traces of TA signal of ZT in THF till 500 ps at 410 nm (black), 420 nm (red) and 430 nm (blue) in the left panel, at 510 nm (red) and 560 nm (blue) in the right panel.

In Figure 6.26 it is particularly important to look at the green curve that represents the EADS relative to the 95 ps time constant: it is negative in the region where Z is absorbing, in the B band region from 420 nm to 440 nm and in the Q bands region from 550 nm to 570 nm and from 590 nm to 620 nm, while it is positive where T is absorbing, confirming our hypothesis that attributes this time constant to the transfer from Z to T.

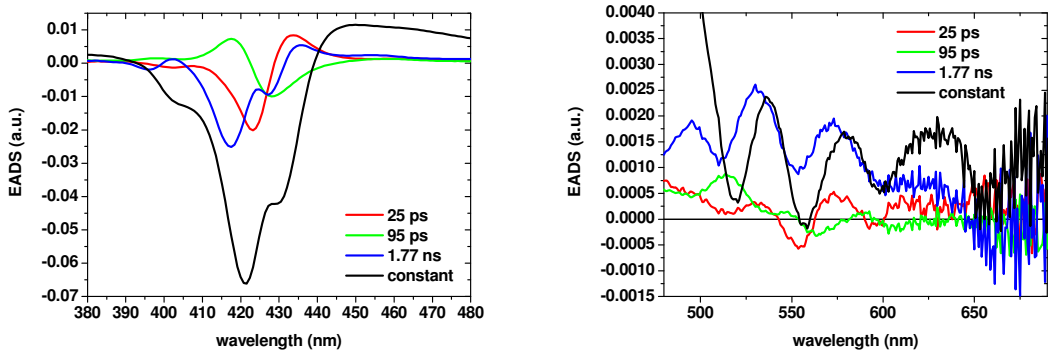

Figure: 6.26: EADS relative of the time constants found in the long time scale in ZT decay. In black is reported the EADS relative to the infinite decay used in the fitting.

In order to excite directly the porphyrins and their dimers in the first excited state, TA measurements were performed exciting at 560 nm. At this wavelength in the heterodimer ZT the Q(1,0) band of the donor Z is prevalently excited. We probe the signal of our samples at

490 nm and 500 nm, where mainly the acceptor T absorbs, and at 570 nm where the donor Z absorbs.

At 490 nm and 500 nm, where only the T absorbs, the bleaching signal increases with a time constant of 95 ps, due to the energy transfer from Z to T moieties in the dimer. No substantial decay can be seen in the monomers measurements at the same wavelengths, as can be seen in Figure 6.27.

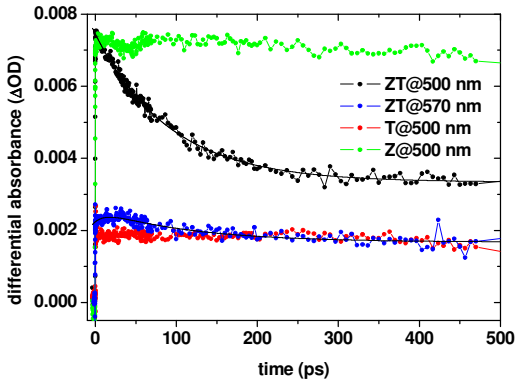

Figure 6.27: TA decay traces for ZT at 500 nm (black) and at 570 nm(green) after excitation in the Q bands region at 560 nm. For comparison also the monomer TPP and ZnTPP at 500 nm are reported.

Having identified that the 95 ps time constant is related to the energy transfer process, it is now possible to calculate the ET efficiency (Φ_{trans}) and the ET rate (k_{trans}). Using the equations defined in Chapter 1.5.3 and the measured values for τ_{DA} = 95 ps and τ_D = 1.77 ns

$$\Phi_{trans} = 1 - \frac{\tau_{DA}}{\tau_D} = 1 - 0.05 = 0.95 \qquad (6.1)$$

An efficiency of 95% is obtained.

The rate of ET is obtained with

$$k_{trans} = \frac{1}{\tau_{DA}} - \frac{1}{\tau_D} = 9.86 ns^{-1} \qquad (6.2)$$

So the effective transfer time is 101 ps.

The efficiency of the process is fairly good, but the rate is not as fast as the one observed for other dimeric structures in literature[3].

It is possible to estimate the theoretical rate of the transfer if we suppose that the mechanism that guides the ET is the one described by Förster that gives:

$$k_T = \left(\frac{9000(\ln 10)\kappa^2 Q_D J}{128\pi^5 n^4 N_{AV} \tau_D} \right) \frac{1}{R^6} \qquad (6.3)$$

In Eq. (6.3) the following parameters are used: the refractive index of THF at 589.3 nm and 298 K n = 1.405, the Avogadro's number N_{AV}, the lifetime of the first excited state of the donor alone τ_D = 1.8*10^{-9} s, the fluorescence quantum yield of the donor alone Q_D = 0.035, while κ is an orientation factor that takes into account the relative orientation of the dipole moment of the donor and the acceptor. As a first approximation the value for an isotropic distribution of the dipole moments is used, so in the following κ = 2/3. A proper model for the κ value in these molecules in which the mobility is constrained due to the linker will be developed.

The overlap integral J expresses the degree of spectral overlap between the donor fluorescence and the acceptor absorption and is defined in Chapter 1.3. For this dimer J = 3.666*10^{-14} M^{-1}cm^3.

R is the distance between the donor and the acceptor. For ZT the distances obtained with the CBK model by Carofiglio in three limit configurations are used. In the syn-syn configuration where the distance between the units is 8 Å the calculated rate is 3.67 ps, in syn –anti the distance is 19 Å and the rate 657 ps, while in anti-anti the distance is 21 Å and the rate 1204 ps[4].

As we expected these data confirm the presence of multiple configurations in solution and do not allow understanding if the transfer can be described only by Förster mechanism or if also the linker plays a role in the transfer.

6.3.4 Transient absorption experiments on ZZ

TA measurements exciting at 403 nm are performed on the ZZ dimer: in the magic angle configuration we expect behaviour similar to the relative monomer ZnTPP, while the ET rates should be seen in the anisotropy decay. After excitation, TA spectrum presents a negative region between 410 and 440 nm, due to the ground state bleaching of the Soret band, a positive region between 450 and 690 nm due to ESA, on top of which are superimposed the bleachings due to the Q bands.

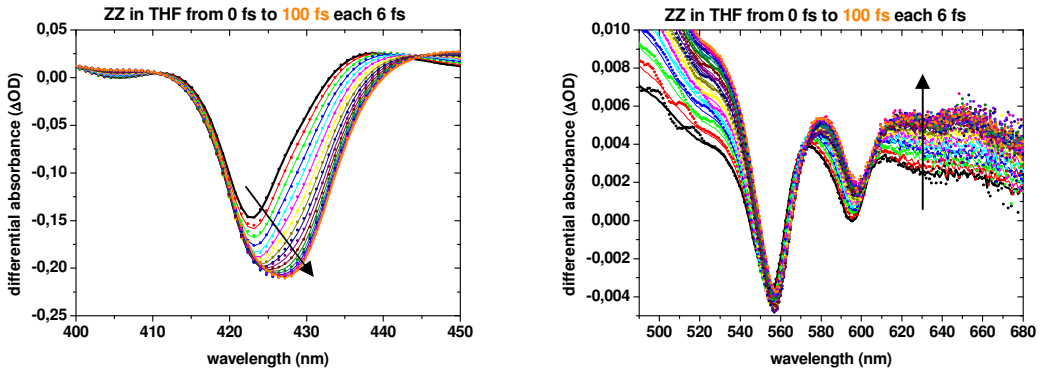

Figure 6.28: Temporal evolution of TA spectrum of the ZZ dimer from 0 fs (black) to 100 fs (orange). On the left in the B band region, on the right in the Q band region.

In Figure 6.28 the evolution of TA spectrum for ZZ in the first 100 fs is reported: in the B band region an increase of the bleaching is visible, together with a peak shift to longer wavelengths from 423.2 nm to 427.2 nm. The ESA increases in the whole range. In the Q band region the Q(1,0) bleaching starts from 555.2 nm, increases untill 60 fs and then decreases, shifting its position at 557.6 nm. The Q(0,0) bleaching decreases its intensity shifting from 595.7 nm to 598.1 nm.

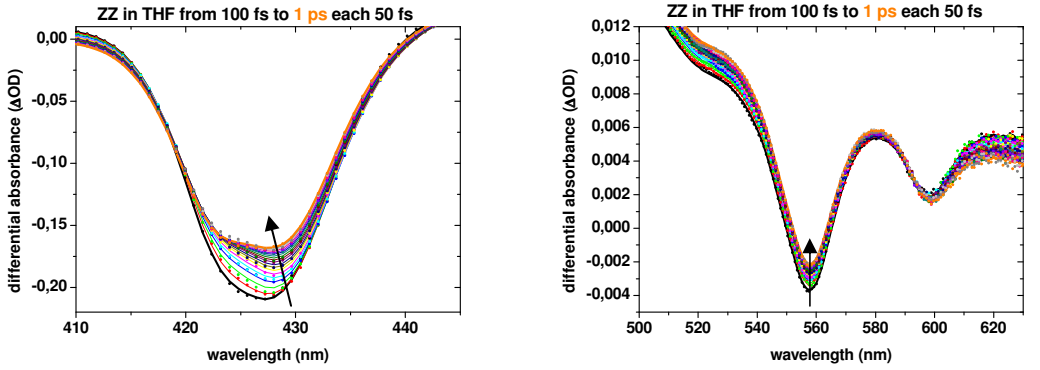

Figure 6.29: Temporal evolution of TA spectrum of the ZZ dimer from 100 fs (black) to 1 ps (orange). On the left in the B band region, on the right in the Q band region.

In Figure 6.29 the evolution of TA spectrum of ZZ from 100 fs to 1 ps is reported: in the B band the bleaching decreases retaining the position of the maximum but slightly changing the shape of the band disclosing the presence of different components underneath. In the Q bands region the ESA increases in this time range, Q(1,0) bleaching decreases retaining its position, while Q(0,0) bleaching is nearly constant.

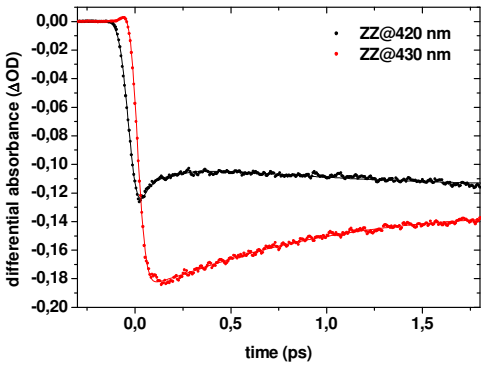

Figure 6.30: Decay traces of TA signal of ZZ in the first 2 ps at 420 nm (black) and at 430 nm (red).

In the first 2 ps after excitation the evolution of TA spectra can be fitted with two time constants of 190 fs and 770 fs. In Figure 11 the decay curves (dots) and the relative fitting (full line) of ZZ in the first 2 ps are reported. From these data it is clear that at 420 nm the fast component contributes in decreasing the bleaching, while the slow one increases the bleaching; at 430 nm the behaviour is just the opposite, with an increase of the bleaching in the first 200 fs and a decrease with 770 fs time constant.

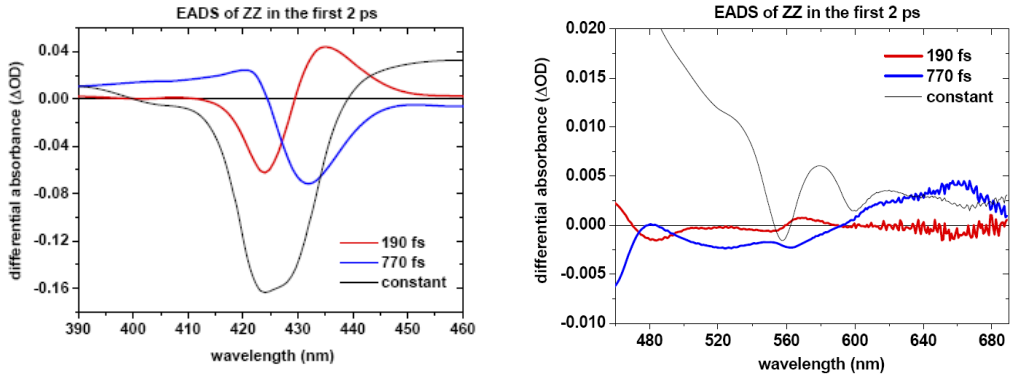

Figure 6.31: EADS relative of the first two time constants in ZT decay. In black is reported the EADS relative to the infinite decay used in the fitting.

Another evidence of the different contributions of these two time constants is visible from the EADS reported in Figure 6.31: the faster constant (190 fs) in the B band region has a nearly sigmoid shape describing a decay of the bleaching centred at 424 nm and an increase of the bleaching at 435.3 nm, while it is nearly zero in the Q bands region. The slower constant (770 fs) instead corresponds to a decay of the bleaching at 432 nm, has positive value around 420 nm and it is slightly positive around 500-580 nm and slightly negative between 600 nm and 690 nm.

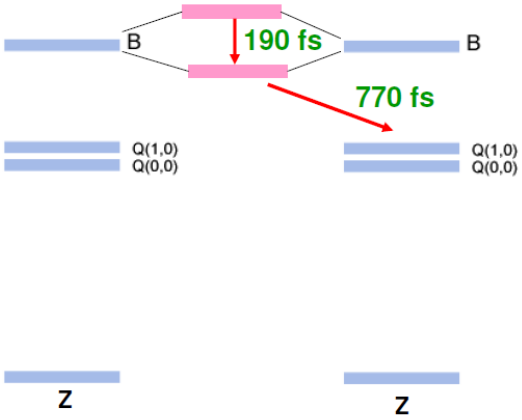

Figure 6.32: Scheme of the possible decay mechanism in ZZ dimer in the first ps.

The experimental data found for ZZ in the first ps can be explained if we invoke the presence of a small excitonic interaction between the B band of the two Z unit in the dimer: if this is the case the first component (190 fs) describes the transfer from the two excitonic states, and the longer component is related to the decay from the lower excitonic state to the Q bands, as depicted in Figure 6.32. This explanation is supported by the fact that the EADS for the faster component involves changes in the population only in the B band region, so it can be attributed to a process involving only the second excited state. There is another possibility, due to the possible removal of the degeneracy between B_X and B_y in each Z unit so the first component of 190 fs can be related to the transfer between the B states on a single Z unit. Also in this case it is important to have the TA spectrum of the asymmetric ZN monomer, to verify the influence of the linker on the degeneracy of the two B states.

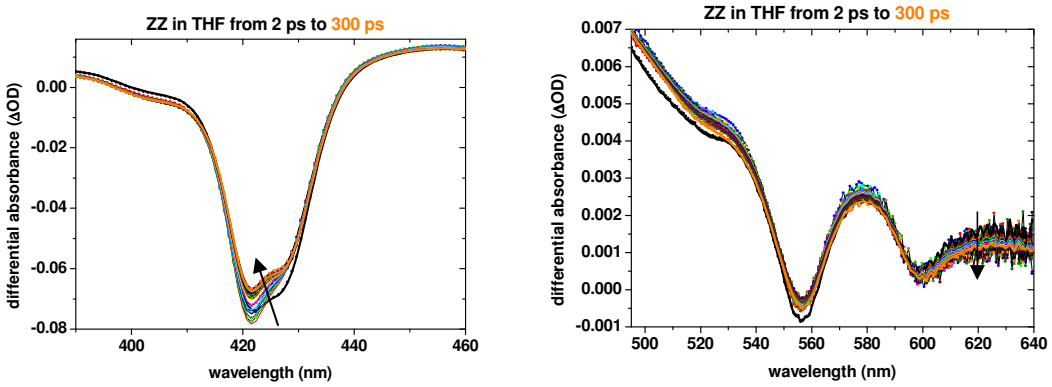

Figure 6.33: Temporal evolution of TA spectrum of the ZZ dimer in the Q bands from 2 ps (black) to 300 ps (orange). On the left in the B band region, on the right in the Q band region.

From 2 ps to 300 ps the evolution of the population in ZZ is identical to the one obtained for the relative monomer, with a main decay to the ground state in 1.69 ns. Only an additional small component with a 27 ps time constant is present: it can be probably attributed to the decay of doubly excited dimers.

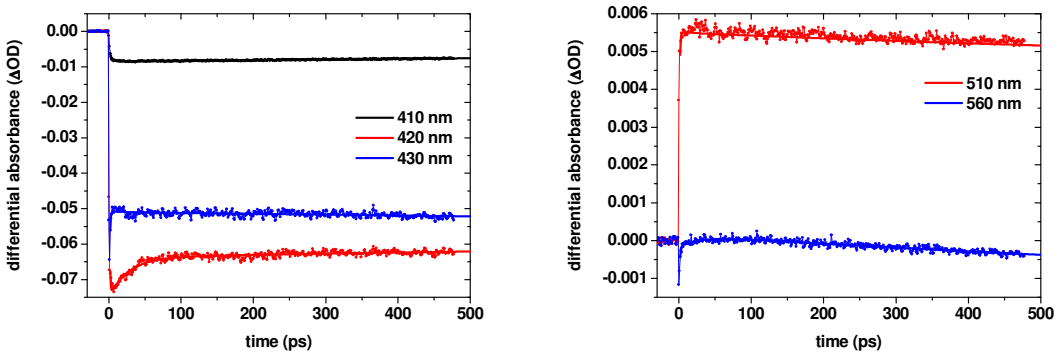

Figure 6.34: Decay traces of TA signal of ZZ in THF till 500 ps at 410 nm (black), 420 nm (red) and 430 nm (blue) in the left panel, at 510 nm (red) and 560 nm (blue) in the right panel.

In Figure 6.35 the EADS relatives to the 27 ps time constant is reported in red: it is negative in correspondence with the bleaching of the ZZ dimer and zero elsewhere.

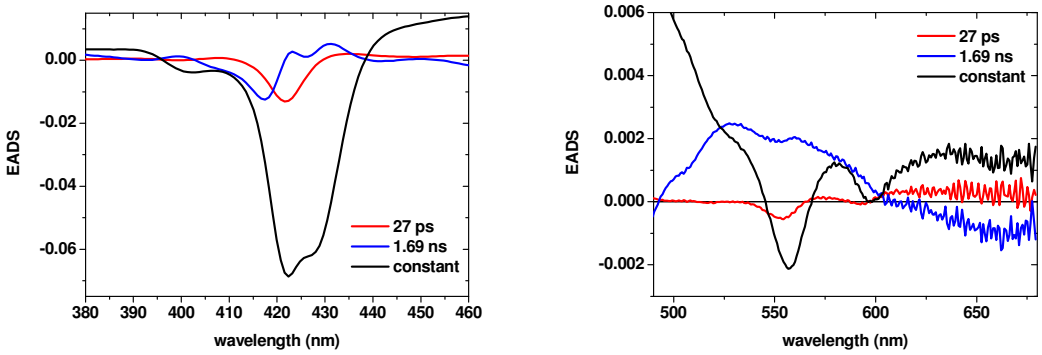

Figure 6.35: EADS relative of the time constants found in the long time scale in ZZ decay. In black is reported the EADS relative to the infinite decay used in the fitting.

Information on the presence and the rate of ET in the lower excited states (Q-bands region) should be looked for in the anisotropy decay.

6.3.5 Transient absorption experiments on TT

After excitation of the homodimer TT at 400 nm the bleaching due to the Soret band is centred at 418 nm, ESA is visible from 440 nm to 690 nm, on top of which the Q bands bleaching is present.

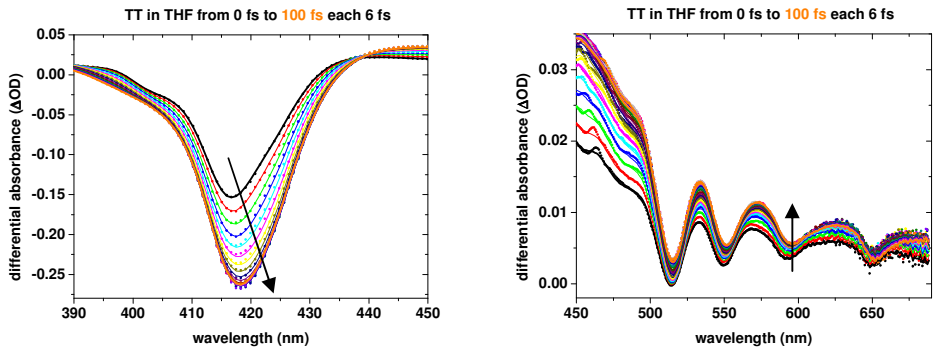

Figure 6.36: Temporal evolution of TA spectrum of the TT dimer from 0 fs (black) to 100 fs (orange). On the left in the B band region, on the right in the Q band region.

In Figure 6.36 TA spectrum of TT in the first 100 fs is reported: the B band bleaching increases and shifts from 416.7 nm to 418.3 nm, ESA increases mainly around 450 nm and all the Q bands decrease in intensity, except for the $Q_x(0,0)$ where, after an initial decrease, then the intensity increases.

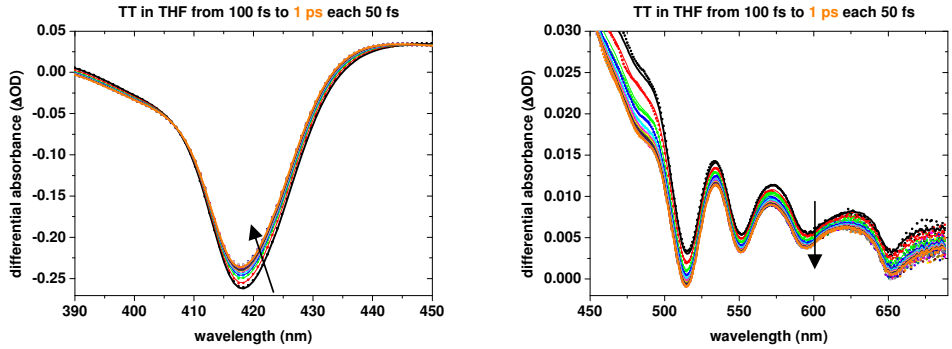

Figure 6.37: Temporal evolution of TA spectrum of the TT dimer from 100 fs (black) to 1 ps (orange). On the left in the B band region, on the right in the Q band region.

In Figure 6.37 TA spectrum of TT from 100 fs to 1 ps shows a small decrease in the B band bleaching without any shift in the position. In the graph on the right, that shows the ESA and the Q bands bleaching, the spectrum decreases in intensity at all the wavelengths.

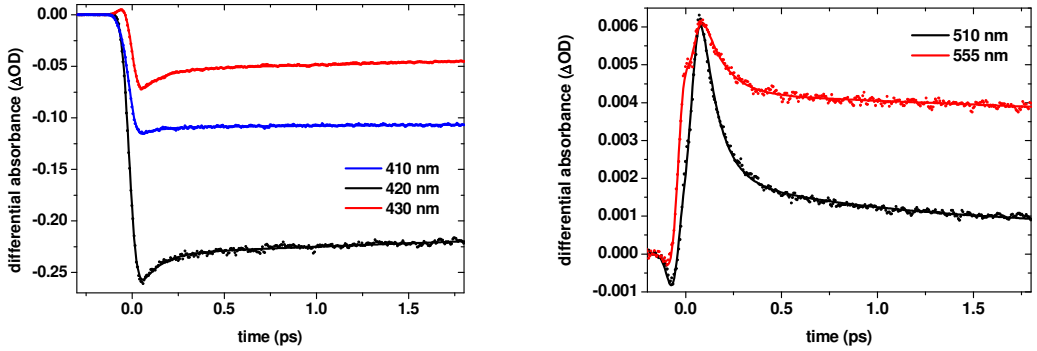

Figure 6.38: Decay traces of TA signal of TT in the first 2 ps at 420 nm (black) and at 430 nm (red).

The evolution of TA of TT in the first 2 ps can be fitted with a single exponential with a time constant of 113 fs. In Figure 6.38 the decay traces at 410 nm, 420 nm and 430 nm are reported: in both of them the 113 fs decay describes a decrease of the bleaching. In the Q band region instead, this time constant describes an increasing of the bleaching. The time constant is smaller than in the monomer TPP, but no traces of double band can be seen in the spectrum. There are two possibilities: or T units have a different behaviour than Z units when incorporated in a dimer or the second component is even shorter and cannot be identified within the resolution of our experiments. (Instrument response function is approximately 80 fs)

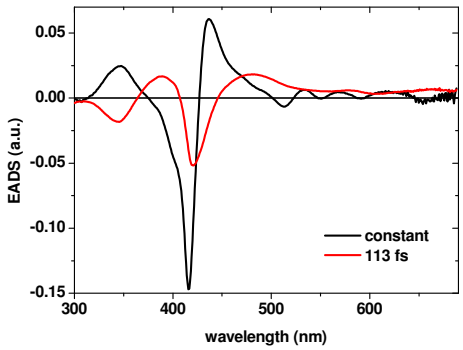

Figure 6.39: EADS relative of the first time constants in TT decay. In black is reported the EADS relative to the infinite decay used in the fitting.

The EADS relative to the 113 fs decay constant in TT is negative in the B band region with a peak at 421 nm; then it is positive in the Q band region till 700 nm.

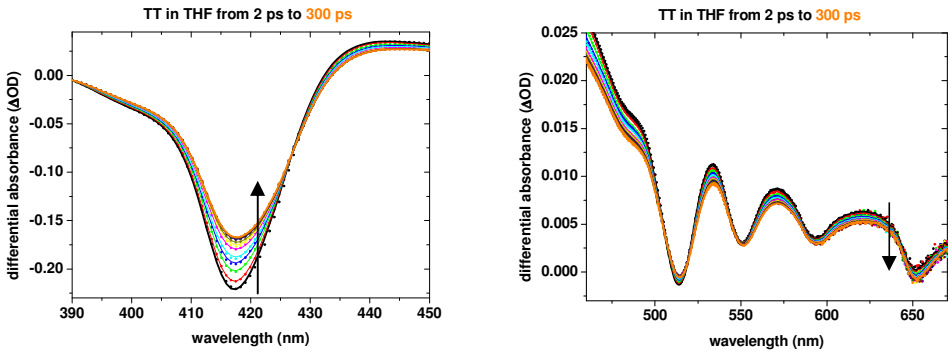

Figure 6.40: Temporal evolution of TA spectrum of the TT dimer in the Q bands from 2 ps (black) to 300 ps (orange). On the left in the B band region, on the right in the Q band region.

In the long time scale spectra, reported in Figure 6.40, the signal decreases, especially in the B band region, in the first tens of picoseconds. Only two time constants are found: the doubly excited dimers decay constant of 17 ps and the first excited state lifetime of 7.85 ns.

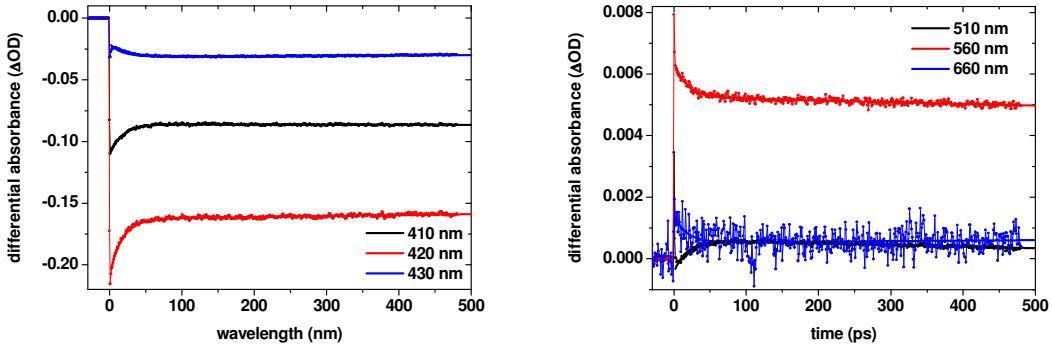

Figure 6.41: Decay traces of TA signal of TT in THF till 500 ps at 410 nm (black), 420 nm (red) and 430 nm (blue) in the left panel, at 510 nm (black), 560 nm (red) and 660 nm (blue) in the right panel.

In Figure 6.41 are reported the decay traces of TT at different wavelengths: the main component is the 17 ps decay constant that describes a decrease of the signal with the same spectral characteristics of the TT linear absorption, as can be seen from its EADS reported in black in Figure 6.42.

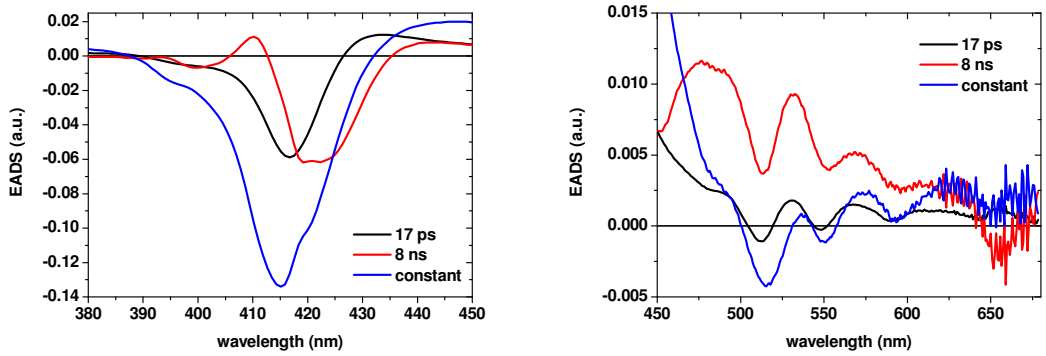

Figure 6.42: EADS relative to the 17 ps and 7.85 ns time constants in TT decay. In black is reported the EADS relative to the infinite decay used in the fitting.

Power dependent measurements were performed to gain information on this intermediate time constant of 17 ps, that was found in all the dimers. Instead in the monomers in this temporal scale, only the vibrational cooling was observed. The two processes, even if they have comparable time constants, are very different: the vibrational cooling in the monomers has much lower amplitude and describes a sharpening of the different peaks in the spectrum. The process observed in the dimers instead has higher amplitude and describes a decrease in the signal. In Figure 6.43 are reported 4 measurements performed on TT dimer with different pump intensity. It is clear that the amplitude of this decay component decreases with the decrease of the pump intensity.

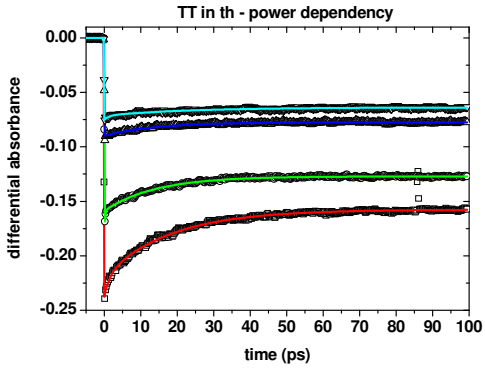

Figure 6.43: Power dependency of the 17 ps time constant in TT dimer.

Also in this dimer, the presence of ET cannot be shown in magic angle measurements, but anisotropy decay‘s analysis is necessary.

6.3.6 Transient absorption experiments on ZZC

TA measurements exciting at 403 nm are performed on the ZZ dimer titrated with cadaverine to investigate the excited state dynamic in a fixed conformation for the dimer. In the following, this blocked dimer will be called ZZC.

After excitation TA spectrum presents a negative region between 420 and 445 nm, due to the ground state bleaching of the Soret band, a positive region between 450 and 690 nm due to ESA, on top of which are superimposed the bleaching due to the Q bands.

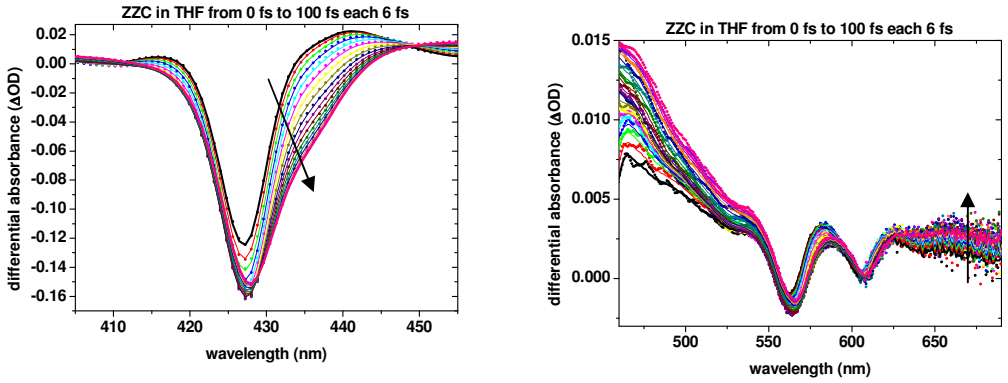

Figure 6.44: Temporal evolution of TA spectrum of the ZZC dimer from 0 fs (black) to 100 fs (pink). On the left in the B band region, on the right in the Q band region.

In Figure 6.44 the evolution of TA spectrum for ZZC in the first 100 fs is reported: in the B band region an initial increase of the bleaching is visible and the growth of a new band at 440 nm can be seen. The ESA increases in the whole range. In the Q band region the Q(1,0) bleaching starts from 561.7 nm, increases up to 60 fs and then decreases, shifting its position at 566.5 nm. The Q(1,0) bleaching is nearly constant but the peak shifts from 603.4 nm to 607.9 nm.

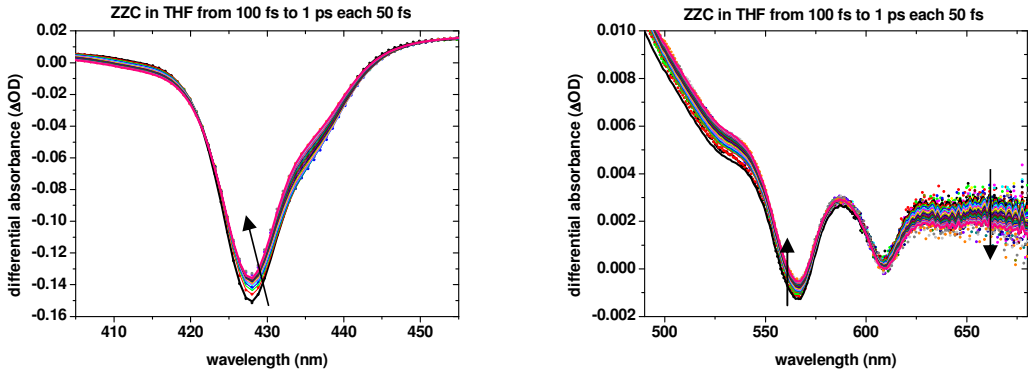

Figure 6.45: Temporal evolution of TA spectrum of the ZZC dimer from 100 fs (black) to 1 ps (pink). On the left in the B band region, on the right in the Q band region.

In Figure 6.45 the evolution of TA spectrum of ZZ from 100 fs to 1 ps is reported: in the B band the bleaching at 428 nm decreases retaining the position of the maximum, while the small band at 440 nm first increases and then decreases. In the Q bands region the ESA increases in this time range, Q(1,0) bleaching decreases retaining its position, while Q(0,0) bleaching slightly increases.

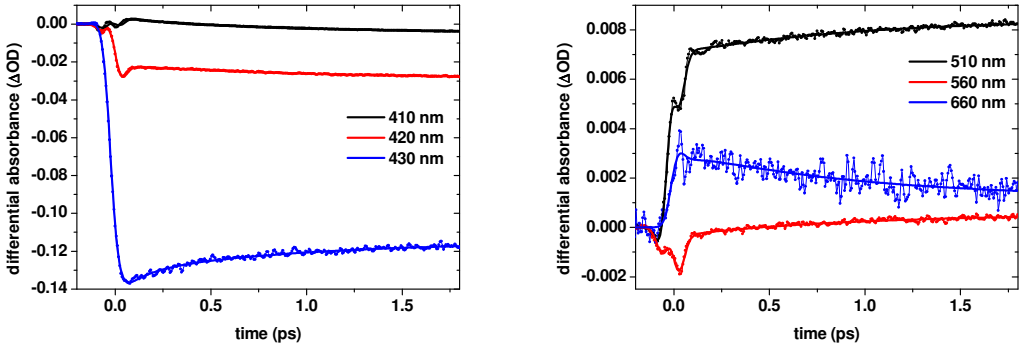

Figure 6.46: Decay traces of TA signal of ZZC in the first 2 ps at 420 nm (black) and at 430 nm (red).

After excitation, in the first 2 ps the evolution of TA spectra can be fitted with two time constants of 120 fs and 930 fs. In Figure 45 the decay curves (dots) and the relative fitting (full line) of ZZC in the first 2 ps are reported. From these data it is clear that at 420 nm the fast component contributes in decreasing the bleaching, while the slow one increases the bleaching; at 435 nm the behaviour is just the opposite, with an increase of the bleaching in the first 120 fs and a decrease with 930 fs time constant.

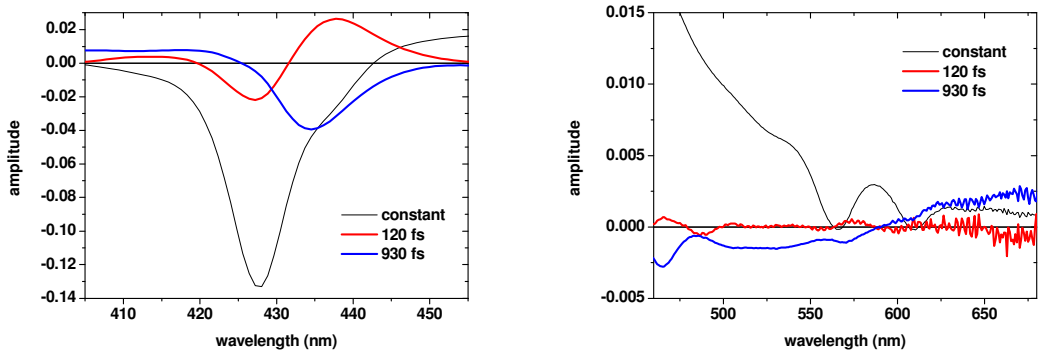

Figure 6.47: EADS relative of the first two time constants in ZZC decay. In black is reported the EADS relative to the infinite decay used in the fitting.

Another evidence of the different contributions of these two time constants is visible from the EADS reported in Figure 6.47: the faster constant (120 fs) in the B band region has a nearly

sigmoid shape describing a decay of the bleaching centred at 427.2 nm and an increase of the bleaching at 437.8 nm, while it is nearly zero in the Q bands region. The slower constant (930 fs) instead corresponds to a decay of the bleaching at 434.5 nm and it is slightly negative around 500-580 nm and slightly positive between 600 nm and 690 nm.

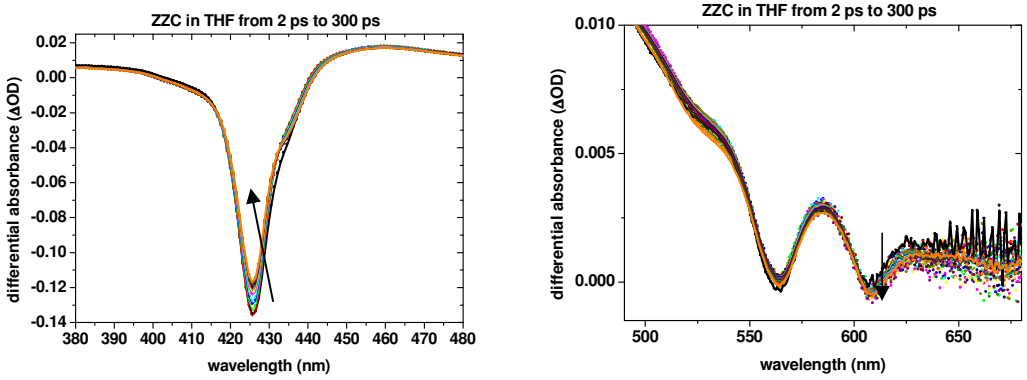

Figure 6.48: Temporal evolution of TA spectrum of the ZZC dimer in the Q bands from 2 ps (black) to 300 ps (orange). On the left in the B band region, on the right in the Q band region.

From 2 ps to 300 ps the evolution of the population in ZZC is identical to the one obtained for the relative monomer, with a main decay to the ground state in 1.7 ns. Only an additional small component with a 19 ps time constant is present: it can be probably attributed to the decay of doubly excited dimers.

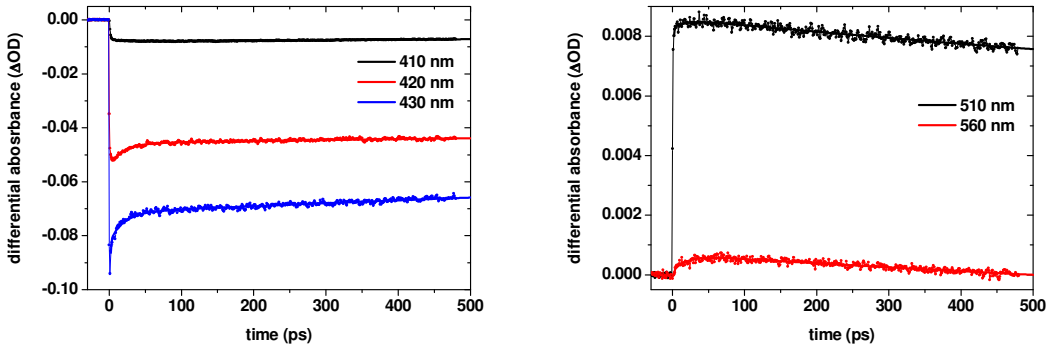

Figure 6.49: Decay traces of TA signal of ZZC in THF till 500 ps at 410 nm (black), 420 nm (red) and 430 nm (blue) in the left panel, at 510 nm (black), 560 nm (red) and 660 nm (blue) in the right panel.

In this long time range the decay traces reported in Figure 6.49 and the EADS reported in Figure 6.50 are almost the same that the ZZ dimer. So the complexation with cadaverine does not change the long time properties of this dimer.

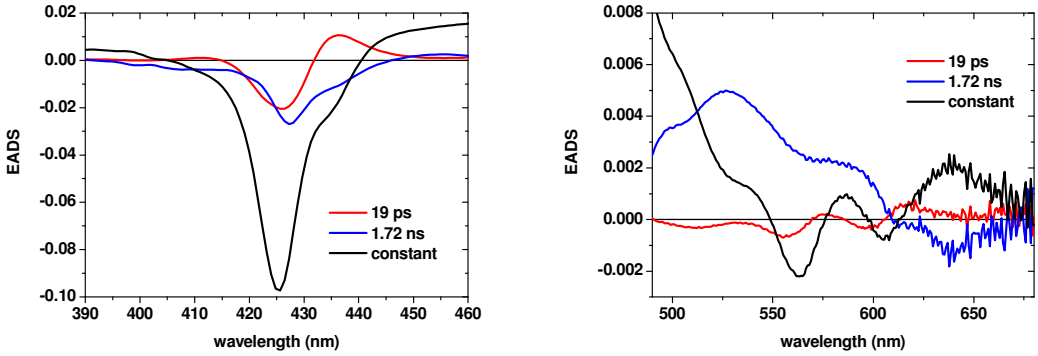

Figure 6.50: EADS relative to the 19 ps and 1.7 ps time constants in ZZC decay. In black is reported the EADS relative to the infinite decay used in the fitting.

Information on the presence and the rate of ET should be looked for in the anisotropy decay.

Table 1: Summary of all the decay constants for the investigated molecules

	S2 lifetime	Vibrational cooling	Doubly excited dimers decay	ET	S1 lifetime
T	108 fs	18 ps	-	-	8.46 ns
TN			-	-	7.95 ns
Z	1.66 ps	13 ps	-	-	1.77 ns
ZN			-	-	1.72 ns
ZT	190 fs 685 fs		25 ps	95 ps	1.63 ns 9.57 ns
TT	113 fs		17 ps	-	7.85 ns
ZZ	190 fs 770 fs		27 ps	-	1.69 ns
ZZC	120 fa 930 fs		19 ps	-	1.70 ns

In Table 6.1 all the decay constant measured for the different compounds are reported.

6.4 Preliminary time-resolved anisotropy data

In order to gain informations on the energy transfer also in the homo-dimers, time-resolved anisotropy data are analyzed for the studied compounds. Only some preliminary results are presented here: as we will see in the following a theoretical model for the analysis of the anisotropy decay in the dimers is needed to extract the energy transfer time constant. This is due to the fact that the reorientational time of the time of the monomers is in the same

temporal range that the expected energy transfer, so it is difficult to distinguish the two processes.

In TPP the initial anisotropy, starting at 0.12 at zero time, decays initially with a time constant of about 60 fs to a value of about 0.08. This first decay is attributed to an ultrafast dephasing of the two transition dipole moments and it is due to the presence of two degenerate levels in the B band of the porphyrins[5,6]. Then the signal reaches zero with a time constant of 91 ps due to rotational diffusion. For ZnTPP the anisoptropy starts at 0.19, decays with almost the same time constants of 120 fs and 94 ps. The data for this molecule are shown in Figure 6.51 as an example. As it is possible to see, the anisotropy data are more noises that the TA data shown until here.

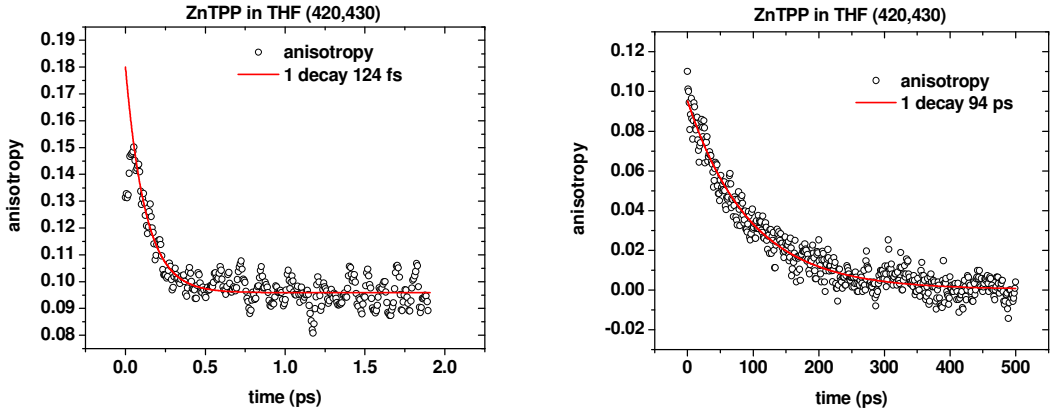

Figure 6.51: Anisotropy decay of ZnTPP in the B band region, On the left the 124 fs decay is reported, while on the right the 94 ps decay due to rotational dynamics is reported.

In all the dimers the anisotropy in the B band region displays a first fast decay of the order of 100 fs due to ultrafast dephasing of the two transition dipole moments, as found in the monomers.

Then a longer decay in the range 100-180 ps is present: this time constant is longer than in the monomers and it is similar to the time constant for the energy transfer process measured with TA for the hetero-dimers ZT. However, the linker used is not rigid, so this time constant can be related to the motion of the single porifirinic units inside the dimer. So a model for the anisotropy decay that takes in accounts both the energy transfer process and the reorientational motions in the dimers is needed, together with a Brownian dynamic simulation of the internal motions of the units.

6.5 Conclusions

The excited states dynamic of homo and hetero dimers of porphyrins was extensively studied in different temporal ranges from fs to ns. In ZT an energy transfer process occurs from Z to T in the first excited state with 101 ps transfer rate, while in homodimers ZZ and TT it is necessary to investigate the anisotropy decay to have information about the presence of ET. In the second excited state the analysis is more complicated due to the strong overlapping of the bands. Moreover a double exponential decay is visible not only in the heterodimer ZT, but also in ZZ and ZZC where unexpected multiple bands are visible, indicating a possible common origin of this behaviour. Only one decay is instead present in TT and in the monomers. This double decay found in the dimers containing a Z unit is faster than in the monomers. Two possible explanations for this behaviour can be hypotized: a transfer of populations between the B bands of the two units or the removal of the degeneracy of the B_x and B_y bands in a single Z unit due to the linker in the dimer, so the transfer is inside the same molecule. The linking position in these dimers has low influence on the electronic properties of the ring, so this second possibility seems less plausible. To remove any doubts on the interpretation of this double decay, measurements on the asymmetric monomer ZN will be performed exciting at 400 nm and probing in the whole absorption spectral range to verify the presence of a double decay. If instead the transfer is between the two units (Z and Z in ZZ and ZZC or from Z to T in ZT), this energy transfer process in the second excited state is one hundred time faster than in the first excited state. Processes of these kind have never been clearly observed and investigated in details up to now in the literature.

References

[1]J.S. Baskin, H.Z. Yu, A.H. Zewail, *J. Phys. Chem. A*., **2002**, 106(42), 9837

[2] H. Z. Yu, J.S. Baskin, A.H. Zewail, *J. Phys. Chem. A*., **2002**, 106(42), 9845

[3] H. Song, M. Taniguchi, M. Speckbacher, L. Yu, D. F. Bocian, J.S. Lindsey D. Holten, *J. Phys. Chem. B*, **2009**, 113, 8011.

[4] T. Carofiglio, A. Varotto, U. Tonellato, *J. Org. Chem*, **2004**, 69 (23), 8121

[5] K.H. Wynne, R.M. Hochstrasser, *Chem. Phys.,* **1993**, 171, 179

[6] K. Razi Naqvi, R.E. Dale, *Chem. Phys Lett.,* **2002**, 357, 147

Final remarks

The work presented in this thesis is mainly focused on the role played by intermolecular interactions in the modification of the optical properties of different classes of molecular dimers with respect to the relative monomers. Taking into considerations different molecules, also the strength of the interactions between the units changes, so two limiting case has been considered: weakly or strongly interacting molecules. As expected, larger modifications in linear and non-linear optical properties are found for strongly interacting molecules. For the weakly interacting structures the main advantages relays in the possibility to predict the properties of larger arrays from the information gained in monomers.

The research work has been focused on three classes of molecules: i) the charge transfer dimer of the radical cation of tetrathiafulvalene (TTF), ii) molecular dimers of dipolar and quadrupolar molecules and iii) chemically linked dimers of free base- or Zn(II)-tetraphenylporphyrin (TPP).

In the first system, the CT dimer created by the radical cation of TTF, the interest is mainly set on the characterization of the two-photon state created by the CT process and predicted by the Hubbard model. This state is investigated using the closed- and open-aperture Z-scan technique to determine the non-linear refractive index and the two-photon absorption cross section. Due to the low stability of the radical cation and to the presence of different species in the investigated solutions, the Z-scan measurements are not easy to perform. Moreover, the interference from residual absorption signal for the transition towards the one-photon allowed CT state masks eventual contributions from the TPA of the second CT state. Furthermore, the signal due to the non-linear refractive index of the solvent used, covers the n_2 signal of the dimer. Instead from the investigation of the excited- state dynamic of both the monomer and the dimer a strongly different dynamic is found for the dimer respect to the monomer. The decay of the dimer is globally one hundred times faster than the monomer, so it can be a promising material for optical devices requiring fast response.

Dimers of dipolar and quadrupolar molecules are synthesized using linear alkyl chains with different lengths. The optical spectra of dimers in solution show a red shift of the linear

absorption band upon decreasing the interchromophore distance, while fluorescence and two-photon absorption are only marginally affected by the interactions. The TPA cross sections of the dimers are slightly less than twice the monomer cross-section. For these dimers, interchromophore interactions are too weak to produce sizeable spectroscopic effects: the one- and two-photon absorption properties of these dimers are almost the sum of those of the corresponding monomers.

In collaboration with the group of Prof. Anna Painelli from the University of Parma, a model is developed to describe the linear and non-linear optical properties of these dimers. The approach used is based on the Mulliken model for charge-transfer excitations in molecular complexes. In this model the low energy states of dipolar and multipolar chromophores are dominated by charge-transfer resonances. This simple effective electronic model, that takes in account the electrostatic interactions between charges, is able to reproduce the experimental shifts of OPA and TPA observed for the dimers when compared to the monomer. The effects on intensity are small, but both theoretical and experimental data are in agreement.

The last investigated systems are chemically linked homo- and hetero-dimers of porphyrins: these molecules are interesting as basic building blocks for the design of artificial light harvesting antennae, so the presence and efficiency of energy transfer processes between the units of these dimers have been studied. The absorption spectra of homo-dimers of suitably modified free base tetraphenylporphyrins (T) of Zn(II)-tetraphenylporphyrins (Z) are nearly the sum of the monomers spectra, especially in the Q bands region, so the interactions between the units are weak.

In the hetero-dimer, formed by a T and a Z units; there is evidence of an energy transfer process in the first excited state from linear fluorescence measurements: the emission spectrum clearly shows that the fluorescence occurs essentially from the T moiety, while the Z unit has a diminished FQY. This process is confirmed also from time resolved optical experiments: time resolved fluorescence and transient absorption. These experiments allow measuring an energy transfer characteristic time of 101 ps from Z to T. For the homo-dimers, in which the donor and acceptor are the same molecule, it is not possible to obtain information from these technique, but it is necessary to study the evolution of the time-resolved anisotropy signal to reveal the energy transfer dynamic.

An unexpected dynamic is instead found in the S_2-S_1 conversion for dimers containing a Z unit. In the hetero-dimer two time constants of 190 fs and 685 fs are found. These constants can be related to an ultrafast energy transfer from Z to T in the second excited state, a process that is for the first time studied in a porphyrins dimer, and the decay of the T unit to the lower

first excited electronic state. There is another possible explanation for the presence of these two time constants. If the presence of the linker is able to remove the degeneracy between the B_x and B_y states in Z, then the two time constants can describe an energy transfer process between these two states inside the same molecular unit of the dimer and the decay of this unit towards its first excited electronic state .

Similarly in the ZZ dimer, two decay times of 190 fs and 770 fs are measured in the TA spectra evolution. These experimental data can be explained if we invoke the presence of a small excitonic interaction between the B band of the two Z unit in the dimer: if this is the case the first component (190 fs) describes the transfer from the two excitonic states, and the longer component is related to the decay from the lower excitonic state to the Q bands. The removal of the degeneracy between B_X and B_y in each Z unit is however still a possibility. If this is the case, the first component of 190 fs can be related to the transfer between the B states on a single Z unit.

In the TT dimer no traces of double decay can be seen, as was observed for the other dimers. There are two possibilities: or T units have a different behaviour than Z units when incorporated in a dimer or the second component is shorter and cannot be identified within the temporal resolution of our experiments.

One- and two-photon absorption and emission properties of heteroaromatic bichromophores

Alessandro Abbotto,*[a] Luca Bellotto,[a] Renato Bozio,[b] Camilla Ferrante,*[b] Ilaria Fortunati,[b] Eleonora Garbin,[b] Chiara Marinzi,[a] Anna Painelli,*[c] Cristina Sissa,[c] Francesca Terenziani[c]

[a]Department of Materials Science and INSTM, University of Milano-Bicocca, Via Cozzi 53, I-20125, Milano, Italy;
[b]Department of Chemical Science, University of Padova, Via Marzolo 1, I-35131, Padova, Italy;
[c]Department of Chemistry GIAF, University of Parma, Parco Area delle Scienze 17/A, 43100, Parma, Italy

ABSTRACT

We present the design, synthesis, and characterization of a class of heteroaromatic bichromophores in order to investigate intermolecular interactions and their effect on optical and nonlinear optical properties. As a design strategy we have linked two dipolar or quadrupolar units through a non-conjugated alkyl chain. The two units are connected either through their donor or their acceptor end-groups. This study represents a first step towards the design of bi- and multichromophoric systems with optimized NLO responses in order to exploit collective and cooperative effects from interchromophore interactions.

Keywords: two-photon absorption, intermolecular interactions, heterocyclic dyes

1. INTRODUCTION

Polar and polarizable π-conjugated organic molecules have been extensively investigated in the past years for their nonlinear optical (NLO) properties[1] such as electrooptic (EO) response (a second-order NLO phenomenon) or two-photon absorption (TPA, a third order phenomenon).[2] Such a great interest has been justified by their potential use in important emerging photonic technologies, including holographic memories based on photorefractive materials, two-photon laser scanning fluorescence microscopy, optical limiting, microfabrication, photodynamic therapy, and upconverted-lasing. By far, the most successful design strategy involved dipolar systems having a general structure D-π-A and/or quadrupolar systems having a general structure of the type D-π-A-π-D or A-π-D-π-A, where A is an acceptor group, D a donating group, and π a conjugated moiety. Based on these concepts several efficient dipolar[3] and quadrupolar[4] chromophores for TPA have been prepared in the last decade. During the last years, we have designed, synthesized and characterized a number of heteroaromatic based dipolar[5] and quadrupolar dyes[6] for TPA. In particular, dipolar molecule **1-M** and quadrupolar molecule **2-M** are the most representative examples of the heteroaromatic based TPA dyes. These two chromophores, endowed with large TPA responses, use the pyrrole and the pyridinium rings as efficient donor and acceptor moieties, respectively.

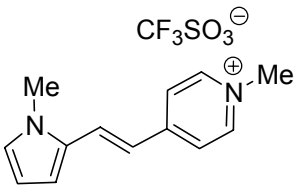

1-M

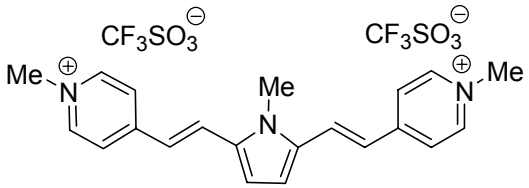

2-M

* alessandro.abbotto@unimib.it (AA); camilla.ferrante@unipd.it (CF); anna.painelli@unipr.it (AP)

Organic Optoelectronics and Photonics III, edited by Paul L. Heremans, Michele Muccini, Eric A. Meulenkamp, Proc. of SPIE Vol. 6999, 69990K, (2008) · 0277-786X/08/$18 · doi: 10.1117/12.783273

The vast majority of the published studies on molecular properties of NLOphores are based on investigations in solution, where intermolecular interactions are neglected. This represents a strong limitation if one considers that most applications are based on NLO materials where intermolecular interactions and dye aggregation are relevant. Few works are found in the literature investigating the effects of intermolecular interactions on TPA properties in discrete multichromophores where two or more dyes are linked by one or more non-conjugated chains.[7] Experimental results have been interpreted in terms of theoretical models for interacting polar and polarizable chromophores. These models have shown how NLO properties are governed by the relative orientation of chromophores.

So far, studies on interacting NLOphores have been limited to dipolar dyes. No systematic studies on discrete multi-quadrupolar chromophores and their TPA properties have been reported in the literature. This appears to be a strong limitation if one considers that quadrupolar systems are generally much more efficient than corresponding D-π-A dyes. Based on these premises we carried out a systematic investigation of linear and nonlinear (TPA) optical properties of bichromophoric assemblies of dipolar and quadrupolar dyes.

Our general design strategy consisted in linking two dipolar or quadrupolar units through a non-conjugated saturated alkyl chain (3, 6, and 12 carbon atoms linear alkyl chain). The dye units were connected either through their donor end-groups (series D-D) or through their acceptor end-groups (series A-A). Keeping dipolar dye **1-M** and quadrupolar dye **2-M** as preferred building units of bichromophores we have therefore designed the dipolar bichromophores **1** and quadrupolar bichromophores **2** (Scheme 1). Bichromophores **1** and **2** are the corresponding "dimers" of dipolar and quadrupolar "monomers" **1-M** and **2-M**, respectively. We have used these two preferred bichromophore patterns to investigate both the effects of the linking geometry (D-D and A-A,) and of the length of the connecting alkyl chain (series a: *n*-C_3H_6; series b: *n*-C_6H_{12}; series c: *n*-$C_{12}H_{24}$). All of these systems have a saline nature.

We present here a systematic and multidisciplinary investigation on linear and nonlinear properties of dipolar and quadrupolar bichromophores **1** and **2**.

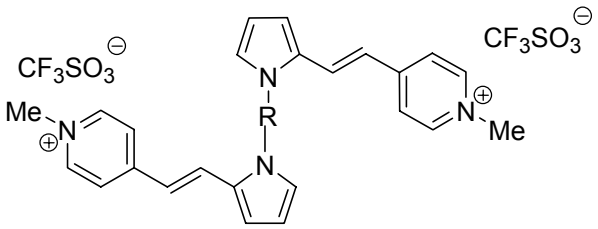

1 D-D a: R = *n*-C_3H_6
1 D-D b: R = *n*-C_6H_{12}
1 D-D c: R = *n*-$C_{12}H_{24}$

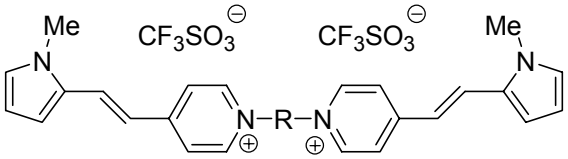

1 A-A a: R = *n*-C_3H_6
1 A-A b: R = *n*-C_6H_{12}

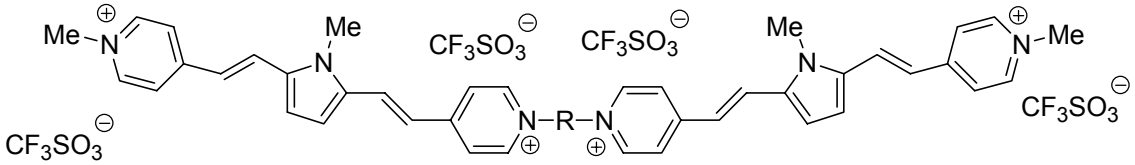

2 A-A a: R = *n*-C_3H_6
2 A-A b: R = *n*-C_6H_{12}

Scheme 1. Bichromophores investigated in this work

2. RESULTS AND DISCUSSION

2.1 Synthesis of chromophores and bichromophores.

The monomers **1-M**[8] and **2-M**[9] were prepared according to the literature. All the dimers were previously unknown in the literature and were synthesized according to different strategies depending on the linking site between the two building units.

The synthesis of the series **1 D-D** is shown in Scheme 2. Knoevenagel-like condensation of the bis-aldehydes **3** with *N*-methyl-4-picolinium triflate in refluxing EtOH and in the presence of a catalytic amount of piperidine led to dimer bis-salts **1 D-D a-c** as orange/red solids in 50-70% yield. The bis-pyrrole-2-carboxaldehydes **3a** - **3c** were previously unknown in the literature, with the exception of a report for **3a**.[10] They were obtained as yellow/orange oils by condensation of pyrrole-2-carboxaldehyde with the proper α,ω-dibromoalkane in presence of potassium *tert*-butoxide as a base.

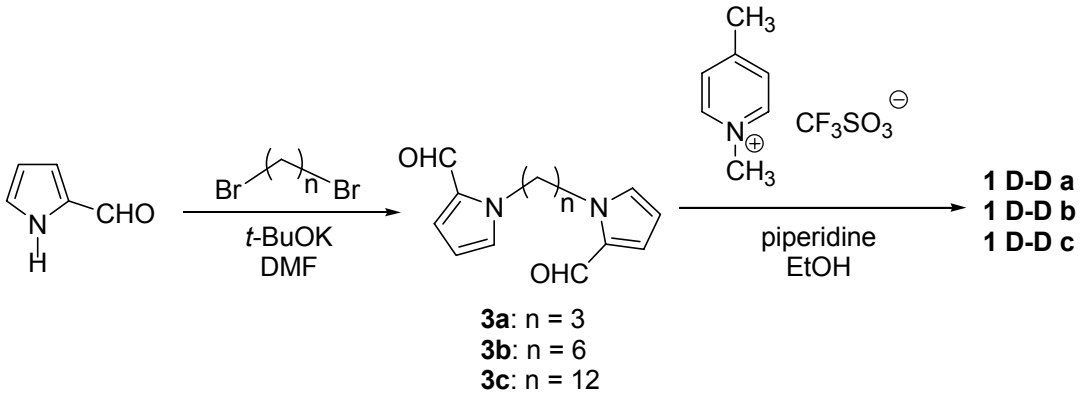

Scheme 2

The reaction of the pyridine-pyrrole ethene precursor **4**, more efficiently prepared through a modification of the literature method,[8a] with the proper α,ω-bis(trifluoromethansulfonyl)alkanes **5a** and **5b** in refluxing $CHCl_3$ afforded the expected products **1 A-A a** and **1 A-A b**, respectively, as orange precipitates in 60-80% yield (Scheme 3). The bis-triflates **5a** and **5b** were obtained in almost quantitative yields by reaction of corresponding alkane-α,ω-diols with trifluoromethanesulfonic anhydride in CH_2Cl_2 and in presence of pyridine, according to the procedure reported in the literature for **5a**.[11]

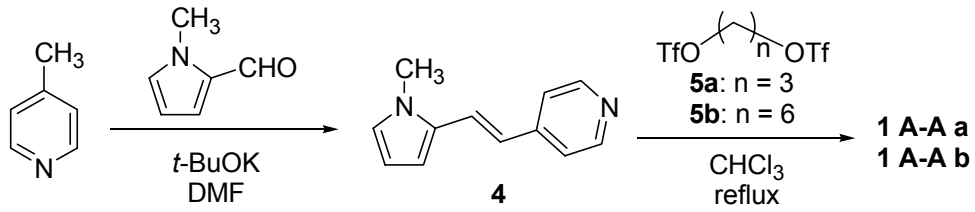

Scheme 3

The quadrupolar bichromophores **2 A-A** have been synthesized according to Scheme 4. Alkylation of two equivalents of the precursor **6**[12] with one equivalent of the proper α,ω-bis(trifluoromethansulfonyl)alkanes **5a** or **5b** in DMF at room temperature afforded the expected products **2 A-A a** and **2 A-A b** as dark violet solids in 70-80% yield.

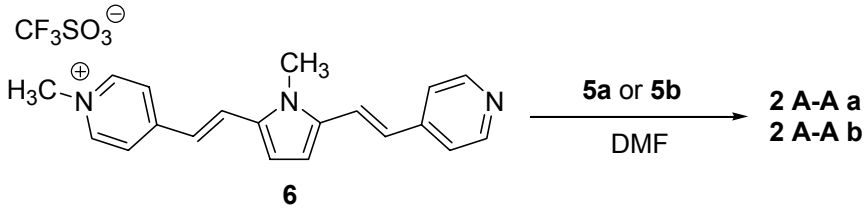

Scheme 4

All of the new bichromophores have been characterized by ^{1}H and ^{13}C NMR spectroscopy and gave satisfactory elemental analyses.

2.2 Linear and nonlinear optical characterization.

Monomeric and dimeric dyes show a strong ICT absorption band in the UV-vis region of the spectrum and are highly transparent in the visible red and NIR region. In addition, they all show a fluorescence emission, very weak for **1-M** and all its dimers, whereas **2-M** and the **2 A-A b** show a sizeable fluorescence, in contrast with **2 A-A a**. Table 1 collects the main one- and two-photon absorption and emission properties of dipolar and quadrupolar monomers and bichromophores in DMSO. Fluorescence quantum yields (FQY) are estimated against the known FQY of fluorescein in water at pH > 10 (0.1 M NaOH). The solutions used for fluorescence measurements are characterized by concentrations in the range $5 \times 10^{-6} \div 5 \times 10^{-7}$ M.

Nonlinear absorption spectra of all compounds are also investigated in DMSO with the Two-Photon Induced Fluorescence (TPIF) technique. For these measurements more concentrated solutions are employed, and they fall in the range $1 \times 10^{-3} \div 1 \times 10^{-4}$ M . TPIF experiments are performed using a tunable Ti:Sapphire femtosecond laser system (Coherent Mira 900-F), with pulses of approximately 150 fs duration and 76 MHz repetition rate. The exciting wavelength is tuned between 740 and 930 nm. The laser beam is focused on the sample cell (a 10 mm quartz cuvette), via a 40 cm focal length lens. The fluorescence spectra excited by two-photon absorption are also measured and compared to linear emission spectra. Figure 1 shows that they fall in the same spectral region and have almost identical shapes, confirming that the emitting states are the same for both processes. The shifts between the linear and two photon induced fluorescence maxima is attributed to a reabsorption effect caused by the higher concentration employed in the two photon measurement with respect to the linear one. Therefore, in the following analysis, it is assumed that the fluorescence quantum yield does not change if one- or two-photon excitation is applied. The TPA cross sections of the investigated compounds are evaluated following the procedure described in the literature[13] and using fluorescein in water at pH > 10 (0.1 M NaOH) as a reference standard. [14]

Figure 1 shows the TPA spectra (symbols) in DMSO of : a) **1-M**, b) **1 D-D a**, and c) **1 A-A a**, together with the linear absorption spectra (full lines). The wavelength scale of TPA spectra is divided by two to allow a direct comparison with linear absorption and the values of TPA cross-section are expressed in Göppert-Mayer units ($1GM=10^{-50}$ cm^4 s $photon^{-1}$ $molecules^{-1}$). The one- and two-photon absorption maxima coincide, as expected for simple dipolar structures. Furthermore it can be noticed that in all the experiments there is a large error bar, due mainly to the extremely low FQY of all compounds. Nevertheless the TPIF signals show the expected quadratic behaviour with respect to the input laser intensity. The TPA maxima, together with the corresponding cross sections are summarized in Table 1.

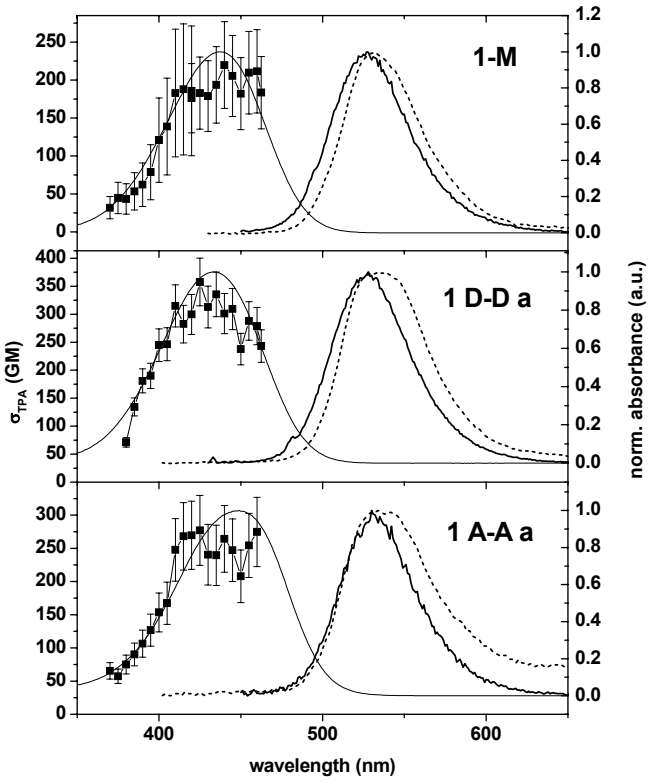

Fig. 1. Linear absorption and fluorescence spectra (full lines), two-photon fluorescence spectra (dash) and TPA (symbols) of **1-M**, **1 D-D a** and **1 A-A a** in DMSO. The TPA wavelengths are halved for a direct comparison with linear absorption.

Table 1. Linear and nonlinear absorption and emission parameters of dipolar chromophores **1-M** and quadrupolar chromophore **2-M** in DMSO.

Compd.	one-photon absorption				two-photon absorption	
	λ_{max}(abs) [nm]	ε [a] [mol^{-1} l cm^{-1}]	λ_{max}(em) [nm]	Φ_F [b] [%]	λ_{max}(abs) [c] [nm]	σ [a,d] [GM]
1-M	438	37300 ± 3000	528	1.1 ± 0.5	430-460	195 ± 60
1 D-D a	434	32850 ± 1000	528	0.8 ± 0.03	410-450	157 ± 20
1 D-D b	438	34600 ± 2000	528	1.2 ± 0.4	420-460	150 ± 35
1 D-D c	440	37240 ± 1000	528	1.2 ± 0.07	420-460	160 ± 20
1 A-A a	447	34300 ± 2500	534	1.3 ± 0.2	420-460	130 ± 25
1 A-A b	443	32500 ± 4000	530	1.3 ± 0.2	420-460	120 ± 20
2-M	521	70300 ± 2500	608	12.8 ± 0.6	410	
2 A-A a	533	61500 ± 2000	608	1.8 ± 0.3	410-420	
2 A-A b	526	68500 ± 2000	610	11 ± 2	410-415	

[a] Values for bichromophores have been divided by two in order to be normalized to single chromophore sub-unit. [b] Fluorescence quantum yield. [c] Values have been divided by two. [d] 1 GM (Göppert-Mayer) = 1 x 10^{-50} cm^4 s $photon^{-1}$ $molecule^{-1}$.

These experimental results show that, for all the dimers with D-D connection, the spectral position of both OPA and TPA is the same as for the monomer **1-M.** Moreover, within experimental errors, the TPA cross sections of the dimers are roughly twice the monomer cross-section. We therefore conclude that for D-D dimers interchromophore interactions are too weak to produce sizeable spectroscopic effects: the one- and two-photon absorption properties of D-D dimers are simply the sum of those of the corresponding monomers.
Concerning **1 A-A a** and **1 A-A b** dimers, we observe significant effects due to interchromophore interactions. The absorption band of A-A dimers is red-shifted with respect to the monomer, while the TPA cross section is lower than twice the monomer cross section. Both effects increase as the length of carbon chain joining the monomeric units decreases, leading to shorter intermolecular distances and hence to larger interchromophore electrostatic interactions.
In Table 1 preliminary data on the TPA spectra of quadrupolar systems are also reported, even if absolute intensities are still to be determined. We can see that the absorption maxima of **2 A-A a** and **2 A-A b** are red-shifted with respect to the corresponding monomer and this shift increases as the length of alkyl chain decreases. The position of the TPA maxima fall around 410 nm, in a different region with respect to the OPA, as expected for quadrupolar chromophores, and it is barely affected by intermolecular interactions. Preliminary data on the intensities also suggest minor effects of intermolecular interactions.

2.3 Essential-state models for dipolar and quadrupolar interacting systems.

Charge resonance in **1-M** can be described as the resonance between two structures: D-π-A^+ and D^+-π-A. Following the same strategy successfully applied for neutral D-π-A chromophores,[15] we describe **1-M** spectra in terms of an essential-state model based on the two resonating states. The electronic two-state Hamiltonian is defined by $2z$, measuring the energy separation between the two basis states, DA^+ and D^+A, and by the matrix element that describes the mixing between the two states, $-\tau$, that measures the probability of electron transfer from D to A and backward. The dipole moment operator is required to calculate optical spectra. Permanent dipole moments are ill-defined for charged species, but only transition dipole moments and differences between permanent dipole moments of relevant states enter the expressions for spectroscopic observables. In our model these quantities can be defined in terms of a single parameter, μ_0, that measures the difference of the dipole moments relevant to the two basis states. Much as for neutral D-π-A chromophores it is proportional to the effective D-A length. The spectroscopically relevant dipole moment operator is then a two by two matrix with a single non-vanishing parameter, μ_0, relevant to the D^+A state. Being not interested in absolute OPA and TPA intensities (see below) the specific value of μ_0 is irrelevant. Spectra are calculated assigning a Lorentzian line-shape to the transitions with a line-width, Γ, that implicitly accounts for the vibronic structure. Just three numbers z, τ and Γ are then needed to reproduce the spectral position and the shape of OPA and TPA spectra of **1-M** (one more, μ_0 would be required to account for intensities). Unfortunately the problem is underdetermined and the set of parameters, $z = 1$ eV, $\tau = 1$ eV and $\Gamma = 0.46$ eV, that we adopt to reproduce optical spectra of **1-M** is not unique. We underline that fluorescence spectra cannot be described in the very simple, purely electronic model discussed here. In fact we do not explicitly account for vibrational and solvation degrees of freedom whose relaxation in the excited state is responsible for the observed Stokes shift. Anyway, the simple model reproduces the spectral position of OPA and TPA, and rationalizes the origin and the effects of interchromophoric interactions on spectral properties.
The two-state model for **1-M** is easily extended to describe bichromophores.[7] Here we explicitly discuss A-A dimers. Analogous models for D-D dimers suggest negligible spectroscopic effects of interchromophore interactions, in agreement with experimental results. In view of the large interchromophore distances in all dimers, we neglect any charge-transfer between the chromophores and account for electrostatic interchromophore interactions. The resulting four-state model is sketched in Fig. 2 (for the sake of simplicity we consider only the three geometries depicted in the figure which are representative of three special cases in a random distribution). The parameters derived for the monomer can be directly transferred to the dimers. We account only for nearest-neighbor electrostatic interactions between point-charges, as measured by V.[7] Results will be presented for variable V: non-interacting chromophores, i.e. two **1-M** molecules at infinite distance, correspond to $V = 0$, while V increases with decreasing the distance of chromophores. For two chromophores at a distance of 5Å, we roughly estimate $V \approx 0.07$eV.
In Fig. 3, color maps show the evolution of OPA and TPA spectra with V for the three different geometries sketched in Fig. 2. The intensity of spectra of non-interacting chromophores are rescaled setting to 1 the maximum intensity calculated for $V = 0$. For all three geometries we regain the red-shift observed experimentally in the OPA spectrum: the electrostatic interaction, V, in fact stabilizes the states with a single (and/or a double, depending on geometry, cf Fig. 2) excitation. The shift of ~10 nm with respect to **1-M** observed for **1 A-A a** is reproduced for $V \approx 0.1$ eV, well in line with the expected value. The intensity of OPA is almost unaffected by electrostatic interactions for such small V values. A

red-shift of TPA spectra is similarly expected, but hard to be confirmed in view of the large experimental errors. Our results can explain the observed small suppression of the TPA upon dimerization: in the linear and perpendicular geometries, in fact, the calculated TPA is essentially unaffected by dimerization in the relevant V range, while in the parallel geometry it sharply decreases.

2-M is a typical quadrupolar chromophore where two acceptor groups are linked to a central donor. It resonates between three limiting structures: $A^+DA^+ \leftrightarrow A^+D^+A \leftrightarrow AD^+A^+$. The basic electronic model for quadrupolar dyes then implies three basis states corresponding to the three resonating structures.[16] The φ_0 state, corresponding to A^+DA^+, is lower in energy and is separated by an energy $2z$ from the two degenerate φ_1, φ_2 states, corresponding to A^+D^+A, AD^+A^+, respectively. A matrix element $-\tau$ mixes φ_0 with φ_1, φ_2 to lead to a ground state, g, and to two excited states, c and e, active by OPA and TPA, respectively.[16] The two experimentally accessible OPA and TPA frequencies of quadrupolar chromophores unambiguously fix the two parameters of the electronic model, and for **2-M** we estimate $z = 0.88$ eV, $\tau = 0.87$ eV. Moreover to approximately reproduce experimental bandshapes we fix $\Gamma = 0.4$ eV.

Following the same strategy adopted for **1-M** dimers we describe dimers of **2-M** accounting for electrostatic interactions between nearest-neighbor point charges, as measured by the parameter V. The three-state model per quadrupolar chromophore leads to a 9-state model for the dimer, with V entering in the diagonal energies of the basis state, along the same lines as shown in Fig. 2 for **1-M** dimers. Color maps in Fig. 4 show the V evolution of OPA and TPA spectra of **2-M** dimers in three different geometries. The first observation is that for all geometries the OPA frequency moves to the red with increasing V, well in line with the experimental observation of a progressive red-shift of the OPA frequency from **2-M** to **2 A-A b** and **2 A-A a.** The observed red-shift of the OPA suggests $V \approx 0.1$ eV for **2 A-A a**. For the same V the bottom panels in Fig. 4 show minor effects on the TPA frequency, again in agreement with experimental observation. Our calculations also suggest minor effects of interchromophore interactions on OPA and TPA intensities. Indeed an increase of the TPA intensity is expected for all three geometries but for extremely large V values hardly relevant to multichromophoric assemblies.

In conclusion, both experimental and theoretical results on dimer of A^+D and of A^+DA^+ chromophores suggest that electrostatic interchromophore interactions are responsible for sizeable effects on OPA and/or TPA frequencies, that can be easily rationalized based on simple essential-state models and a point-charge approximation for electrostatic interactions. However both OPA and TPA intensities are barely affected: for these classes of *charged* molecules, at variance with neutral DA dyes, we conclude that important cooperative/collective amplification or suppression of one- and two-photon absorption cross sections require unphysically large interchromophore interactions (i.e. unphysically small intermolecular distances).

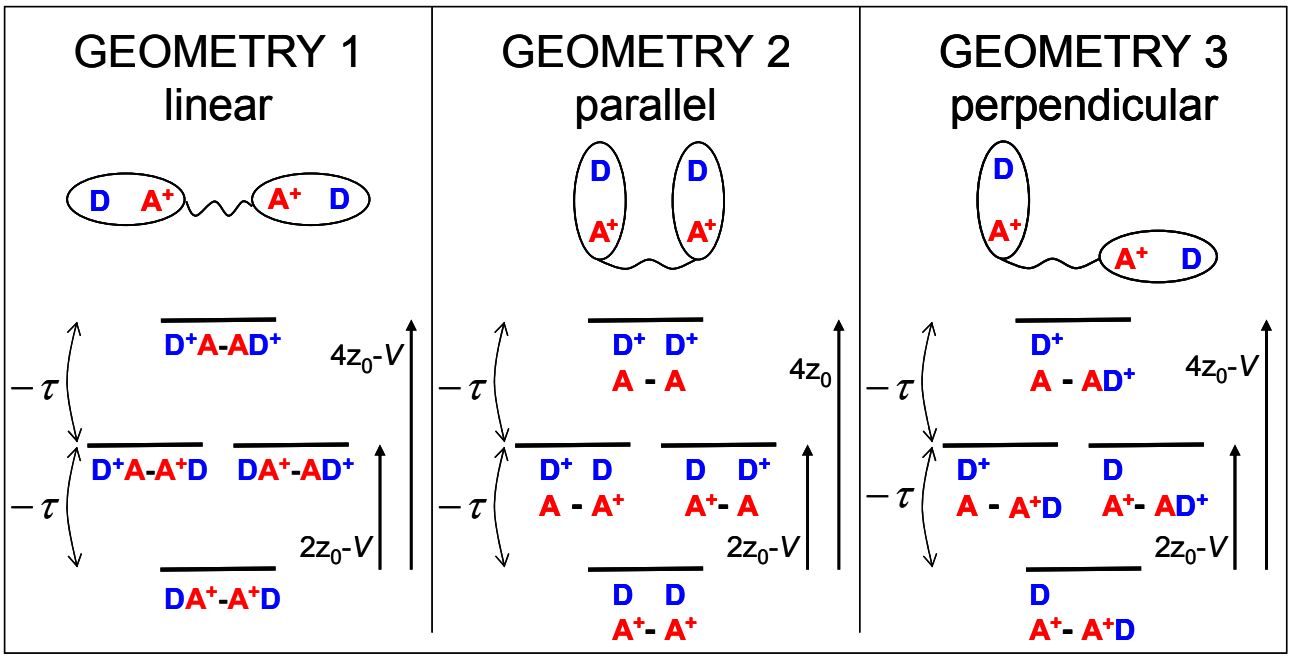

Fig. 2. Representation of the three geometries considered for **1-M** dimers and the corresponding schemes of energy levels.

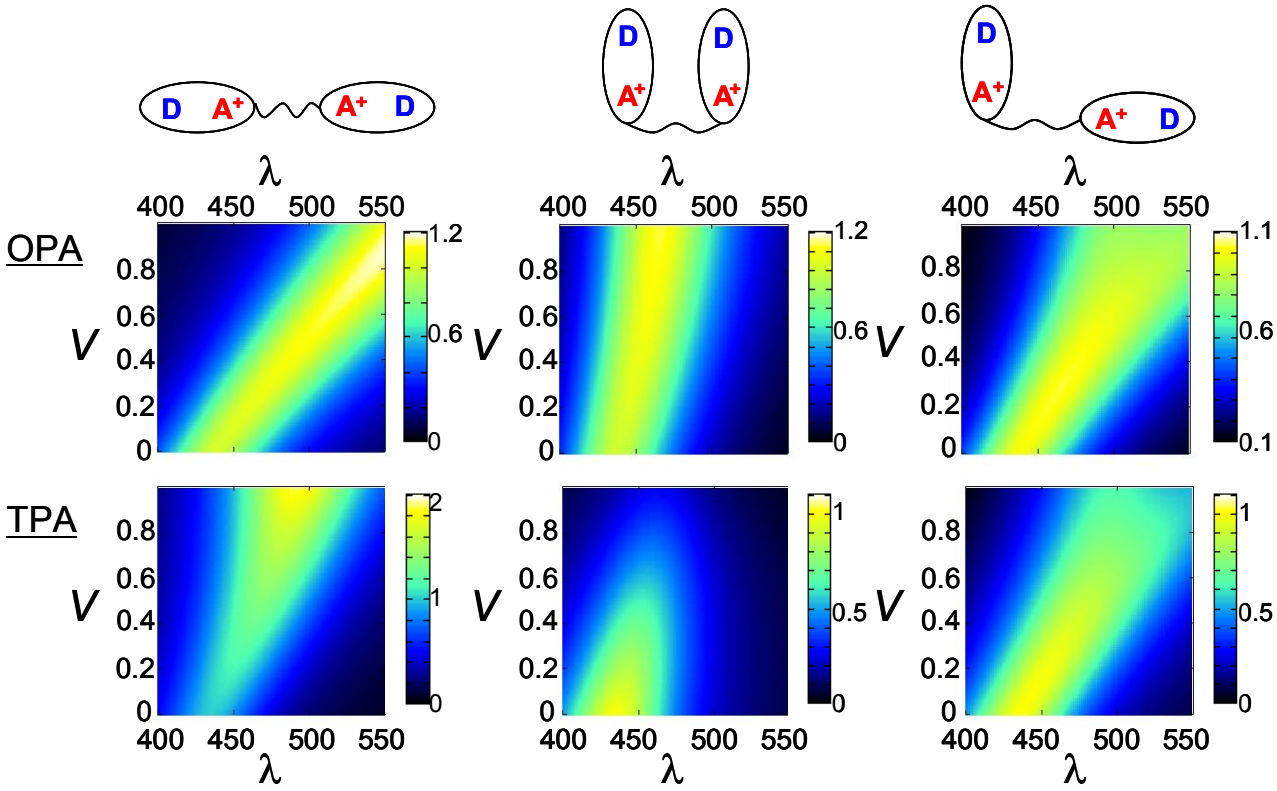

Fig. 3. Evolution of OPA and TPA spectra (top and bottom panels, respectively) with the strength of intermolecular electrostatic interaction, V (see text) calculated for three dimers of **1-M** in three different geometries. Molecular parameters for **1-M** are fixed as z = 1 eV, τ = 1 eV and Γ = 0.46 eV.

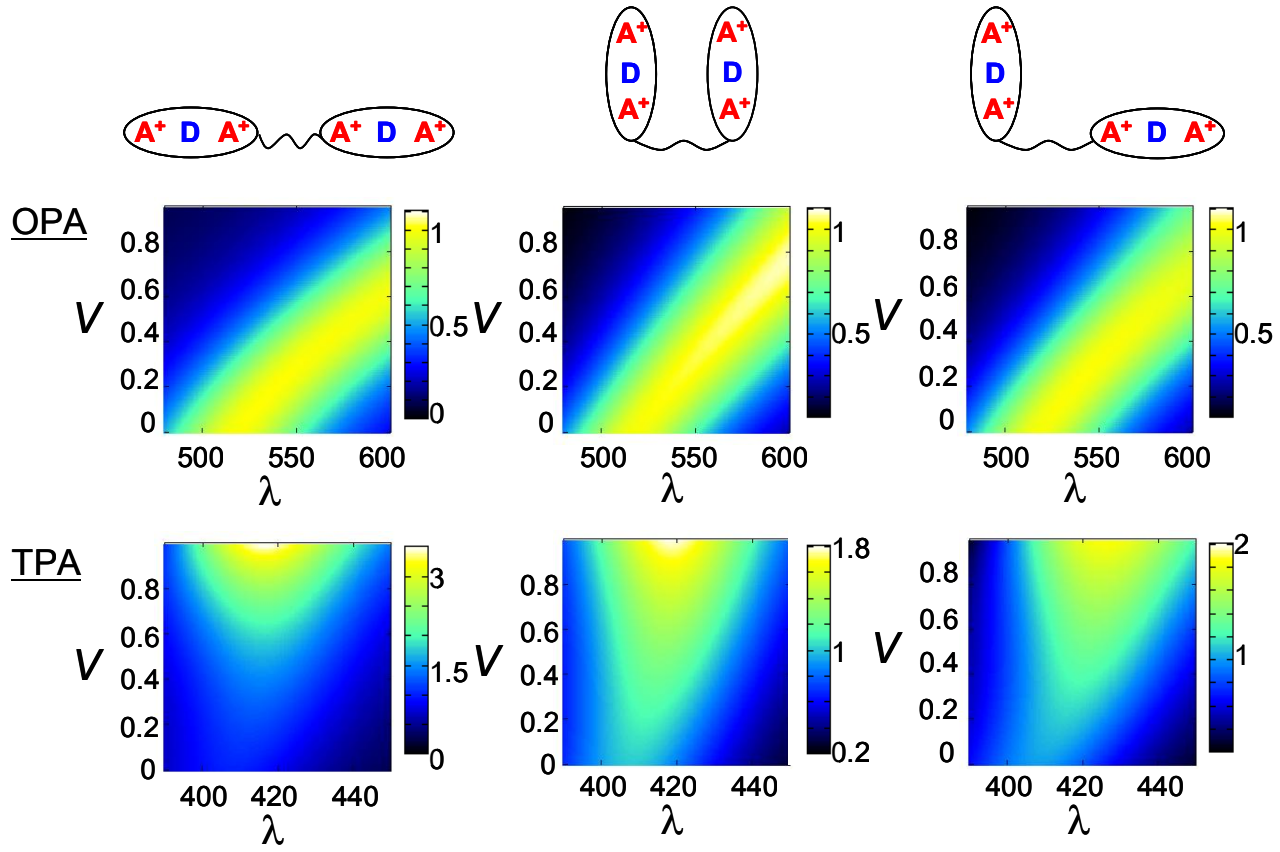

Fig. 4. Evolution of OPA and TPA spectra (top and bottom panels, respectively) with the strength of intermolecular electrostatic interaction, V (see text) calculated for three dimers of **2-M** in three different geometries. Molecular parameters for **2-M** are fixed as $z = 0.88$, $\tau = 0.87$, $\Gamma = 0.4$.

ACKNOWLEDGMENTS

Research was supported by MIUR-PRIN 2007-09 (Grant no. 2006031511).

REFERENCES

[1] a) *Molecular Nonlinear Optics*, Zyss, J., Ed.; Academic Press: New York, 1994; b) *Optical Nonlinearities in Chemistry*, Burland, D. M., Ed. *Chem. Rev.* **1994**, *94*, 1-278; c) Prasad, P.N.; Williams, D. J. *Introduction to Nonlinear Optical Effects in Molecules and Polymers*; Wiley: New York, 1991.

[2] Goppert-Mayer, M., "Elementary processes with two quantum jumps", Ann. Physik. 9, 273-294 (1931).

[3] Beverina, L., Fu, J., Leclercq, A., Zojer, E., Pacher, P., Barlow, S., Van Stryland, E., W., Hagan, D., J., Bredas, J., -L. and Marder, S., R., "Two-Photon Absorption at Telecommunications Wavelengths in a Dipolar Chromophore with a Pyrrole Auxiliary Donor and Thiazole Auxiliary Acceptor", J. Am. Chem. Soc. 127, 7282-7283 (2005).

[4] Albota, M., Beljonne, D., Bredas, J., L., Ehrlich, J., E., Fu, J., Y., Heikal, A., A., Hess, S., E., Kogej, T., Levin, M., D., Marder, S., R., Mccordmaughon, D., Perry, J., W., Rockel, H., Rumi, M., Subramaniam, C., Webb, W., W., Wu, I., L. and Xu, C., "Design of organic molecules with large two-photon absorption cross sections", Science 281, 1653-1656 (1998).

[5] Abbotto, A., Beverina, L., Bozio, R., Bradamante, S., Ferrante, C., Pagani, G., A. and Signorini, R., "Push-pull organic chromophores for frequency-upconverted lasing", Adv. Mater. 12, 1963-1967 (2000).

[6] Abbotto, A., Beverina, L., Bozio, R., Facchetti, A., Ferrante, C., Pagani, G., A., Pedron, D. and Signorini, R., "Novel Heterocycle-Based Two-Photon Absorbing Dyes", Org. Lett. 4, 1495-1498 (2002).

[7] a) Terenziani, F., D'Avino, G. and Painelli, A., "Multichromophores for Nonlinear Optics: Designing the Material Properties by Electrostatic Interactions", Chemphyschem 8, 2433-2444 (2007); b) D'Avino, G., Terenziani, F. and Painelli, A., "Aggregates of Quadrupolar Dyes: Giant Two-Photon Absorption from Biexciton States", J. Phys. Chem. B Condens. Matter Mater. Surf. Interfaces Biophys. 110, 25590-25592 (2006); c) Terenziani, F., Mongin, O., Katan, C., Bhattula, B., K., G. and Blanchard-Desce, M., "Effects of dipolar interactions on linear and nonlinear optical properties of multichromophore assemblies: a case study", Chemistry 12, 3089-3102 (2006); d) Terenziani, F., Morone, M., Gmouh, S. and Blanchard-Desce, M., "Linear and two-photon absorption properties of interacting polar chromophores: standard and unconventional effects", Chemphyschem 7, 685-696 (2006).

[8] a) Bradamante, S., Facchetti, A. and Pagani, G., A., "Heterocycles as donor and acceptor units in push-pull conjugated molecules. Part 1", J. Phys. Org. Chem. 10, 514-524 (1997); b) Abbotto, A., Beverina, L., Bradamante, S., Facchetti, A., Pagani, G., A., Bozio, R., Ferrante, C., Pedron, D. and Signorini, R., "Design and synthesis of heterocyclic multi-branched dyes for two-photon absorption", Synthetic Metals 139, 795-797 (2003).

[9] Abbotto, A., Beverina, L., Bozio, R., Facchetti, A., Ferrante, C., Pagani, G., A., Pedron, D. and Signorini, R., "Novel Heterocycle-Based Two-Photon Absorbing Dyes", Org. Lett. 4, 1495-1498 (2002).

[10] Likhosherstov, A., M., Peresada, V., P., Vinokurov, V., G. and Skoldinov, A., P., "Azacycloalkanes. XXXVII: 3,4-Dihydro-5H-pyrrolo[1,2-a]-diazepine and its conversions", Pharmac. Chem. J. 39, 504-507 (2005).

[11] Raghavan, S. and Rajender, A., "Stereoselective synthesis of (-)-allosedamine and (1R,3R)-HPA-12 from β-p-toluenesulfonamido-unsaturated sulfoxide", Tetrahedron 60, 5059-5067 (2004).

[12] a) Abbotto, A., Beverina, L., Pagani, G., A., Collini, M., Chirico, G., D'Alfonso, L. and Baldini, G., "Novel efficient and stable heteroaromatic two-photon absorbing dyes", SPIE Proceed. 5139, 223-230 (2003); b) Facchetti, A., Beverina, L., Van der Boom, M., E., Dutta, P., Evmenenko, G., Shukla, A., D., Stern, C., E., Pagani, G., A. and Marks, T., J., "Strategies for Electrooptic Film Fabrication. Influence of Pyrrole-Pyridine-Based Dibranched Chromophore Architecture on Covalent Self-Assembly, Thin-Film Microstructure, and Nonlinear Optical Response", J. Am. Chem. Soc. 128, 2142-2153 (2006).

[13] Rumi, M., Ehrlich, J. E., Heikal, A. A., Perry, J. W., Barlow, S., Hu, Z. Y., McCord-Maughon, D., Parker, T. C., Rockel, H., Thayumanavan, S., Marder, S. R., Beljonne, D. and Bredas, J. L., 'Structure-properties relationships for two-photon absorbing chromophores: Bis-donor diphenylene and Bis(styryl)benzene derivatives", J. Am. Chem. Soc. 122, 9500-9510 (2000).

[14] Xu, C., William, R. M., Zipfel, W. and Webb, W. W. "Multiphoton excitation cross-sections of molecular fluorophores", Bioimag., 4, 198 (1996).

[15] a) Painelli, A. "Vibronic contribution to static NLO properties: exact result for the DA dimer", Chem. Phys. Lett. 285, 352 (1998); b) Boldrini, B., Cavalli, E., Painelli, A. and Terenziani, F., "Polar Dyes in Solution: A Joint Experimental and Theoretical Study of Absorption and Emission Band Shapes", J. Phys. Chem. A 106, 6286-6294 (2002).

[16] Terenziani, F. , Painelli, A., Katan, C., Charlot, M. and Blanchard-Desce, M., "Charge instability in quadrupolar chromophores: symmetry-breaking and solvatochromism", J. Am. Chem. Soc. 128, 15742 (2006).

Dimers of Quadrupolar Chromophores in Solution: Electrostatic Interactions and Optical Spectra

Cristina Sissa,[†] Francesca Terenziani,[†] Anna Painelli,[†,*] Alessandro Abbotto,[‡,*] Luca Bellotto,[‡] Chiara Marinzi,[‡] Eleonora Garbin,[§] Camilla Ferrante,[§,*] and Renato Bozio[§]

Dip. Chimica GIAF, Università di Parma & INSTM UdR Parma, Parco Area delle Scienze 17/A, 43100 Parma, Italy, Dip. Scienza dei Materiali & INSTM, Università di Milano-Bicocca, via Cozzi 53, 20125 Milano, Italy, and Dip. Scienze Chimiche, Università di Padova & INSTM UdR Padova, Via Marzolo 1, 35131 Padova, Italy

Received: October 2, 2009; Revised Manuscript Received: November 26, 2009

Two dimers of a heteroaromatic quadrupolar (acceptor−donor−acceptor) chromophore have been synthesized with different interchromophoric distances. Optical spectra of dimers in solution show a red shift of the linear absorption band upon decreasing the interchromophore distance, while fluorescence and two-photon absorption spectra are only marginally affected by the interactions. A bottom up approach is adopted to describe the spectra: via a detailed spectroscopic analysis of the monomeric species in solution, we define an essential-state model for the isolated chromophore and use this information to set up a model for the dimers also accounting for interchromophore electrostatic interactions. To discriminate between static screening governed by the static dielectric constant and dynamical screening at optical frequencies, we first solve the problem in the mean-field approximation and then define the excitonic Hamiltonian on the resulting best excitonic basis. Along this line, the evolution of spectral properties with the interchromophore distance is properly rationalized.

1. Introduction

Polar and polarizable π-conjugated organic molecules have been extensively investigated in the past years for nonlinear optical (NLO) applications[1] such as electrooptic (EO) response[2] or two-photon absorption (TPA).[3] Such interest is justified by the potential use of these molecules in emerging photonic technologies, including broad-band communications and optical networking,[4] holographic memories,[5] two-photon laser scanning fluorescence microscopy,[6] optical limiting,[7] microfabrication,[8] photodynamic therapy,[9] and upconverted-lasing.[10] By far, the most successful design strategy involved π-conjugated molecules with electron donor (D) and acceptor (A) groups, and specifically, dipolar D-π-A, quadrupolar, D−π−A−π−D or A−π−D−π−A, and octupolar, D$(-\pi-A)_3$ or A$(-\pi-D)_3$, structures. On the basis of these concepts and with the guidance of relevant structure/property relationships,[11,12] several efficient dyes for NLO applications have been prepared in the past decade.[10,13–16]

In this context, some of us have designed, synthesized, and characterized a number of heteroaromatic-based dipolar dyes for EO,[17] and dipolar,[10] quadrupolar,[18] and octupolar dyes[19] for TPA. The design strategy was based on the efficient donor and accepting properties of π-excessive and π-deficient simple heteroaromatic rings.[20,21] 2,5-Bis[1-(4-*N*-methylpyridinium)ethen-2-yl)]-*N*-methylpyrrole ditriflate, **M** in Chart 1, is the most representative example of quadrupolar heteroaromatic dyes for TPA. This chromophore, with the pyrrole and the pyridinium rings acting as highly efficient D and A moieties, respectively, has a large TPA cross section[18] and found interesting applications in cellular imaging.[22]

CHART 1: Structure of the Model Chromophore and of the Dimers

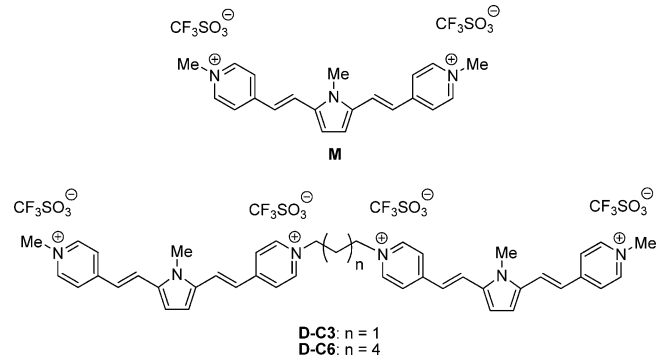

The vast majority of published studies on NLOphores is based on investigations in solution. The solvatochromism of polar (DA) chromophores has been known since 1994,[23] and the subtle effects of solvent polarity on linear and nonlinear spectra of DA chromophores have been investigated experimentally and modeled at different levels.[24,25] The anomalous solvatochromism observed in fluorescence spectra of quadrupolar and octupolar dyes has been recently explained in terms of solvent-induced symmetry breaking in the relaxed excited state.[26,27] More generally, dyes for NLO applications are largely polarizable and strongly respond to the charge distribution in the local environment.[28] Electrostatic intermolecular interactions are therefore expected to play a major role[28–30] in systems like molecular crystals,[31] films,[32] aggregates, or multichromophoric assemblies.[33,34] Possibly, one of the most impressive consequences of interchromophore interactions in clusters of dipolar dyes is the

* Corresponding author. E-mail: anna.painelli@unipr.it; alessandro.abbotto@unimib.it; camilla.ferrante@unipd.it.
† Università di Parma & INSTM UdR Parma.
‡ Università di Milano-Bicocca.
§ Università di Padova & INSTM UdR Padova.

10.1021/jp909475d
Published on Web 12/23/2009

occurrence of bistability in crystals of polar chromophores that, predicted in 2003,[29] was recently experimentally confirmed.[31]

If properly understood, interchromophore interactions offer a powerful tool to design new materials for NLO applications.[28–30] Of interest in this respect is the work done on properly engineered molecules where two or more chromophores are held together by chemical bonds: linear and nonlinear optical spectra of such multichromophoric assemblies confirmed the importance of electrostatic interactions in optical spectra.[33,34] Essential-state models for the chromophoric units[25–27] offer a general and comparatively simple scheme to describe linear and nonlinear optical properties of multichromophores, accounting for electrostatic interactions as well as for molecular vibrations and polar solvation. Modeling electrostatic interchromophore interactions while accounting for the screening from polar solvents is, however, a delicate issue.[33a,34] In the simplest approximation, two different regimes can be considered for screening. The first one corresponds to a static (or quasi static) regime: in this regime the dynamics of screened charges is much slower than all relevant degrees of freedom of the solvent, so that the screening factor is properly described by the static dielectric constant of the solvent. The second regime applies to charges with a characteristic dynamics faster than the slow (orientational, vibrational) degrees of freedom of the solvent, but slower than the fast (electronic) degrees of freedom of the solvent. In this regime, typically corresponding to optical frequencies, interactions are screened by the squared refractive index (usually measured at the sodium D line). The difference between the two screening factors is minor in nonpolar or mildly polar solvents (see as an example data in Table 1) but is very large in polar solvents ($\varepsilon/n^2 \approx 22$ for DMSO). It is therefore important to devise methods that distinguish between static interactions, like, e.g., those that determine the ground-state charge distribution in the chromophore, and dynamic interactions, like the interactions between transition dipole moments.

So far, studies on interacting chromophores for NLO have been limited to dipolar dyes. No systematic studies on discrete multichromophoric assemblies of quadrupolar dyes and on their TPA properties have been reported in the literature. This represents a strong limitation in the present investigation on TPA (multi)chromophores if one considers that quadrupolar systems are generally much more efficient two-photon absorbers than corresponding D−π−A dyes. On the basis of these premises, we present a detailed experimental and theoretical analysis of linear and nonlinear (TPA) optical properties of bichromophoric assemblies of quadrupolar dyes. To such an aim, two dimers of **M** have been synthesized where the two **M** units are joint by saturated hydrocarbon chains of different length (saturated alkyl chains having three and six carbon atoms, for **D-C3** and **D-C6**, respectively; see Chart 1). The absence of π bonds in the linking chain ensures the lack of conjugation between the two units, whereas the different length is included to control interchromophore distances. **M** bears two positive charges, and electrostatic interactions are expected to be important even in the ground state. Moreover, the two molecular arms of each **M** unit become nonequivalent in the dimer, and such symmetry lowering may induce relevant spectroscopic consequences. A proper description of the screening from the solvent becomes crucial under these conditions.

Our discussion starts with the spectroscopic analysis of **M**, whose linear absorption, fluorescence, and TPA spectra were collected in solution: a detailed analysis of these data allows the definition of a reliable essential-state model for the **M**-unit, which properly accounts for the role of molecular vibrations and polar solvation. This model sets the basis to describe interacting chromophores in the dimeric structures. Solution spectra of **D-C3** and **D-C6** dimers show an intriguing behavior: the red shift of the absorption band upon dimerization evidence sizable interchromophore interactions, while fluorescence and TPA spectra are basically unaffected by dimerization. To rationalize such behavior, on the basis of the model developed for **M**, we describe the dimer accounting for interchromophore interactions and for the coupling with slow degrees of freedom. The model is first solved in the mean-field approximation for the ground state: only static charges enter in this approximation, so that, at this stage, all interactions are screened by the static dielectric constant. The diagonalization of the mean-field problem quite naturally leads to the definition of the excitonic basis: residual electrostatic interactions in this basis describe interactions between charge distributions oscillating at optical frequencies and are screened by the squared refractive index. Along these lines we rationalize linear and nonlinear absorption spectra. The calculation of fluorescence spectra is more delicate, due to relaxation of the molecular geometry in the excited state. A mean-field approximation to the first excited state suggests the localization of the excited state and quite naturally explains the insensitivity of fluorescence spectra to interchromophore interactions.

SCHEME 1: Synthesis of the dimers D-C3 and D-C6

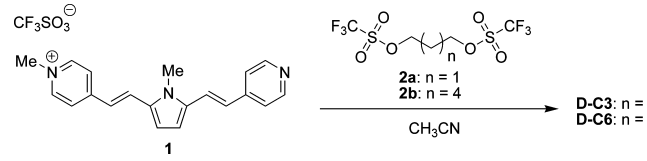

2. Experimental Section

2.1. Chromophores: General Information. NMR spectra were recorded on a Bruker AMX-500 instrument operating at 500.13 (^{1}H) and 125.77 MHz (^{13}C). Coupling constants are given in hertz. High resolution mass spectra (HRMS) were recorded using a Bruker Daltonics ICR-FTMS APEX II spectrometer equipped with an electrospray ion source (ESI). All reagents and solvents, including anhydrous solvents, were obtained from commercial suppliers and used without further purification. Reactions were monitored by thin layer chromatography using UV light (254 and 365 nm) as visualizing agent. Melting points are uncorrected. All reactions were performed in oven-dried glassware under nitrogen.

2.2. Chromophores: Synthesis. The monomer **M** was prepared according to the literature.[18] The bichromophores **D-C3** and **D-C6** were synthesized according to Scheme 1. Two equivalents of the monotriflate precursor **1**[35] were submitted to alkylation with 1 equiv of α,ω-bis(trifluoromethansulfonyl)alkane **2a**[36] or **2b**[36] in acetonitrile at room temperature, affording the expected products as dark violet solids in 70−80% yield. The quadruple saline nature (four formal positive and four formal negative charges) of the bichromophores does not make the common isolation and purification procedures (e.g., chromatography) viable. Therefore, stronger electrophiles (triflates rather than commercially available halides) needed to be synthesized for the final alkylation step, to reach high conversion yields and no presence of byproduct. Purification of the two dimers was accomplished by crystallization.

1,2-Bis{4-{{N-methyl-5-[1-(N-methylpyrid-4-yl)ethen-2-yl]pyrrol-2-yl}-ethen-2-yl}pyridinium}propane Tetratrifluoromethanesulfonate (D-C3). Trifluoromethanesulfonic anhydride (1.60 g, 954 μL, 5.67 mmol) was added dropwise to an ice cold solution

of 1,3-propanediol (0.20 g, 2.63 mmol) in anhydrous CH_2Cl_2 (20 mL), and the resulting mixture was stirred for 2 h at 0 °C. Saturated aqueous K_2CO_3 (150 mL) and CH_2Cl_2 (150 mL) were added, and the layers were separated. The aqueous layer was extracted with CH_2Cl_2 (3 × 150 mL), and the combined organic layers were dried (Na_2SO_4) and evaporated under reduced pressure, affording **2a** as a colorless oil, which was used without further purification for the next reaction (653 mg, 1.92 mmol, 73%). A solution of **1** (0.903 g, 2.00 mmol) in dry CH_3CN (45 mL) was added dropwise to a solution of ditriflate **2a** (0.34 g, 1.0 mmol) in the same solvent (35 mL), and the resulting mixture was stirred for 6 h. After cooling to 0 °C, a precipitate was obtained and collected upon filtration to afford **D-C3** as a purple solid which was submitted to recrystallization from *i*-PrOH (1.01 g, 0.81 mmol, 81%), mp >250 °C. ^{1}H NMR (DMSO-d_6): δ 8.78 (d, J = 6.4, 4 H), 8.73 (d, J = 6.4, 4 H), 8.19 (d, J = 6.4, 4 H), 8.13 (d, J = 6.4, 4 H), 8.00 (d, J = 15.8, 2 H), 7.97 (d, J = 15.8, 2 H), 7.31 (d, J = 15.7, 2 H), 7.25 (d, J = 15.8, 2 H), 7.13 (d, J = 4.4, 2 H), 7.10 (d, J = 4.4, 2 H), 4.59 (t, J = 6.8, 4 H), 4.22 (s, 6 H), 3.91 (s, 6 H), 2.65 (quintuplet, J = 6.8, 2 H). ^{13}C NMR (DMSO-d_6): δ 153.7 (C), 152.9 (C), 145.0 (CH), 144.2 (CH), 136.3 (C), 136.0 (C), 129.0 (CH), 128.4(CH), 123.5 (CH), 123.2 (CH), 121.9 (CH), 121.5 (CH), 114.2 (CH), 114.0 (CH), 57.0 (CH_2), 47.1 (CH_3), 31.4 (CH_2), 31.3 (CH_3). Anal. Calcd for $C_{47}H_{46}F_{12}N_6O_{12}S_4 \cdot 2H_2O$: C, 44.13; H, 3.94; N, 6.57. Found: C, 44.10; H, 4.03; N, 6.75.

1,2-Bis{4-{{N-methyl-5-[1-(N-methylpyrid-4-yl)ethen-2-yl]pyrrol-2-yl}ethen-2-yl}pyridinium}hexane Tetratrifluoromethanesulfonate (D-C6). Trifluoromethansulfonic anhydride (0.99 g, 590 μL, 3.5 mmol) was added dropwise to an ice cold solution of 1,6-hexanediol (450 mg, 1.60 mmol) in CH_2Cl_2 (20 mL) and the resulting mixture was stirred for 2 h at 0 °C. Saturated aqueous K_2CO_3 (100 mL) and CH_2Cl_2 (100 mL) were added, and the layers were separated. The aqueous layer was extracted with CH_2Cl_2 (3 × 100 mL), and the combined organic layers were dried and evaporated under reduced pressure affording **2b** as a colorless oil, which was used without further purification for the next reaction (500 mg, 1.36 mmol, 85%). A solution of **1** (1.26 g, 2.79 mmol) in CH_3CN (30 mL) was added dropwise to a solution of ditriflate **2b** (500 mg, 1.36 mmol) in the same solvent (25 mL), and the resulting mixture was stirred for 6 h. After cooling to 0 °C, a precipitate was obtained and collected upon filtration to afford **D-C6** as a purple solid, which was submitted to recrystallization from *i*-PrOH (1.31 g, 1.02 mmol, 75%), mp >250 °C. ^{1}H NMR (DMSO-d_6): δ 8.82 (d, J = 6.8, 4 H), 8.75 (d, J = 6.8, 4 H), 8.20 (d, J = 6.9, 4 H), 8.17 (d, J = 6.8, 4 H), 8.02 (d, J = 16.0, 2 H), 8.00 (d, J = 16.0, 2 H), 7.32 (d, J = 16.0, 2 H), 7.29 (d, J = 16.0, 2 H), 7.12 (s, 4 H), 4.45 (t, J = 7.3, 4 H), 4.21 (s, 6 H), 3.96 (s, 6 H), 1.92 (bs, 4 H), 1.35 (bs, 4 H). ^{13}C NMR (DMSO-d_6): δ 153.4 (C), 152.9 (C), 145.0 (CH), 144.1 (CH), 136.2 (C), 136.0 (C), 128.8 (CH), 128.5 (CH), 123.5 (CH), 123.2 (CH), 121.8 (CH), 121.6 (CH), 114.1 (CH), 114.0 (CH), 59.8 (CH_2), 47.1 (CH_3), 31.3 (CH_3), 30.7 (CH_2), 25.4 (CH_2). Anal. Calcd for $C_{50}H_{52}F_{12}N_6O_{12}S_4 \cdot 3H_2O$: C, 44.84; H, 4.37; N, 6.28. Found: C, 44.55; H, 4.28; N, 5.95.

2.3. Spectroscopic Measurements. Spectroscopic grade solvents were obtained by Aldrich. UV/vis spectra were collected on a Perkin-Elmer Lambda 650 spectrophotometer. Emission spectra at room temperature were recorded using a Horiba Jobin Ivon FluoroMax-3 spectrophotometer on dilute solutions (typical concentrations ~10^{-6} M). Fluorescein in NaOH 0.1 M was used as a standard (Φ = 0.9) to estimate fluorescence quantum yields. Fluorescence spectra were collected by exciting at the maximum of absorption. Fluorescence and fluorescence-excitation spectra at low temperature were measured using a liquid nitrogen cooled optical cryostat (OptistatDN, Oxford Instrument) equipped with temperature controller (ITC601, Oxford Instrument).

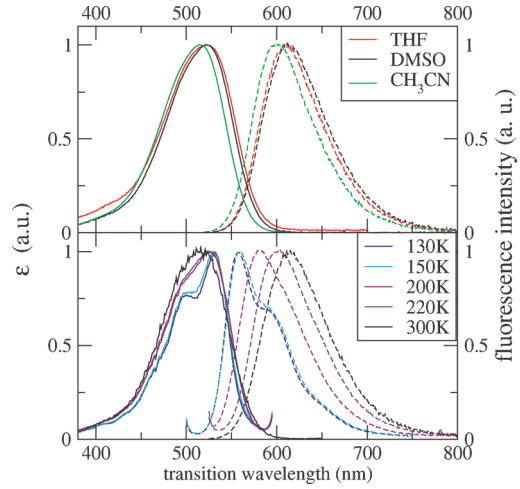

Figure 1. Top panel: absorbance (continuous lines) and fluorescence (dashed lines) spectra of **M** in three solvents of different polarity. Bottom panel: temperature evolution of absorption and fluorescence spectra of **M** in DMSO.

The TPA properties of all compounds were investigated in DMSO by the two-photon induced fluorescence (TPIF) technique.[12d] Typical concentrations for the solutions are in the range 5 × 10^{-6} to 2 × 10^{-5} M. TPIF experiments were performed using 150 fs pulses delivered from a tunable Ti:sapphire femtosecond laser system (Coherent Mira 900-F) at 76 MHz repetition rate. The TPIF excitation spectra are recorded from 740 to 930 nm with 10 nm steps. The laser beam was focused on the sample cell (a 10 mm quartz cell), via a 40 cm focal length lens. The fluorescence spectra excited by one- and two-photon excitation fell in the same spectral region, confirming that the emitting states are the same for both processes. Therefore, in the following analysis, we assume the same fluorescence quantum yield for both one- or two-photon excitation. TPA cross sections were evaluated following the procedure described in the literature[12d] and using a ~10^{-5} M solution of fluorescein in water at pH >10 (0.1 M NaOH) as a reference standard.

3. Optical Spectra of M: Essential-State Model

Due to its multisaline nature, **M** is poorly soluble in nonpolar solvents. The top panel of Figure 1 shows absorption and fluorescence spectra of **M** collected in THF (tetrahydrofuran), DMSO (dimethyl sulfoxide), and CH_3CN (acetonitrile). Figure 2 shows the TPA spectrum collected in DMSO. Table 2 summarizes experimental results for DMSO solutions. As expected for quadrupolar chromophores,[12,26] the TPA state is located at higher energies than the OPA state. The physical properties of the three solvents (dielectric constant and refractive index) are reported in Table 1: THF is a medium polarity solvent to be compared with the strongly polar DMSO and acetonitrile. We assume that the ion pairs exist as solvated free ions or solvent-separated ion pairs rather than contact ion pairs.[37] This is supported by the dissociating properties of the strongly polar DMSO and acetonitrile solvents. The similarity of optical spectra collected in THF and DMSO suggest that the same hypothesis applies in this solvent as well. Absorbance and fluorescence spectra in Figure 1a are marginally affected by the polarity of

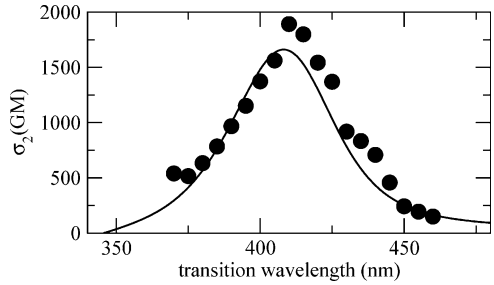

Figure 2. TPA spectrum of **M** in DMSO. Symbols show experimental data; the line represents the spectrum calculated using the model parameters in Table 3. Literature data for **M** (ref 18c) were affected by a systematic error caused by defective calibration of the fluorescence spectrometer.

TABLE 1: Dielectric Constant (ε) and Refractive Index (n) of the Solvents

solvent	ε	n
THF	7.6	1.405
CH_3CN	35.9	1.342
DMSO	46.5	1.478

TABLE 2: Spectroscopic Data for M, D-C6, and D-C3 in DMSO Solution

	λ_{abs} (nm)[a]	λ_{em} (nm)[a]	ε (cm^{-1} M^{-1})[a–c]	Φ (%)[c,d]	λ_{TPA} (nm)[a]	σ_{TPA} (GM)[a,d]
M	522	612	70 300	36	410−415	1892
D-C6	527	613	68 500	35	410−415	1857
D-C3	532	615	61 500	5.1	410−415	1807

[a] All data refer to the band maxima. [b] One- and two-photon absorption intensities are given per chromophore unit. [c] Experimental uncertainty does not exceed ±5% for ε, ± 10% for Φ, ±20% for σ_{TPA}. [d] Fluorescence quantum yield, obtained using fluorescein in NaOH 0.1 M ($\Phi = 0.9$) as a reference compound.

the solvent, suggesting that both the ground and the excited (fluorescent) states of **M** maintain a nonpolar structure: **M** is therefore classified as a class II quadrupolar dye.[26] However, when compared with spectra of typical class II quadrupolar dyes, like the squaraine dyes,[26] spectra in Figure 1a show an important Stokes-shift, suggesting that the model previously proposed for optical spectra of quadrupolar dyes[26] must be extended to account for other slow degrees of freedom in **M**. The insensitivity of the Stokes shift to the solvent polarity suggests that it is related to some internal degree of freedom not breaking the molecular symmetry. Further support to the intramolecular nature of the Stokes-shift is offered by thermochromic data in Figure 1b. The Stokes shift observed in the frozen DMSO solution at 220 K (DMSO melts at 292 K) is similar to that measured at room temperature and, in the frozen solvent, cannot be ascribed to the reorientation of solvent molecules. A sharp reduction of the Stokes shift is observed at about 150 K, where both absorption and fluorescence spectra acquire a well-developed vibronic structure. Optical spectra are only marginally affected by a further decrease of T down to 130 K. This behavior is consistent with the presence of a slow vibrational or conformational mode whose relaxation at high enough temperature is responsible for the observed Stokes shift as well as for the broadening of optical spectra. At low temperatures, this conformational mode is frozen out, resulting in a sharp reduction of both the Stokes shift and of the inhomogeneous broadening. With these considerations in mind, we propose here an essential-state model for optical spectra of **M** that represents an extension of the model originally presented in ref 26 to account for the presence of a conformational degree of freedom.

The presence of two equivalent arms in **M** immediately suggests the presence of two excited states with different symmetry. As for other multibranched chromphores,[12e] an excitonic picture of the intramolecular excitations offers a first understanding of electronic spectra. The model introduces a phenomenological interaction, J, between the two degenerate excitations in the left and right arms. As a result, the two states split into an antisymmetric and a symmetric state, whose relative energy depends on the sign of J. The two states are OPA- and TPA-active, respectively. Excitonic models were originally developed to account for intermolecular interactions in molecular aggregates and crystals.[38] In these applications, optical spectra of the isolated molecules yield information on molecular transition energies and dipole moments. Therefore, only the interaction energy J enters the model as an adjustable parameter. On the opposite, when excitonic models are applied to multibranched chromophores, the definition of excitations energies and transition dipole moments relevant to the single molecular arms is a delicate issue. As a result, most often all model parameters are freely adjustable in excitonic descriptions of multibranched chromophores.[12e] Moreover, excitonic models rely on the implicit assumption that the nature of the ground state is not affected by the interaction with the surrounding.[38] This is a poor approximation for highly polarizable and hyperpolarizable molecules like **M** and, more generally, for molecules where charge-transfer degrees of freedom play a role. In fact, in these systems the weight of charge-separated states in the ground state changes with the polarity of the local molecular environment, heavily affecting the nature of the ground as well as of the local excited states. As a consequence, different excitonic models should be defined for the same molecule in different environments, leading to a proliferation of model parameters. To overcome these difficulties and to develop a sound understanding of environmental effects on molecular spectra, in recent years some of us have developed a different strategy to describe optical spectra of dipolar and multipolar chromophores.[25–27] The approach is rooted in the well-known Mulliken model for charge-transfer excitations in molecular complexes.[39] The idea is simple and general: the low-energy states of dipolar and multipolar chromophores are dominated by charge-transfer resonances (e.g., $DA \leftrightarrow D^+A^-$ in dipolar dyes, $D^+A^-D \leftrightarrow DAD \leftrightarrow DA^-D^+$ in quadrupolar dyes, etc.). The relevant resonance structures are then chosen as basis states in the description of the system, so that the ground and excited states are expressed as linear combinations of the charge-resonating states. The nature of the ground and excited states, i.e., the weight of the resonating structures, is not fixed from the outset and, for each molecule, it readjusts in response to the local environment. The resulting families of models proved extremely powerful and were successfully applied to understand linear and nonlinear optical spectra of dipolar and multibranched chromophores in different environments.[25–34]

M is a doubly charged quadrupolar dye, whose low-energy physics can be understood accounting for the resonance between the three limiting structures: $AD^+A^+ \leftrightarrow A^+DA^+ \leftrightarrow A^+D^+A$. In the spirit of essential state models, we represent these main resonating structures in terms of three states that define the minimal basis set to describe the electronic structure of **M**. The symmetrical A^+DA^+ state, φ_0, is the lowest-energy state and plays the same role as the so-called $|N\rangle$ state in neutral quadrupolar dyes (see ref 26). Two degenerate states, φ_c and φ_s (the rationale for the c and s lettering will be clear in the next section), correspond to AD^+A^+ and A^+D^+A, respectively, and represent states where an electron is transferred from the

central donor toward one of the two lateral acceptor groups. Accordingly, a matrix element $-2^{1/2}t$ mixes φ_0 with either φ_c or φ_s to account for the finite probability of electron hopping along each molecular arm. The two degenerate states, φ_c and φ_s, play the same role as $|Z1\rangle$ and $|Z2\rangle$ in ref 26 and are separated from φ_0 by an energy gap 2η. The electronic Hamiltonian reads

$$H_{el} = -\sqrt{2}t(\hat{\sigma}_c + \hat{\sigma}_s) + 2\eta(\hat{\rho}_c + \hat{\rho}_s) \quad (1)$$

where

$$\begin{aligned}
\hat{\rho}_c &= |AD^+A^+\rangle\langle AD^+A^+| \\
\hat{\rho}_s &= |A^+D^+A\rangle\langle A^+D^+A| \\
\hat{\sigma}_c &= |A^+DA^+\rangle\langle AD^+A^+| + |AD^+A^+\rangle\langle A^+DA^+| \\
\hat{\sigma}_s &= |A^+DA^+\rangle\langle A^+D^+A| + |A^+D^+A\rangle\langle A^+DA^+|
\end{aligned} \quad (2)$$

In principle, the dipole moment of charged species is ill defined; however, we take advantage of the symmetric nature of **M** and describe its charge distribution in terms of a monopole and a dipole located in the molecular center. Because the monopole is invariant in all basis states, it becomes irrelevant in the discussion of solvation. On the opposite, the dipole moment vanishes in state φ_0, while φ_c and φ_s have equal and opposite dipole moments of magnitude μ_0. This dipole moment refers to states where an electronic charge is displaced along one of the molecular arms: μ_0 is therefore very large and, following Mulliken,[39] we neglect all other matrix elements of the dipole moment operator on the chosen basis. Under this approximation the dipole moment operator reads: $\hat{\mu} = \mu_0(\hat{\rho}_c - \hat{\rho}_s)$.

When an electron is transferred from the central donor toward one of the two acceptors, the relevant molecular arm relaxes: to account for this relaxation we introduce two effective molecular vibrations, q_c and q_s, with the same frequency, ω_v, and relaxation energy, ε_v.[26] Polar solvation enters the model with a reaction field, F_R, which measures the electric field generated at the solute location by the reorientation of polar solvent molecules. F_R describes a very slow motion and can be treated as a classical adiabatic coordinate. The relevant relaxation energy, ε_{or}, increases with the solvent polarity.[25] The electronic component of the reaction field, related to the deformation of the electronic charge distribution in solvent molecules surrounding the solute, corresponds instead to a fast motion with respect to the relevant degrees of freedom of the solute. It therefore enters the model with a renormalization of model parameters that, in the simplest approximation, acquire a dependence on the solvent refractive index.[25]

The Hamiltonian describing the three electronic states coupled to the two molecular coordinates and to the reaction field was derived in ref 26. However, the large and solvent-independent Stokes shift observed at room temperature cannot be reproduced unless an additional slow degree of freedom is introduced. The insensitivity of the observed Stokes shift on the solvent polarity suggests that the relevant mode corresponds to a molecular deformation. Therefore, we introduce an effective conformational coordinate, Q, with frequency ω_Q and relaxation energy ε_Q. The total Hamiltonian reads

$$\begin{aligned}
H = H_{el} &- \omega_v\sqrt{2\varepsilon_v}q_c\hat{\rho}_c - \omega_v\sqrt{2\varepsilon_v}q_s\hat{\rho}_s - \omega_Q\sqrt{2\varepsilon_Q}Q(\hat{\rho}_c + \hat{\rho}_s) - \\
&\mu_0F_R(\hat{\rho}_c - \hat{\rho}_s) + \frac{1}{2}(\omega_v{}^2q_c{}^2 + p_c{}^2) + \frac{1}{2}(\omega_v{}^2q_s{}^2 + p_s{}^2) \\
&+ \frac{1}{2}\omega_Q{}^2Q^2 + \frac{\mu_0{}^2}{4\varepsilon_{or}}F_R{}^2
\end{aligned} \quad (3)$$

where H_{el} is the electronic Hamiltonian in eq 1, the second and third terms describe the linear coupling of electrons to molecular vibrations, and the fourth and fifth terms describe the coupling to the conformational coordinate and to the polar reaction field. The last four terms describe the harmonic oscillators associated with the four slow degrees of freedom: we explicitly account for the kinetic energy associated with molecular vibrations (p_c and p_s are the conjugated momenta to q_c and q_s, respectively), while the conformational coordinate Q and the solvation reaction field, F_R, are treated in the adiabatic approximation, and the relevant kinetic energy is disregarded. We assume that the two vibrational frequencies ω_v and ω_Q entering the Hamiltonian do not change with the basis state, so that the two basis states are assigned two harmonic potential energy surfaces with equal curvature but displaced minima. In other terms, we account for linear electron-vibration coupling, neglecting higher order, and quadratic terms. Assigning different frequencies to the two basis states would not alter the main physics of the system[25c-e] and would have negligible spectroscopic effects, particularly in view of the lack of resolved vibronic structure in experimental spectra.

In the isolated **M** unit the two molecular arms are equivalent and it is convenient to define symmetrized basis states, $|Z_\pm\rangle = (\varphi_c \pm \varphi_s)/2^{1/2}$, and vibrational coordinates: $q_\pm = (q_c \pm q_s)/2^{1/2}$. Only the symmetrical $|Z_+\rangle$ state is mixed to φ_0, while $|Z_-\rangle$ stays unmixed. On this basis, the electronic Hamiltonian, dependent on slow coordinates, reads

$$H_{el}^{(M)}(q_+,q_-,\tilde{Q},F_R) = \begin{pmatrix} 0 & 2t & 0 \\ 2t & 2\eta - \omega_v\sqrt{\varepsilon_v}q_+ - \sqrt{\varepsilon_Q}\tilde{Q} & -\omega_v\sqrt{\varepsilon_v}q_- - \mu_0F_R \\ 0 & -\omega_v\sqrt{\varepsilon_v}q_- - \mu_0F_R & 2\eta - \omega_v\sqrt{\varepsilon_v}q_+ - \sqrt{\varepsilon_Q}\tilde{Q} \end{pmatrix} \quad (4)$$

where the renormalized coordinate, $\tilde{Q} = \omega_Q Q$, is introduced to eliminate any explicit reference to the conformational frequency, ω_Q, that becomes irrelevant in the adiabatic approximation.

Both F_R and $\tilde{Q}$ are treated as classical coordinates, while q_+ and q_- are treated exactly, i.e., via a numerical diagonalization of the nonadiabatic Hamiltonian. Specifically, eq 1 defines, for fixed $\tilde{Q}$ and F_R values, a Hamiltonian that describes the electrons coupled to molecular vibrations. The relevant Hamiltonian matrix can be written and numerically diagonalized on a basis obtained as the direct product of the three electronic basis states (φ_0, $|Z_+\rangle$, and $|Z_-\rangle$) times the eigenstates of the two harmonic oscillators described by the sixth and seventh terms in the right-hand side of eq 1.[26] The infinite vibrational basis is truncated to include a finite number of vibrational states for each oscillator, leading to a basis of dimension $3N^2$, where N is the number of phonon states included in the basis for each oscillator. Results reported here were typically obtained setting $N = 7$. The results are not affected upon a further increase of N. Linear absorption and fluorescence spectra and two-photon absorption spectra are calculated from the resulting eigenvectors as described in detail in ref 26. The calculation is repeated for different $\tilde{Q}$ and F_R values. Resulting spectra are summed up by weighting each

TABLE 3: Essential-State Model Parameters for M

η	0.95 eV
$2^{1/2}t$	0.87 eV
ω_v	0.12 eV
ε_v	0.15 eV
ε_Q	0.25 eV
μ_0	22 D
Γ	0.1 eV
ε_{or}	THF 0.1 eV DMSO 0.25 eV

spectrum on the basis of the Boltzmann population: the ground-state energy is used to calculate populations relevant to absorption spectra, whereas fluorescence spectra are weighted on the basis of the Boltzmann population relevant to the fluorescent state.[26]

Table 3 lists the model parameters for **M**, chosen to reproduce absorption and fluorescence spectra in THF and DMSO and its TPA spectra in DMSO. Calculated spectra depend in a highly nonlinear way on the model parameters, and the optimization procedure goes via trial and error. The vibrational frequency, ω_v, and the intrinsic line width, Γ (see ref 26), have minor spectroscopic effects in view of the unresolved vibronic structure of experimental bands. Therefore, they have been fixed to reasonable values by comparison with similar systems. μ_0 only affects the intensity of the absorption spectra, while the shape and the position of absorption and fluorescence spectra show a complex interdependence on the two electronic parameters, $2^{1/2}t$ and η, and on the relaxation energies, ε_v and ε_Q. The solvent polarity plays a minor spectroscopic role in **M**, resulting in large uncertainties in the ε_{or} estimates. Calculated linear spectra are shown in Figure 3, to be compared with experimental data in the top panel of Figure 1. Calculated TPA spectra are compared with experimental data in Figure 2. We stress that all molecular parameters, including the intrinsic line width, are kept fixed in the simulations, *independent* of the solvent: only the solvent relaxation energy is tuned to account for the solvent polarity.

Both absorption and fluorescence spectra collected in CH_3CN are slightly blue-shifted with respect to spectra measured in DMSO, in spite of the similar dielectric constant of the two solvents. This anomalous behavior can be ascribed to the different refractive index of the two solvents: the smaller refractive index of CH_3CN suggests a lower stabilization of ionic states with respect to the other solvent and hence an increased η value.[25] Indeed, spectra collected in acetonitrile are very well reproduced using the same model parameters adopted for DMSO (including ε_{or}), but a slightly larger $\eta = 0.99$ eV (cf. Figure 3). We did not attempt a detailed analysis of the temperature dependence of spectra collected in DMSO in Figure 1b. In fact, both the solvent dielectric constant and refractive index depend on temperature so that not only the solvent relaxation energy (ε_{or}) but also η should be adjusted at each temperature, leading to an excessive proliferation of model parameters.

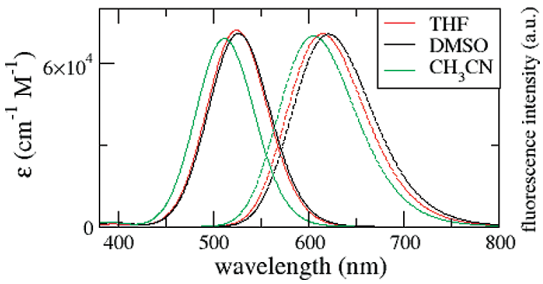

Figure 3. Calculated absorption and fluorescence spectra (continuous and dashed lines, respectively) of **M** using the model parameters listed in Table 3 (THF and DMSO). For CH_3CN we adopt the same model parameters as for DMSO with the exception of $\eta = 0.99$ eV.

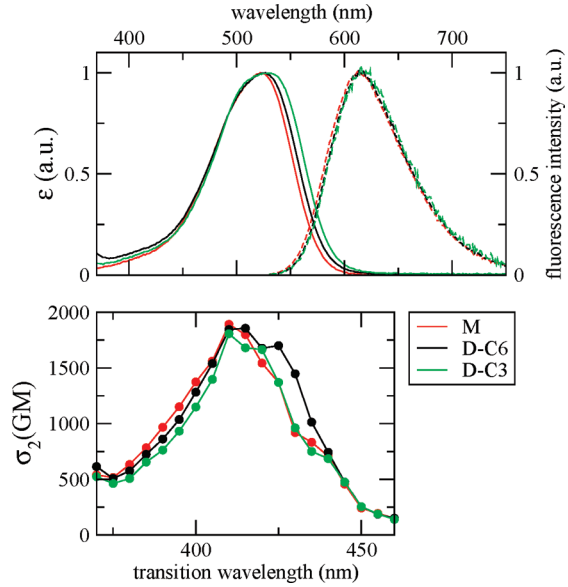

Figure 4. Optical spectra of solutions of **M**, **D-C6**, and **D-C3** in DMSO. Top panel: absorption and fluorescence spectra are shown as continuous and dashed lines, respectively; all spectra are normalized to 1. Bottom panel: dots report TPA spectra; lines are drawn as guides to the eyes. The *x*-axis is the wavelength of the transition, half the wavelength of the absorbed photon. The *y*-axis is the TPA cross section in GM: all data refer to normalized concentrations per monomeric unit.

4. Optical Spectra of Dimers: Modeling Interchromophore Electrostatic Interactions in Solution

As expected due to the presence of multiple charges (four ion pairs per molecule) the solubility of **D-C6** and **D-C3** dimers is rather poor in common organic solvents. Absorption and fluorescence spectra were successfully collected only in the strongly polar solvent DMSO. The top panel of Figure 4 shows experimental absorption and fluorescence spectra of **M**, **D-C6**, and **D-C3** in DMSO, while the bottom panel shows the corresponding TPA spectra. Fluorescence and TPA spectra of the dimeric species do not show any significant deviation from monomer spectra, whereas OPA spectra are red-shifted on going from **M** to **D-C6** and **D-C3** as a result of increasing interchromophore interactions. Understanding this behavior requires a detailed modeling of electrostatic interchromophore interactions, also accounting for screening from the surrounding solvent. DMSO is a polar solvent whose large dielectric constant almost completely suppresses static electrostatic interactions. However, excitonic interactions are screened by the squared refractive index of the solvent, with an effect more than 20 times smaller in DMSO than that due to the dielectric constant, and possibly leading to non-negligible spectroscopic effects. To distinguish between static and optical screening, we adopt a step-by-step approach: first we derive a mean-field Hamiltonian for the dimeric species that, describing the ground-state properties, accounts for static screening. Extending a procedure originally developed and exploited for clusters of dipolar (DA) chromophores,[34a,b] we then define the excitonic Hamiltonian. In this procedure, the distinction between static and optical screening emerges quite naturally leading to a proper understanding of experimental data.

TABLE 4: Basis Set for the Dimeric Structures

wave functions		charge distribution	energy	rescaled energy[a]
Φ_1	$\varphi_0\varphi_0$	$A^+DA^-A^+DA^+$	V_1	0
Φ_2	$\varphi_0\varphi_c$	$A^+DA^-AD^+A^+$	$2\eta + V_2$	$2\eta + v_2$
Φ_3	$\varphi_c\varphi_0$	$A^+D^+A-A^+DA^+$	$2\eta + V_2$	$2\eta + v_2$
Φ_4	$\varphi_0\varphi_s$	$A^+DA^-A^+D^+A$	$2\eta + V_3$	$2\eta + v_3$
Φ_5	$\varphi_s\varphi_0$	$AD^+A^-A^+DA^+$	$2\eta + V_3$	$2\eta + v_3$
Φ_6	$\varphi_c\varphi_c$	$A^+D^+A-AD^+A^+$	$4\eta + V_4$	$2\eta + v_4$
Φ_7	$\varphi_c\varphi_s$	$A^+D^+A-A^+D^+A$	$4\eta + V_5$	$2\eta + v_5$
Φ_8	$\varphi_s\varphi_c$	$AD^+A^-AD^+A^+$	$4\eta + V_5$	$2\eta + v_5$
Φ_9	$\varphi_s\varphi_s$	$AD^+A^-A^+D^+A$	$4\eta + V_6$	$2\eta + v_6$

[a] $v_i = V_i - V_1$.

4.1. Ground-State Properties: Mean-Field Approximation. In **D-C6** and **D-C3**, two **M** species are joined by a (flexible) chain through one of the two terminal A sites to define an ADA−ADA dimeric unit (Scheme 1). Accounting for three resonating structures for each chromophore, yields to nine basis states for the dimers (Table 4). The two states AD^+A^+ and A^+D^+A of each one of the two chromophores, equivalent for the isolated **M** species, become nonequivalent in the dimer. For each **M** unit in the dimer we then define the two states AD^+A^+ and A^+D^+A as φ_c or φ_s (cf Table 4) depending on the *central* (c) or *side* (s) position in each chromophore of the neutral A moiety (the A site in one **M**-unit is *central* when linked to the other chromophore, whereas it is defined as *side* when it is referred to the other A site). Electrostatic interchromophore interactions affect the energy of the basis states, as shown in the last two columns of Table 4. Specifically, the V_i energies (or the rescaled energies $v_i = V_i - V_1$) describe the electrostatic interactions between the different charge distributions and can therefore be calculated from the mutual arrangement of the monomers once a specific model is adopted for the charge distribution.[28–30] As schematically shown in Figure 5, we represent each chromophore as a rigid rod of total length $2l$ (l is the effective length of a D−A subunit), where two positive point charges are located, depending on the state, either at the two A groups at the extreme sites of the rod and/or at the D group in the middle. The two chromophores are joined through the A sites by a link of length r. Finally, different geometries are defined by varying the angle φ from 0, accounting for two faced **M** units, up to 180°, corresponding to two aligned **M** units pointing in opposite directions (Figure 5, right panel). As shown in Figure 5, we have constrained the two chromophores in perpendicular planes with respect to the joining link: the resulting geometries, however, span a wide enough subset of geometries to reliably understand spectroscopic effects of interchromophore interactions. On the basis of these premises, the V_i interactions shown in Table 4 are calculated by summing up interchromophore interactions between point charges. For fixed l, the V_i interactions depend on r and φ, and being interested in ground-state (i.e., static) properties, they are screened by the static dielectric constant (explicit expressions for V_i energies are given in the Supporting Information).

First, we focus our attention on the electronic problem. The relevant Hamiltonian is the sum of the two electronic Hamiltonians for each unit (eq 1) and of a term that describes electrostatic interchromophore interactions:

$$H_{el} = -\sqrt{2}t\sum_i(\hat{o}_c^i + \hat{o}_s^i) + (2\eta + v_2)\sum_i \hat{\rho}_c^i + (2\eta + v_3)\sum_i \hat{\rho}_s^i + (v_4 - 2v_2 - 2v_3)\hat{\rho}_c^1\hat{\rho}_c^2 + (v_6 - 2v_2 - 2v_3)\hat{\rho}_s^1\hat{\rho}_s^2 + (v_5 - v_2 - v_3)(\hat{\rho}_c^1\hat{\rho}_s^2 + \hat{\rho}_s^1\hat{\rho}_c^2) \quad (5)$$

where the $i = 1, 2$ apex on the $\hat{o}$ and $\hat{\rho}$ operators (cf. eq 3) runs on the two chromophoric units. In the ground state the two molecules are equivalent so that just two order parameters are required, $\rho_c = \langle\hat{\rho}_c^1\rangle = \langle\hat{\rho}_c^2\rangle$ and $\rho_s = \langle\hat{\rho}_s^1\rangle = \langle\hat{\rho}_s^2\rangle$, where $\langle\ \rangle$ indicates the ground-state expectation value. We define the deviation operators as $\hat{\delta}_{c/s}^i = \hat{\rho}_{c/s}^i - \langle\hat{\rho}_{c/s}^i\rangle$: the mean-field approximation neglects in the above Hamiltonian all nonlinear terms in the deviation operators. In this approximation, the problem reduces to the diagonalization of the Hamiltonian for an isolated chromophore subject to the electrostatic potential generated by the (frozen) charge distribution on the nearby chromophore:

$$H_{el}^{mf} = -\sqrt{2}t(\hat{o}_c^i + \hat{o}_s^i) + 2\eta_c\hat{\rho}_c^i + 2\eta_s\hat{\rho}_s^i \quad (6)$$

The mean-field Hamiltonian coincides in fact with the Hamiltonian of the isolated **M** molecule (cf. eq 1), but the η energy is substituted by effective $\eta_{c/s}$ energies that account for the interaction of each chromophore with the average charge distribution on the nearby chromophore. The two arms of each **M** unit are not equivalent in the dimer and two different η values are associated with the φ_c and φ_s states, as follows:

$$2\eta_c = 2\eta + v_2 + (v_4 - 2v_2 - 2v_3)\rho_c + (v_5 - v_2 - v_3)\rho_s$$
$$2\eta_s = 2\eta + v_3 + (v_6 - 2v_2 - 2v_3)\rho_s + (v_5 - v_2 - v_3)\rho_c \quad (7)$$

These equations show that the energies of the φ_c and φ_s states of each **M** unit self-consistently depend on the charge distribution on the nearby molecule, as described by the two order parameters ρ_c and ρ_s. The mean-field Hamiltonian matrix is easily written and diagonalized on the basis of the three states, φ_0, φ_c, and φ_s. We impose self-consistency with the requirement that the $\rho_{c/s}$ values entering the mean-field Hamiltonian matrix coincide with the squared coefficients of the $\varphi_{c/s}$ in the ground-state wave function. Specifically, we start with a guess for $\rho_{c/s}$, diagonalize the resulting mean-field Hamiltonian, calculate new estimates of $\rho_{c/s}$ as the squared coefficient of the $\varphi_{c/s}$ functions, and repeat the procedure until successive $\rho_{c/s}$ values differ less than a predefined precision (typically set to 10^{-8}).

Each chromophoric unit in the dimer is described in terms of the same model derived for the isolated **M** unit in the previous section. Therefore, we introduce two vibrational coordinates

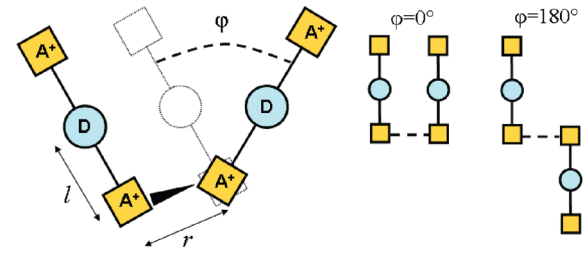

Figure 5. Left panel: schematic view of the dimer geometry, with the definition of geometrical parameters. Right panel: top view of two special cases $\varphi = 0$ and $\varphi = 180°$.

$q^i_{c/s}$ ($i = 1, 2$), one conformational coordinate $\tilde{Q}^i$ and one solvent reaction field F^i_R for each chromophore. These slow coordinates are coupled to the charge distribution in each chromophore as described in eq 3. We work in the adiabatic approximation and use the Hellman−Feynman theorem to minimize the ground-state energy and find the equilibrium positions for the slow coordinates as follows (cf. eq 3):

$$\begin{aligned}(q^i_{c/s})_{eq} &= \frac{\sqrt{2\varepsilon_v}}{\omega_v}\rho_{c/s}\\ (\tilde{Q}^i)_{eq} &= \sqrt{2\varepsilon_Q}(\rho_c + \rho_s)\\ (F^i_R)_{eq} &= \frac{2\varepsilon_{or}}{\mu_0}(\rho_c - \rho_s)\end{aligned} \tag{8}$$

Inserting these equilibrium coordinates into the coupling Hamiltonian in eq 3, we end up with a complete mean-field Hamiltonian that accounts in an averaged form for the mutual interaction between the two chromophores and for the coupling to slow (vibrational, conformational, and environmental) degrees of freedom. This Hamiltonian has again the form in eq 6, but with renormalized $\eta_{c/s}$ parameters:

$$\begin{aligned}2\eta_c = 2\eta + v_2 + (v_4 - 2v_2 - 2v_3)\rho_c + (v_5 - v_2 - v_3)\rho_s\\ - 2\varepsilon_v\rho_c - 2\varepsilon_Q(\rho_c + \rho_s) - 2\varepsilon_{or}(\rho_c - \rho_s)\\ 2\eta_s = 2\eta + v_3 + (v_6 - 2v_2 - 2v_3)\rho_s\\ + (v_5 - v_2 - v_3)\quad \rho_c - 2\varepsilon_v\rho_s - 2\varepsilon_Q(\rho_c + \rho_s) - 2\varepsilon_{or}(\rho_c - \rho_s)\end{aligned} \tag{9}$$

The complete mean-field Hamiltonian is finally diagonalized, following the same self-consistent procedure described above, to get the ground state, g, and the two excited states, c and e, with excitation energies E_c and E_e, respectively.

The large screening of electrostatic interactions in DMSO results in minor effects of interchromophore interactions in the ground-state properties of dimeric species. In particular, as discussed above, each chromophore in the dimer has a lower symmetry than the isolated **M** unit, but the effects of this symmetry lowering are very weak. In particular, Figure 6 shows the evolution of $\rho_c - \rho_s$ as a function of the intermolecular distance and of the torsion angle (cf. Figure 5) calculated in the mean-field approximation for a **D** unit in DMSO. We adopt for the **M** subunits the same model parameters as obtained in the previous section (Table 2) and calculate the electrostatic interchromophore interactions, v_i, setting $l = 8$ Å, and accounting for the screening due to the static dielectric constant of DMSO (Table 1, cf. Supporting Information). When the two molecules are faced ($\varphi = 0$), the symmetry of the isolated **M** unit is maintained, irrespective of the interchromophore distance,

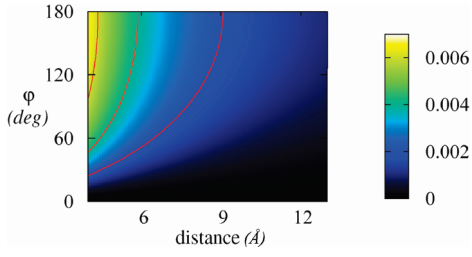

Figure 6. Mean-field results for **D**. The color map shows $\rho_c - \rho_s$ as a function of r and φ (cf. Figure 5). Molecular parameters are taken from Table 2, and we set $l = 8$ Å.

TABLE 5: Excitonic Basis for the Dimeric Structures

wave functions		mf energies
Ψ_1	gg	0
Ψ_2	gc	E_c
Ψ_3	cg	E_c
Ψ_4	ge	E_e
Ψ_5	eg	E_e
Ψ_6	cc	$E_c + E_c$
Ψ_7	ce	$E_c + E_e$
Ψ_8	ec	$E_c + E_e$
Ψ_9	ee	$E_e + E_e$

and $\rho_c - \rho_s = 0$. Deviations from this limit are observed at small distances and large φ angles. However, on an absolute scale, $\rho_c - \rho_s$ stays small, and in fact no hint of the symmetry lowering is recognized in optical spectra of either **D-C6** or **D-C3**.

4.2. Linear and Nonlinear Absorption Spectra: Setting up the Exciton Approximation. As long as we are interested in static properties of dimeric units, relevant interchromophore interactions are screened by the static dielectric constant. However, the energies of optical excitations are strongly affected by excitonic interactions.[38] These describe electrostatic interactions between transition dipoles oscillating at optical frequencies and are therefore screened by the squared refractive index at optical frequency.[38] A strategy is required to single out excitonic interactions as to properly screen them.

A good starting point to set up the excitonic model is offered by the solution of the mean-field problem.[29,30] According to the literature,[29,30] we define the best excitonic basis functions, Ψ_i in Table 5, as the direct product of the mean-field eigenstates g, c, and e obtained by the self-consistent diagonalization of the mean-field Hamiltonian for the two **M** units. In other words, we choose the excitonic basis as the eigenstates of the dimer Hamiltonian in the mean-field approximation. Among the basis states we recognize the ground state, Ψ_1, two states with a single c excitation (Ψ_2 and Ψ_3), two states with a single e excitation (Ψ_4 and Ψ_5), and states where both molecules are excited (Ψ_{6-9}). The corresponding mean-field energies (third column in Table 5) are simply the sum of the mean-field energies relevant to the two chromophores. The g, c, and e states, obtained from the diagonalization of the monomer Hamiltonian, are expressed as linear combinations of the basis states φ_0, φ_c, and φ_s on each chromophore, so that the Ψ_i functions are linear combinations of the Φ_i functions. Then a linear transformation allows us to rewrite the dimer Hamiltonian from the Φ_i to the Ψ_i basis. If the excitonic approximation works well,[28,29,38] the off-diagonal elements of the Hamiltonian matrix written on the excitonic basis are small with respect to the excitation energies, and the nondiagonal matrix elements of the Hamiltonian matrix have negligible effects, with the notable exception of those nondiagonal elements mixing up degenerate states (i.e., Ψ_2 and Ψ_3, Ψ_4 and Ψ_5, Ψ_7 and Ψ_8, cf. Table 5).

The excitonic Hamiltonian for the dimer is then obtained by neglecting all off-diagonal elements of the Hamiltonian written on the excitonic basis, with the exception of those connecting degenerate states. Moreover, in the residual off-diagonal terms, the contributions arising from electrostatic interchromophore interactions is multiplied by a factor ε/n^2, to renormalize the excitonic interaction energies for the screening at optical frequencies. The diagonalization of the resulting excitonic Hamiltonian finally leads to the excited states calculated for all slow coordinates fixed at their equilibrium position obtained in the adiabatic approximation for the ground state. With this information we can calculate *vertical* OPA and TPA frequencies

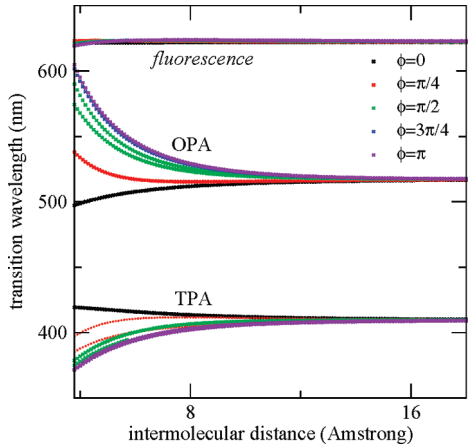

Figure 7. Transition (OPA, TPA, and fluorescence) energies calculated in the excitonic model (see text) for **D** as a function of the intermolecular distance and for different torsion angles. Molecular parameters are taken from Table 3, and $l = 8$ Å. Only the most intense transitions are shown for OPA and TPA spectra. For some φ values, due to the lowering of the molecular symmetry as due to electrostatic interactions, a splitting of the OPA and TPA transitions is observed.

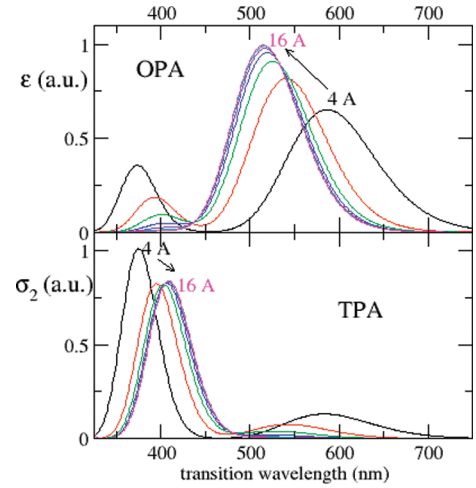

Figure 8. OPA (top) and TPA (bottom) spectra calculated for a dimeric unit with $\varphi = 135°$ and variable interchromophore distance (from 4 to 16 Å, with 2 Å steps).

and intensities. Figure 7 collects information on transition energies, calculated for a dimer **D** as a function of the interchromophore distance for different angles φ. As expected, when the intermolecular distance becomes large ($\gtrsim$12 Å) we regain the result for the **M** molecule in DMSO, irrespective of the mutual orientation of the chromophores. Sizeable and φ-dependent excitonic effects are observed upon decreasing r below ~10 Å. Quite interestingly, excitonic interactions affect both OPA and TPA frequencies, a result that points to the failure of the dipolar approximation for electrostatic interactions.[29] We notice that, for $\varphi > 0$, interchromophore interactions lower the symmetry of each **M** unit; as a result, a sizable splitting of the OPA and/or TPA bands is observed in some cases (cf. Figure 7). The splitting is, however, too small to be recognized in the broad experimental spectra.

With regard to OPA, the transition is red-shifted by interchromophore interactions for all angles apart from the special case of $\varphi = 0$ (i.e., for faced **M** units) where it is blue-shifted. This special geometry is unlikely to occur because of electrostatic repulsion (at least when interchromophore distances are small enough to give rise to sizable interaction). On this basis, data in Figure 7 nicely agree with the experimentally observed red shift of the linear absorption band upon decreasing the interchromophore distance. Of course, our model for electrostatic interactions is fairly rough, so that intermolecular distances represent effective values. However, results in Figure 7 suggest that for **D-C6**, with an approximate interchromophore distance of about 8 Å, OPA and TPA spectra are marginally affected by interchromophore interactions. On the contrary, in **D-C3** $r \approx 6$ Å and a sizable red shift (≈10−20 nm) is predicted in OPA spectra, in good agreement with experimental data. The smaller red shift expected for the TPA band is hardly recognized in experimental spectra, mainly due to the intrinsic lower resolution of TPA data (spectral resolution of TPA data is dictated by the spectral width of the Gaussian-shaped excitation pulses produced by the laser). The intensities of the OPA and TPA bands are only marginally affected up to the distances relevant for the species **D-C3**, with just a small decrease of the OPA intensity (as shown in Figure 8 for $\varphi = 135°$).

The detailed calculation of OPA and TPA spectra, including the vibronic structure and accounting for the inhomogeneous broadening from polar solvent, is extremely demanding for the dimeric unit. In fact, this would require the diagonalization of the nonadiabatic Hamiltonian for a system with 9 electronic states and 4 vibrational degrees of freedom. With the conservative estimate of 5 vibrational states for each degree of freedom, one should diagonalize (getting all eigenstates and transition dipole moments) a square matrix of dimension 5625,[2] and the calculation should be repeated by exploring the phase space spanned by 4 classical fields, leading to an overwhelmingly big number of calculations. Therefore, we limit attention to vertical transition frequencies and intensities, obtained in the excitonic approximation. To offer some information on the calculated spectral evolution, the two panels of Figure 8 describe, as a typical example, the evolution with the interchromophore distance of OPA and TPA spectra for a dimer with $\varphi = 135°$, calculated by assigning to each electronic state (as obtained from the diagonalization of the excitonic model) a Gaussian line shape with full-width at half-maximum of ≈2000 cm^{-1}.

As previously discussed,[28] when mean-field excitation energies are comparable with electrostatic interactions, the off-diagonal matrix elements neglected in the excitonic approximation may play a role. For some of these ultraexcitonic terms, like for instance those mixing the ground and excited states, it is not obvious which kind of screening, either static or optical, should be adopted. We have explicitly verified that these terms, irrespective of the adopted screening model, marginally affect calculated spectra: the excitonic approximation works well in our case.

4.3. Fluorescence Spectra: The Relaxed Excited State. Steady-state fluorescence occurs from the relaxed first excited state. Therefore, the calculation of the fluorescence spectrum requires, as a first step, a mean-field model for the relaxed fluorescent state. The problem is more delicate than the one described in section 4.1 because the first excited state of the dimeric unit corresponds to a state where only one out of the two chromophores is excited, whereas the ground state is unique. To account for the nonequivalence of the two molecular units, we have developed a mean-field model based on four order parameters, and specifically, $\rho_{c1} = \langle \hat{\rho}_c^! \rangle$, $\rho_{s1} = \langle \hat{\rho}_s^! \rangle$, for the first chromophore (chromophore 1), and the two corresponding parameters for the second chromophore (chromophore 2). In the mean-field approximation, the dimer Hamiltonian splits in two Hamiltonians, H_i^{mf}, relevant to each **M** unit. Each one of these Hamiltonians has exactly the same form as the mean field Hamiltonian in eq 6:

$$H_1^{\mathrm{mf-fluo}} = -\sqrt{2}t(\hat{\sigma}_c^1 + \hat{\sigma}_s^1) + 2\eta_{c1}\hat{\rho}_c^1 + 2\eta_{s1}\hat{\rho}_s^1$$
$$H_2^{\mathrm{mf-fluo}} = -\sqrt{2}t(\hat{\sigma}_c^2 + \hat{\sigma}_s^2) + 2\eta_{c2}\hat{\rho}_c^2 + 2\eta_{s2}\hat{\rho}_s^2 \quad (10)$$

but a different sets of η energies is now defined for each **M** unit, as follows:

$$\begin{aligned}
2\eta_{c1} &= 2\eta + v_2 + (v_4 - 2v_2 - 2v_3)\rho_{c2} + (v_5 - v_2 - v_3)\rho_{s2} \\
&\quad - 2\varepsilon_v\rho_{c1} - 2\varepsilon_Q(\rho_{c1} + \rho_{s1}) - 2\varepsilon_{or}(\rho_{c1} - \rho_{s1}) \\
2\eta_{s1} &= 2\eta + v_3 + (v_6 - 2v_2 - 2v_3)\rho_{s2} + (v_5 - v_2 - v_3)\rho_{c2} \\
&\quad - 2\varepsilon_v\rho_{c1} - 2\varepsilon_Q(\rho_{c1} + \rho_{s1}) - 2\varepsilon_{or}(\rho_{c1} - \rho_{s1}) \\
2\eta_{c2} &= 2\eta + v_2 + (v_4 - 2v_2 - 2v_3)\rho_{c1} + (v_5 - v_2 - v_3)\rho_{s1} \\
&\quad - 2\varepsilon_v\rho_{c2} - 2\varepsilon_Q(\rho_{c2} + \rho_{s2}) - 2\varepsilon_{or}(\rho_{c2} - \rho_{s2}) \\
2\eta_{s2} &= 2\eta + v_3 + (v_6 - 2v_2 - 2v_3)\rho_{s1} + (v_5 - v_2 - v_3)\rho_{c1} \\
&\quad - 2\varepsilon_v\rho_{c2} - 2\varepsilon_Q(\rho_{c2} + \rho_{s2}) - 2\varepsilon_{or}(\rho_{c2} - \rho_{s2})
\end{aligned} \quad (11)$$

The effective η energies for each chromophoric unit depend, through electrostatic interactions, on the charge distribution on the nearby chromophore, and through the coupling to slow degrees of freedom, on the charge distribution on the chromophore itself. Of course, being interested in stationary results, the electrostatic interactions in the above equations are screened by the static dielectric constant. To solve the mean-field problem, we start with a guess for the four order parameters, diagonalize the two Hamiltonians in eq 10, and recalculate the order parameters as the expectation values of the relevant operators on the *ground states* for chromophore 1 and on the *first excited state* for chromophore 2. The new estimates for the order parameters enter the mean-field Hamiltonians in eq 10, and the procedure is repeated until convergence.

Figure 9 shows results obtained along these lines: in particular, the asymmetry, $\rho_{ci} - \rho_{si}$, calculated for each chromophore ($i = 1, 2$) is shown as a function of r and φ. In the proposed approach the excitation is localized (by construction) on chromophore 2, and in fact, the results shown in the figure for chromophore 1 are similar to those calculated for the ground state (cf. Figure 6). On the opposite, chromophore 2 shows a much larger asymmetry, with $\rho_{c2} - \rho_{s2}$ ranging from 0.25 to 0.45, a result easily rationalized on the basis of the larger polarizability of the chromophore in the excited state.

Once the mean-field solution is obtained, one can proceed to the construction of the excitonic model relevant to fluorescence, along the same lines as discussed in section 4.1. In particular, the total dimer Hamiltonian is rewritten on the relevant excitonic basis, obtained as the direct product of the mean field eigenstates for the first and second chromophore. The excitonic approximation now amounts to neglect of all off-diagonal elements of the second row and column that would mix the first excited state, already optimized at the mean-field level, to the other states. All non-neglected matrix elements of the transformed matrix coming from electrostatic interactions are then renormalized by n^2/ε, to account for screening at optical frequencies. Finally, transition energies and dipole moments are obtained via a numerical diagonalization. In agreement with experimental data, the calculated fluorescence frequency is marginally affected by intermolecular interactions (Figure 7), due to the effective localization of the relaxed excited state.

5. Conclusions

Interchromophore interactions play a major role in the definition of the properties and behavior of molecular materials.[28–31,38] The effects are particularly intriguing in materials for NLO that are made up by chromophores that, by definition, respond in a large and nonlinear way to external stimuli.[28–30] If properly investigated and rationalized, interchromophore interactions may offer a powerful tool to tune the material response and design efficient and custom-tailored materials.

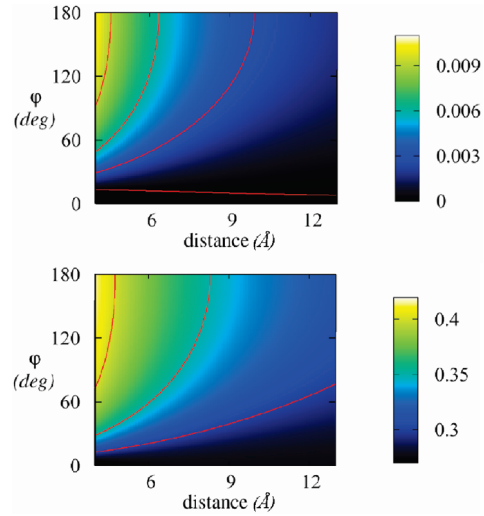

Figure 9. Mean-field results for the fluorescent state. Top and bottom panels show $\rho_c - \rho_s$ values obtained for the first and second chromophore, respectively. Molecular parameters are taken from Table 3, and $l = 8$ Å.

We have presented a multidisciplinary investigation (organic synthesis, linear and nonlinear spectroscopic investigation, theoretical modeling) on bichromophoric assemblies based on a highly efficient TPA quadrupolar (ADA) dye. The dimers were obtained by linking two quadrupolar chromophores through their terminal acceptor moieties. The use of saturated alkyl chains of different length excludes π-conjugation effects between the two units and accounts for different interchromophore distances. Linear absorption and fluorescence spectra were collected in several solvents for the monomeric unit **M**, whereas linear absorption and fluorescence spectra and TPA spectra of the two dimeric species were collected in DMSO. The linear absorption peak is red-shifted on going from **M** to **D** with a slight decrease of the molar extinction coefficient (normalized per chromophore unit). In contrast, TPA maximum wavelengths and cross sections are unaffected, within experimental uncertainties, by intermolecular interactions. The fluorescence quantum yield decreases with increasing interchromophore interactions, probably due to the opening of new relaxation channels, but the position and shape of the fluorescence band is not affected upon dimerization.

Bottom-up modeling strategies[28–30] proved very useful to investigate the role of electrostatic interchromophore interactions in materials based on polar donor−acceptor molecules.[31,32,33a,b,34] These strategies take advantage of the molecular nature of the materials of interest and start from a detailed analysis of optical spectra of isolated chromophores in solution to define reliable essential-state models for the specific chromophores. This information is then used to build models for interacting chromophores in molecular crystals, films, aggregates, and multichromophoric assemblies. When discussing electrostatic interactions in multichromophoric assemblies in solution, particular attention must be paid to screening effects from the solvent.[33a,34] Indeed, the dielectric constant of typical organic solvents spans more than 1 order of magnitude from ≈2 for nonpolar solvents up to ≈50 for strongly polar solvents. The screening of electrostatic interaction would suggest negligible effects of interchromophore interactions in strongly polar

solvents. However, it is well-known[38] that excitonic interactions involve transition charge densities and, as such, should be screened by the squared refractive index of the solvent as measured at optical frequencies: the resulting screening constant is rather small (again of the order of 2) and similar for most organic solvents. Discriminating between static and dynamic screening is a tough problem that has been addressed for interacting dipolar chromophores in solution[34a,b] exploiting the analytical transformation toward the excitonic basis.[29] The approach is based on the solution of the mean-field problem for interacting chromophores and the subsequent transformation of the Hamiltonian for interacting chromophores in the so-called excitonic basis, i.e., the eigenstates of the mean-field Hamiltonian. Adopting the same procedure for interacting quadrupolar (or multipolar) chromophores is nontrivial. First of all, interchromophore interactions in general lower the symmetry of the chromophores so that multiparameter mean-field approaches must be devised. Moreover, the analytical transformation toward the excitonic basis adopted for interacting DA chromophore does not apply to multipolar dyes and one has to resort to a numerical transformation.

All these problems have been faced and solved in this work that describes a numerical approach to treat interchromophore interactions in dimers of quadrupolar chromophores in solution. We notice that the model also accounts for the coupling to solvation and vibrational degrees of freedom in the adiabatic approximation. The proposed strategy is general and can be extended to larger clusters of multipolar chromophores as well. In the process, in line with the bottom-up modeling strategy, we have analyzed in detail optical spectra of the isolated **M** chromophore in different solvents and have defined a reliable three-state model for this interesting dye, also accounting for the coupling between electrons and slow degrees of freedom, including molecular vibrations and effective solvation coordinates. The effects of electrostatic interchromophore interactions observed in the investigated systems are rather small, mainly as a result of the fairly large interchromophore distances in both dimers. We have adopted a very simple model for electrostatic interactions, based on point charges centered on D and A sites. More refined models can be envisaged, on the basis of more realistic descriptions of the charge distribution in the chromophoric units,[31] leading to different V_i values. However, the proposed approach to account for interchromophore interactions and to discriminate between static and dynamic screening applies quite irrespective of the specific model adopted for the electrostatic interactions. In spite of using a fairly simple model for electrostatic interactions, the spectroscopic effects of interchromophore interactions are well accounted for in the proposed model. In particular, the absorption band red-shifts upon decreasing the interchromophore distance from the solvated **M** to **D-C6** and **D-C3**, while the fluorescence band is totally unaffected by the interchromophore separation. This puzzling result is well reproduced by our calculation, and the insensitivity of the fluorescence band to the interchromophore distance is safely ascribed to the localized nature of the relaxed fluorescent state.

Acknowledgment. Work supported by MIUR-PRIN 2006-031511 "Chromophores in organic and hybrid nanostructures: supramolecular engineering of photonic properties" and MIUR-FIRB RBNE033KMA.

Supporting Information Available: Explicit expressions for the electrostatic interactions energies v_i in Table 4. This material is available free of charge via the Internet at http://pubs.acs.org.

References and Notes

(1) (a) *Molecular Nonlinear Optics*; Zyss, J., Ed.; Academic Press: New York, 1994. (b) Burland, D. M. Optical Nonlinearities in Chemistry. *Chem. Rev.* **1994**, *94*, 1–278. (c) Prasad, P. N.; Williams, D. J. *Introduction to Nonlinear Optical Effects in Molecules and Polymers*; Wiley: New York, 1991.

(2) *Polymers for Second-Order Nonlinear Optics*; Lindsay, G. A.; Singer, K. D.; Eds.; ACS Symposium Series 601; American Chemical Society: Washington, DC, 1995.

(3) (a) Terenziani, F.; Katan, C.; Blanchard-Desce, M.; Badaeva, E.; Tretiak, S. *Adv. Mater.* **2008**, *20*, 4641–4678. (b) He, G. S.; Tan, L. S.; Zheng, Q.; Prasad, P. N. *Chem. Rev.* **2008**, *108*, 1245–1330. (c) Pawlicki, M.; Collins, H. A.; Denning, R. G.; Anderson, H. L. *Angew. Chem., Int. Ed.* **2009**, *48*, 3244–3266.

(4) (a) Dalton, L. R. *J. Phys.: Condens. Matter* **2003**, *15*, R897–R934. (b) Ma, H.; Jen, A. K.-Y.; Dalton, L. R. *Adv. Mater.* **2002**, *14*, 1339–1365. (c) Ermer, S.; Lovejoy, S. M.; Bedworth, P. V.; Leung, D. S.; Warren, H. B.; Epstein, J. A.; Girton, D. G.; Dries, L. S.; Taylor, R. E.; Barto, R. R. J.; Eades, W.; Van Eck, T. E.; Moss, A. S.; Anderson, W. W. *Adv. Funct. Mater.* **2002**, *12*, 605–610. (d) Lee, M.; Katz, H. E.; Erben, C.; Gill, D. M.; Gopalan, P.; Heber, J. D.; McGee, D. J. *Science* **2002**, *298*, 1401–1404. (e) Shi, Y. Q.; Zhang, C.; Zhang, H.; Bechtel, J. H.; Dalton, L. R.; Robinson, B. H.; Steier, W. H. *Science* **2000**, *288*, 119–122.

(5) Kippelen, B.; Blanche, P.-A.; Schulzgen, A.; Fuentes-Hernandez, C.; Ramos-Ortiz, G.; Wang, J.-F.; Peyghambarian, N.; Marder, S. R.; Leclercq, A.; Beljonne, D.; Brédas, J.-L. *Adv. Funct. Mater.* **2002**, *12*, 615–620.

(6) (a) Denk, W.; Strickler, J. H.; Webb, W. W. *Science* **1990**, *248*, 73–76. (b) Gura, T. *Science* **1997**, *276*, 1988–1990. (c) Cox, G. *Mater. Today* **2002**, *5*, 34–41. (d) Larson, D. R.; Zipfel, W. R.; Williams, R. M.; Clark, S. W.; Bruchez, M. P.; Wise, F. W.; Webb, W. W. *Science* **2003**, *300*, 1434–1437.

(7) (a) Signorini, R.; Pedron, D.; Ferrante, C.; Bozio, R.; Brusatin, G.; Innocenzi, P.; Della Negra, F.; Maggini, M.; Abbotto, A.; Beverina, L.; Pagani, G. *SPIE Proc.* **2003**, *4797*, 1–14. (b) Ehrlich, J. E.; Wu, X. L.; Lee, L. Y. S.; Hu, Z. Y.; Rockel, H.; Marder, S. R.; Perry, J. W. *Opt. Lett.* **1997**, *22*, 1843–1845.

(8) (a) Zhou, W.; Kuebler, S. M.; Braun, K. L.; Yu, T.; Cammack, J. K.; Ober, C. K.; Perry, J. W.; Marder, S. R. *Science* **2002**, *296*, 1106–1109. (b) Cumpston, B. H.; Ananthavel, S. P.; Barlow, S.; Dyer, D. L.; Ehrlich, J. E.; Erskine, L. L.; Heikal, A. A.; Kuebler, S. M.; Lee, I. Y. S.; McCord-Maughon, D.; Qin, J. Q.; Rockel, H.; Rumi, M.; Wu, X. L.; Marder, S. R.; Perry, J. W. *Nature* **1999**, *398*, 51–54. (c) La Fratta, C. N.; Fourkas, J. T.; Baldacchini, T.; Farrer, R. A. *Angew. Chem. Int. Ed.* **2007**, *46*, 6238–6258.

(9) (a) Konan, Y. N.; Gurny, R.; Allemann, E. *J. Photochem. Photobiol. B* **2002**, *66*, 89–106. (b) Frederiksen, P. K.; Jorgensen, M.; Ogilby, P. R. *J. Am. Chem. Soc.* **2001**, *123*, 1215–1221. (c) Breitenbach, T.; Kuimova, M. K.; Gbur, P.; Hatz, S.; Schack, N. B.; Pedersen, B. W.; Lambert, J. D. C.; Poulsen, L.; Ogilby, P. R. *Photochem. Photobiol. Sci.* **2009**, *8*, 442–452.

(10) Abbotto, A.; Beverina, L.; Bozio, R.; Bradamante, S.; Ferrante, C.; Pagani, G. A.; Signorini, R. *Adv. Mater.* **2000**, *12*, 1963–1967.

(11) (a) Marder, S. R.; Perry, J. W.; Bourhill, G.; Gorman, C. B.; Tiemann, B. G.; Mansour, K. *Science* **1993**, *261*, 186. (b) Wortmann, R.; Poga, C.; Twieg, R. J.; Geletneky, C. *J. Chem. Phys.* **1996**, *105*, 10637–10647.

(12) (a) Zojer, E.; Beljonne, D.; Pacher, P.; Bredas, J.-L. *Chem.—Eur. J.* **2004**, *10*, 2668–2680. (b) Zojer, E.; Beljonne, D.; Kogej, T.; Vogel, H.; Marder, S. R.; Perry, J. W.; Brédas, J. L. *J. Chem. Phys.* **2002**, *116*, 3646–3658. (c) Barzoukas, M.; Blanchard-Desce, M. *J. Chem. Phys.* **2000**, *113*, 3951–3959. (d) Rumi, M.; Ehrlich, J. E.; Heikal, A. A.; Perry, J. W.; Barlow, S.; Hu, Z. Y.; McCord-Maughon, D.; Parker, T. C.; Rockel, H.; Thayumanavan, S.; Marder, S. R.; Beljonne, D.; Bredas, J. L. *J. Am. Chem. Soc.* **2000**, *122*, 9500–9510. (e) Beljonne, D.; Wenseleers, W.; Zojer, E.; Shuai, Z.; Vogel, H.; Pond, S. J. K; Perry, J. W.; Marder, S. R.; Brédas, J.-L. *Adv. Funct. Mater.* **2002**, *12*, 631–641.

(13) *Characterization Techniques and Tabulations for Organic Nonlinear Optical Materials*; Kuzyk, M. G., Dirk, C. W., Eds.; Marcel Dekker: New York, 1998.

(14) (a) Beverina, L.; Fu, J.; Leclercq, A.; Zojer, E.; Pacher, P.; Barlow, S.; Van Stryland, E. W.; Hagan, D. J.; Brédas, J.-L.; Marder, S. R. *J. Am. Chem. Soc.* **2005**, *127*, 7282–7283. (b) Kannan, R.; He, G. S.; Yuan, L. X.; Xu, F. M.; Prasad, P. N.; Dombroskie, A. G.; Reinhardt, B. A.; Baur, J. W.; Vaia, R. A.; Tan, L. S. *Chem. Mater.* **2001**, *13*, 1896–1904. (c) Belfield, K. D.; Schafer, K. J.; Mourad, W.; Reinhardt, B. A. *J. Org. Chem.* **2000**, *65*, 4475–4481. (d) Reinhardt, B. A.; Brott, L. L.; Clarson, S. J.; Dillard, A. G.; Bhatt, J. C.; Kannan, R.; Yuan, L. X.; He, G. S.; Prasad, P. N. *Chem. Mater.* **1998**, *10*, 1863–1874.

(15) Albota, M.; Beljonne, D.; Bredas, J. L.; Ehrlich, J. E.; Fu, J. Y.; Heikal, A. A.; Hess, S. E.; Kogej, T.; Levin, M. D.; Marder, S. R.; Mccordmaughon, D.; Perry, J. W.; Rockel, H.; Rumi, M.; Subramaniam, C.; Webb, W. W.; Wu, I. L.; Xu, C. *Science* **1998**, *281*, 1653–1656.

(16) Selected examples:(a) Chung, S.-J.; Zheng, S.; Odani, T.; Beverina, L.; Fu, J.; Padilha, L. A.; Biesso, A.; Hales, J. M.; Zhan, X.; Schmidt, K.; Ye, A.; Zojer, E.; Barlow, S.; Hagan, D. J.; VanStryland, E. W.; Yi, Y.; Shuai, Z.; Pagani, G. A.; Bredas, J. L.; Perry, J. W.; Marder, S. R. *J. Am. Chem. Soc.* **2006**, *128*, 14444–14445. (b) Kato, S.-I.; Matsumoto, T.; Shigeiwa, M.; Gorohmaru, H.; Maeda, S.; Ishi-i, T.; Mataka, S. *Chem.—Eur. J.* **2006**, *12*, 2303–2317. (c) Chung, S.-J.; Rumi, M.; Alain, V.; Barlow, S.; Perry, J. W.; Marder, S. R. *J. Am. Chem. Soc.* **2005**, *127*, 10844–10845. (d) Parent, M.; Mongin, O.; Kamada, K.; Katan, C.; Blanchard-Desce, M. *Chem. Commun.* **2005**, *15*, 2029–2031. (e) Woo, H. Y.; Liu, B.; Kohler, B.; Korystov, D.; Mikhailovsky, A.; Bazan, G. C. *J. Am. Chem. Soc.* **2005**, *127*, 14721–14729. (f) Halik, M.; Wenseleers, W.; Grasso, C.; Stellacci, F.; Zojer, E.; Barlow, S.; Bredas, J.-L.; Perry, J. W.; Marder, S. R. *Chem. Commun.* **2003**, *13*, 1490–1491. (g) Mongin, O.; Porres, L.; Moreaux, L.; Mertz, J.; Blanchard-Desce, M. *Org. Lett.* **2002**, *4*, 719–722. (h) He, G. S.; Lin, T.-C.; Prasad, P. N.; Kannan, R.; Vaia, R. A.; Tan, L.-S. *J. Phys. Chem. B* **2002**, *106*, 11081–11084. (i) Kim, O. K.; Lee, K. S.; Woo, H. Y.; Kim, K. S.; He, G. S.; Swiatkiewicz, J.; Prasad, P. N. *Chem. Mater.* **2000**, *12*, 284–286. (j) Ventelon, L.; Moreaux, L.; Mertz, J.; Blanchard-Desce, M. *J. Chem. Soc., Chem. Commun.* **1999**, *20*, 2055–2056. (k) Belfield, K. D.; Hagan, D. J.; Van Stryland, E. W.; Schafer, K. J.; Negres, R. A. *Org. Lett.* **1999**, *1*, 1575–1578.

(17) (a) Abbotto, A.; Beverina, L.; Manfredi, N.; Pagani, G. A.; Archetti, G.; Kuball, H.-G.; Wittenburg, C.; Heck, J.; Holtmann, J. *Chem.—Eur. J.* **2009**, *15*, 6175–6185. (b) Archetti, G.; Abbotto, A.; Wortmann, R. *Chem.—Eur. J.* **2006**, *12*, 7151–7160. (c) Abbotto, A.; Beverina, L.; Bradamante, S.; Facchetti, A.; Klein, C.; Pagani, G. A.; Redi-Abshiro, M.; Wortmann, R. *Chem.—Eur. J.* **2003**, *9*, 1991–2007. (d) Abbotto, A.; Bradamante, S.; Pagani, G. A. *J. Org. Chem.* **2001**, *66*, 8883–8892. (e) Abbotto, A.; Bradamante, S.; Facchetti, A.; Pagani, G. A. *J. Org. Chem.* **1997**, *62*, 5755–5765.

(18) (a) Abbotto, A.; Beverina, L.; Bozio, R.; Facchetti, A.; Ferrante, C.; Pagani, G. A.; Pedron, D.; Signorini, R. *Org. Lett.* **2002**, *4*, 1495–1498. (b) Abbotto, A.; Beverina, L.; Bozio, R.; Bradamante, S.; Facchetti, A.; Ferrante, C.; Pagani, G. A.; Pedron, D.; Signorini, R. *NATO Sci. Ser. II* **2003**, *100*, 385–393. (c) Signorini, R.; Ferrante, C.; Pedron, D.; Zerbetto, M.; Cecchetto, E.; Slaviero, M.; Fortunati, I.; Collini, E.; Bozio, R.; Abbotto, A.; Beverina, L.; Pagani, G. A. *J. Phys. Chem. A* **2008**, *112*, 4224–4234.

(19) Abbotto, A.; Beverina, L.; Bozio, R.; Facchetti, A.; Ferrante, C.; Pagani, G. A.; Pedron, D.; Signorini, R. *Chem. Commun.* **2003**, *17*, 2144–2145.

(20) Katritzky, A. R. *Handbook of Heterocyclic Chemistry*; Pergamon Press: Oxford, U.K., 1983. Bradamante, S.; Pagani, G. In *Advances in Carbanion Chemistry*; Snieckus, V., Ed.; JAI Press: Greenwich CT, 1996; Vol. 2, pp 189−263.

(21) (a) Abbotto, A.; Bradamante, S.; Facchetti, A.; Pagani, G. A. *J. Org. Chem.* **1999**, *64*, 6756–6763. (b) Abbotto, A.; Bradamante, S.; Facchetti, A.; Pagani, G. A. *J. Org. Chem.* **1998**, *63*, 436–444. (c) Abbotto, A.; Bradamante, S.; Pagani, G. A.; Rzepa, H.; Stoppa, F. *Heterocycles* **1995**, *40*, 757–776. (d) Abbotto, A.; Alanzo, V.; Bradamante, S.; Pagani, G. A. *J. Chem. Soc., Perkin Trans. 2* **1991**, 481–488. (e) Bradamante, S.; Pagani, G. A. *Pure Appl. Chem.* **1989**, *61*, 709–716. (f) Raposo, M. M. M.; Sousa, A. M. R. C.; Kirsch, G.; Cardoso, P.; Belsley, M.; De Matos Gomes, E.; Fonseca, A. M. C. *Org. Lett.* **2006**, *8*, 3681–3684.

(22) (a) Abbotto, A.; Baldini, G.; Beverina, L.; Chirico, G.; Collini, M.; D'Alfonso, L.; Diaspro, A.; Magrassi, R.; Nardo, L.; Pagani, G. A. *Biophys. Chem.* **2005**, *114*, 35–41. (b) Versari, S.; Villa, A. M.; Villa, A.; Doglia, S. M.; Pagani, G. A.; Bradamante, S. *J. Biomed. Opt.* **2006**, *11*, 034014−4.

(23) Reichardt, C. *Chem. Rev.* **1994**, *94*, 2319–2358.

(24) (a) Kanis, D. R.; Ratner, M. A.; Marks, T. J. *Chem. Rev.* **1994**, *94*, 195–242. Bredas, J. L.; Cornil, K.; Meyers, F.; Beljonne, D., in: SkotheimT. A. Elsenbaumer, R. L., Reynolds, J. R. *Handbook of Conducting Polymers*; Marcel Dekker: New York, 1998; p. 1. (b) Bishop, D. M. *Int. Rev. Phys. Chem.* **1994**, *13*, 21–39, and references therein.

(25) (a) Painelli, A. *Chem. Phys.* **1999**, *245*, 185–197. (b) Painelli, A.; Terenziani, F. *Chem. Phys. Lett.* **1999**, *312*, 211–220. (c) Painelli, A.; Terenziani, F. *J. Phys. Chem. A* **2000**, *104*, 11041–11048. (d) Terenziani, F.; Painelli, A.; Comoretto, D. *J. Phys. Chem. A* **2000**, *104*, 11049–11054. (e) Boldrini, B.; Cavalli, E.; Painelli, A.; Terenziani, F. *J. Phys. Chem. A* **2002**, *106*, 6286–6294. (f) Terenziani, F.; Painelli, A.; Girlando, A.; Metzger, R. M. *J. Phys.Chem. B* **2004**, *108*, 10743–10750.

(26) Terenziani, F.; Painelli, A.; Katan, C.; Charlot, M.; Blanchard-Desce, M. *J. Am. Chem. Soc.* **2006**, *128*, 15742–15755.

(27) (a) Terenziani, F.; Sissa, C.; Painelli, A. *J. Phys. Chem. B* **2008**, *112*, 5079–5087. (b) Sissa, C.; Terenziani, F.; Painelli, A. *J. Phys. Chem. A* **2008**, *112*, 8697–8705.

(28) (a) Painelli, A.; Terenziani, F. In *Non-linear optical properties of matter: From molecule to condensed phases*; Papadopoulos, M. G., Leszczynski, J., Sadlej, J., Eds.; Springer: Dordrecht, The Netherlands, 2006; pp 251−282. (b) Painelli, A.; Terenziani, F.; Soos, Z. G. *Theor. Chem. Acc.* **2007**, *117*, 915–931. (c) Terenziani, F.; D'Avino, G.; Painelli, A. *ChemPhysChem* **2007**, *8*, 2433–2444.

(29) (a) Painelli, A.; Terenziani, F. *J. Am. Chem. Soc.* **2003**, *125*, 5624–5625. (b) Terenziani, F.; Painelli, A. *Phys. Rev. B* **2003**, *68*, 155405.

(30) D'Avino, G.; Terenziani, F.; Painelli, A. *J. Phys. Chem. B* **2006**, *110*, 25590–25592.

(31) (a) D'Avino, G.; Grisanti, L.; Guasch, J.; Ratera, I.; Veciana, J.; Painelli, A. *J. Am. Chem. Soc.* **2008**, *130*, 12064–12072. (b) D'Avino, G.; Grisanti, L.; Painelli, A.; Guasch, J.; Ratera, I.; Veciana, J. *Cryst. Eng. Commun.* **2009**, *11*, 2040–2046.

(32) Girlando, A.; Sissa, C.; Terenziani, F.; Painelli, A.; Chwialkowska, A.; Ashwell, G. J. *ChemPhysChem.* **2007**, *8*, 2195.

(33) (a) Terenziani, F.; Angiolini, L.; Benelli, T.; Giorgini, L. *Chem.—Eur. J.* **2005**, *11*, 6053–6063. (b) Datta, A.; Terenziani, F.; Painelli, A. *ChemPhysChem* **2006**, *7*, 2168–2174. (c) Liang, K.; Farahat, M. S.; Perlstein, J.; Law, K.-Y.; Whitten, D. G. *J. Am. Chem. Soc.* **1997**, *119*, 830–831. (d) Ajayaghosh, A.; Arunkumar, E.; Daub, J. *Angew. Chem., Int. Ed.* **2002**, *41*, 1766–1769. (e) Arunkumar, E.; Chithra, P.; Ajayaghosh, A. *J. Am. Chem. Soc.* **2004**, *126*, 6590–6598. (f) Arunkumar, E.; Ajayaghosh, A.; Daub, J. *J. Am. Chem. Soc.* **2005**, *127*, 3156–3164. (g) Liao, Y.; Bhattacharjee, S.; Firestone, K. A.; Eichinger, B. E.; Paranji, R.; Anderson, C. A.; Robinson, B. H.; Reid, P. J.; Dalton, L. R. *J. Am. Chem. Soc.* **2006**, *128*, 6847–6853. (h) Liao, Y.; Firestone, K. A.; Bhattacharjee, S.; Luo, J.; Haller, M.; Hau, S.; Anderson, C. A.; Lao, D.; Eichinger, B. E.; Robinson, B. H.; Reid, P. J.; Jen, A. K.-Y.; Dalton, L. R. *J. Phys. Chem. B* **2006**, *110*, 5434–5438. (i) Hennrich, G.; Murillo, M. T.; Prados, P.; Song, K.; Asselberghs, I.; Clays, K.; Persoons, A.; Benet-Buchholz, J.; de Mendoza, J. *Chem. Commun.* **2005**, *21*, 2747–2749.

(34) (a) Terenziani, F.; Morone, M.; Gmouh, S.; Blanchard-Desce, M. *ChemPhysChem* **2006**, *7*, 685–696. (b) Terenziani, F.; Ghosh, S.; Robin, A.-C.; Das, P. K.; Blanchard-Desce, M. *J. Phys. Chem. B* **2008**, *112*, 11498–11505. (c) Terenziani, F.; Mongin, O.; Katan, V; Bhatthula, B. K. G.; Blanchard-Desce, M. *Chem.—Eur. J.* **2006**, *12*, 3089–3102.

(35) (a) Abbotto, A.; Beverina, L.; Pagani, G. A.; Collini, M.; Chirico, G.; D'Alfonso, L.; Baldini, G. *SPIE Proc.* **2003**, *5139*, 223–230. (b) Facchetti, A.; Beverina, L.; Van der Boom, M., E.; Dutta, P.; Evmenenko, G.; Shukla, A. D.; Stern, C. E.; Pagani, G. A.; Marks, T. J *J. Am. Chem. Soc.* **2006**, *128*, 2142–2153.

(36) Salomon, M. F.; Salomon, R. G. *J. Am. Chem. Soc.* **1979**, *101*, 4290–4299.

(37) Gutman, V. *The Donor-Acceptor Approach to Molecular Interactions*; Plenum Press: New York, 1978; Chapters 7 and 10.

(38) (a) Craig, D. P.; Walmsley, S. H. *Excitons in Molecular Crystals*; Benjamin: New York 1968. (b) Davydov, A. S. *Theory of Molecular Excitons*; Plenum Press: New York, 1971. (c) Craig, D. P. *J. Chem. Soc.* **1955**, 2302–2308. (d) Pope, M.; Swenberg, C. E. *Electronic Processes in Organic Crystals and Polymers*; Oxford Univeristy Press: New York, 1999. (e) Silinsh, E. A.; Capek, V. *Organic Molecular Crystals*; AIP Press: New York, 1994. (f) Knoester, J. In *Organic Nanostructures: Science and Applications*; Proceedings of the International School of Physics Enrico Fermi, CXLIX Course; Agranovich, M., La Rocca, G. C., Eds.; IOS Press: Amsterdam, 2002.

(39) Mulliken, R. S. *J. Am. Chem. Soc.* **1952**, *74*, 811–824.

JP909475D

Dimers of quadrupolar chromophores in solution: electrostatic interactions and optical spectra

Cristina Sissa,[†] Francesca Terenziani,[†] Anna Painelli,[†] Alessandro Abbotto,[‡*] Luca Bellotto,[‡] Chiara Marinzi,[‡] Eleonora Garbin,[§] Camilla Ferrante,[§*] Renato Bozio[§]*

Supporting Information

Explicit expressions for the electrostatic interactions energies, v_i , in Table 4.

To simplify notation, we define the following distances:

$$a = r$$
$$b = \sqrt{r^2 + 4l^2}$$
$$c = \sqrt{r^2 + 4l^2(1-\cos\varphi)^2 + 4l^2\sin^2\varphi}$$
$$d = \sqrt{r^2 + 4l^2\left(1-\frac{1}{2}\cos\varphi\right)^2 + l^2\sin^2\varphi}$$
$$e = \sqrt{r^2 + l^2}$$
$$f = \sqrt{r^2 + l^2(1-\cos\varphi)^2 + l^2\sin^2\varphi}$$

with these definitions:

$$v_2 = \frac{14.4}{\varepsilon}\left(-\frac{1}{a}-\frac{1}{b}+\frac{1}{d}+\frac{1}{e}\right)$$
$$v_3 = \frac{14.4}{\varepsilon}\left(-\frac{1}{b}-\frac{1}{c}+\frac{1}{d}+\frac{1}{e}\right)$$
$$v_4 = \frac{14.4}{\varepsilon}\left(-\frac{1}{a}-\frac{2}{b}+\frac{2}{d}+\frac{1}{f}\right)$$
$$v_5 = \frac{14.4}{\varepsilon}\left(-\frac{1}{a}-\frac{1}{b}-\frac{1}{c}+\frac{1}{d}+\frac{1}{e}+\frac{1}{f}\right)$$
$$v_6 = \frac{14.4}{\varepsilon}\left(-\frac{2}{b}-\frac{1}{c}+\frac{2}{e}+\frac{1}{f}\right)$$

where ε is the solvent dielectric constant, v_i are in eV, and distances in Å.

2010, Volume 114B

Cristina Sissa, Francesca Terenziani, Anna Painelli,* Alessandro Abbotto,* Luca Bellotto, Chiara Marinzi, Eleonora Garbin, Camilla Ferrante,* and Renato Bozio: Dimers of Quadrupolar Chromophores in Solution: Electrostatic Interactions and Optical Spectra

Page 882. A few errors were found in the paper. Neither the discussion nor the conclusions of the paper are affected by the corrections listed below.

1. The length of the D−A arm, l, was set to 4 Å in all calculations.

2. In eq 4 the $2t$ matrix elements should read $-2t$.

3. In eq 11 two c indices should be replaced with s as follows:

$$
\begin{aligned}
2\eta_{c1} &= 2\eta + v_2 + (v_4 - 2v_2 - 2v_3)\rho_{c2} + \\
&(v_5 - v_2 - v_3)\rho_{s2} - 2\varepsilon_v\rho_{c1} - \\
&\qquad 2\varepsilon_Q(\rho_{c1} + \rho_{s1}) - 2\varepsilon_{or}(\rho_{c1} - \rho_{s1}) \\
2\eta_{s1} &= 2\eta + v_3 + (v_6 - 2v_2 - 2v_3)\rho_{s2} + \\
&(v_5 - v_2 - v_3)\rho_{c2} - 2\varepsilon_v\rho_{s1} - \\
&\qquad 2\varepsilon_Q(\rho_{c1} + \rho_{s1}) - 2\varepsilon_{or}(\rho_{c1} - \rho_{s1}) \\
2\eta_{c2} &= 2\eta + v_2 + (v_4 - 2v_2 - 2v_3)\rho_{c1} + \\
&(v_5 - v_2 - v_3)\rho_{s1} - 2\varepsilon_v\rho_{c2} - \\
&\qquad 2\varepsilon_Q(\rho_{c2} + \rho_{s2}) - 2\varepsilon_{or}(\rho_{c2} - \rho_{s2}) \\
2\eta_{s2} &= 2\eta + v_3 + (v_6 - 2v_2 - 2v_3)\rho_{s1} + \\
&(v_5 - v_2 - v_3)\rho_{c1} - 2\varepsilon_v\rho_{s2} - \\
&\qquad 2\varepsilon_Q(\rho_{c2} + \rho_{s2}) - 2\varepsilon_{or}(\rho_{c2} - \rho_{s2})
\end{aligned}
$$

4. At the end of section 4.3, the renormalization factor for the matrix elements of electrostatic interactions should read ε/n^2.

5. One of the curves in Figure 7 was incorrect. The amended version of Figure 7 is provided.

6. Some of the equations in the Supporting Information are corrected in the new version.

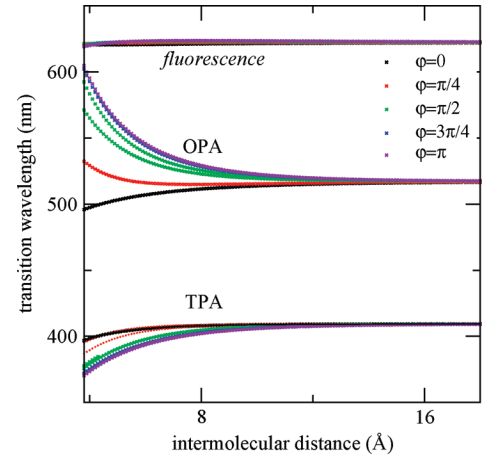

Figure 7. Only the TPA calculated at $\varphi = 0$ differs from the original figure.

Supporting Information Available: Explicit expressions for the electrostatic interactions energies, v_i, in Table 4. This material is available free of charge via the Internet at http://pubs.acs.org.

10.1021/jp100418b
Published on Web 02/04/2010